

**Calcium dynamics in dendrites and spines  
of spiny neurons in the somatosensory  
'barrel' cortex of the rat**

**Referees: Prof. Dr. Bert Sakmann  
Prof. Dr. Dr. Christoph Cremer**

**Dissertation**  
**submitted to the**  
**Combined Faculties for the Natural Sciences and for Mathematics**  
**of the Ruperto-Carola University of Heidelberg, Germany**  
**for the degree of**  
**Doctor of Natural Sciences**

**presented by**  
**Diplom-Physicist Thomas Nevian**  
**born in Oberhausen, Germany**

**Oral examination: 12.02.2003**

## **Calcium dynamics in dendrites and spines of spiny neurons in the somatosensory ‘barrel’ cortex of the rat**

Two-photon excitation fluorescence microscopy was combined with the patch-clamp technique to study the  $\text{Ca}^{2+}$  dynamics in dendrites and spines of spiny neurons of layer 4 of the somatosensory cortex in acute thalamocortical brain slices of young (P13-P15) rats. Back-propagating action potentials (bAPs) resulted in a transient rise in  $\text{Ca}^{2+}$  in all dendrites and spines tested, representing a global intracellular chemical signal about the activity of the cell. In contrast, synaptically evoked excitatory postsynaptic potentials (EPSPs) resulted in a synapse specific, local increase in  $\text{Ca}^{2+}$ . Pairing both stimuli at different inter-stimulus intervals revealed a precisely tuned coincidence detection mechanism for pre- and postsynaptic activity, coded in the peak  $\text{Ca}^{2+}$  transient amplitude. Linear, sub- and supralinear summation of the  $\text{Ca}^{2+}$  transients, depending on the time interval and the order of bAP and EPSP, was found.  $\text{Ca}^{2+}$  influx was maximal when the action potential followed synaptic stimulation within less than 20 ms. The mechanism of maximal  $\text{Ca}^{2+}$  influx could be explained by the properties of the NMDA receptor channel, which was activated by binding glutamate during synaptic stimulation and subsequent relief of the  $\text{Mg}^{2+}$  block by the bAP. Coincidence detection was restricted to the synaptic contact and it did not depend on the distance of the contact from the soma. This temporally and spatially highly restricted coincidence detection mechanism, which employed the  $\text{Ca}^{2+}$  transient amplitude as a readout signal might serve as an input specific trigger for spike-timing dependent plasticity. Indeed potentiation of EPSPs to 150% of the baseline amplitude could be induced by pairing extracellular stimulation with bAPs within the coincidence detection interval. Reversing the order of the stimuli resulted in depression of the EPSP amplitude to 70%. Thus it was concluded that spiny neurons in layer 4 of the juvenile rat barrel cortex exhibit spike-timing dependent plasticity, which corresponded well to the  $\text{Ca}^{2+}$  code used by their spines for coincidence detection.

## **Kalzium Dynamik in Dendriten und Dornen von Sternzellen im Fäßchenfeld des somatosensorischen Kortex der Ratte**

Ein Zwei-Photonen Fluoreszenz Mikroskop wurde mit einem Aufbau für Patch-Clamp kombiniert, um die Kalzium Dynamik in Sternzellen in Schicht 4 des somatosensorischen Kortex in Gehirnschnitten von jungen Ratten (P13-P15) zu untersuchen. Zurücklaufende Aktionspotentiale verursachten einen kurzzeitigen Anstieg des intrazellulären Kalziums in allen Dendriten und Dornen. Dieser Anstieg repräsentierte ein globales intrazelluläres, chemisches Signal über den Aktionszustand der Zelle. Im Gegensatz dazu, resultierten synaptisch ausgelöste postsynaptische Potentiale in einem lokalen Anstieg der intrazellulären Kalziumkonzentration. Das Paaren beider Stimuli mit variierendem zeitlichen Abstand zeigte einen genau abgestimmten Koinzidenz-Detektions Mechanismus für prä- und postsynaptische Aktivität, dessen Ergebnis in der absoluten Kalziumamplitude kodiert wurde. Die lineare, sub- oder supralineare Summation der Kalziumtransienten war von dem zeitlichen Abstand und der Reihenfolge von prä- und postsynaptischer Aktivität abhängig. Der Kalziumeinstrom war maximal, wenn das Aktionspotential der synaptischen Aktivierung innerhalb von 20 ms folgte. Der Mechanismus konnte durch die Eigenschaften des NMDA Rezeptors erklärt werden. Die Koinzidenz-Detektion war ebenfalls räumlich auf die aktive Dorne beschränkt und war nicht von der Entfernung der Dorne vom Zellkörper abhängig. Dieses zeitlich und räumlich sehr beschränkte Koinzidenz-Signal, welches den Grad der Koinzidenz in der Kalziumamplitude kodierte, könnte eingangsspezifisch zur Veränderung der synaptischen Verbindungstärke während korrelierter Aktivität genutzt werden. In der Tat konnte durch koinzidente prä- und postsynaptische Aktivität die Amplitude postsynaptischer Potentiale auf 150% im Vergleich zur Referenzamplitude verstärkt werden. Ein Umkehren der Abfolge der Stimulierung resultierte in einer Depression der postsynaptischen Potentiale auf 70%. Damit wurde gezeigt, dass Sternzellen in Schicht 4 des Fäßchenkortex von jungen Ratten aktivitätsabhängige Plastizität zeigen, welche gut mit dem Kalziumkode der Koinzidenzdetektion übereinstimmt.

# Contents

<b>1 Summary</b>	<b>1</b>
<b>2 Introduction</b>	<b>7</b>
<b>2.1 Preface</b>	<b>7</b>
<b>2.2 Biological neuronal networks</b>	<b>8</b>
2.2.1 Neurons	8
<i>Morphology &amp; types</i>	9
<i>Resting membrane potential</i>	10
<i>Action potentials</i>	11
2.2.2 Synapses	12
<i>Synaptic transmission</i>	13
<b>2.3 LTP, LTD &amp; memory</b>	<b>16</b>
2.3.1 The Hebb postulate	18
2.3.2 Coincidence detection	18
2.3.3 Spike-timing dependent plasticity	19
2.3.4 The role of Ca <sup>2+</sup> as a second messenger and permanent synaptic modifications	20
<b>2.4 The barrel cortex</b>	<b>21</b>
2.4.1 Sensory information and cortical maps	21
2.4.2 Sensory pathway	23
2.4.3 Columnar and layered information processing in the neocortex	23
<b>2.5 Motivation</b>	<b>25</b>
<b>3 Methods</b>	<b>27</b>
<b>3.1 Slice preparation</b>	<b>27</b>
<b>3.2 Electrophysiology</b>	<b>28</b>
3.2.1 The patch-clamp technique	28
3.2.2 The patch-clamp experiment	28
<i>Experimental patch-clamp setup</i>	28
<i>Pipettes</i>	30
<i>Solutions</i>	30
<i>Patching</i>	31
<i>Pharmacology</i>	32

## Contents

---

3.2.3 Stimulation protocols	33
<i>Current injection</i>	33
<i>Extracellular stimulation</i>	33
<i>Induction protocol for long term plasticity</i>	34
<b>3.3 Two-photon microscopy</b>	<b>34</b>
3.3.1 Principles of fluorescence excitation	34
3.3.2 Experimental Setup	37
<i>Setup components</i>	37
<i>The femtosecond laser system</i>	40
<i>Optical setup</i>	41
3.3.3 Quantitative analysis of the optical system	43
<i>Pulse width in the object plane</i>	43
<i>Resolution</i>	44
<i>Photon count</i>	47
3.3.4 $Ca^{2+}$ imaging	49
<i><math>Ca^{2+}</math> indicators</i>	49
<i><math>Ca^{2+}</math> buffering</i>	51
<i>Line scan, frame scan and xyz scan</i>	52
<i>Data analysis of fluorescence traces</i>	56
<b>3.4 IR-scanning gradient contrast</b>	<b>58</b>
3.4.1 IR-video microscopy	58
3.4.2 Setup components for IR-scanning gradient contrast	59
3.4.3 IR-SGC principle	60
3.4.4 Advantages	63
3.4.5 Alignment free overlay of IR-SGC and fluorescence images	65
3.4.6 Single spines can be resolved	66
<b>3.5 Electroporation of <math>Ca^{2+}</math> indicators</b>	<b>67</b>
3.5.1 Single cell electroporation	67
<b>4 Results</b>	<b>69</b>
<b>4.1 Two-photon imaging of spiny stellate neurons</b>	<b>69</b>
<b>4.2 <math>Ca^{2+}</math> dynamics in spiny stellate neurons</b>	<b>73</b>
4.2.1 Backpropagation of action potentials in dendrites and spines	74
<i><math>Ca^{2+}</math> transients evoked by back-propagating APs</i>	74
<i>Effect of TTX and <math>Cd^{2+}</math> on <math>Ca^{2+}</math> transients.</i>	75
<i>Spine and shaft [<math>Ca^{2+}</math>] transients depend on distance to the soma.</i>	76
4.2.2 Buffer capacity	80
<i>Frequency dependence of <math>Ca^{2+}</math> transients</i>	81

4.2.3 Synaptically evoked $Ca^{2+}$ transients	83
$Ca^{2+}$ transients evoked by EPSPs	83
$Ca^{2+}$ transients in spines and shafts	85
Comparison of $Ca^{2+}$ transients in spiny stellates and star pyramids	86
Comparison of bAP and EPSP evoked $Ca^{2+}$ transients	87
Effect of GluR-channel antagonists	90
4.2.4 Pre- and postsynaptic coincident activity	92
$Ca^{2+}$ transients evoked by coincident EPSPs and back-propagating APs	92
Non-linear summation of $Ca^{2+}$ influx in spines.	93
Tuning curve of spine $Ca^{2+}$ influx evoked by coincident bAPs and EPSPs	95
Decay time constants of $Ca^{2+}$ transients	99
Supralinear $Ca^{2+}$ transients are localized to the spinehead	100
Dependence on spine location	100
Pharmacological dissection of supralinear $Ca^{2+}$ influx into spines	102
<b>4.3 Spike-timing dependent plasticity in spiny stellates</b>	<b>105</b>
4.3.1 Introductory remarks	105
4.3.2 LTP experiments	107
4.3.3 LTD experiments	108
4.3.4 Plasticity Conclusion	109
<b>5 Discussion</b>	<b>111</b>
5.1 Two-photon microscopy for imaging spiny neurons in acute brain slices	111
5.2 IR-scanning gradient contrast imaging	112
5.3 $Ca^{2+}$ transients in dendrites and spines of spiny neurons	114
Spiny stellate neurons and star pyramidal neurons have the same $Ca^{2+}$ dynamics	114
Back-propagating action potentials	115
Estimation of absolute $[Ca^{2+}]$ levels evoked by single APs	115
Buffer capacity	116
Spineous $Ca^{2+}$ transients	117
Coincidence detection	118
Electrically "silent" synaptic contacts	120
Physiological relevance of bAPs and spine $Ca^{2+}$ transients for L4 cells	121
5.3 LTP induction in spiny neurons	122
<b>6 Outlook</b>	<b>123</b>
6.1 Acknowledgements	125
<b>7 References</b>	<b>127</b>

# 1 Summary

Spiny neurons in layer 4 of the rat barrel cortex receive whisker specific sensory input via thalamic afferents. They feed-forward amplify incoming excitation and then relay it to supragranular layers within the same cortical column. Spiny neurons are highly interconnected with other spiny cells of the same barrel and synaptic transmission is very reliable. Their dendritic tree is exclusively restricted to the barrel in which the cell soma is located reflecting the local network anatomy. The distinct anatomy and visualizability of the barrel cortex in acute brain slices make it a good model system to study information processing and plasticity within a well described cortical map on the single cell level.

$\text{Ca}^{2+}$  is an important second messenger for synaptic modification in spiny neurons. Based on electrophysiological evidence it was proposed that spiny neurons possess different  $\text{Ca}^{2+}$  dynamics properties from other excitatory neocortical neurons. Despite the detailed electrophysiological characterization of spiny neurons in the barrel cortex no  $\text{Ca}^{2+}$  imaging studies had been performed to date. The three-dimensional morphology of the dendritic tree with small diameter branches prevented detailed imaging studies of the elementary  $\text{Ca}^{2+}$  transients so far. The aim of this study was to characterize the  $\text{Ca}^{2+}$  transients in spiny neurons evoked by different patterns of activity to understand the dynamics of this important second messenger.

A combination of electrophysiological whole-cell recordings with two-photon excitation (TPE) fluorescence microscopy was used to image the  $\text{Ca}^{2+}$  dynamics in spiny neurons of layer 4 of the barrel cortex in acute brain slices. The whole-cell measurements allowed to record and to manipulate the electrical activity of the neuron and to load it via the recording pipette with  $\text{Ca}^{2+}$  sensitive indicator dyes. Simultaneous fluorescence measurements allowed to correlate the electrical activity to the corresponding  $\text{Ca}^{2+}$  influx. TPE microscopy was particularly suited for imaging small structures, like spines and dendrites, in the highly scattering environment of acute brain slices with with enough contrast and high spatial and temporal resolution to follow physiological events. This non-linear optical imaging method with its intrinsic optical sectioning properties enabled the visualization of the three-dimensional morphology of the dendritic tree of spiny neurons and to image the  $\text{Ca}^{2+}$  dynamics for certain patterns of activity in small dendrites and individual spines.

## Summary

---

A new imaging mode, the IR-scanning gradient contrast (IR-SGC) technique, was discovered and applied to imaging in brain slices. It allowed the online-overlay of a highly contrasted IR image of a brain slice with the fluorescence image of a spiny neuron. The resulting combined image greatly facilitated the precise targeting of an extracellular stimulation pipette along the dendritic tree, thus enabling the study of synaptic contacts at different distances from the soma. This allowed the spatial mapping of synaptically evoked  $\text{Ca}^{2+}$  transients.

The  $\text{Ca}^{2+}$  transients evoked by action potential (AP) firing, synaptic stimulation and the combination of these two stimuli were recorded in the dendrites and spines of spiny neurons in thalamocortical brain slices of young (P13 - P15) rats at physiological temperature (34 - 36° C). Most of the cells were filled with the  $\text{Ca}^{2+}$  indicator Oregon Green Bapta-1 (OGB-1, 200  $\mu\text{M}$ ).

Two subtypes of spiny neurons were identified based on the morphology of their dendritic tree in the TPE image. The majority of the cells were spiny stellate neurons (80%) characterized by their typical asymmetric dendritic arbor, confined to the barrel borders. The rest (20%) were classified as star pyramidal neurons with a small, but prominent apical dendrite and a symmetrical basal dendritic arbor. Even though the two cell types had a different morphology, no significant differences in the  $\text{Ca}^{2+}$  dynamics were found for any of the stimulation protocols used. Thus the results were pooled.

Brief somatic current injection evoked a single AP, which resulted in a transient rise in  $[\text{Ca}^{2+}]_i$  in all dendrites and spines tested from a low resting level ( $[\text{Ca}^{2+}]_0 = 42 \pm 4$  nM) to  $[\text{Ca}^{2+}]_{\text{AP}} = 105 \pm 22$  nM (OGB-1, 200  $\mu\text{M}$ ). Fluorescence transients measured in a spine and the adjacent shaft had similar peak fluorescence amplitudes ( $(F/F)_{\text{max}}$ ) and similar fluorescence decay time constants ( $\tau = 402 \pm 196$  ms), indicating similar buffering and extrusion mechanisms.  $\text{Ca}^{2+}$  transients were blocked by the voltage dependent  $\text{Na}^+$  channel blocker tetrodotoxin (TTX) and the voltage dependent  $\text{Ca}^{2+}$  channel (VDCC) blocker  $\text{Cd}^{2+}$ , suggesting that  $\text{Ca}^{2+}$  influx was mediated by VDCCs activated by back-propagating APs (bAPs).  $(F/F)_{\text{max}}$  evoked by a single bAP decayed with the distance from the soma with an apparent length constant of 195  $\mu\text{m}$ . Single AP evoked  $\text{Ca}^{2+}$  transients and trains of APs up to 20 Hz showed no indication for branchpoint failures in the dendritic tree. The frequency of AP firing was linearly coded in the dendrites by a plateau level of  $[\text{Ca}^{2+}]_i$  up to 100 Hz. Thus AP initiation at the soma resulted in a global signal in the dendrites and spines of spiny neurons, coded by the  $[\text{Ca}^{2+}]_i$  amplitude.



Estimation of the endogenous  $\text{Ca}^{2+}$  binding ratio yielded similar values in spines ( $\tau_s = 20$ ) and dendrites ( $\tau_s = 22$ ), as well as similar endogenous decay time constants ( $\tau_{\text{spine}} = 46$  ms,  $\tau_{\text{shaft}} = 36$  ms). This confirmed the notion, that dendrites and spines in spiny neurons comprise a homogenous compartment in terms of endogenous  $\text{Ca}^{2+}$  buffers and extrusion mechanisms. Taking the rise in free  $[\text{Ca}^{2+}]_i$  in the presence of  $\text{Ca}^{2+}$  indicator into account, a peak  $[\text{Ca}^{2+}]_i$  amplitude of  $1.2 \mu\text{M}$  evoked by a single AP was estimated. A functional implication of the fast decay time constant was that suprathreshold activity at the behavioral relevant ‘whisking frequency’ of 10 Hz evoked  $\text{Ca}^{2+}$  transients in dendrites and spines, which were well separated, decaying back to resting  $\text{Ca}^{2+}$  levels before the onset of the next AP evoked  $\text{Ca}^{2+}$  transient.

Synaptically evoked subthreshold activity resulted in somatically recorded excitatory postsynaptic potentials (EPSP) with corresponding  $\text{Ca}^{2+}$  transients in the active synaptic contact, mainly mediated by n-methyl-d-aspartate receptors (NMDARs). The  $\alpha$ -amino-3-hydroxy-5-methyl-isoxazole-4-propionic acid sensitive receptors (AMPA), which were coactivated during synaptic transmission provided the membrane depolarization to partially relieve the  $\text{Mg}^{2+}$  block from the NMDARs. The  $\text{Ca}^{2+}$  transients were restricted to the spinehead with only little spread into the adjacent shaft. Comparison to AP evoked  $\text{Ca}^{2+}$  transients in the same spines yielded a larger peak fluorescence amplitude evoked by an EPSP ( $(F/F)_{\text{EPSP}} = 0.6 \pm 0.3$ ) than by an AP ( $(F/F)_{\text{AP}} = 0.4 \pm 0.2$ ). The spatial profile of  $(F/F)_{\text{EPSP}}$  measured in active spines at different distances from the soma showed no distance dependence, whereas  $(F/F)_{\text{AP}}$  decreased with the distance of the spine from the soma. Analysis of the decay time constants revealed a correlation between the decay time of an EPSP evoked  $\text{Ca}^{2+}$  transient and the length of the spine. Thus  $\text{Ca}^{2+}$  transients evoked by synaptic activity represent an input specific, localized signal, which is shaped by the morphology of the spine.

Pairing of EPSPs with bAPs at different inter-stimulus time intervals resulted in linear, sub- and supralinear summation of the  $\text{Ca}^{2+}$  transients. The  $\text{Ca}^{2+}$  transients did not only depend on the order of the stimuli, but they also depended critically on the relative timing. This was revealed by measuring a ‘timing’ curve ranging from  $-300$  ms (AP-EPSP) to  $300$  ms (EPSP-AP). If an AP followed an EPSP within less than  $20$  ms a maximal supralinear  $\text{Ca}^{2+}$  influx was discovered (linearity =  $2.3$ ). This time window is proposed as the ‘coincidence detection window’ of spines of spiny neurons, in which the peak  $\text{Ca}^{2+}$  transient amplitude was significantly increased. At larger time intervals the  $\text{Ca}^{2+}$  influx corresponded to the expected linear sum. Strong evidence was found that the supralinear summation was mainly mediated

by NMDARs. The decay time of the supralinearity of 35 ms corresponded well to the kinetics of the NMDAR and the supralinear  $\text{Ca}^{2+}$  influx could be completely abolished by blocking NMDARs. Thus the bAP was thought to relieve the  $\text{Mg}^{2+}$  block of the number of NMDARs, which were activated by glutamate resulting in an amplification of the NMDAR mediated  $\text{Ca}^{2+}$  influx. It was found that this signal was restricted to spineheads and independent of the distance of the spine from the soma. This temporally and spatially highly restricted coincidence detection mechanism, which employed the  $\text{Ca}^{2+}$  transient amplitude as a readout signal, might serve as a trigger for input specific synaptic modifications. The distance-independence rendered it as an universal mechanism for spike-timing dependent modifications of synaptic strength.

It was shown that blocking AMPARs had no effect on the supralinear  $\text{Ca}^{2+}$  influx during coincidence activity even though the EPSP evoked peak  $\text{Ca}^{2+}$  transient amplitude was in abolished completely. This resembled the situation in 'silent synapses' which possess no functional AMPARs. The results suggest that NMDAR-only containing synapses also code coincident activity in a supralinear  $\text{Ca}^{2+}$  influx, which could trigger the activation or insertion of AMPARs.

The asymmetric shape of the 'timing curve' and the strong dependence on the NMDAR suggested that coincident activity might trigger, despite previous reports, long-term potentiation (LTP). Indeed LTP could be induced by pairing extracellular stimulation with bAPs within the coincidence detection time interval defined by the supralinear  $\text{Ca}^{2+}$  influx (EPSP-AP,  $t = 10$  ms). The EPSP amplitudes were significantly increased to  $146 \pm 7\%$ . Reversing the order of pre and postsynaptic activity (AP-EPSP,  $t = -10$  ms) resulted in long-term depression to  $68 \pm 4\%$  of control. Thus spiny neurons showed spike-timing dependent plasticity, which is consistent with the  $\text{Ca}^{2+}$  code used by their spines for coincidence detection.



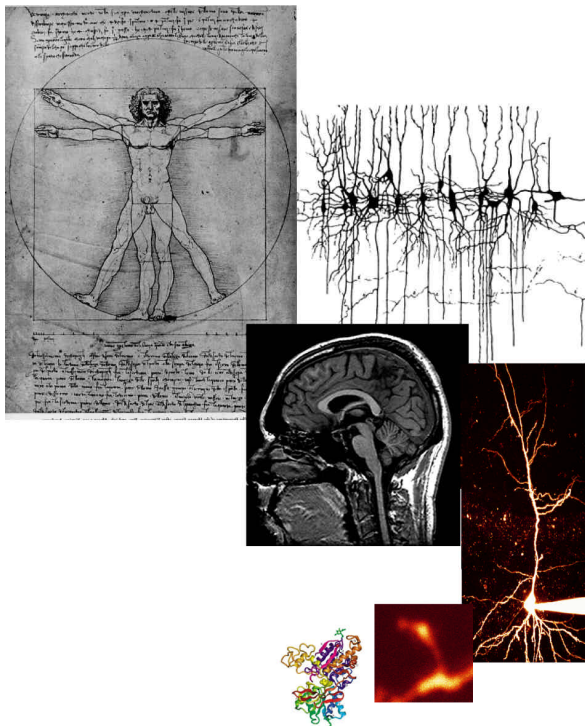


**Figure 2.1** *The brain and its different levels of complexity*

*Neurobiological research addresses the different levels of complexity of the brain. Behavioral output is studied on the intact organism. Non-invasive imaging techniques can visualize the metabolic state of different brain regions and they have given insight into the working brain. On the level of neuronal networks the brain seems to be organized in small basic units of computation with a distinct local anatomy. The basic building block of these networks is the neuron. Its properties and its signal processing capabilities are just about to be understood. Each individual synaptic contact acts as a basic integration unit for synaptic input and it is thought that they encode memory traces. Thus understanding the properties of a single synaptic contact is very important. On the last level of biological information processing are the structure and function of individual proteins. They determine the macroscopic behaviour of single spines and of cells.*

## 2 Introduction

### 2.1 Preface

Understanding the brain is one of the last great challenges in science. The final goal of neuroscience is to gain an insight into human behaviour and the emergence of consciousness. Despite the brain being a complex structure with about 100 billion cells, which have on average 10000 connections (Stevens 1979), there are general principles ruling the anatomy, connectivity and signal transmission within this vast number of cells. The function of the brain can be investigated on different levels of complexity which range from the behaviour of an organism, the anatomy of neuronal networks, the properties of single cells down to the functioning and molecular structure of single proteins (Fig 2.1). The basic building block of information processes in the brain is the neuron, a highly specialized cell that codes information in electrical activity. Whether higher brain functions, behaviour or the emergence of consciousness can be explained by the properties of the individual neuron or by emergent system effects occurring on the level of large ensembles of neurons is still a point at issue. Erwin Schrödinger states the problem of the physical principles of consciousness like this:

*“Die Welt ist ein Konstrukt aus unseren Empfindungen, Wahrnehmungen, Erinnerungen. ... Das Manifestwerden der Welt ist an sehr spezielle Vorgänge in sehr speziellen Teilen eben dieser Welt gebunden, nämlich an gewisse Vorgänge in einem Gehirn. Das ist ein außerordentlich merkwürdiges Bedingungsverhältnis, und man kann nicht umhin, sich zu fragen: durch welche besonderen Eigenschaften sind diese Gehirnvorgänge ausgezeichnet, daß gerade sie die Manifestation herbeiführen? Läßt sich vermuten, welchen materiellen Vorgängen diese Fähigkeit zukommt, welchen nicht? Einfacher ausgedrückt: welche materiellen Vorgänge sind direkt mit Bewußtsein verknüpft?”*

(Schrödinger 1982)

The brain is constantly active and its constituents are in a constant dynamic change continuously adapting to new situations. Electrical and chemical signals are transmitted and processed. The neuronal networks are rewired, connections between neurons are broken, new

synapses are formed and their strengths are adjusted. It is thought that memory traces are stored in the strength of the synaptic contacts. Even though solving the problem of consciousness is definitely not the aim of this study it is very important to study and understand neuronal networks at the cellular level to gather insight into the processes that govern and underlie the modifications of single synaptic contacts.

## 2.2 Biological neuronal networks

In this paragraph a basic introduction into the principles of biological neuronal networks is

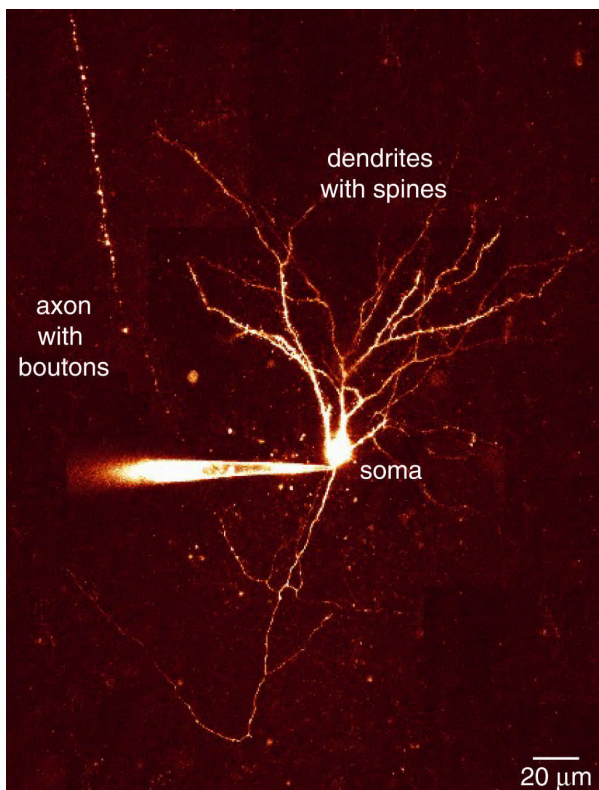


**Figure 2.2 The neuron**

*Two-photon fluorescence excitation image of a neuron in a brain slice depicting the general morphology of a neuron. Neurons are polarized cells with their inputs arriving from other cells mainly on their dendrites and spines. The input is integrated close to the soma at the axon initial segment and if a threshold is reached an action potential travels down the axon to the sites of transmitter release in the boutons and axon terminals.*

given. The properties of neurons, signal transduction at a synapse and activity dependent modifications of synaptic strength are covered.

### 2.2.1 Neurons

The nervous system consists of individual nerve cells called neurons and neuro glia cells (Fig 2.3). Whereas neurons are generally perceived to be the major cells to process information glia cells are thought to build a supportive framework for homeostasis of the neuronal network. Recent work indicates that this passive role of the glia cells is not their only function and that they might be involved in long range signaling, coordinating activity in different parts of the brain (Fields and Stevens-Graham 2002). Nevertheless neurons are the electrical excitable cells, which process and exchange signals with one another. The anatomy and distinct cellular shape of neurons

were first described by Ramón y Cajal by staining neuronal tissue with the Golgi staining method (Cajal 1894).

### *Morphology & types*

The morphology and size of individual neurons differ greatly within the nervous system, depending on location and on function. However some general morphological features are common to all neurons (Fig 2.2). Every neuron consists of a soma, which contains the nucleus and the organelles for homeostasis and protein synthesis. In contrast to other cell types, neurons are highly polarized cells with distinct, specialized input and output regions. The regions where neurons receive input from other neurons are the dendrites. Dendrites are characterized by a highly branching, treelike shape. Little protrusions from the dendrite are called spines. These are the structures, which form the points of contact, called synapses, to other cells. The output region of a neuron is the axon. It also shows extensive branching. The structure, which contacts other neurons, mainly on spines and dendritic shafts, are the so

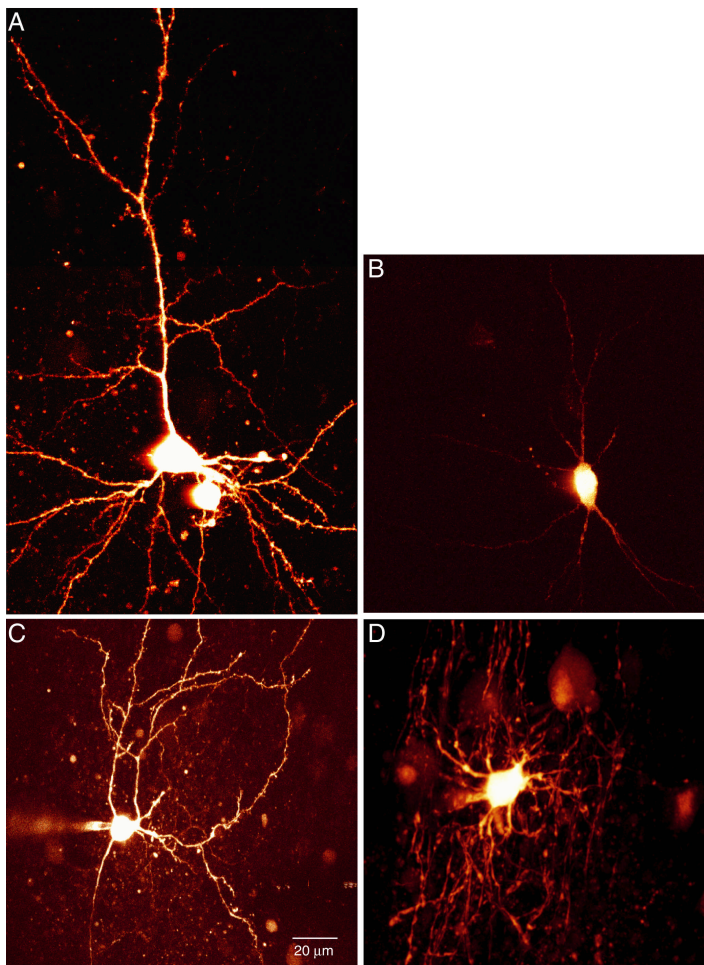


**Figure 2.3** *Types of cells in the neocortex*

**A** A Layer 2/3 pyramidal neuron. Pyramidal neurons are the most abundant cell type in the neocortex. They can be easily identified by their prominent apical dendrite pointing towards layer 1.

**B** A bitufted inhibitory interneuron in layer 2/3. This type of interneuron receives excitatory input from pyramidal neurons and inhibits neighbouring cells.

**C** A spiny stellate neuron in layer 4 of the barrel cortex. This type of cell receives input from the thalamus and other spiny stellate cells. The morphology of the dendritic arbor respects the barrel boundaries in which the soma of the cell is located.

**D** Glia cells are mainly thought to support excitable neuronal cells. They possess highly branching, fine processes, which engulf the surrounding neurons.

called boutons. Most boutons in neocortical neurons appear as an ‘enpassant’ thickening of the axonal cable.

The largest population of neurons in the neocortex belongs to the type of pyramidal neurons. They make up about 80% of the excitable cells. Pyramidal neurons have a typical ‘pyramidal’ shape with a large, prominent apical dendrite pointing up to the pia terminating in a tuft and basal dendrites spreading laterally (Fig 2.3A). This type of neuron can be found in layer 2/3, layer 5 and layer 6 of the neocortex. Layer 5 pyramidal neurons are much larger than the pyramidal neurons found in layer 2/3. Since their apical dendrite extends up to layer 1 these neurons are thought to integrate input from different cortical layers. In layer 4, the input layer of the neocortex (see below), another type of neuron, called spiny stellate neuron, is prominent. This type’s dendrites are much shorter than the apical dendrites of pyramidal neurons and they are more compact (Fig 2.3C). The distinct dendritic morphology might correspond to different functions of the cell types. Whereas pyramidal neurons integrate information from different layers and other cortical regions, spiny stellate neurons amplify and relay incoming input from subcortical nuclei. Pyramidal and spiny stellate neurons both belong to the class of excitatory neurons due to the release of glutamate and its depolarizing effect on postsynaptic cells. A second class of neurons with a large variety of different cell types are inhibitory interneurons. They exert a hyperpolarizing inhibitory effect on postsynaptic cells. Inhibitory interneurons show a whole range of different morphologies (Fig 2.3B). They are distributed throughout the cortex and shape the spread of excitation in the cortical networks.

### ***Resting membrane potential***

Like other cell membranes, the neuronal cell membrane is made up of a lipid bilayer into which various membrane proteins are incorporated. Next to structural proteins these are enzymes, receptors, pumps and channels. The combination of special kinds of receptors, pumps and channels enables a neuron to transmit and receive electrical signals, a feature other cells do not show. Ion pumps and ion channels make the cell membrane permeable to charged ions. By means of metabolic energy, mainly in the form of hydrolyzing ATP, ion pumps generate an ion gradient across the membrane against the electrochemical gradient. The different distribution of charges across a semipermeable membrane gives rise to a potential difference across the membrane. At steady-state equilibrium the resting membrane potential is given by the Goldman-Hodgkin-Katz equation

$$V_m = \frac{RT}{F} \ln \frac{z_k P_k [X_k]_o + z_l P_l [Y_l]_i}{z_k P_k [X_k]_i + z_l P_l [Y_l]_o}$$



for different positively charged ionic species  $X$  and different negatively charged ionic species  $Y$ , with their respective valencies  $z$  and total permeabilities  $P$  on the outside (o) and inside (i) respectively.  $R$  is the gas constant ( $R = 8.31 \text{ Jmol}^{-1}\text{K}^{-1}$ ),  $T$  the absolute temperature and  $F$  the Faraday constant ( $F = 96485.31 \text{ Cmol}^{-1}$ ). The ion channels of neurons make the membrane mainly permeable to potassium, sodium, chloride and calcium ions, thus the resting membrane potential can be calculated taking only these ion species into account. The resting membrane potential ranges typically from  $-80 \text{ mV}$  to  $-60 \text{ mV}$  depending on the cell type.

ion	$[x_i]$ (mM)	$[x_o]$ (mM)
$\text{Na}^+$	10	151.25
$\text{K}^+$	145	2.5
$\text{Ca}^{2+}$	0.000046	2
$\text{Cl}^-$	20	133.5

**Table 2.1 Ionic concentrations**

*Concentrations of the main ion species responsible for the resting membrane potential inside of the cell  $[x_i]$  and in the extracellular space  $[x_o]$ .*

### **Action potentials**

The most important feature for signal transmission of a neuron is the ability to generate an action potential, a stereotyped, all-or-none transient depolarizing electrical signal, which spreads along the axon actively without attenuation. The molecular basis of the action potential are voltage sensitive ion channels. The generation and shape of an action potential can be explained by the interplay of voltage sensitive sodium and potassium channels. Above a certain membrane potential threshold, which is reached by depolarizing postsynaptic potentials terminating on the neuron, voltage sensitive sodium channels have a higher probability to be in the open configuration (i.e. the channel opens). This results in a further depolarization, since the membrane potential is driven toward the equilibrium potential for sodium (around  $+50 \text{ mV}$ ). Neighbouring stretches of membrane, which also contain voltage dependent sodium channels, are subsequently equally depolarized resulting in a spread of the excitation along the membrane. By way of this regenerative self-amplifying process, most of the sodium channels can switch to their open state in less than  $1 \text{ ms}$ . Then the voltage sensitive sodium channels rapidly inactivate, thereby reducing the sodium permeability of the

membrane. Voltage gated potassium channels, which have opened during the depolarization, lead to a potassium influx into the cell and cause a rapid hyperpolarization of the membrane back to the resting potential.

The process of action potential generation can be explained by looking at the current  $I$  across the cell membrane for a given ion species  $X$  with a conductivity of  $g$ , which is given by

$$I_x = g_x (V_m - V_{rev})$$

$V_m$  is the membrane potential and  $V_{rev}$  the reversal potential for the ion species  $g_x$  is voltage dependent and it can be described for the different ion channels and their different kinetic properties by the Hodgkin-Huxley equation, a system of differential equations for the rate constants of channel opening, closing and inactivation (Hodgkin and Huxley 1952).

The axon initial segment close to the soma, also called the axon hillock, has a high density of voltage sensitive sodium channels. In this region the incoming excitatory and inhibitory postsynaptic potentials are 'integrated' and 'compared' to the threshold value (determined by the channel density) of action potential firing, i.e. if a certain depolarization is reached an action potential is initiated. The action potential is then transmitted along the axon actively in an all-or-none fashion and with a stereotyped shape.

Action potentials do not just travel down the axon to cause transmitter release at the presynaptic boutons and terminals, they also invade the dendritic tree, which is mainly the input region of a neuron. Dendrites of most neurons also contain voltage sensitive sodium channels, which allow the back-propagation of action potentials initiated at the soma (Stuart 1994). The back-propagating action potential signals the state of activity (i.e. firing of an action potential) of a neuron back to its input region.

### 2.2.2 Synapses

Signal transmission between neurons can either be electrical or chemical. Electrical coupling of neurons functions via gap junctions, established through protein pores connecting the two membranes. The pore forming transmembrane proteins linking the lumen of both cells across the extracellular space are connexins. The connexin composition of the gap junction results in rectifying or nonrectifying electrical connections of different conductances. Electrical signaling via gap junctions is fast, without latency and it can result in the synchronization of the coupled neurons. Graded, subthreshold deviations from the resting membrane potential can be equally transmitted. Gap junction coupling is development dependent and seems to decrease with age (Bennett 1997).

The most important pathway for signal transmission is via chemical synaptic contacts. These are specialized structures, where the membrane of the presynaptic neuron is in close vicinity, just separated by the synaptic cleft, from the postsynaptic membrane. At the point of contact, both membranes contain a high density of proteins for signal transduction (Husi 2000). The sum of all single synaptic contacts existing between two neurons is referred to by the term synapse, coined by Sherrington. The distributed strength of all synapses has been proposed to be the basis of memory traces. Signal transmission at a single synaptic contact is now considered in more detail.

### *Synaptic transmission*

The anatomical basis of the synaptic contact is the presynaptic density located in a bouton or terminal in close vicinity to the postsynaptic density, mainly located on a spine head or a dendritic shaft. Pre- and postsynaptic membranes are spatially separated (and thus electrically isolated) by a 10 nm gap, the synaptic cleft. The presynaptic active zone is characterized by a cluster of vesicles containing neurotransmitter close to the membrane and a high density of voltage sensitive  $\text{Ca}^{2+}$  channels (Fig 2.4).

Upon invasion of the axonal tree by an action potential the voltage sensitive  $\text{Ca}^{2+}$  channels open. This results in a  $\text{Ca}^{2+}$  influx into the bouton.  $\text{Ca}^{2+}$  binds to proteins that trigger the fusion of the vesicles with the plasma membrane. Subsequently a fusion pore opens, expands and leads to the release of neurotransmitter from the lumen of the vesicle into the synaptic cleft. This mechanism of neurotransmitter release is called exocytosis, a highly regulated process of multiple protein-protein interactions for which influx and binding of  $\text{Ca}^{2+}$  is a prerequisite. The vesicle membrane is recovered from the plasma membrane again by endocytosis and the vesicles are either recycled and reloaded with neurotransmitter or degraded.

The neurotransmitter diffuses across the synaptic cleft and binds to receptors on the postsynaptic membrane. In the case of excitatory synaptic transmission the neurotransmitter released by pyramidal neurons and spiny stellate neurons is glutamate, a low molecular weight amino acid. On the postsynaptic membrane specialized glutamate receptors bind this ligand. There are three distinct groups of glutamate receptors with different pharmacological properties and functions. Depending on their subgroup composition the detailed properties might vary but here only the most important properties shall be discussed.

The first group of glutamate receptors form cationic ion channels, which after binding of glutamate are mainly permeable to  $\text{Na}^+$  and  $\text{K}^+$  ions. They are categorized into two groups depending on their sensitivity to the glutamate analogues kainate and  $\alpha$ -amino-3-hydroxy-5-methyl-isoxazole-4-propionic acid (AMPA). An opening of these channels at the resting

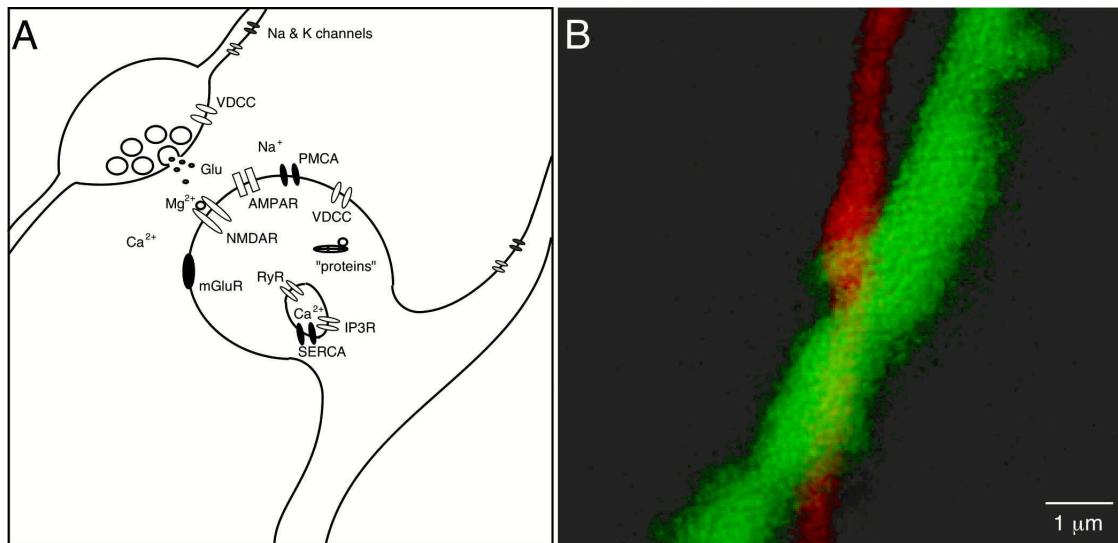


**Figure 2.4 Chemical synaptic transmission**

**A** Sketch of a single excitatory synaptic contact with the presynaptic bouton (left) and the postsynaptic spine (right). The most important proteins for the transduction process of electrical to chemical to electrical activity again and  $\text{Ca}^{2+}$  signaling are indicated. The voltage sensitive  $\text{Na}^+$  and  $\text{K}^+$  ion channels giving rise to AP propagation are outlined in the axonal and dendritic membrane in grey. If an AP invades the axonal tree voltage sensitive  $\text{Ca}^{2+}$  channels open leading to a  $\text{Ca}^{2+}$  influx triggering the release of the neurotransmitter glutamate. Glutamate diffuses across the synaptic cleft to the postsynaptic membrane where it binds to glutamate receptors. The AMPA type receptor becomes permeable to  $\text{Na}^+$  and  $\text{K}^+$  depolarizing the postsynaptic membrane. The NMDA receptor at resting membrane potential is blocked by  $\text{Mg}^{2+}$  thus it opens only if glutamate is bound and the membrane is depolarized as compared to the resting membrane potential. Then the NMDA receptor channel is the main source of  $\text{Ca}^{2+}$  influx into the spine. The mGluRs exhibit complex second messenger cascades in the postsynaptic cell.  $\text{Ca}^{2+}$  can also be released from internal stores. The low basal  $\text{Ca}^{2+}$  level inside the cell is restored by plasma membrane  $\text{Ca}^{2+}$  pumps (PMCA) and by pumps refilling the internal stores (SERCA). The local depolarization spreads passively along the dendritic tree giving rise to a EPSP, which can be measured at the soma. Another source of  $\text{Ca}^{2+}$  influx into the postsynaptic spine and dendrite is through voltage sensitive  $\text{Ca}^{2+}$  channels (VDCCs), which are opened by back-propagating action potentials.

**B** Two-photon fluorescence excitation image of a putative single synaptic contact. The axon and the bouton are labeled with a red indicator dye. The postsynaptic spine and dendritic shaft are visualized with a green fluorescent indicator dye. Presynaptic bouton and postsynaptic spine are in close proximity with a separation by the synaptic cleft of typically 10 nm.

membrane potential leads to a rapid depolarization of the postsynaptic membrane. The second type of glutamate receptor is the n-methyl-d-aspartate (NMDA) receptor channel. In contrast to the AMPA receptor channel, which has a linear current to voltage relationship, the NMDA receptor is an ion channel that under normal physiological conditions has a strongly rectifying current to voltage curve. The NMDA receptor has several conductance states. The prevailing conductance state of the NMDA receptor is determined not only by binding of

glutamate, but also by the membrane potential. At resting membrane potential the ion channel pore is blocked by  $Mg^{2+}$ . In this state, binding of glutamate only makes the receptor channel permeable to a small extent, and then only to  $Na^+$  and  $K^+$  ions. If the membrane is depolarized more strongly the  $Mg^{2+}$  is removed. So if binding of glutamate to the NMDA receptor is accompanied by membrane depolarization to relieve the  $Mg^{2+}$  block, the receptor channel also becomes permeable to  $Ca^{2+}$ . Thus the NMDA receptor channel needs two modalities occurring at the same time to become activated. This property of the NMDA receptor is assumed to be the underlying mechanism for coincidence detection during pre- and postsynaptic activity (Yuste 1995; Koester 1998), which might be important to induce usage dependent changes in synaptic strength on the single synaptic contact level. Thus to summarize so far: The release of glutamate from the presynaptic terminal results in a small depolarization of the postsynaptic membrane and some  $Ca^{2+}$  influx through the NMDA receptor.

The third class of glutamate receptors present on the postsynaptic membrane are metabotropic glutamate receptors (mGluRs). These are membrane spanning receptor proteins which trigger biochemical reactions mainly through G-protein coupled signaling cascades. Biochemical signaling can directly influence ion channels and hence regulate the permeability of the postsynaptic membrane. Other cascades activate second messengers, which in turn influence protein kinases, which can finally phosphorylate various protein substrates and thereby change their properties. Other second messengers like  $IP_3$  can trigger  $Ca^{2+}$  release from internal stores present in the postsynaptic cell.

Thus synaptic transmission at chemical synapses after firing of an action potential in the presynaptic cell leads to the transduction of the electrical signal into a chemical signal, which is then converted into an electrical signal and an elevation in the level of  $Ca^{2+}$  in the postsynaptic cell again. Proteins in the pre- and postsynaptic membrane functioning as ion pumps rapidly reestablish the ion concentration gradient across the membrane and drive the membrane potential back to the resting potential. Especially  $Ca^{2+}$  is pumped actively out of the cytosol into the extracellular space or into intracellular  $Ca^{2+}$  stores. Proteins binding  $Ca^{2+}$  can shape and reduce the free  $Ca^{2+}$  concentration in the cytosol.

In case of the transmission at glutamatergic synapses the resulting electrical postsynaptic signal is a small excitatory postsynaptic potential (EPSP) determined by the conductance change after binding of glutamate to the receptor ion channels and the current membrane potential. The small depolarization of the postsynaptic membrane then spreads passively along the dendritic tree. The shape, size and passive membrane properties of the dendrites determine the attenuation and filtering of the initial EPSP as it travels towards the soma and the axon initial segment (Bekkers 1996; Hausser 2001), where integration of all postsynaptic potentials occurs. The size and shape of an EPSP at the postsynaptic membrane is determined

by the number and timecourse of discrete neurotransmitter quanta released from the presynaptic terminal and the postsynaptic channel density (Silver 1996).

Synaptic transmission is not reliable. The release of a quantum (of neurotransmitter) of quantal size  $q$  from a presynaptic terminal occurs only with a certain probability  $p$ . According to the quantal hypothesis of synaptic transmission should the size of the postsynaptic potentials measured at the soma be binomially distributed (Castillo and Katz 1954; Bekkers 1994). Quantal analysis can yield  $q$ ,  $p$  and the number of synaptic contacts  $n$  (Redman 1990). Since the release probability and the quantal size can vary between single synaptic contacts, a clear cut binomial distribution of EPSP amplitudes can not be measured at all synapses (Wahl, Stratford et al. 1995). Optical quantal analysis at an individual synaptic contact can yield a direct measure of  $p$  and  $q$ , overcoming this problem.

Synaptic transmission also depends on the history, i.e. previous activity, of the synaptic contact. Long term modifications induced by specific patterns of pre- and postsynaptic activity, which result in permanent changes of synaptic transmission properties, will be investigated in the next paragraph. Usage dependent short term plasticity can result in facilitation or depression of synaptic transmission to a subsequent action potential (Thomson 1993; Stevens 1995; Markram 1996). Short term effects are mainly accounted for by presynaptic mechanisms (Katz 1968; Rahamimoff 1968; Betz 1970; Zucker 1989). An action potential arriving at a terminal can result in the failure of transmitter release and thus in the failure of a postsynaptic potential even though the action potential causes presynaptic  $\text{Ca}^{2+}$  influx. A second action potential arriving with a short delay might add additional  $\text{Ca}^{2+}$  ions to the residual  $\text{Ca}^{2+}$  from the first action potential thus increasing the total amount of  $\text{Ca}^{2+}$  in the terminal. This higher concentration of  $\text{Ca}^{2+}$  might trigger release more reliably and it can result in the release of more quanta giving rise to a larger postsynaptic potential. On the other hand a high release probability due to the first action potential might deplete the pool of readily releasable vesicles for a subsequent second action potential resulting in a smaller postsynaptic potential. The exact determinants of facilitation and depression at a synapse are more complicated, but it seems that the type of postsynaptic cell determines the direction of the short term plasticity effects (Reyes 1998).

## 2.3 LTP, LTD & memory

It makes sense to assume that since behaviour is reflected in a certain pattern of electrical activity experience dependent modifications of behavioural output are based on changes of the electrical excitability of the underlying neuronal circuits. Long term potentiation (LTP)

and long term depression (LTD) are long lasting activity dependent changes in synaptic strength between neurons (Isaac 1995; Nicoll 1995; Luscher 2000; Malinow 2000). It is widely believed that these phenomena provide an important key to understand the cellular and molecular mechanisms by which memories are formed and stored (Bliss 1993). Furthermore they might underlie the development and refinement of neuronal networks (Crair 1995). But whether LTP is really triggered during learning and is causally related to memory formation is still a matter of debate (Zamanillo 1999).

Long lasting modifications of synaptic strength were first reported experimentally by Bliss and Lomo in hippocampal slices (Bliss 1970). Since then LTP and LTD have been observed at many synapses in the hippocampus (Liao 1995), neocortical layer 5 (Markram 1996) and layer 2/3 pyramidal neurons (Feldman 2000), retinotectal synapses in *Xenopus* tadpoles

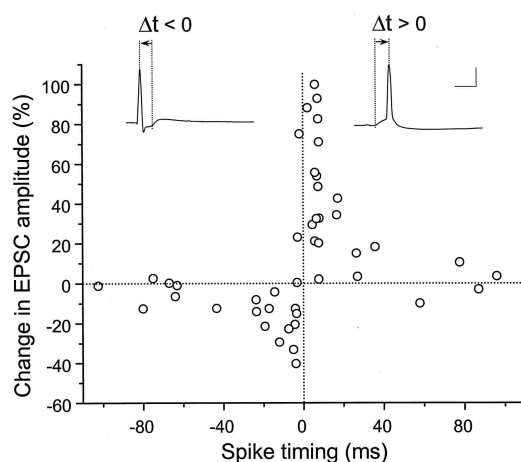


**Figure 2.5 Spike-timing dependent plasticity**

*The change in the EPSC amplitude after repetitive correlated spiking (60 pulses at 1 Hz) plotted against the spike-timing interval  $\Delta t$ . The synaptic potentiation and depression depends on the sequence (see insets) and the spike-timing interval of pre- and postsynaptic activity. The critical window for LTP and LTD induction is  $< 50$  ms. Coincident activity ( $\Delta t > 0$ ) results in LTP, whereas the reversed order results in LTD. Taken from (Bi 1998).*

(Zhang 2000; Engert 2002) and electrosensory lobe in mormyrid electric fish (Han 2000).

Despite the enormous work dedicated to LTP, the detailed cellular and molecular changes are still under investigation. It is not clear to what extent the changes are pre- or postsynaptic or both in origin (Malenka 1999). Some sorts of LTP (e.g. at the mossy fiber synapse in the hippocampus, (Nicoll 1995)) show different properties than other forms of LTP (e.g. in the cortex). The induction protocols, i.e. the different patterns of electrical activity that induce long term changes at the different synapses, vary a lot. Nevertheless some common features can be derived.  $\text{Ca}^{2+}$  plays a very important role in the induction of long term plasticity. Blocking the  $\text{Ca}^{2+}$  entry pathways during synaptic transmission as described above abolishes long term plasticity (Zucker 1999). LTP is input specific, since only the synapses which have been activated are modified. Another requirement seems to be the correlated electrical activity of the pre- and postsynaptic cells, that is in first approximation a depolarization of the postsynaptic membrane to some degree and simultaneous synaptic activation.

Following an idea by Hebb for correlated activity (see below), recent results show that synaptic modifications depend on the relative timing between pre- and postsynaptic activity (Markram 1997; Debanne 1998; Feldman 1998). The stimulation patterns for spike-timing dependent plasticity might be more physiological for plasticity induction than the commonly used tetanic stimulation protocols (Shi 1999). In the next paragraphs spike-timing dependent plasticity, the role of the NMDA receptor for coincidence detection, and the role of  $\text{Ca}^{2+}$  will be discussed.

### 2.3.1 The Hebb postulate

In 1949 D.O. Hebb published “Organization of Behaviour: A Neuropsychological Theory”. In this book he states his famous idea, which has since become known as the Hebb learning rule:

*“When an axon of cell A is near enough to excite cell B and repeatedly or persistently takes part in firing it, some growth process or metabolic change takes place in one or both cells such that A’s efficiency, as one of the cells firing B, is increased.”*

His idea was that memory traces, which influence behaviour, are stored in the connections between cells. In order to fine-tune a neuronal circuit these connections can be modified through the activity of the cells. The modification only takes place if the activity is correlated, thus obeying the rule of causality. This led to the idea that synaptic plasticity should be based on coincidence detection.

### 2.3.2 Coincidence detection

Best suited for coincidence detection are the properties of the NMDA receptor channel (Johnson 1987). As described above, its opening requires the binding of glutamate and the relieve of the  $\text{Mg}^{2+}$  block by depolarization. The NMDA receptor thus senses simultaneous activity at a synapse (glutamate release from the presynaptic cell) and activity of the cell (depolarization of the postsynaptic membrane by a backpropagating action potential (bAP)). Since the depolarization by a bAP is only brief (1-2 ms) the exact timing of pre- and postsynaptic activity is important. Firstly the bAP has to follow the synaptic activation and secondly it has to follow within the time window in which glutamate is bound to the NMDA



receptor. The amount of coincidence is encoded by the influx of  $\text{Ca}^{2+}$  through the open NMDA receptor channel.

### 2.3.3 Spike-timing dependent plasticity

Recent experiments have shown that the timing interval and the sequence of pre- and postsynaptic activity determine the amount and the direction of synaptic plasticity (Bi 1998; Feldman 2000; Froemke 2002). This led to the notion of spike-timing dependent plasticity. Reliable LTP was found when the presynaptic stimulus preceded the postsynaptic spike, but LTD was induced when the presynaptic spike followed the postsynaptic spike. Furthermore the amount of LTP or LTD is dependent on the relative spike-timing interval (Fig 2.5).

Spike-timing dependent modifications of synaptic strength can be found at many synapses, most of which show an asymmetric timing curve with a sharp transition from LTD to LTP (Bi 1998). Some synapses however, like the layer 4 spiny stellate to spiny stellate connection seem to exhibit a symmetric STDP curve (Egger 1999). In all cases the window for plasticity is restricted to  $\pm 20$  ms.

Spike-timing dependent plasticity (STDP) is an attractive model for the modification of synapses. Firstly, most synapses can be modified in both ways, giving the possibility to fine tune synaptic contacts without the risk of saturating or diminishing them. Secondly, during random activity, coincidence should happen with equal probability with positive or negative time delays, thus leaving the synaptic strength unaltered. Thirdly, during periods of learning, when sequences of input are repeatedly presented to a network of neurons with recurrent excitatory connections, a STDP learning rule based network will learn the sequence. The resulting pattern of activity in the network will tend to predict future input.

The mechanism underlying the asymmetric STDP curve can be explained for the LTP part, which obeys Hebb's learning rule, by the coincidence detection properties of the NMDA receptor. Yet the mechanism underlying induction of LTD cannot solely be explained by a moderate level of  $\text{Ca}^{2+}$  influx. An involvement of a second detector for LTD has been hypothesized (Karmarkar and Buonomano 2002). A good candidate could be the action of mGluRs (Anwyl 1999).

In conclusion spike-timing dependent plasticity is a physiological model that is based on the occurrence of spikes and their relative timing for synaptic modifications and it can be seen as a generalization of Hebb's learning rule.

### **2.3.4 The role of Ca<sup>2+</sup> as a second messenger and permanent synaptic modifications**

Resting levels of Ca<sup>2+</sup> in neurons are very low (~ 100 nM, (Maravall, Mainen et al. 2000)). During electrical activity, which opens Ca<sup>2+</sup> permeable ion channels, intracellular Ca<sup>2+</sup> levels can reach concentrations in the order of mM. In most forms of LTP postsynaptic Ca<sup>2+</sup> influx through NMDA receptors is required (Nicoll 1995). Ca<sup>2+</sup> is a second messenger which binds to many proteins bringing them into an active state for further downstream activity (Malenka 1989). One important step in the induction of LTP is Ca<sup>2+</sup> binding to Calmodulin, which then binds to Ca<sup>2+</sup>- and calmodulin-dependent protein kinase II (CaMKII) (Hudmon and Schulman 2002). CaMKII can phosphorylate inactive AMPA receptors, thereby directly increasing the depolarizing current flow through AMPA receptors and thus the size of the EPSP after subsequent synaptic stimulation (Hayashi, Shi et al. 2000; Poncer, Esteban et al. 2002).

Other Ca<sup>2+</sup> dependent signaling cascades can lead to the recruitment of new receptors to the postsynaptic density (Shi 1999) and even to protein synthesis from local mRNA (Aakalu 2001; Smith 2001). A further step is signaling to the nucleus for gene transcription (Kandel 2001; Steward 2001). All these steps have been shown to be important on different time scales of memory formation and consolidation (Dudai 2002). Recent studies showed an outgrowth of new spines after the induction of LTP (Engert 1999).

LTP and LTD as understood in this study is measured on the timescale of up to 60 min, because this is the time scale in which stable recordings in the whole cell configuration in acute slices can be made. Studies using extracellular recording electrodes in acute slices and cultures have reported LTP lasting for several hours (Bliss 1993). In vivo experiments have shown robust changes in the electrical properties of cells for days and even months (Abraham, Logan et al. 2002).

It is thought that the level of Ca<sup>2+</sup> during induction protocols determines which proteins become activated and thus determines the direction and magnitude of plasticity and the initiation of further signaling cascades (Zucker 1999). Moderate levels of Ca<sup>2+</sup> are thought to induce LTD, whereas high levels of Ca<sup>2+</sup>, which are reached during coincident activity, result in LTP. The pattern of activity (most induction protocols use repeated bursts of stimuli) might also be important. It has been shown that CaMKII can act as a local molecular memory for periodic Ca<sup>2+</sup> transients (Bayer 2001; Frankland 2001).

It is unlikely that the level of Ca<sup>2+</sup> is the only determinant for plasticity, since isolated firing of trains of APs in a cell also increase the Ca<sup>2+</sup> levels in the dendrites to a substantial level

(Helmchen 1996) and would result in global, unspecific changes in synaptic strength which has not as yet been reported.

## 2.4 The barrel cortex

### 2.4.1 Sensory information and cortical maps

All higher organisms receive information about their environment through specialized receptor neurons. These neurons are excitable cells which respond to different modalities of stimulation. Receptor neurons in the olfactory epithelium are sensitive to odors, in the retina of the eye to light, in the cochlea to sound and in the skin to touch. The amplitude and temporal pattern of the physical or chemical stimulus is coded by the receptor neuron in a certain pattern of electrical activity, which is transmitted to the nervous system for further processing. The task of higher order neuronal networks is then to integrate, associate and

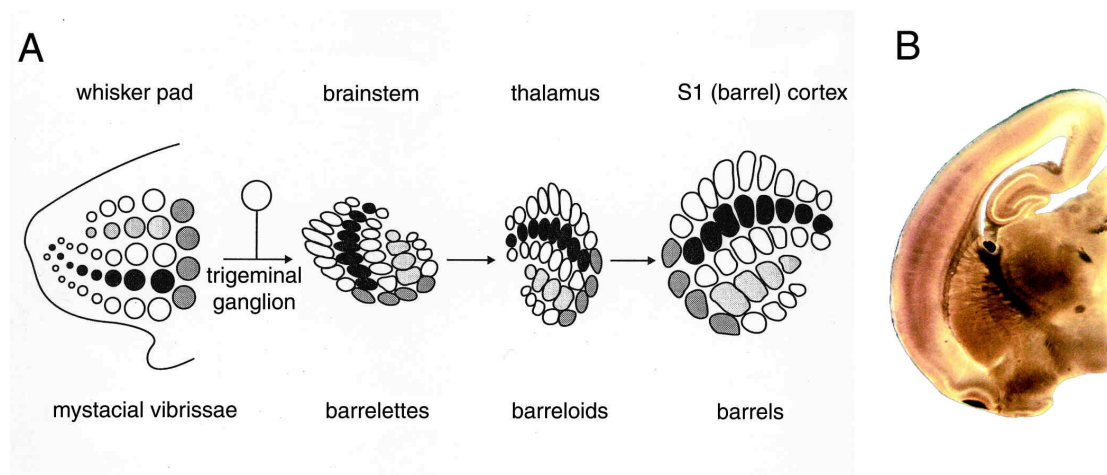


**Figure 2.6** *The sensory pathway of somatosensory signal transmission*

**A** *The stimulus transmission from the mystacial vibrissae to the barrel cortex is somatotopically organized. That is, the ordered representation of the vibrissae is conserved in neuronal maps in each step. The complete cortical map is here presented in a tangential plane through layer 4 of the barrel cortex. After (O'Leary 1994).*

**B** *Thalamocortical brain slice under brightfield illumination. The barrel structure in layer 4 can clearly be seen. It represents the (semi) saggital section through the representation of the whiskers in one row (e.g. the whiskers indicated in black in A). Modified from (Petersen 2000).*

categorize the electrical afferent activity and to respond with an output resulting in a certain behaviour.

Rats, like most rodents, are mainly active in the dark. They rely on olfactory cues and somatosensory cues received by their whiskers. Being one of the most important stimulus modalities for a rodent, the somatosensory system occupies a large region of the neocortex. The whiskers on the whisker pad of a rodent are arranged in an ordered fashion in arcs and rows and decreasing in size from posterior to anterior. This topographic order is conserved throughout the sensory pathway to the neocortex (O'Leary 1994). The spatial order allows to encode the stimulus position by activating different regions in the cortex. This somatotopic information processing results in spatially ordered cortical maps (Kleinfeld 1996). In case of the part of the somatosensory cortex representing the whiskers, the structure of the cortical map can directly be visualized in a brain slice preparation (Agmon 1991). In thalamocortical

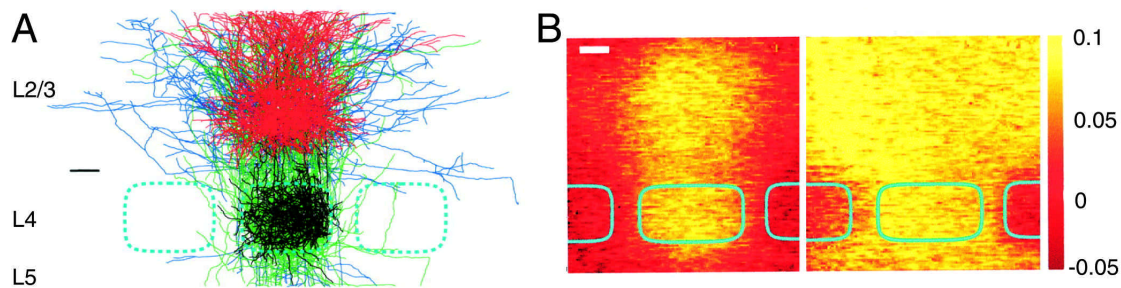


**Figure 2.7** *The spread of excitation within a cortical column*

**A** A normalized barrel visualizing the potential local network in a cortical column of the barrel cortex. Morphologically reconstructed layer 4 spiny stellate neurons and layer 2/3 pyramidal neurons are overlaid according to their position within one barrel. Spiny stellate dendrites are coloured in black and their axons in green. Pyramidal dendrites are indicated in red and their axons in blue. Note that the spiny stellate dendrites are confined to the barrel and that their dendrites mainly project up and down within the cortical column defined by the barrel borders. In contrast the axons of the pyramidal neurons spread horizontally to neighbouring barrels. The basal dendrites of the pyramidal neurons also seem to be mainly located above the home barrel.

**B** The spread of excitation after extracellular stimulation in layer 4 is visualized with voltage sensitive dye imaging. The left image is taken 15 ms after stimulation. The confinement of the axons and dendrites of the layer 4 cells seems to correspond to local excitation within the barrel borders. The signal in layer 2/3 is more spread out laterally at this timepoint. The right image shows the excitation 15 ms after the same stimulation after blocking inhibitory interneurons by bicuculline. Activity as recorded by the voltage sensitive dye is greatly enhanced. The spread of excitation in layer 2/3 is significantly further than under control conditions whereas the spread of excitation in layer 4 is still confined to the barrel. This experiment stresses the influence of inhibitory interneurons in shaping the spread of excitation in cortical layer 2/3 and in contrast the confined local connectivity of the network in layer 4. Images modified from (Petersen 2001). The scale bars represent 200  $\mu\text{m}$ .

slices distinct dark regions (~400  $\mu\text{m}$  in width) separated by lighter borders can be distinguished (Fig 2.6B). Electrophysiological *in vivo* recordings have established that each of these so called barrels receives the strongest input from just one whisker, the principal whisker (Brecht and Sakmann 2002; Margrie, Brecht et al. 2002). Thus the somatosensory cortex represents one example of spatially structured information processing in cortical maps, a fundamental feature of cortical organization. Other examples of cortical maps are the somatosensory “homunculus”, which represents a projection of the body surface onto the human cortex (Yang 1993), or ocular dominance columns in the visual system (Lowel 1987).

### **2.1.2 Sensory pathway**

The sensory information received by the whiskers is transmitted via different relay nuclei to the cortex (Fig 2.6A). The sensory mechanoreceptors located in the whisker follicle excite trigeminal ganglion cells upon deflection of a whisker. The excitation is then transmitted mainly via the principal trigeminal nucleus of the brain stem and the spinal trigeminal complex to the thalamus (ventral posteromedial (VPM), posterior group (Po) and intralaminar nuclei of the contralateral thalamus). Thalamic afferents project to layer 4 of the primary somatosensory cortex (S1). The somatotopic representation on the whisker pad is conserved in the neuronal architecture (cellular aggregates) of spatial representation at each stage of the afferent sensory pathway. In the brain stem principle whiskers are represented by barrelettes, in the thalamus by barreloids and in the cortex by a barrel (Fig 2.6). The cortex can modify the transmission of afferent sensory information by reciprocal corticothalamic connections, which serve as a feedback loop (Deschenes, Veinante et al. 1998).

On each level of signal transmission, integration of information from multiple whiskers occurs, which results in more complex response properties of the cells (Brecht and Sakmann 2002). The receptive fields of single cells can range from being single-whisker excited to being multi-whisker excited (Veinante 1999). Nevertheless, the principle whisker, which gives the strongest excitatory response, can be identified in each given cell aggregate. Parallel to more complex response properties, the number of cells on each level increases. In the thalamus a number of 200 cells in one barreloid make diverging connections to about 2000 cells in layer 4 of a single barrel.

### **2.1.3 Columnar and layered information processing in the neocortex**

Cortical information processing is organized in a layered structure (Fig 2.8). The neocortex can be divided into 6 distinct layers according to cell types, cell density and functionality. In sensory cortical areas layer 4 is the main input layer for sensory information from the

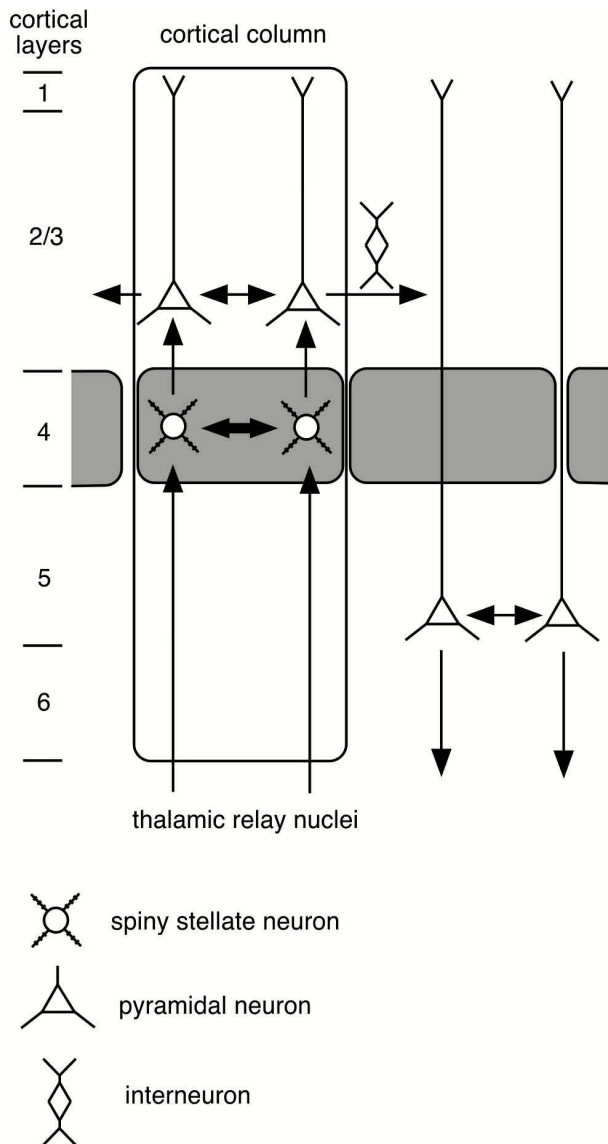


**Figure 2.8 Flow of information in the barrel cortex**

*This figure presents a simplified flow chart of information through the barrel cortex. Thalamic input is received and amplified mainly in layer 4 and is transmitted to layer 2/3. There pyramidal neurons perform interbarrel computation and transmit information to other cortical areas. Local inhibitory neurons shape the spread of excitation to neighbouring barrels. Interlaminar computation is then performed by layer 5 pyramids, which transmit their results to subcortical regions. Modified from (Luebke 2000).*

thalamus to the cortex (Killackey 1973; Ebner 1990). Some thalamic afferents also project to layer 6. The information is spread vertically from layer 4 to the layers directly above and below. This vertical flow of information is thought to occur in a columnar fashion (Feldmeyer 1999; Luebke, Egger et al. 2000). The division in cortical columns seems to be one general building principle of sensory information processing. A cortical column is an independent functional module, which processes the information of a particular feature of the afferent stimulus. In the somatosensory cortex layer 4 is characterized by the typical barrel like structure, in which one barrel receives the input from one principle whisker. This morphological feature seems to mark the cortical column for the signal processing from a single whisker (Fig 2.7A).

In layer 4 the main population of excitatory neurons are spiny stellate cells with a smaller population being classified as star pyramids (Feldmeyer 1999). They receive whisker specific input from strongly branching thalamic afferents. It is thought that they feed-forward amplify incoming excitation from the thalamus and then relay it to supragranular layers mainly within the same cortical column. Spiny stellate cells have spherical to oval somata of a diameter ranging

from 10-15  $\mu\text{m}$ . Their dendritic arbor is confined to a single barrel and their axons project vertically throughout all cortical layers with their targets predominantly in layer 4 and layer 2/3 of the same cortical column. These targets are mainly other spiny stellate neurons and layer 2/3 pyramidal neurons (Luebke, Egger et al. 2000). Spiny stellate cells have a high connectivity and their synapses have a low failure rate with a low coefficient of variation. Consequently the layer 4 circuit can be seen as an excitatory neuronal network that acts independently of neighbouring barrels (Petersen 2000; Petersen and Sakmann 2001). Inter-barrel computation and integration is then subsequently performed by layer 2/3 pyramids and layer 5 pyramids. The extent and shape of the spread of horizontal excitation is limited by local inhibitory networks and feed-forward inhibitory circuits receiving input from the thalamus. Lateral inhibition sharpens the response of one cortical column to the input from its principle whisker, thereby increasing the spatial focus of receptive fields by inhibiting excitation from surrounding whiskers (Fig 2.7B).

The output of the cortical somatosensory network is from layer 2/3 to other cortical areas including the motor cortex. Layer 5 and layer 6 pyramids project to subcortical regions like the spinal cord, the brain stem and the thalamus. Hence, the integrated sensory information is output to structures controlling the motor response and it is also fed-back to the sensory pathway to modify the response properties of subsequent afferent stimuli.

The distinct anatomy and visualizability of the barrel cortex makes it a good model system to study information processing and plasticity within a neocortical map in brain slices. Furthermore, the possibility to relate the barrel pattern of the neocortex directly to the somatosensory map allows to investigate the neuronal circuitry at the level of individual neurons and their synaptic connections in the context of the functional architecture of this map.

## 2.2 Motivation

$\text{Ca}^{2+}$  is very important for synaptic modifications in any neuron. The aim of this study was to understand and elucidate the  $\text{Ca}^{2+}$  dynamics in dendrites and spines of neurons of spiny neurons in layer 4 of the barrel cortex during different patterns of activity. Up to now, no  $\text{Ca}^{2+}$  imaging data had been acquired from spiny neurons due to the small size of their dendrites and elaborate three dimensional arborization. The  $\text{Ca}^{2+}$  dynamics in pyramidal neurons in layer 2/3, layer 5 and the hippocampus have extensively been studied (Denk 1996; Helmchen 1996; Koester 1998; Helmchen 1999; Svoboda 1999; Koester 2000; Sabatini 2000). The influx of  $\text{Ca}^{2+}$  into pyramidal neurons is an intracellular code for their electrical

activity with sophisticated computational properties for sub- and supralinear summation of the  $\text{Ca}^{2+}$  transients (Koester 1998). Whether the activity associated rise in dendritic and spineous  $\text{Ca}^{2+}$  is also a property of spiny stellate cells is an open question.

Recent studies have shown that these cells are plastic and that activity dependent modifications of the connectivity of cells in the barrel cortex can be achieved even after the critical period for whisker specific wiring (Crair 1995; Egger 1999). It was hypothesized, based on the pharmacology of LTD induction in spiny neurons, that the  $\text{Ca}^{2+}$  dynamics in this cell type might be different from other excitatory neurons in the neocortex. Thus by analyzing the fundamental principles of the  $\text{Ca}^{2+}$  dynamics in the cells which receive the first input from the thalamus to the cortex, general rules for synaptic plasticity might be derived.



## 3 Methods

Two-photon excitation (TPE) fluorescence microscopy (Denk 1990; Denk 1994) was combined with whole-cell patch clamp recordings (Stuart 1993) to measure  $\text{Ca}^{2+}$  transients in neurons of the barrel cortex in acute brain slices. The experimental setup of the microscope and the methods of brain slice preparation and patch-clamp recordings are explained in detail in this chapter. Furthermore the new imaging mode of IR-scanning gradient contrast (IR-SGC) is presented. Additionally a novel technique to fill cortical neurons with  $\text{Ca}^{2+}$  indicator dyes by electroporation is introduced.

### 3.1 Slice preparation

Thalamocortical slices were prepared from the somatosensory cortex of 13-15 day old (P13-15) Wistar rats. The rat was decapitated and the brain was quickly removed. All experimental procedures were in accordance with the German animal protection law. The brain was then placed on a slope and a diagonal cut was performed as described by Agmon and Connors (Agmon 1991). The brain was glued with the cut surface facing down onto a horizontally aligned piece of metal in a slicing chamber. First, the upper part of the brain was removed by cutting off a 2 mm thick slice and then 350  $\mu\text{m}$  thick slices were cut using a vibratome (home built) equipped with a razor blade in ice cold extracellular medium. The blade frequency and blade advancement speed were adjusted to yield the highest viability of the cells. The brain slices were incubated at 37 °C for 30 min and then stored at room temperature before recording. All experiments were performed at physiological temperatures (34-36 °C).

The extracellular solution contained 125 mM NaCl, 25 mM  $\text{NaHCO}_3$ , 2.5 mM KCl, 1.25 mM  $\text{NaH}_2\text{PO}_4$ , 1 mM  $\text{MgCl}_2$ , 25mM glucose and 2 mM  $\text{CaCl}_2$  (Biometra, Goettingen, Germany), bubbled with 95%  $\text{O}_2$  and 5%  $\text{CO}_2$ . 10  $\mu\text{M}$  glycine was always added to the extracellular solution (Johnson 1987).

The described slice preparation method results in brain slices with the barrel structure of layer 4 of the somatosensory cortex clearly visible with bright field microscopy (Feldmeyer 1999; Petersen 2000) and the thalamocortical projection fibers and the thalamus were present and still intact.

Sagittal brain slices were prepared in a similar way to the thalamocortical brain slice preparation. The difference was the orientation of the slicing plane. The brain was cut in two halves along the midline. One hemisphere was glued with the cut sagittal plane onto the tilted ( $\sim 20^\circ$ ) metal plane. Discarding the upper 1 mm of the brain, 300  $\mu\text{m}$  thick slices were cut and further processed as described above.

In contrast to the thalamocortical brain slice preparation some of the sagittal slices are aligned so that the apical dendrites of layer 2/3 and layer 5 pyramidal neurons run parallel to the slice surface increasing the number of viable cells of this cell type.

## **3.2 Electrophysiology**

### **3.2.1 The patch-clamp technique**

The electrical activity of individual neurons can be recorded with the patch-clamp technique developed by Neher and Sakmann (Neher 1976; Hamill 1981). The main principle is that a tight seal, a so called giga-seal, is formed between a glass pipette and the membrane of a neuron. This configuration allows to measure the small currents and voltages that are involved in neuronal activity. Originally developed to measure the currents flowing through single ion channels (Neher 1976; Brenner 1978), patch-clamp, especially in the whole-cell configuration, has been very useful to measure and control the electrical activity of individual neurons (Stuart 1994; Markram 1995; Schiller 1995) and of synaptically coupled pairs of neurons (Markram 1997; Markram 1997) in acute brain slices.

### **3.2.2 The patch-clamp experiment**

#### *Experimental patch-clamp setup*

Electrical recordings from layer 4 spiny stellate neurons were made with the patch-clamp amplifier EPC-9/2 (List-Electronics, Darmstadt, Germany) operated in current clamp mode. The patch-clamp amplifier can measure currents in the picoampere and voltages in the microvolt range. The preamplifier headstage holding the patch pipette was mounted on a three axis motorized micromanipulator (Luigs&Neumann, Ratingen, Germany) allowing precise control of the position of the pipette tip. Pressure or suction could be applied to the

pipette by a manual seal sucker (Sigmann Elektronik, Hüffenhardt, Germany). A second micromanipulator was either equipped with a second preamplifier headstage for dual whole cell recordings or a pipette holder attached to a stimulation isolator (Sigmann Elektronik, Hüffenhardt, Germany) for extracellular stimulation. Both micromanipulators together with the brainslice recording chamber were mounted on a motorized xy-translation table. In this way, the sample together with the patch electrodes could be moved below the fixed optical axis of the microscope (see below). This allowed for scanning the entire dendritic tree and following the axons of fluorescently labeled cells. The brain slice in the recording chamber

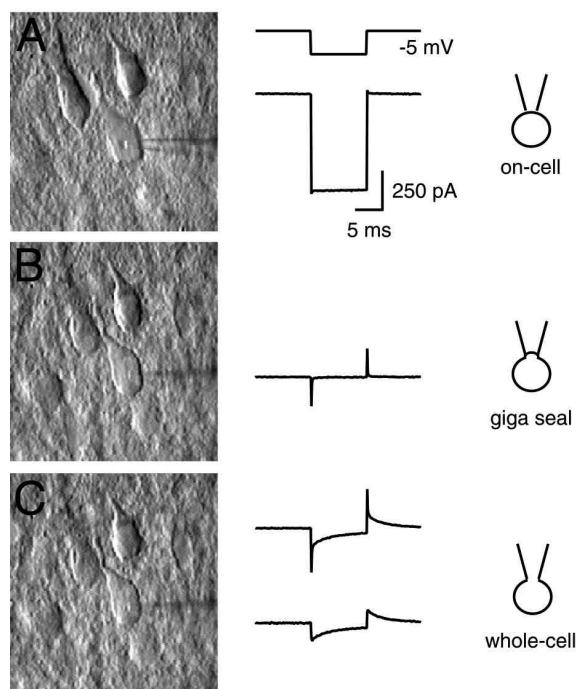


**Figure 3.1** *The patch-clamp technique*

*The formation of a giga-seal and the whole-cell configuration in a brain slice are depicted in this figure. The left row shows an IR-video image sequence, the middle row shows the corresponding electrical current traces and the right row is a schematic drawing of the process of seal formation.*

**A** *The soma of a cell is approached by a patch-pipette. The current through the pipette due to a small voltage step is recorded. Positive pressure is applied to keep the pipette clean. The outflowing liquid causes a 'dimple' in the plasma membrane.*

**B** *The pressure is released and slightly negative pressure by suction results in the formation of a giga-seal. The resistance between the pipette and the bath solution is of the order of  $G\Omega$  and no measurable current is flowing in this conformation even though the command voltage is set to  $-70$  mV.*

**C** *Brief suction disrupts the membrane patch below the pipette tip. This is called whole-cell. The capacitative transients are compensated.*

was fixed with a grid made of a platinum frame spanned with dental sloth. The chamber was always perfused (peristaltic pump, Ismatec, Zürich, Switzerland) with extracellular medium, which was heated to physiological temperatures ( $34\text{--}37$  °C) by a flow heater (Sigmann Elektronik, Hüffenhardt, Germany) before entering the recording chamber. The bath was grounded with a Ag/AgCl pellet via the reference input of the preamplifier headstage. The solution in the patch pipette was in electrical contact with the preamplifier via a chlorinated silver wire.

The voltage signals were filtered at 3 kHz and digitized at 10 kHz by the on-board AD-converter of the EPC-9 (ITC-16, Instrutech, Great Neck, NY, USA). The amplifier and the ITC-16 were both controlled by the program Pulse (version 8.21, Heka Elektronik, Lambrecht, Germany) on a Macintosh computer (Apple, Cupertino, CA, USA).

Recordings from layer 2/3 pyramidal neurons were made with the patch clamp amplifier Axoclamp 2A (Axon Instruments, Union City, CA, USA) and signals were again filtered at 3kHz and digitized at 10 kHz by an ITC-16 board. The ITC-16 was controlled by home written software based on Igor Pro 4.1 (Wavemetrics, Lake Oswego, OR, USA) running on an Apple Mac.

Dual whole-cell recordings were performed with two Axopatch-200B amplifiers (Axon Instruments, Union City, CA, USA). The electrical signals were recorded as described for the EPC-9 amplifier.

The complete setup was mounted on a vibration isolation table (Newport, Irvine, CA, USA) to minimize vibrations. In order to minimize electrical noise in the recording the electrical setup was surrounded by a Faraday cage and all setup components were carefully grounded.

### *Pipettes*

Patch pipettes with a resistance of 3-8 M $\Omega$  depending on the cell type were pulled from borosilicate glass on a horizontal pipette puller (P87, Sutter Company, Novato, CA, USA). Double barrel theta-glass tubes were pulled to pipettes with a tip diameter of 1–2  $\mu\text{m}$  for extracellular stimulation.

### *Solutions*

The patch pipettes for whole-cell recording were filled with an intracellular solution containing 125 mM K-gluconate, 20 mM KCl, 10 mM HEPES, 4 mM ATP-Mg, 10 mM Naphosphocreatine and 0.3 mM GTP. Different fluorescence Ca<sup>2+</sup> indicators (Molecular Probes, Eugene, OR, USA) with varying concentrations were added to the intracellular solution depending on the Ca<sup>2+</sup> imaging experiments. Their properties will be explained in more detail in the following chapter. Cells were loaded with the indicator for >20 min before fluorescence measurements to allow sufficient equilibration of the indicator concentration between the pipette and the cytoplasm. Chemicals were purchased from Tocris (Bristol, U.K.), Sigma (Steinheim, Germany) and Boehringer (Mannheim, Germany).

### Patching

The “blow and seal” technique was developed by Stuart and Sakmann to form a high resistance seal onto the soma of a neuron in a brain slice (Stuart 1993). This technique guarantees success rates of near 100% to routinely patch neurons in brain slices. Fig 3.1 depicts the individual steps of the patch-clamp technique. Briefly, the patch clamp amplifier

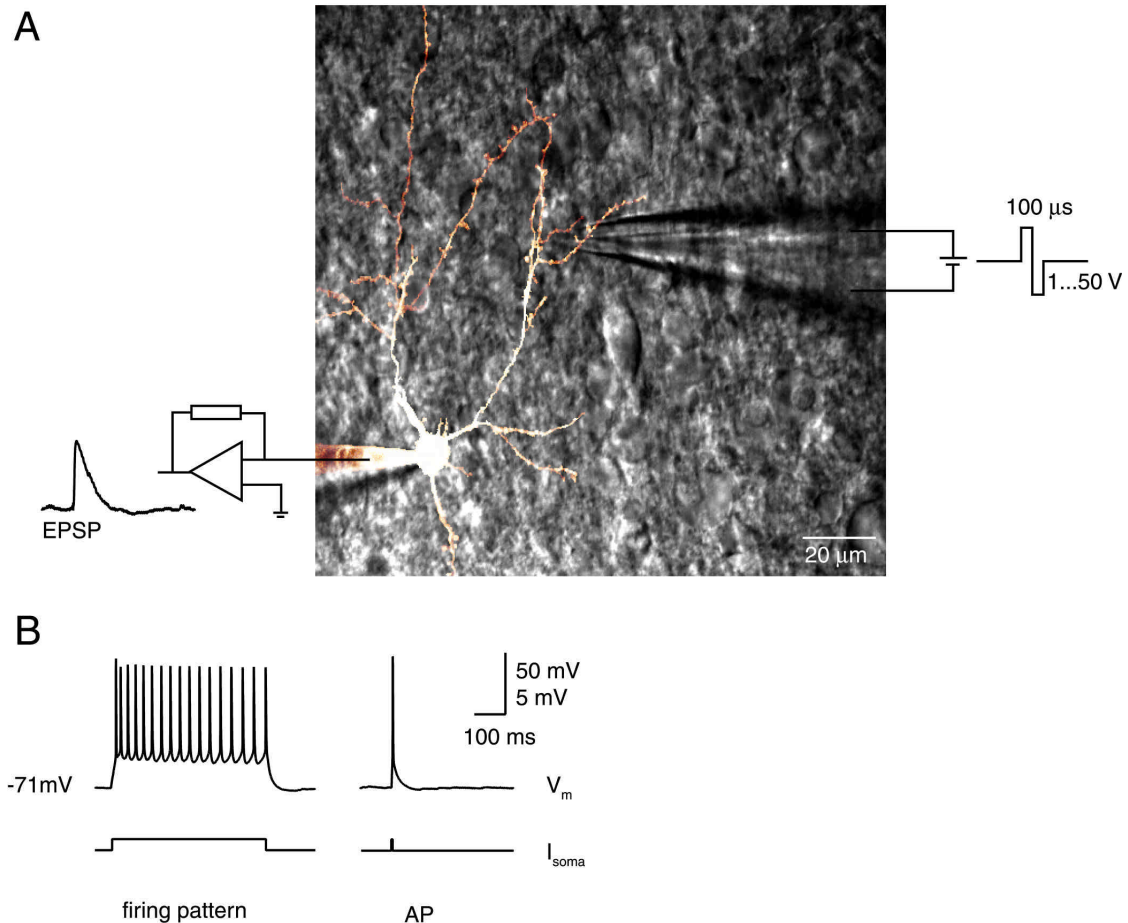


**Figure 3.2 Current-clamp recordings**

**A** A typical recording situation in an acute brain slice. A spiny stellate neuron was filled with the  $\text{Ca}^{2+}$  indicator Oregon Green Bapta-1 (OGB-1) during whole-cell recording in current clamp. The image is an overlay of the IR-SGC image and a maximum projection of a fluorescence stack. The patch electrode can be seen on the lower left with a sketch of the patch-clamp amplifier recording the voltage signals. To the upper right an extracellular stimulation electrode is placed close to a dendrite. A short bipolar voltage pulse results in an EPSP in the spiny stellate neuron.

**B** In the whole-cell current clamp mode one has complete electrical control over the cell. Somatic current injection results in firing of APs. On the left hand side, current injection for 500 ms results in a stereotyped burst of APs the so called firing pattern. Spiny stellate neurons show a slight accommodation of the AP frequency. Brief current injection for 5 ms (right hand side) results in the firing of a single AP.

is set to the voltage clamp mode and a command voltage pulse of  $-5$  mV and 10 ms duration is continuously applied to the electrode. In the voltage clamp mode the amplifier keeps the voltage at the set value and measures the resulting current. Positive pressure is applied to the pipette to keep the tip clean from dirt, a prerequisite for successful formation of a giga-seal. From the amplitude of the current response to the  $-5$  mV voltage step the pipette tip resistance can be calculated applying Ohm's law. Pipette resistance was usually between 3–8 M $\Omega$ . The pipette is lowered onto the top of the slice, where the positive pressure is reduced to 10–15 mbar. The potential of the bath solution is set to 0 mV. The pipette tip is then targeted to the soma of a preselected neuron under visual control. As soon as the pipette penetrates the brain slice, a wave of pressure can be seen in the slice clearing the surface of the targeted neuron. The pipette is slowly advanced to the soma until a dimple in the cell membrane becomes visible (Fig 3.1A). Then the pressure is released and slight suction is applied. The membrane starts to seal onto the tip of the pipette. This process can be observed in the electrical current recording. The initial command voltage is set to  $-70$  mV. The leak current from the tip of the pipette then decreases rapidly within a few seconds to a few pA. This corresponds to the formation of a high resistance seal between the cell membrane and the pipette. Since the membrane acts as a capacitor, transient capacitive currents can be observed when the command voltage is stepped to  $-5$  mV and back to ground potential (Fig 3.1B). The amplifier is equipped with circuits which can compensate for the membrane capacitance and the pipette resistance.

After the giga-seal is established, a transient suction pulse disrupts the membrane below the pipette without disrupting the tight seal. This whole-cell configuration now gives good electrical access to the cell (Fig 3.1C). The pipette and the lumen of the neuron represent one electrical compartment, which can be modeled by an equivalent circuit (Sigworth 1995). Small molecules like  $\text{Ca}^{2+}$  sensitive indicator dyes can easily diffuse into the cell, filling it within 15 min after break-in. Access resistance was usually between 5–15 M $\Omega$ . The amplifier was then routinely switched to the current-clamp mode. In current-clamp the current across the membrane is kept constant and the resulting membrane potential is measured. At rest, i.e. without electrical activity, this membrane potential corresponds to the resting membrane potential which in spiny stellate neurons is around  $-70$  mV. Brief depolarizing current pulses can excite the cell and result in the firing of an action potential (Fig 3.2).

### ***Pharmacology***

In order to pharmacologically characterize and isolate different pathways of  $\text{Ca}^{2+}$  influx into the cells, drugs which specifically block certain ion channels or receptors were all

bathapplied to the extracellular solution. Pharmacological agents were washed in for at least 15 min to allow sufficient equilibration of the drug in the brain slice. To prevent action potential generation 1  $\mu\text{M}$  of tetrodotoxin (TTX, RBI, Natick, MA, USA) to block voltage dependent sodium channels were applied. 100  $\mu\text{M}$  of  $\text{Cd}^{2+}$  were used to block voltage dependent  $\text{Ca}^{2+}$  channels. The glutamate receptors of the AMPA type were blocked with 10  $\mu\text{M}$  1,2,3,4-tetrahydro-6-nitro-2,3-dioxo-benzoquinoline-7-sulfonamide (NBQX, Tocris, Bristol, U.K.). NMDA receptor channels were blocked with 15  $\mu\text{M}$  dl-2-amino-5-phosphonopentanoic acid (APV, Tocris). The specific mGluR group II antagonist 2-(s)- -ethylglutamic acid (EGlu, 50  $\mu\text{M}$ , Tocris) was used to block mGluRs.

### 3.1.3 Stimulation protocols

#### *Current injection*

During whole-cell current clamp recordings somatic current injection from 100 to 1000 pA results in the firing of an action potential (AP). A burst of APs can be evoked by prolonged current injection above a threshold for 500 ms (Fig 3.2B). This firing pattern is typical for a certain cell type and helps to identify the cell type during electrophysiological recordings. Single APs were elicited by somatic current injection for typically 5 ms above the threshold for spike initiation. Controlled bursts of APs at varying frequencies were elicited by repetitive current injections at the desired frequency. Current injection protocols were controlled by the respective software controlling the ITC16 digital to analogue output channels.

#### *Extracellular stimulation*

Synapses were stimulated by extracellular stimulation of axonal projections with a bipolar voltage pulse. The double barrel extracellular stimulation electrode was filled with extracellular solution and each barrel was connected to the output of a stimulation isolator with a silver electrode. Stimulation strength and duration could be adjusted manually. Stimulation durations for each phase of the bipolar pulse were set to 100  $\mu\text{s}$ . Stimulation intensities were varied between 1 and 50 V until a stable EPSP could be observed (Fig 3.2A). The local change in voltage close to the tip of the extracellular stimulation pipette can excite nearby axons to fire an action potential which results in an somatic EPSP in the postsynaptic cell. The voltage step was triggered by the trigger output channel of the ITC16.

In double stimulus protocols single APs and EPSPs were elicited at varying time intervals by somatic current injection and extracellular stimulation respectively.

### ***Induction protocol for long term plasticity***

Plasticity experiments were performed in layer 4 spiny stellate neurons. After recording a stable baseline of extracellularly evoked EPSPs, an induction protocol for either LTP or LTD was delivered. The LTP induction protocol consisted of the pairing of 5 EPSPs with 5 APs at a frequency of 20 Hz and a relative time delay between an EPSP and an AP of +10 ms. This sequence was repeated 10 times with a 10 s interval between each sequence. LTD was induced by the same protocol except the relative time delay between each EPSP and each AP was now -10 ms, i.e. in this case the EPSPs followed the APs. These sequences have been used in pairs of layer 5 pyramidal neurons and in pairs of layer 4 spiny stellate cells (Markram 1997; Egger 1999).

## **3.3 Two-photon microscopy**

### **3.3.1 Principles of fluorescence excitation**

Fluorescence imaging (Inoue 1986; Pawley 1995) is a powerful tool in biology to enhance contrast, label individual proteins or structures (Chalfie 1994; Marshall 1995; Siegel 1997; Tsien 1998; Shi 1999) and to do functional imaging of ionic concentrations (Eilers 1995; Yuste 1995; Denk 1996; Helmchen 1997; Svoboda, Denk et al. 1997; Rose 1999; Majewska 2000; Holthoff, Tsay et al. 2002) or membrane potential (Peleg 1999; Spors 2002) with the corresponding fluorescent markers .

Fluorescence is generated when a molecule is electronically excited from its ground state to an excited state by absorption of a photon of the corresponding energy and then relaxes rapidly (  $\sim 1$  ns) by emission of a red-shifted photon again to its ground state (Fig 3.9A). One photon excitation is not the only possibility to excite a fluorophore from its ground state to an excited state. A fluorophore can also absorb two photons of (approximately) half the energy (or twice the wavelength), as compared to the one photon case, simultaneously to make the energy transition to the excited state (Denk 1990). In terms of transition probabilities there is a non-zero probability for this two-photon transition. It is via an intermediate, virtual state, which results in different selection rules for the two photon transition as for the one photon transition (Nakamura 1999). So the absorption spectrum for one photon excitation does not necessarily predict the absorption spectrum for the two-



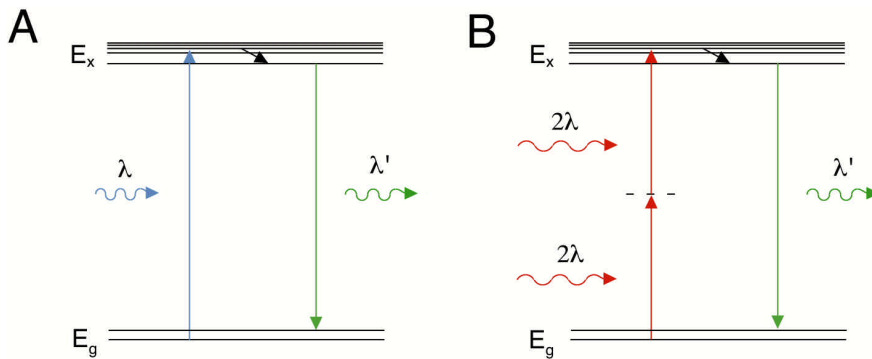


**Figure 3.3 One and two-photon excitation**

**A** Jablonski diagram of an one photon absorption event. A fluorophore is electronically excited to an excited state by absorption of one photon of the corresponding energy. After rapid relaxation from a vibrational state a fluorescence photon is emitted. This photon is red shifted, i.e. it has a longer wavelength than the absorbed photon.

**B** In the case of two-photon excitation two photons of half the energy (double wavelength) are absorbed. The energy transition is via a virtual intermediate state. The emitted photon has the same wavelength as in the one-photon case.

photon excitation (Denk, Piston et al. 1995). This is especially true for the case of complex organic dye molecules with their complex electronic and vibrational energy levels.

Two-photon excitation was first described theoretically by Göppert-Mayer in 1931 (Göppert-Mayer 1931). Because the probability for two-photon excitation is very small, the experimental observation was first possible with the introduction of short-pulse lasers, a source of high intensity photon fluxes (Spence, Kean et al. 1991).

In 1990 Denk et al. described two-photon excitation fluorescence microscopy for imaging biological specimen (Denk 1990). Since then a large number of studies have employed this technique in biology to image fluorescent probes and to measure  $\text{Ca}^{2+}$  transients in small neuronal compartments in vitro and in vivo (for review see (Konig 2000; Euler and Denk 2001; Nimchinsky, Sabatini et al. 2002)).

The advantages of two-photon microscopy are firstly that the excitation light is in the infrared (IR). The energy of two of these photons combined matches the energy necessary to excite a large number of fluorescence indicators designed for one photon excitation. As a rule of thumb the two-photon absorption spectra are relatively broad and the absorption maximum is almost twice the wavelength of the absorption maximum for the single photon excitation case (Denk, Piston et al. 1995). Since Rayleigh scattering is proportional to  $\lambda^{-4}$ , the IR light is scattered less in thick biological samples. Additionally the ‘biological window’ for electromagnetic radiation is around the excitation wavelength for two-photon excitation

(Svoboda 1994). Absorption in this spectral range is quite low, also facilitating tissue penetration (Gu, Gan et al. 2000).

The most important feature of two-photon excitation is the quadratic dependence on the intensity of the transition matrix elements (Nakamura 1999). The two-photon excitation probability is given, using the paraxial approximation and assuming a low probability of a single fluorophore to be excited during a single pulse, by

$$n_{2p} = \frac{\sigma_{2p} \bar{P}^2}{f} \frac{\pi(\text{NA})^2}{hc\lambda} \xi$$

with  $\sigma_{2p}$  being the two-photon cross section of the fluophore,  $\bar{P}$  is the average laser power,  $f$  the repetition frequency of the pulsed laser system, NA denotes the numerical aperture of the objective lens,  $h$  the Planck's constant,  $c$  the speed of light,  $\lambda$  the wavelength and  $\xi$  is the two-photon advantage factor, which depends on the properties of the laser pulse (Denk 1990; Denk, Piston et al. 1995). For a pulse with a Gaussian temporal pulse envelope and a pulse width  $\tau$  one finds

$$\xi = (f\tau)^{-1} 0.664$$

Two photon cross sections for common fluorophores are typically  $\sigma_{2p} = 10^{-49} \text{ cm}^4\text{s}$  (Xu, Guild et al. 1995; Xu and Webb 1996). Thus two-photon excitation requires high peak powers, which can be reached with femtosecond pulsed laser systems at low average powers, focused into a diffraction limited spot (Koester, Baur et al. 1999). As several tens of mW of average power comprised in a pulse of 100 fs can saturate the fluophores the repetition rate of the laser system should be of the order of the fluorescence lifetime decay in the ns range.

Since the intensity of a focused laser beam drops quadratically with the distance from the focus, the two-photon excitation probability drops with the fourth power. Hence there is no excitation above and below the focus (in contrast to the one photon case). This intrinsic optical sectioning property of two-photon fluorescence microscopy reduces photobleaching (Piston 1999) and phototoxic stress for out of focus regions (Konig, So et al. 1996; Konig, So et al. 1997; Koester, Baur et al. 1999). Above all, there is no contribution to the fluorescence signal from out of focus regions. All fluorescence is generated in the small focal volume of the diffraction limited focal spot. Therefore the detectors for fluorescence detection can be placed close around the specimen (see below for a detailed discussion) to collect a large fraction of the emitted fluorescence photons, in which ballistic and scattered photons equally

contribute to the fluorescence signal and thereby increase the signal strength (Koester, Baur et al. 1999; Gu, Gan et al. 2000; Beaurepaire, Oheim et al. 2001; Oheim 2001).

### 3.3.2 Experimental setup

#### *Setup components*

Two two-photon microscopes were set up for this study. They were based on commercially available confocal laser scanning units from Leica Microsystems, Mannheim, Germany. One system was equipped with the TCS-NT scan head and the other system used the TCS-SP2RS scanner. The two scan heads only differed in the design of the galvanometric scanning units. Both units employ a single mirror to point-scan a laser beam across the sample. The mirror is fixed to a small galvanometer, which is mounted on a larger scan unit. The galvanometer performs the fast movement and the scan unit provides the tilt along the slow axis. The center of the single mirror is placed in a conjugate telecentric plane of the optical system, which results in accurate scanning of the whole field of view. The TCS-SP2RS uses a resonant scanner with a resonant frequency of 4 kHz for the fast axis. This results in a higher scan speed for the resonant system as compared to the standard galvanometer scanner. For a detailed discussion on the scan speed performance see below. The scanning unit of the TCS-SP2RS is mounted on a so called k-scanner, which allows the rotation of the image. The additional parts of the setups are identical for the two systems.

The scan heads are mounted on an upright microscope (DMLFS, Leica, Wetzlar, Germany) equipped with a 63x objective (HCX APO, 63x, NA 0.9, water immersion, Leica) or a 40x objective (HCX APO, 40x, NA 0.8, water immersion, Leica) and an oil immersion condenser (P, NA 1.4, Leica). The details of the attached IR gradient contrast imaging system are given below.

Fluorescence was detected in the whole-field, non-descanned detection mode with photomultiplier tubes (PMT, R6547, Hamamatsu Photonics, Herrsching, Germany). Since fluorescence is just generated in the diffraction limited focal volume the detectors could be placed directly behind the objective and also directly behind the condenser (Fig 3.4). This detection scheme resulted in a high photon collection efficiency, because also scattered fluorescent photons could be collected over a large detection angle (NA of objective and NA of condenser).

Suitable dichroic mirrors and block filters to separate the excitation light in the IR from the fluorescence light in the visible spectrum were purchased from AHF (Tübingen, Germany)

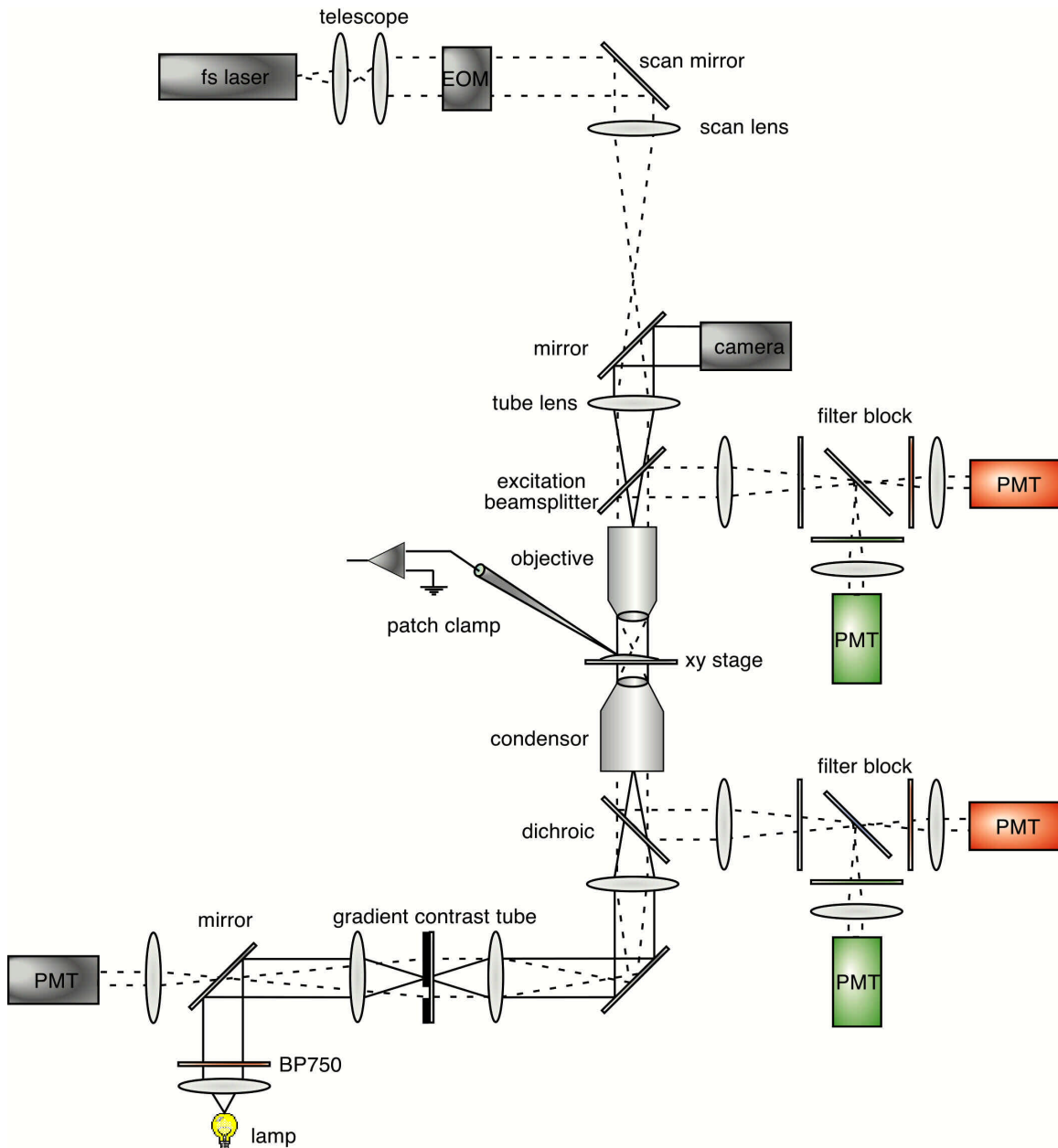


**Figure 3.4 Experimental setup**

*Schematic drawing of the two-photon microscope used in this study. For details refer to the text. The dashed lines represent the excitation and fluorescence light path. The solid lines represent the bright-field illumination light path. Two movable mirrors switch between the two imaging modes.*

*Details of the filters in the filter blocks in front of the PMTs are given in the text. The PMTs are coloured to represent the colour of the detected fluorescence light.*

and Chroma (Battleboro, VT, USA). As the excitation beam splitter a LP750 was used to separate the IR excitation light from the fluorescence light. On the transmission detector side the IR light was separated from the visible light by a transmission beamsplitter (LP750). IR block filters (E700SP or BG39) had to be placed in front of the detectors to reduce noise from stray IR light. Dual colour fluorescence imaging was realized with two photomultipliers behind the objective and two photomultipliers behind the condensor. The fluorescence light was split for each detector pair (see parts labeled “filter block” in Fig. 3.4) by a dichroic (560DCXR) separating green and red fluorescence. Bandpass filters (green, HQ525/50M, red, HQ610/75M) in front of each detector further limited the spectral bandwidth of the detected fluorescence light for each channel. The signals of the two photomultipliers detecting the same colour were summed offline. The described filter sets resulted in a very good separation of the green from the red channel with no spectral overlap from the red channel.

As the light source for two-photon excitation a femtosecond pulsed titan sapphire laser (Mira 900, Coherent, Santa Clara, CA, USA) pumped with a 5 W solid state laser (Verdi, Coherent) was used. The laser could be tuned from 780 nm to 920 nm. Typically excitation wavelength between 820 nm to and 890 nm were used at a pulse length of 150 fs and a pulse repetition rate of 78 MHz. The physical principles of ultra-short laser pulse generation will be discussed in the next paragraph.

The laser beam was expanded by a beam expander telescope and then attenuated by an electro-optical modulator (Linos, Göttingen, Germany) to typical average power levels of 1 to 10 mW in the object plane. A shutter blocked the laser beam when no images were acquired and during the flyback of the mirror. The beam was guided by mirrors to the direct laser coupling port of the scan head.

An motorized xy-stage moved the specimen together with the micromanipulator/headstage assembly for patch-clamp below the fixed optical axis of the microscope.

Image acquisition was controlled by the confocal scanner software (LCS, Leica) on a PC. Visual basic (Microsoft, Redmond, WA, USA) based macro programs allowed fast control of the scanner during an experiment. Image acquisition and the electrophysiological recordings were synchronized by the frame-trigger output of the scanner hardware. The xy-stage could also be controlled by the confocal software giving the possibility to measure the distance from the soma to the position of the linescan measurement along a dendritic branch. At each dendritic branchpoint a new marker was set. The geometric distance from the previous marker was calculated and added to the total distance from the soma. Since the dendritic length between two markers was extrapolated with a straight line, the real dendritic distance was slightly underestimated. Comparing the distance measured during an experiment by this

method with the distance derived from a reconstruction of the path from a fluorescence three dimensional stack gave an upper error estimate of 10%.

### *The femtosecond laser system*

The femtosecond IR laser pulses necessary for efficient two-photon fluorescence excitation are generated by a titanium sapphire laser (Mira 900, Coherent) pumped with a solid state continuous wave laser (Verdi, 5 W, Coherent). The generation of short laser pulses shall be reviewed briefly.

A mode-locked fs laser requires a broadband gain medium, which will sustain a large number of longitudinal modes in a typical laser cavity. If these modes have equal phases they are mode-locked in the frequency domain. The Fourier transform of such a spectrum will correspond to an intense, short burst of light in the time domain, since all waves of different frequency will add constructively. To achieve mode-locking additional functional elements are necessary. The Mira 900 employs passive mode-locking. In this case an intensity dependent loss or dispersion mechanism is used to favour operation of pulsed over continuous radiation.

The titanium doped sapphire (Ti:Sa) crystal is the high gain medium, which can sustain many longitudinal modes in the laser cavity. A birefringence filter in the cavity selects the center wavelength which is favoured for amplification. A pair of prisms compensate for beam broadening in the cavity and determine the total chirp and pulse width of the beam. A slit in front of the output coupler acts as a dissipative element, which favours pulsed operation over continuous radiation.

The pulse forming process is initiated by a piece of glass wiggling in the beam path, thus slightly modifying the laser cavity length at the right frequency inducing the formation of additional longitudinal modes in the cavity and thus generating high intensity fluctuations. The transient high intensity fluctuations, in which some of the modes are locked together, can induce a change of the physical properties of the titanium sapphire crystal.

The crystal shows an intensity dependent change of refractive index, which is described by the Kerr-effect. In consequence is the refractive index in the center stronger influenced by a spherical beam with a Gaussian intensity profile than the less intensely illuminated outer parts and thus a gradient index lens or Kerr-lens is formed. The high intensity pulsed fluctuations are focused by the Ti:Sa crystal whereas low intensity continuous wave beams cannot induce the Kerr-lens effect and are not focused. This results in a smaller beam diameters for the high intensity mode-locked versus the continuous randomly phased longitudinal modes in the cavity. A slit in front of the laser output coupler can now be adjusted so that the continuous wave components are blocked and not further amplified. The

high intensity laser pulse, which was focused by the Kerr-lens has a smaller diameter and can thus be reflected by the output coupler mirror and its components can further be amplified.

Another consequence of the intensity dependence of the refractive index in the gain medium is that the wavelengths at the leading and trailing edges of a pulse, which are less intense encounter a different refractive index than the wavelength at the intense center of the pulse. Group velocity dispersion (GVD)  $d^2n(\lambda)/d\lambda^2$  in the crystal, which results in a temporal reshaping of the wavepackets is, in the case of high intensity electromagnetic fields which change the refractive index of the crystal, not only dependent on the wavelength, but also dependent on the intensity. This results in self-phase modulation, a phase shift of the individual components of the pulse depending on when they occur in the pulse. Frequency components at the blue and red end of the pulse are added. This effect induces positive GVD and tends to broaden the pulse. This is compensated by a pair of prisms. The interplay of the self-phase modulation and the adjustment of the total dispersion in the cavity determines the width of the laser pulse.

Determined by the dispersion of the cavity, self-phase modulation, Kerr-effect and setting of the slit width, there is a stable equilibrium for a pulse with a constant width and amplitude, which remains unchanged upon one trip through the cavity. The pulse adjusts itself to a bandwidth-limited pulse with a  $\text{sech}^2$  (secans hyperbolicus) or Gaussian temporal pulse profile.

This non-linear pulse formation process results in a periodically reforming wave (soliton-formation) with a stable pulse output.

The Ti:Sa crystal can amplify pulses with a center wavelength from 680 to 1100 nm. One roundtrip of a pulse in the Mira 900 cavity takes 13.2 ns, corresponding to a repetition rate of 76 MHz with pulses of 100 fs and peak powers of 2 TW/cm<sup>2</sup>. The Fourier transform of a short laser pulse of 100 fs shows that the pulse consists of a wavelength interval of some nm around the center wavelength.

### ***Optical setup***

The basic principle of laser scanning microscopy is to scan the laser beam across the sample point by point in a raster fashion (Stelzer 1995). The excited fluorescence at each point is detected, digitized and then an image is constructed by a computer coding the detected fluorescence in a pseudo colour pixel value for each pixel. The movement of the focal spot in the object plane is accomplished by a telecentric imaging system. The angle of deflection of a parallel laserbeam is continuously changed by a scanning mirror. The pivot point of the scanning mirror sits at a conjugate telecentric plane of the objective (the backfocal plane), which is accomplished by an intermediate telescope consisting of the scan lens and the

microscope's tube lens (Fig 3.4). In the backfocal plane of the objective is the laser beam again parallel and the initial angle of the laser beam in relation to the optical axis is conserved (scaled by the angular magnification factor of the intermediate telescope). Thus the laser beam pivots around the backfocal plane of the objective, without lateral shift, following the movement of the scan mirror. The objective lens finally focuses the laser beam to a spot in the focal plane. The position of the spot is determined by the incident angle of the

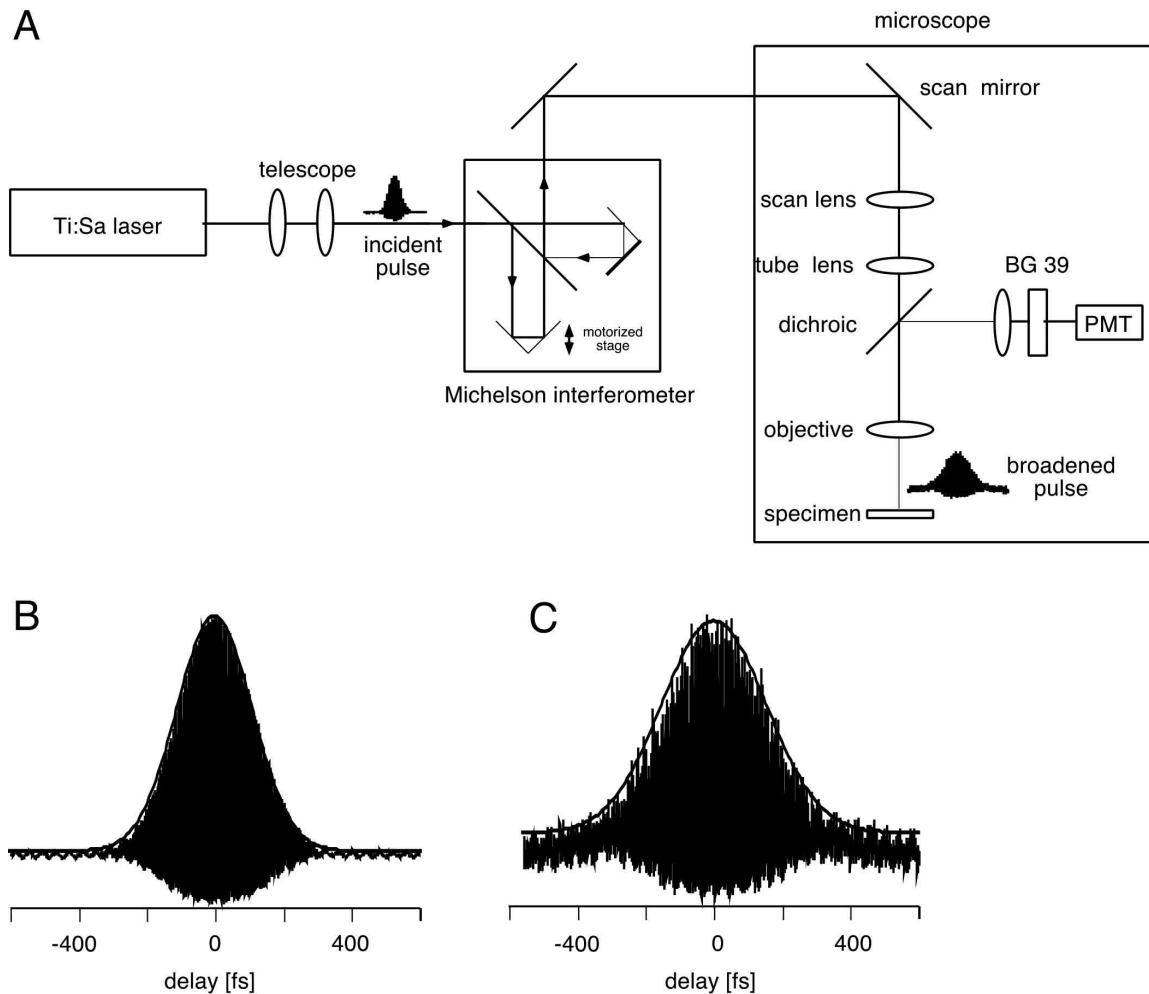


**Figure 3.5 Pulse broadening in the microscope**

*A Drawing of the setup for the measurement of the pulse width of the fs-laser. A Michelson interferometer for background free autocorrelation measurements is placed in the beam path to determine the pulse width of the laser beam before it enters the microscope and in the specimen plane.*

*B Pulse width before the microscope. The autocorrelation signal corresponds to a pulsewidth of 107 fs.*

*C After passing the optical components of the microscope the pulse is broadened due to group velocity dispersion. The pulse width in the specimen plane was 158 fs.*



light bundle. Thus the change of the deflection angle by the scan mirror is translated into a lateral movement of the focal spot.

In order to obtain a diffraction limited spot in the object plane and thus the best optical resolution the backfocal plane of the objective has to be overfilled to homogeneously illuminate the aperture with a planar wave. Assuming a Gaussian beam profile the back aperture is overfilled by a factor of two, i.e. the  $1/e^2$  diameter of the Gaussian beam should be twice as large as the backfocal aperture. Taking the backfocal aperture size of the used objectives and the divergence angle of the laser system into account a two times magnification telescope ( $f = 50$  mm and  $f = 100$  mm, Newport) was used to expand the beam. Fluorescence detection was performed in the non-descanned detection mode. Since the image is generated by a computer, recording the photon counts for each pixel, the optical system for fluorescence detection needs not to be aberration free as for an imaging system. Rather a short distance from the specimen plane and large angles of acceptance for scattered photons determine the design considerations (Oheim 2001). The detectors were placed in a conjugate telecentric plane of the backfocal plane of the objective.

Fig 3.4 shows a schematic drawing of the setup with the major components described above. The dotted line represents the light path of the IR laser light and the resulting fluorescence light through the optical system. Parallel lines indicate parallel light bundles and the crossing of the lines indicate conjugate image planes. The solid lines represent the lightpath of the bright-field illumination system for IR-video microscopy. Crossing lines in this case indicate the telecentric conjugate planes (backfocal planes of the objective and the condensor). The mirrors can be moved out of and into the lightpath to switch from the scanning mode to the video mode respectively.

### 3.3.3 Quantitative analysis of the optical system

#### *Pulse width in the object plane*

Short laser pulses are subject to broadening due to group velocity dispersion (GVD) when they pass through glass. For a constant average power this results in a reduced two-photon excitation efficiency (Denk, Piston et al. 1995). The effect of pulse broadening as a pulse travels through the optical setup of the two-photon microscope was assessed using background free autocorrelation by non-collinear phase matching (Muller, Squier et al. 1995). Fig 3.5A shows the setup with the Michelson-interferometer in the beam path to measure the pulsewidth before the microscope and in the object plane. For a detailed description of the method see (Diels, Fontaine et al. 1985; Brakenhoff, Muller et al. 1995).

Fig 3.5B shows the resulting interferometric autocorrelation signal of the pulse before entering the microscope. In the object plane this pulse was broadened. The measurement in Fig 3.5C was performed with the 63x HCX APO objective. The autocorrelation signal outside the microscope had a full width at half maximum (FWHM) of 155 fs and increased to 224 fs in the focal plane. Using the correction factor of 0.707 for a Gaussian pulse shape envelope to calculate the actual pulse width from the autocorrelation signal this corresponds to an actual pulsewidth of 107 fs and 158 fs respectively. Pulse width broadening in the focal plane was very similar for the other objectives of the HCX APO series (to 151 fs for the 10x, 151 fs for the 20x and 157 fs for the 40x). Since the pulse width was not significantly broadened by passing through the optics no pulsewidth compensation was employed (Guild, Xu et al. 1997; Muller, Squier et al. 1998).

To calculate the pulse width  $\tau_p$  of the laser system on a daily basis the width (FWHM) of the spectrum  $\Delta\lambda$  and the center wavelength  $\lambda$  of the mode-locked laser beam was measured with a spectrometer. From the measured bandwidth the pulsewidth was derived from the time-bandwidth product for a Gaussian pulse envelope by

$$\tau_p = \frac{0.441\lambda^2}{c \Delta\lambda}$$

where  $c$  is the speed of light.

### **Resolution**

The resolution of a conventional two-photon excitation laser scanning microscope is at best diffraction limited (Gu and Sheppard 1995). Due to the finite apertures of the optical system a point is imaged in two dimensions as an extended disc, the so called Airy-disc. The three dimensional point-spread function (PSF) determines the resolution of an optical system.

The PSF of a two-photon microscope is given by (Sheppard and Gu 1990)

$$I_{2p}(u, v) = I^2(u/2, v/2)$$

where

$$I(u, v) = \left| \int_0^1 J_0(v\rho) \exp\left(\frac{1}{2}iu\rho^2\right) \rho d\rho \right|^2$$

is the intensity in the focal region assuming an aberration free lens of circular aperture and

$$u = 4kzn \sin^2(\alpha/2)$$

$$v = krn \sin(\alpha)$$

are the axial and radial normalized optical coordinates.  $k = 2\pi/\lambda$  is the wavevector, if  $\lambda$  is the wavelength of the fluorescence and  $2\lambda$  is the wavelength for two-photon excitation.  $n \sin(\alpha)$  is the numerical aperture (NA) of the lens and  $r = \sqrt{x^2 + y^2}$  is the radial distance from the optical axis.  $J_n$  denotes the  $n^{\text{th}}$  order Bessel function. The PSF is thus given laterally by

$$I_{2,p}(v) = \frac{2J_1(v/2)}{(v/2)}^4$$

and in the axial direction by

$$I_{2,p}(u) = \int_0^u I^2(u/2, v/2) v dv$$

Using the paraxial approximation and the Rayleigh criterion for the optical resolution one can finally derive for the lateral resolution

$$x = 0.43 \frac{\lambda}{\text{NA}}$$

and for the axial resolution

$$z = 0.22 \frac{\lambda}{n \sin^2(\alpha/2)}.$$

Note that the resolution for a two-photon microscope is derived from the quadratic dependence of the two-photon excitation probability on the illumination intensity and that the axial resolution is an intrinsic property of two-photon excitation.

The resolution of the two-photon microscope was measured by imaging subresolution fluorescent beads (100 nm, FluoSpheres, yellow-green fluorescent, Molecular Probes) embedded in agarose. The excitation wavelength was 820 nm. Serial sections of the sample were performed at highest digital zoom (32x) at an stepsize of 0.1  $\mu\text{m}$ . Fig 3.6A shows an xz

projection of such a stack with two fluorescent beads next to each other. Intensity profiles along and perpendicular to the optical axis through the bead (Fig 3.6A, dashed lines) were calculated (Fig 3.6B, C) and the full width at half maximum (FWHM) was taken as a measure for the optical resolution of the system. The two most commonly used objectives (HCX APO w, 63x , NA 0.9 and HCX APO w, 40x, NA 0.8) in this study are compared in Tab 3.1.

As expected from the theory is the axial resolution about 3 times worse than the lateral resolution. The measured values for the lateral resolution almost reach the theoretical values.

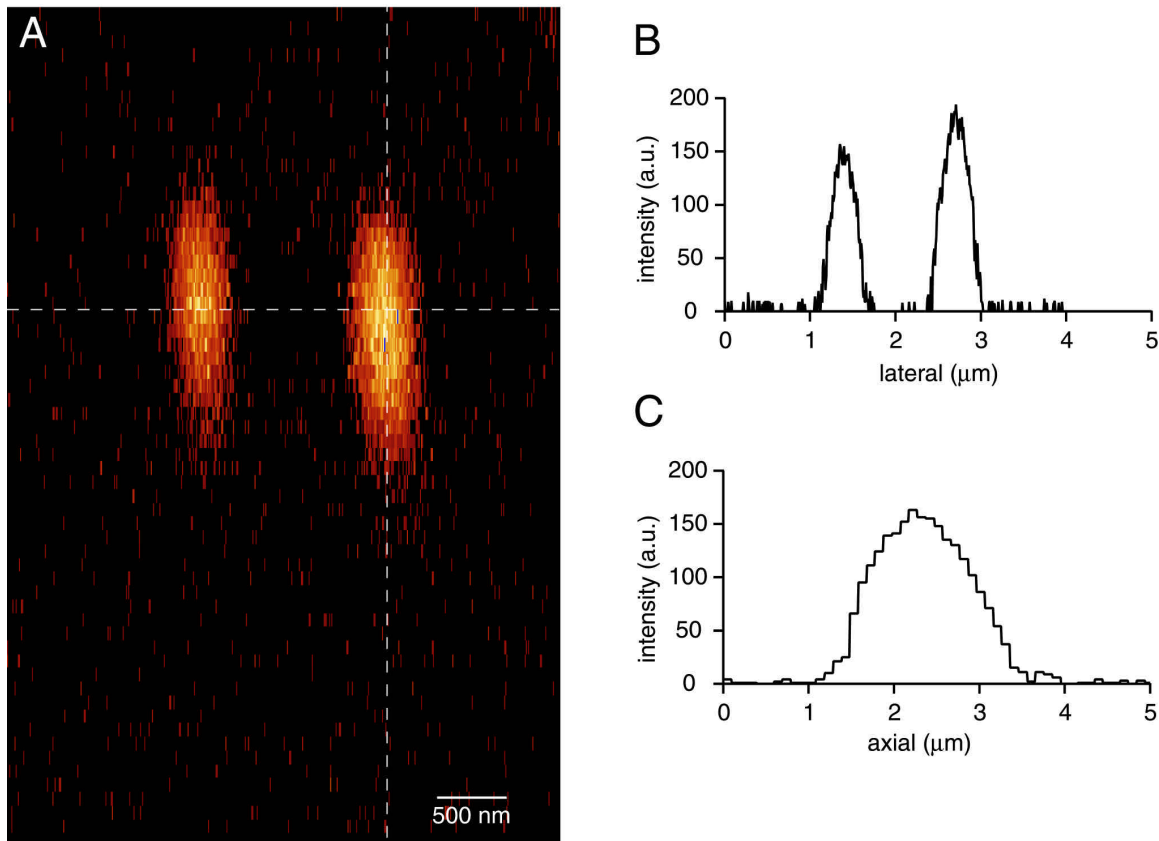


**Figure 3.6 Point spread function**

The optical point spread function of the system was determined by imaging subresolution fluorescent beads (100 nm). The excitation wavelength was 820 nm.

**A** xz projection of a fluorescent image stack of two fluorescent beads acquired with the HCX APO 63x objective. The dashed lines indicate the lines along which the intensity profiles were measured.

**B** Intensity profile along the lateral direction giving two peaks for the two beads. The FWHM for each bead was taken as a measure of the optical resolution. The FWHM distance for the right bead was 0.46 μm.

**C** Intensity profile along the axial direction of the right bead. The resolution in the axial direction was determined to be 1.7 μm in this case.

In the axial direction the deviation is larger. The deviations can be explained by the fact that the objective lens together with the water immersion-agarose interface is not aberration free. Additionally, the theory assumes a homogeneously illumination with planar wavefronts of the objective lens. In the experimental setup this is accomplished by overfilling the backfocal aperture of the objective (assuming a Gaussian beam profile, overfilling is by a factor of  $1/e^2$ ). The trade-off between enough power passing the aperture and homogeneous illumination might reduce the effective NA of the experimental system, explaining the deviations from the theory.

In conclusion, these experiments show that with the current setup a lateral resolution of 0.5

objective	experiment		theory	
	lateral ( $\mu\text{m}$ )	axial ( $\mu\text{m}$ )	lateral ( $\mu\text{m}$ )	axial ( $\mu\text{m}$ )
HCX APO 40x	$0.48 \pm 0.03$	$1.86 \pm 0.17$	0.44	1.35
HCX APO 63x	$0.47 \pm 0.03$	$1.60 \pm 0.09$	0.39	1.03

**Table 3.1 Optical resolution**

*Summary of the optical resolution of the two most commonly used objectives in the axial and the lateral direction. The experimental results are compared to the theoretical values ( $\lambda = 820 \text{ nm}$ ).*

$\mu\text{m}$  and an axial resolution of  $1.8 \mu\text{m}$  can be reached. This gives good resolution to image small structures like spines in brain slices, which have a diameter of about  $1 \mu\text{m}$  (Yuste 1995).

### **Photon count**

For imaging small structures in brain slices it is desirable to collect as many photons as possible (Koester, Baur et al. 1999). The collection efficiency of the non-descanned detectors were evaluated (Denk 1994).

Fluorescence emission was measured from a homogeneous sample of MgGreen ( $500 \mu\text{M}$ ) indicator solution containing  $500 \text{ nM Ca}^{2+}$ . One frame with 512 by 512 pixels was acquired for the non-descanned epifluorescence and transmission detector respectively (Fig 3.7A) showing statistical noise fluctuations. Fluorescence photon emission follows Poisson statistics, which is reflected in the grey-value histogram calculated from this image.  $n$  photons amplified by the PMT detector set at gain  $u$  and an offset of  $u_0$  result in the grey value

$$g = n \quad u - u_0$$

From the Poisson-distribution

$$p(n) = \frac{x^n}{n!} e^{-x}$$

one derives for the probability  $p(g)$  to find a grey values of  $g$  if  $x$  signal electrons were generated on average per pixel

$$p(g) = \frac{x^{\frac{g+u_0}{u}}}{1 + \frac{g+u_0}{u}} e^{-x}$$

This function with the free parameters  $x$  and  $u$  was fitted to the histogram obtained from the fluorescence image yielding the number of signal electrons per pixel and thus the number of photons per pixel.

The measurements were repeated for different laser powers. Fig 3.7C shows the logarithmic plot of the average laser power in the object plane versus the number of collected photons per

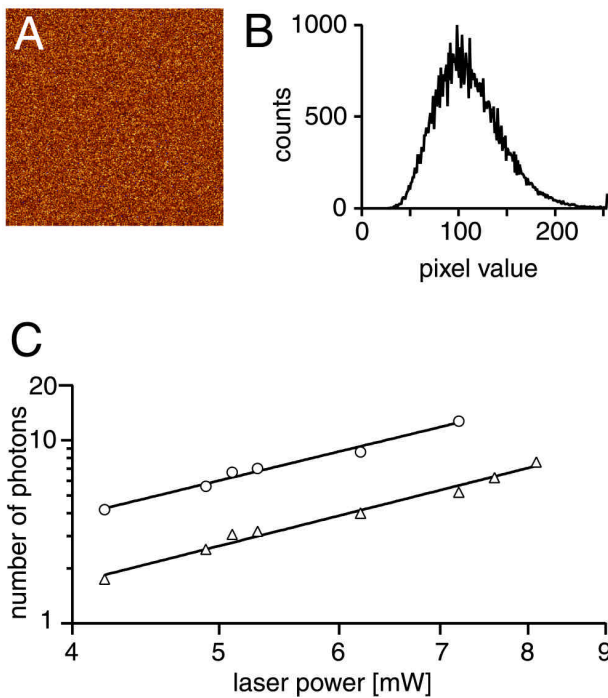


**Figure 3.7 Photon count**

**A** Fluorescence image from a uniformly stained sample.

**B** The histogram of the pixel value distribution from the image in A. Assuming Poisson statistics the number of fluorescence photons corresponding to the measured distribution were derived.

**C** Logarithmic plot of the number of photons per pixel for the epifluorescence non-descanned detector (triangles) and the condensor detector (circles) for different laser powers. The solid lines represent linear fits to the data points. Both fits yield a slope of 2 indicating two-photon excitation. Note that the condensor collects twice as many photons as the objective.

pixel for both detector pathways. The linear fits to the data points have a slope of  $2.1 \pm 0.1$  and  $2.0 \pm 0.1$  for the photons collected in the epifluorescence detector and the condensor detector respectively, revealing that the number of photons per pixels increases with the square of the average laser power. This confirms that the fluorescence was generated by two-photon excitation. Furthermore, it shows that the transmission detector collects twice as many photons as the epifluorescence detector. This is in agreement with the ratio of the numerical apertures of the condensor (NA 1.3, oil) and the objective (NA 0.9, water). The condensor has a larger acceptance angle and can collect more photons than the objective. Addition of the signals from the two detector pathways results in a high collection efficiency, which allows to image small fluorescence structures in highly scattering brain slices.

### 3.3.4 $\text{Ca}^{2+}$ imaging

#### *Ca<sup>2+</sup> indicators*

$\text{Ca}^{2+}$  is an important second messenger to trigger many signaling cascades in neurons. Functional imaging of  $\text{Ca}^{2+}$  influx is possible with a large number of  $\text{Ca}^{2+}$  ion sensitive indicator dyes. These dyes change their spectral properties upon binding  $\text{Ca}^{2+}$  ions. Some dyes change their absorption spectrum, whereas other dyes change their emission spectrum. So called ratiometric dyes, like Fura-2, have an isosbestic point at which the properties of the dye are independent of ion concentration. From measurements with ratiometric dyes absolute

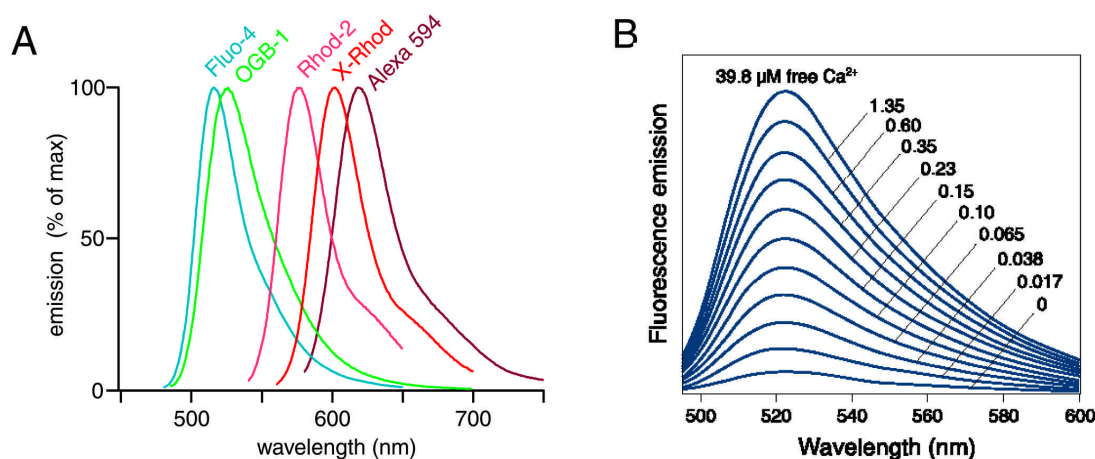


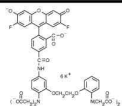
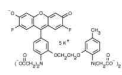
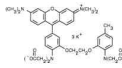
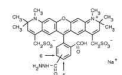
**Figure 3.8 Fluorescence emission spectra**

**A** Normalized fluorescence emission spectra of the dyes used in this study. The spectra are taken from the Molecular Probes website. All but Alexa 594 are  $\text{Ca}^{2+}$  indicators.

**B** Fluorescence emission spectra of Oregon Green Bapta-1 (OGB-1) at different free  $\text{Ca}^{2+}$  concentrations.

values of  $\text{Ca}^{2+}$  concentration can be derived (Grynkiewicz 1985). Most dyes were developed and optimized for one photon excitation in the visible or UV spectrum, but it has been shown that most of these dyes are equally well suited for two photon excitation (Xu and Webb 1996). The dyes used in this study were non-ratiometric and they increased their quantum efficiency (fluorescence emission) upon binding  $\text{Ca}^{2+}$ . They were all purchased from Molecular Probes (Eugene, OR, USA). They all showed good two-photon excitation between 820 nm and 890 nm. Some of the properties of the dyes are summarized in Table 3.2. Alexa 594 is not sensitive to  $\text{Ca}^{2+}$  and it was used to label the morphology of neuronal structures. It was used in conjunction with the  $\text{Ca}^{2+}$  indicator Fluo-4, which has a low basal fluorescence, not sufficient to visualize fine neuronal compartments (Oertner, Sabatini et al. 2002).

The emission spectra at saturating  $\text{Ca}^{2+}$  levels of some dyes, taken from the Molecular Probes catalogue, are shown in Fig 3.8. This figure illustrates the problem of spectrally separating two dyes. The above mentioned combination of Fluo-4 and Alexa 594 can well be separated because there is little overlap in the emission spectra and appropriate filter combinations can

dye	$k_D$ (nM)	$\lambda_{em}$ (nm)	structure
OGB-1	170	520	
OGB-5N	20000	520	
Fluo-4	345	520	
Rhod-2	570	580	
XRhod-1	700	600	
Alexa 594	/	618	

**Table 3.2 Properties of fluorescence indicators**

The  $\text{Ca}^{2+}$  dissociation constant and the peak emission wavelength are given for the dyes used in this study. The values and the structures are taken from the Molecular Probes website.



block the overlapping part of the spectrum. Other dye combinations used in this study, like the combination of Oregon Green Bapta-1 (OGB-1) and Rhod-2, to measure pre- and postsynaptic  $\text{Ca}^{2+}$  transients simultaneously could well be separated in the green channel, but there was some overlap from the green fluorescence into the red channel. So far the number of commercially available dyes with the desired properties are limited. New dyes with improved two-photon cross sections and different spectral characteristics might improve the possibility of spectral separation of two dyes (Albota 1998).

Spectral unmixing procedures, in which the characteristic differences of the emission spectra of two dyes is used to separate their relative contribution to the signal in the corresponding channel of the other dye, might help to separate even dyes with largely overlapping emission spectra (Tsurui, Nishimura et al. 2000). The method of spectral unmixing, briefly explained, tries to linearly separate the contributions of the two dyes  $s_i$  to a given detector signal  $s_i'$  in a certain spectral range. Formally this can be written as

$$\begin{pmatrix} s_1' \\ s_2' \end{pmatrix} = \begin{pmatrix} a_{11} & a_{12} \\ a_{21} & a_{22} \end{pmatrix} \begin{pmatrix} s_1 \\ s_2 \end{pmatrix}$$

The matrix coefficients  $a_{ij}$  represent the contribution of one dye to the corresponding detector signal. Deriving the coefficients for the inverse unmixing matrix is a problem of linear algebra and it has been solved mainly for analyzing spectral data from satellites (Weltje 1997; Zibulevsky and Pearlmutter 2001). In biological fluorescence microscopy it has been shown that even spectrally closely overlapping GFP variants can be separated by this approach (Lansford, Bearman et al. 2001). This method might also prove useful to separate the signals from two spectrally overlapping  $\text{Ca}^{2+}$  indicators.

### ***Ca<sup>2+</sup> buffering***

In order to do any  $\text{Ca}^{2+}$  measurement in neurons they have to be loaded with a fluorescent  $\text{Ca}^{2+}$  indicator, which changes its properties upon binding  $\text{Ca}^{2+}$ . The indicator is in competition with endogenous  $\text{Ca}^{2+}$  binding proteins and it alters the decay time dynamics of the  $\text{Ca}^{2+}$  transients. As can be seen from table 3.2, the indicator dyes have different affinities for  $\text{Ca}^{2+}$ . Low affinity  $\text{Ca}^{2+}$  indicators report the timecourse of the  $\text{Ca}^{2+}$  transient more faithfully, but the increase in fluorescence is smaller (Koester 2000).

By loading a cell with a known concentration of indicator the added buffer capacity can be calculated (Helmchen 1996; Maravall, Mainen et al. 2000). For low affinity dyes the incremental binding ratio can be expressed by

$$\kappa_B = \frac{[B]}{k_d}$$

where [B] is the concentration of the exogenous added buffer and  $k_d$  is the dissociation constant given by

$$k_d = \frac{[Ca^{2+}][B]}{[CaB]}$$

derived from a simple first order chemical reaction, where  $[Ca^{2+}]$  and [CaB] are the equilibrium concentrations of free  $Ca^{2+}$  and bound  $Ca^{2+}$  respectively (Neher 1992; Koester 2000).

Varying the concentration and measuring the effect on the decay time of the fluorescence transient elicited by a single bAP allowed to extrapolate to the endogenous situation with no buffer added. This gave an estimate of the endogenous decay time constant of the  $Ca^{2+}$  transients in a cell and an estimate of the endogenous buffer capacity (Helmchen 1997).

### ***Line scan, frame scan and xytz scan***

$Ca^{2+}$  transients were typically recorded in the line scan mode with both microscopes used. One spatial dimension is given up to increase the temporal resolution of the recording. The laser beam is continuously scanned back and forth along the same line and the fluorescence over time is recorded. The resulting images consist of one spatial axis (along which the beam is scanned) and one axis in time. Fig 3.9A shows a xy-image of a spine and a dendritic shaft. The white line indicates the position of the linescan and the arrows indicate that both scan directions were used (bidirectional scan) increasing the temporal resolution. The right image shows the resulting line scan. A single line was scanned within 2.2 ms. Two subsequent time points were averaged resulting in a temporal resolution of 4.4 ms. Typically 512 lines were acquired for each transient. Stimulation started 150 ms after the beginning of the linescan. In the example in Fig 3.9A a single bAP evokes a transient increase in  $Ca^{2+}$  in the spine and the dendritic shaft. The time resolution of 4.4 ms was fast enough to image the volume averaged peak  $Ca^{2+}$  influx in dendrites and spines. The timescale of  $Ca^{2+}$  influx due to bAPs is around 1 ms. It is below the time resolution used in the measurement, thus the increase in fluorescence evoked by a bAP appeared to be instantaneous.  $Ca^{2+}$  transients evoked by synaptic transmission have a slightly slower time course, which is attributable to the slower kinetics of the NMDA receptor, but it is still faster than the time resolution of the imaging

system. Hence, peak volume averaged  $\text{Ca}^{2+}$  levels and the slow decay of the  $\text{Ca}^{2+}$  fluorescence transient back to baseline could be reliably resolved, but the fast rise in intracellular  $\text{Ca}^{2+}$  was not investigated. Using faster scan speeds would allow to measure the fast dynamics of the initial  $\text{Ca}^{2+}$  inflow.

Frame scan imaging in time is slower than line scan imaging because a full frame was to be acquired for each time point and then the slow axis scanner has to return to its initial position for the next sweep. Reducing the frame format and pixel integration time can increase the frequency of image acquisition. The second system set up for this study uses additionally a fast resonant scanner to scan one line. The resonance frequency is set at 4 kHz, thus a single line is scanned every 0.25 ms. The bidirectional scan mode uses both scan directions, thus a line can be scanned within 0.125 ms. Even though a slow axis is still present the frame rates could be greatly increased. Frame rates up to 56 Hz are now possible with a format of 512 by 32 pixels. These frame rates allow imaging of extended regions of the dendritic tree and multiple spines at the same time. Fig 3.9B shows an example of a frame scan series of a dendritic shaft and two spines. After the first frame a single bAP was evoked. In the second frame an increase in fluorescence can be observed. The image sequence was recorded at 9 Hz and a frame format of 256 by 256 pixels. In the frame scan mode  $\text{Ca}^{2+}$  transients can be observed in multiple compartments at the same time. Fig 3.9C shows an example of a bAP invading the apical dendrite of a layer 2/3 pyramidal neuron. The rectangular frame format (512 by 64 pixels) was oriented to contain the entire apical dendrite. Images were acquired near video rate (31 Hz, 32 ms per frame) to measure the bAP evoked  $\text{Ca}^{2+}$  transient. A background image was subtracted from the sequence to yield the fluorescence change  $F(t)$  in the apical dendrite.

Format	LCS SP2 RS		LCS NT	
	time per frame (ms)	frequency (Hz)	time per frame (ms)	frequency (Hz)
512 x 512	144	7	342	3
256 x 256	109	9	207	5
128 x 128	56	19	140	7
64 x 64	32	31	77	12
32 x 32	18	56	/	/

**Table 3.3 Comparison of the frame scan speeds for the LCS SP2 RS and the LCS NT scanning units**

*Note that the SP2 RS can achieve the same frame rates given for the square image format also for rectangular formats of 512 by n pixels since the amplitude of the resonant scan mirror is constant. The maximal time resolution for a line scan is for the SP2 RS 0.125 ms and for the NT 0.54 ms.*

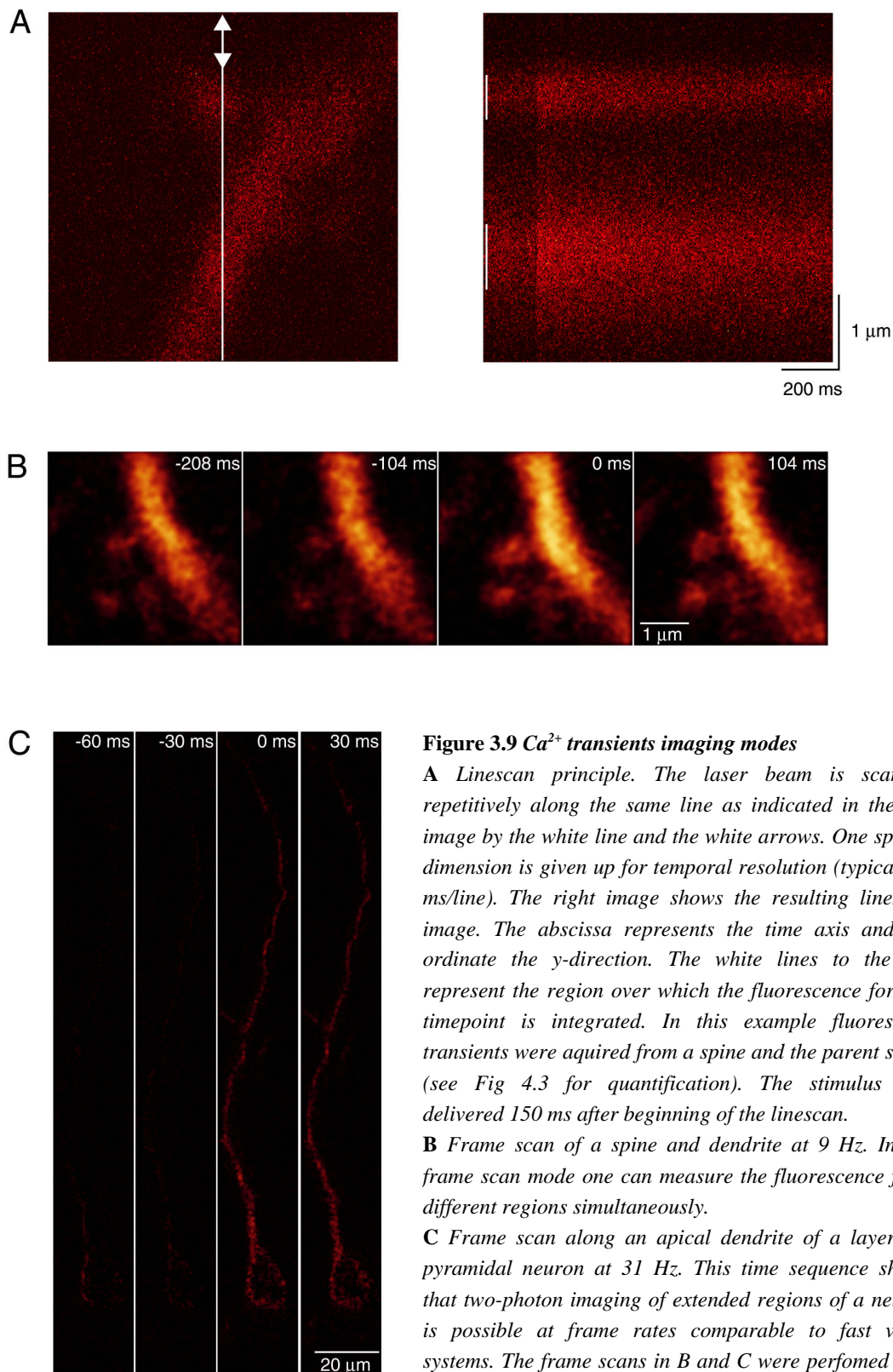


**Figure 3.9  $Ca^{2+}$  transients imaging modes**

**A** Linescan principle. The laser beam is scanned repetitively along the same line as indicated in the left image by the white line and the white arrows. One spatial dimension is given up for temporal resolution (typically 2 ms/line). The right image shows the resulting linescan image. The abscissa represents the time axis and the ordinate the y-direction. The white lines to the left represent the region over which the fluorescence for one timepoint is integrated. In this example fluorescence transients were acquired from a spine and the parent shaft. (see Fig 4.3 for quantification). The stimulus was delivered 150 ms after beginning of the linescan.

**B** Frame scan of a spine and dendrite at 9 Hz. In the frame scan mode one can measure the fluorescence from different regions simultaneously.

**C** Frame scan along an apical dendrite of a layer 2/3 pyramidal neuron at 31 Hz. This time sequence shows that two-photon imaging of extended regions of a neuron is possible at frame rates comparable to fast video systems. The frame scans in B and C were performed with the LCS SP2 RS resonant scanhead. Stimuli were delivered before the frame at time 0.

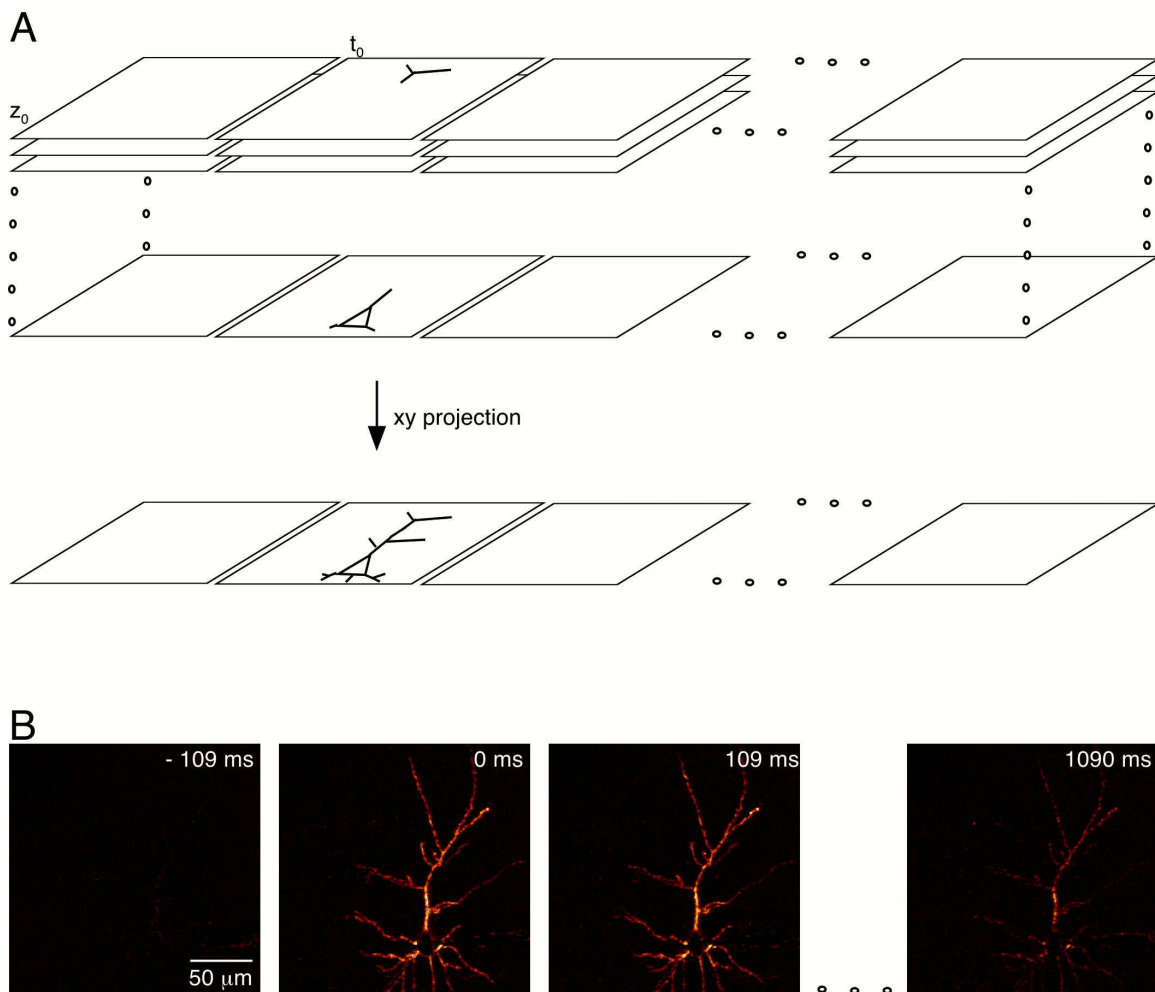


**Figure 3.10 Time resolved  $\text{Ca}^{2+}$  transient imaging in 3D with the xytz-scan mode**

**A** The xytz-scan mode is based on the fast frame scanning capability of the resonant scanning system. Time series at different focal positions are combined to a 4D-image stack. The stimulus is always delivered before the same frame of each time series. Full frames with a frame format of 256 by 256 pixels and a field of view of  $200\ \mu\text{m}$  by  $200\ \mu\text{m}$  are imaged at a frame rate of 9 Hz.

**B** Example experiment from a layer 2/3 pyramidal neuron. The xy-projections of 40 sections ( $1\ \mu\text{m}$  separation) of the 4D-image stack are shown at different time points. Averaged frames before stimulation are subtracted from the time series resulting in a  $\Delta F(t)$  representation of the fluorescence increase. The cell was stimulated by brief current injection to fire a single AP.

The dendrites of a neuron are usually not nicely aligned in one optical section. The dendritic tree has a more complex three dimensional structure (see Fig 4.2). Acquiring a complete 3D-stack for each time point over time is much too slow for imaging the fast  $\text{Ca}^{2+}$  transients in dendrites. The intrinsic optical sectioning properties of the two-photon microscope were combined with the fast frame scan capabilities of the resonant scanning system to measure the  $\text{Ca}^{2+}$  transients of bAPs in large parts of the dendritic tree in three dimensions. Therefore

a new imaging mode was developed. Fig 3.10 explains the principle of the xytz scanning mode. Fast frame scans at 9 Hz were acquired in each section covering a field of view of 200  $\mu\text{m}$  by 200  $\mu\text{m}$ . After the first 4 images during each time series a stimulus was delivered and the fluorescence increase in the structures, which were visible in the section were recorded. The sequence was repeated for the same optical section and the time series were averaged to increase the signal to noise ratio. Then the focus was shifted down to repeat the sequence in the next focal plane. After a complete focus series was acquired the time series for each optical section were merged resulting in a 3D data stack in time. For each structure in the sampled 3D volume the fluorescence transients could be analyzed. Fig 3.10B shows for illustration the xy projection of a xytz image stack of a layer 2/3 pyramidal neuron for some timepoints. To enhance contrast the fluorescence change  $F(t)$  was calculated from the time series. A single bAP was elicited by somatic current injection before the frame with the timestamp marked 0 ms was acquired. The increase in fluorescence in all parts of the dendritic tree can clearly be seen. To exploit the capabilities of the xytz scanning method the stimulus elicited for each time series has to result in a repetitive, stereotyped and reliable  $\text{Ca}^{2+}$  transient in all structures of the neuron. bAPs fulfill these requirements (Helmchen 1996; Koester 2000; Holthoff, Tsay et al. 2002). The  $\text{Ca}^{2+}$  profile induced by single and variable events cannot be imaged in 3D. For these cases line scan recordings are better suited. Nevertheless it was possible to detect single synaptic contacts based on the localized increase of fluorescence due to the  $\text{Ca}^{2+}$  influx during synaptic transmission.

In conclusion, this method might help to localize single synaptic contacts in connected pairs of neurons automatically. To then further characterize the exact time course for  $\text{Ca}^{2+}$  influx during synaptic transmission at these contacts the higher temporal resolution of line scan imaging is better suited.

### *Data analysis of fluorescence traces*

Fluorescent line scan traces were analyzed as follows. Regions of interest (ROIs) were placed around the fluorescent structures and one ROI was placed in a region with no fluorescent structure to measure the background fluorescence. The fluorescence in each region was averaged line by line to yield the raw fluorescence over time  $F(t)$ . In the background ROI all pixels were averaged over time to yield the background fluorescence  $F_B$ . The fluorescence intensity from the raw fluorescence traces was averaged during the first 100 ms before a physiological stimulus was evoked to yield the basal fluorescence  $F_0$ . Relative fluorescence changes were now calculated from

$$\frac{F(t)}{F_0} = \frac{F(t) - F_B}{F_0 - F_B}$$

The relative fluorescence transients were fitted by least square fit algorithms based on Igor Pro (Wavemetrics, Lake Oswego, OR, USA). Single stimuli  $\text{Ca}^{2+}$  transients were readily fitted by a single exponential function

$$F/F(t) = Ae^{-t/\tau}$$

yielding the amplitude  $A$  and the decay time constant  $\tau$ .

Paired stimuli  $\text{Ca}^{2+}$  transients were fitted by the sum of two single exponentials

$$F/F(t) = A_1e^{-t/\tau} + A_2e^{-(t-\Delta t)/\tau}$$

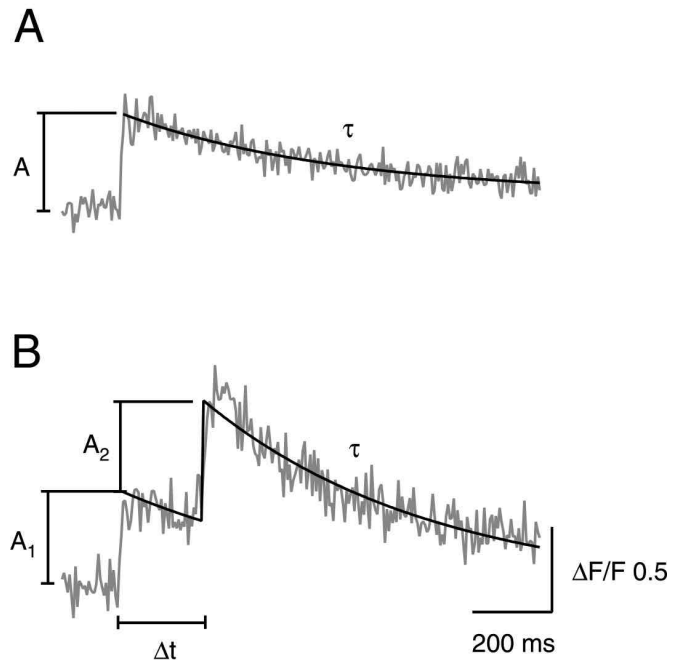
separated by the corresponding time interval  $\Delta t$ .  $A_1$  and the decay time constant  $\tau$  derived from a single stimulus transient fit were often kept constant during the fit yielding the value for the amplitude  $A_2$ .

$\text{Ca}^{2+}$  plateau levels were derived from a single exponential fit again.

### Figure 3.11 $\text{Ca}^{2+}$ transients fits

**A** Single stimuli evoked  $\text{Ca}^{2+}$  transients were fitted with a single exponential function, yielding the maximal amplitude  $A$  and the decay time constant  $\tau$ .

**B** Double stimulus protocols were fitted with the sum of two single exponentials, separated by the stimulus interval  $\Delta t$ . The fits yielded the amplitudes  $A_1$  and  $A_2$  and the decay time  $\tau$ . Often  $A_1$  was kept constant. See also Fig 4.12 for further details.



## 3.4 IR-scanning gradient contrast

### 3.4.1 IR-video microscopy

Neurons and small neuronal compartments in brain slices can be visualized by IR-video microscopy (Dodt 1990). This allows optically guided patching of identified cell types and dendrites (Stuart 1993). Biological samples absorb and scatter IR light less than visible light. This allows imaging of neuronal structures in the slice with high spatial resolution. Cells deeper into the slice, which are less damaged by the slicing process, can be targeted. Somata down to 100  $\mu\text{m}$  below the slice surface can be visualized. A near IR bandpass filter can be used to filter the light from a standard halogen lamp. The image is acquired with an IR sensitive video camera. As brain slices are mainly phase objects, the contrast can be generated by differential-interference contrast (DIC) optics (Inoue 1986). Another contrast generation principle has been developed by H.U. Dodt (Dodt 1998; Dodt 1998; Dodt 1999). The so-called IR-gradient contrast produces an inhomogeneous illumination in the back focal plane of the condenser, the result of which is an oblique illumination of the specimen. This method is an improvement of earlier single-sideband modulation imaging modes (Kachar

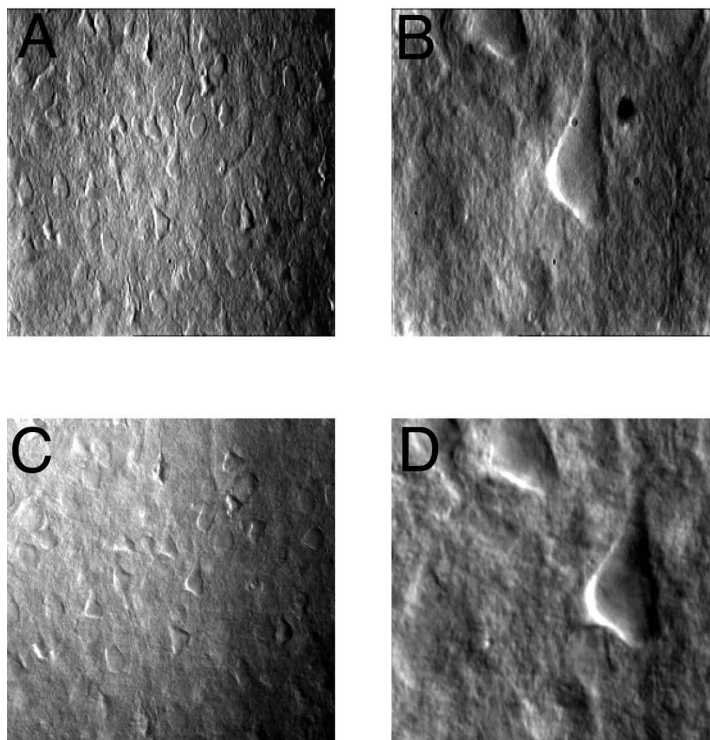


**Figure 3.12 Comparison of the IR-video and IR-scanning gradient contrast (IR-SGC) imaging modes**

**A** IR-video image of a brain slice with gradient contrast illumination.

**B** Four times magnification of the center of the image in A showing a pyramidal neuron.

**C** The same field of view as in A is imaged in the IR-SGC mode.

**D** Four times digital zoom of the center region of the image in C.

The images show that the two imaging modes are equivalent and they show the typical relief-like appearance. The images in A and B were distorted due to the frame grabber card. The field of view in A and C is 200  $\mu\text{m}$  by 200  $\mu\text{m}$  and in B and D 50  $\mu\text{m}$  by 50  $\mu\text{m}$  respectively.



1985; Bretschneider and Teunis 1994). The image shows light and dark edges at the borders of cellular compartments with high resolution similar to a DIC image. Further contrast enhancement in video-based microscopy is achieved by electronic modification of the video signal (video-enhanced microscopy, (Inoue 1986)).

The presented setup used the IR-gradient contrast for contrast formation and imaging of neurons and the patch-pipette during the patching process. Based on Dodt's principle a combination of two-photon fluorescence excitation and IR imaging was achieved. This completely new imaging mode will be presented in the next paragraphs. It facilitated the precise targeting of small fluorescent neuronal structures with stimulation pipettes. It therefore allowed to selectively study  $\text{Ca}^{2+}$  transients in spines located at different distances from the soma.

### 3.4.2 Setup components for IR-scanning gradient contrast

The two-photon microscope setup was additionally equipped with IR-gradient contrast video microscopy to visualize neurons for patching in brain slices (Fig 3.4, light path depicted by the solid lines). A halogen lamp (Leica, Wetzlar, Germany) was mounted to one port of a mirror housing, which allowed reflection of the light into the optical path of the microscope. A  $780 \pm 50$  nm bandpass filter (Luigs&Neumann, Ratingen, Germany) was placed in front of the lamp. The mirror house was connected to a so-called gradient contrast tube (Luigs&Neumann, Ratingen, Germany), which consists of two lenses forming a one-to-one telescope and a rotateable semi-circular aperture and a diffusor placed between the lenses. The gradient contrast tube was mounted on the microscope stand. Its optical components image the semi-circular aperture spatial filter into the back-focal plane of the microscope condenser. The transmitted IR light is collected by the objective and imaged onto an IR-sensitive video camera (Newvicon, Hamamatsu, Herrsching, Germany). An intermediate magnification changer (1x, 4x, Leica, Wetzlar, Germany) gave additional magnification to precisely target smaller cells.

During two-photon excitation fluorescence imaging the IR-laser beam is scanned, as described above, point by point across the specimen. The light rays in this case follow the reverse light path of the rays emerging from the lamp. The forward scattered laser light is collected by the condenser and is then filtered by the semi-annular aperture. By removing the mirror in the mirror house from the light path the laser light is focused through a 30 mm lens onto a PMT attached to the second port of the mirror house. The PMT is connected to the acquisition electronics of the confocal scanning unit and is therefore synchronized to the image acquisition in the fluorescence channels. Contrast enhancement during image acquisition was achieved by setting the gain and offset of the PMT to appropriate values.

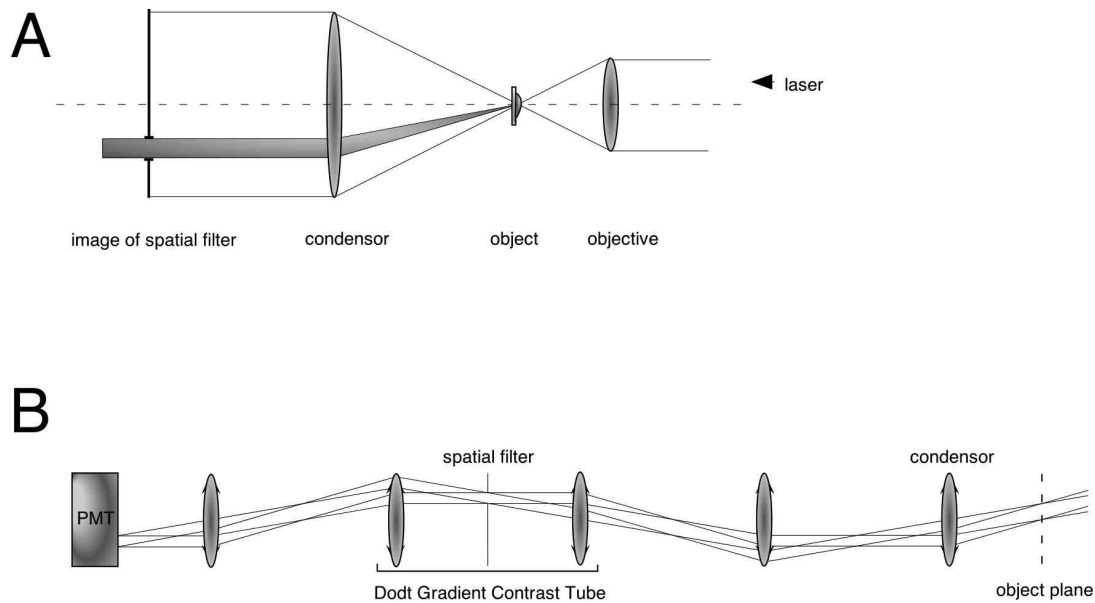


**Figure 3.13 Principle of IR-SGC**

**A** The image of the spatial filter in the back focal plane of the condenser allows passage only of light, which is scattered by the object into a certain angular direction.

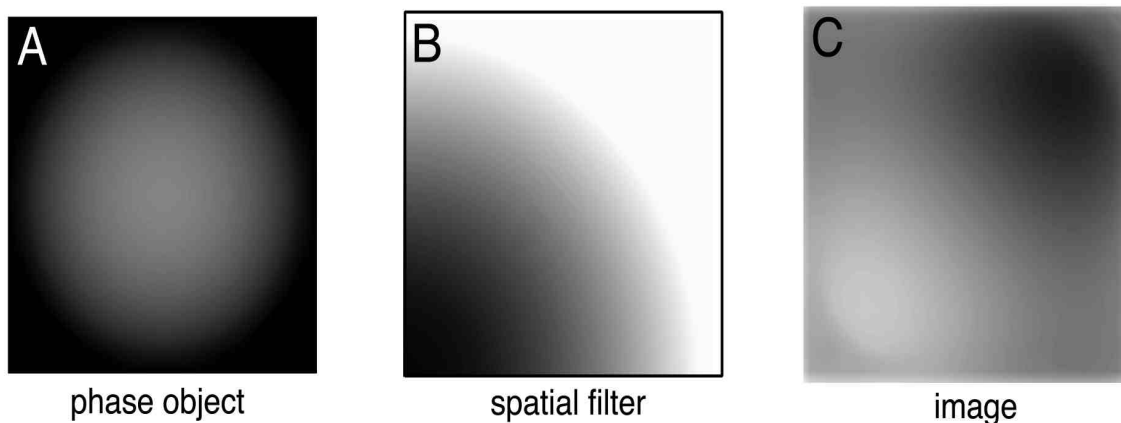
**B** The spatial filter is placed in a telecentric conjugate plane of the optical system. Thus the acceptance angle is the same for each point in the object plane. This is depicted by ray tracing the light emerging from two points in the object plane through the optical system.

### 3.4.3 IR-SGC principle

A spatial filter of the shape of a quarter annulus is imaged into the back focal plane of the condenser. A diffusor, which can be shifted relative to the spatial filter, smears the sharp edges of the spatial filter and results in a gradient of illumination in the back focal plane of the condenser (Dodt 1999). This results in an oblique illumination of the specimen with all Fourier-components (i.e. all angles) present, but with each component weighed differently (Dodt 1998). Less light is transmitted than with full cone illumination, resulting in less stray light from out of focus regions. Differences in refractive indices in the specimen scatter the incident oblique light cone and result in dark and light edges.

Light rays passing through the microscope in the opposite direction resulted in the same image (interchangeability of the direction of light propagation). Thus illuminating the specimen by a laser beam focused by the objective and scanned point by point yielded an image equivalent to the IR-gradient contrast video image. To understand the contrast

formation in the point scanning mode one can consider the spatial filter as a light stop, which only permits light scattered under a certain angle to pass (Fig 3.13A). Since the spatial filter is imaged into the back aperture of the condenser the allowed angle is the same for each point in the specimen plane (Fig 3.13B). Thus the IR-scanning gradient contrast is generated by the different scattering properties of each point ('point' refers to the illuminated, diffraction limited laser beam spot) in the specimen due to differences in the refractive index by collecting only the light which is scattered into the angular direction admitted by the spatial



*A* A simple computer simulation based on Abbe's theory of image formation uses the Fourier transform properties of a lens.

*A* The imaginary part of a circular phase object with varying phase retardation is depicted.

*B* The gradient contrast filter is modelled by a semi circular gradient spatial filter.

*C* The resulting image after Fourier-transforming the phase object, multiplying the result with the spatial filter and a second Fourier transform in the image space. The same procedure without spatial filtering would result in a homogeneous image, i.e. in no contrast. The simulated image resembles the experimental results.

filter. This scattered light mainly represents structures of higher spatial frequencies of the specimen or higher order diffracted light of lower spatial frequencies. IR-SGC can be considered as a spatial filtering process, which enhances features of high spatial frequencies in the specimen (Meyer-Arendt 1982). Only one sideband of light diffracted by the specimen is transmitted (Bretschneider and Teunis 1994). The phase differences between the undiffracted and the transmitted diffracted sideband result in intensity differences in the image. They enhance mainly edges of neurons in the brain slice.

A computer simulation with Mathematica (Wolfram Research, Champaign, IL, USA) was performed to demonstrate the image formation process for the gradient contrast method. A transparent (half-) sphere was modeled as a pure phase object with a constant real amplitude and a spherically changing phase. Fig 3.14A shows the imaginary part of the object. Since

the object is a pure phase object the image would yield only a constant amplitude, i.e. the object would be invisible. In the simulation the object was Fourier-transformed, which yields the complex diffraction pattern in the back focal plane of the condenser. To avoid artifacts due to the square shape of the object plane matrix the object was placed periodically on a grid in the object plane. A gradient spatial frequency filter was devised corresponding to the annular quarter aperture which is smeared by the diffusor (Fig 3.14B). The optical filtering corresponds to multiplying the frequency spectrum of the object with the spatial frequency filter. A second Fourier transformation of the filtered diffraction pattern results in the complex image function. The actual image (intensity) is the square of this function. Thus the process of image formation can be written as

$$image = |\mathcal{F}(\mathcal{F}(object) \cdot filter)|^2$$

where  $\mathcal{F}$  is the discrete Fourier-transform (Press, Teukolsky et al. 2002). The resulting image of the simulation is shown in Fig 3.14C. The typical relief like contrast can be seen.

Fig 3.15 compares the simulation to experimental data. Qualitatively, the contrast generated by the simulation is similar to the appearance of a bead in water and a spine in a brain slice.

Accordingly, the contrast formation in IR-SGC imaging can be explained by spatial frequency filtering. The special spatial frequency filter developed by Dodt is very similar to other spatial frequency filtering methods like reduced-carrier single-sideband microscopy

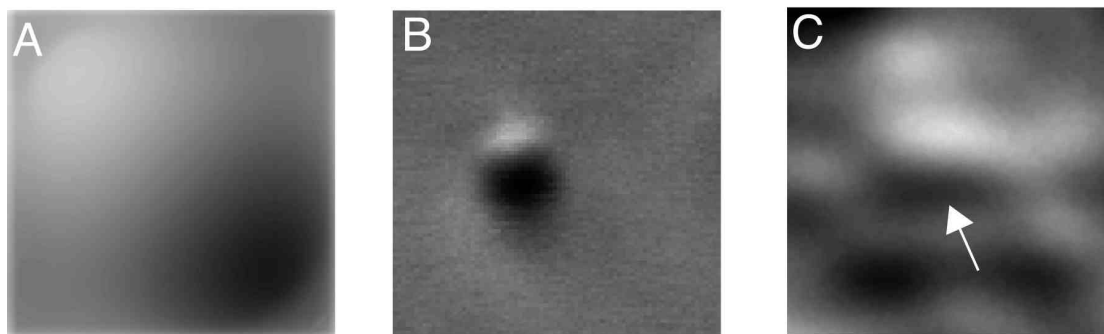


**Figure 3.15 Comparison of the simulation with experimental images**

**A** The image from the computer simulation.

**B** A latex bead with a diameter of  $1 \mu\text{m}$  in water.

**C** Image detail of a brain slice. Several structures in this image show dark and light edges resembling the bead in B and the simulation image in A. The arrow is pointing to an identified spine (see Fig 3.17C). The length of the arrow is  $1 \mu\text{m}$ .

(Bretschneider and Teunis 1994), Hoffman modulation contrast (Hoffman 1975), ‘schlieren’ contrast, dark-field reflection confocal microscopy (Torok 1995), single sideband edge

enhancement (Ellis 1978) and asymmetric illumination contrast (Kachar 1985). This study demonstrated that it is possible to make use of contrast enhancement by spatial frequency filtering in the scanning mode of a laser scanning microscope.

#### 3.4.4 Advantages

Images of similar resolution and contrast to the technique presented here have been achieved with scanning DIC imaging (Cogswell and Sheppard 1992). In order to do this, a confocal scanning unit was equipped with DIC optics and the forward scattered light was collected by a PMT. To produce DIC images polarizers and prisms have to be introduced into the optical path of the microscope. Especially for the highest photon collection efficiency in two-photon excitation fluorescence microscopy in brain slices these additional optical parts are not desired. The gradient contrast tube is outside of the fluorescence imaging axis so that no parts obstruct the fluorescence path. The gradient contrast tube can easily be fitted to different microscopes and the same tube can be used for different objectives.

The depth penetration of IR-SGC was comparable to or slightly better than the video gradient contrast image due to the longer wavelength used ( $\lambda$  is in the range from 820 nm to 890 nm as compared to 750 nm in the video imaging mode). Somata could easily be identified down to 120  $\mu\text{m}$  below the slice surface (Fig 3.16A).

The IR-SGC image is generated by scanning the laser beam point by point across the sample. By modifying the amplitude of the scanning mirrors smaller regions can be scanned with the same image format. This results in a digital zoom capability similar to an additional optical magnification. The digital zoom can be adjusted continuously (corresponding to a 1 to 32 times optical magnification factor). Thus the IR-SGC image can be magnified accordingly (Fig 3.16B). This is a great advantage over the regular video imaging mode, where the digital zoom is limited by the pixel size of the camera.

Even though the frame rate of the IR-SGC image is smaller than that of the regular video imaging system, patching neurons in brain slices was feasible.

It has been shown that patching in the IR-SGC mode is feasible. The variable digital zoom facilitates a precise positioning of the patch-pipette on the soma of small cells. Patching small dendritic compartments should also be possible (Larkum, Zhu et al. 1999; Larkum, Zhu et al. 2001).

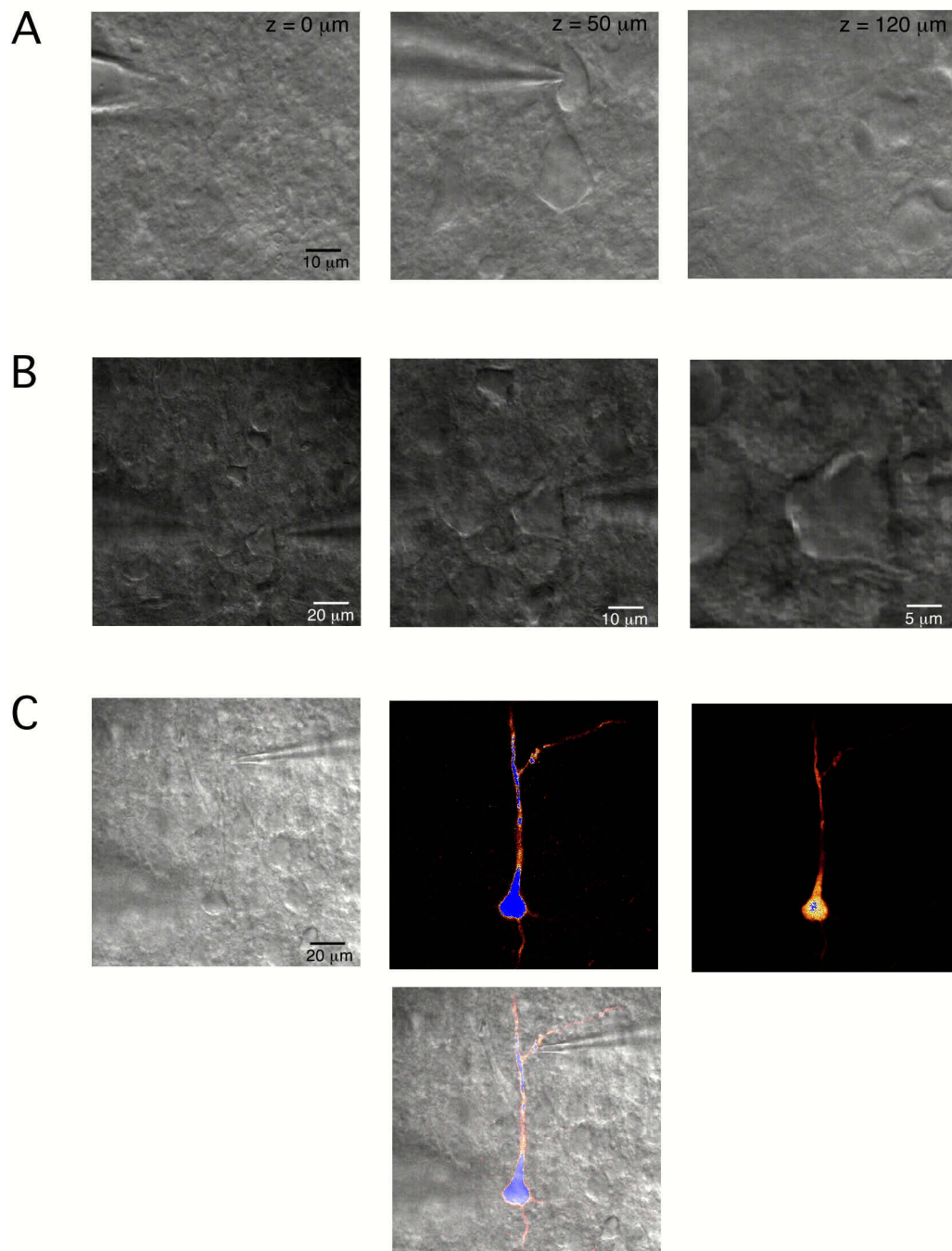


**Figure 3.16 IR-SGC advantages**

**A** IR-SGC images taken at different focal positions show the depth penetration capabilities. Somata can clearly be visualized down to  $120 \mu\text{m}$ .

**B** The digital zoom of the scanning unit can be used to continuously magnify the IR-SGC image.

**C** Simultaneously acquired IR-SGC image and fluorescence images from the condensor detector (middle) and objective detector (right) can be overlaid online to visualize fluorescent structures and the surrounding brain slice.

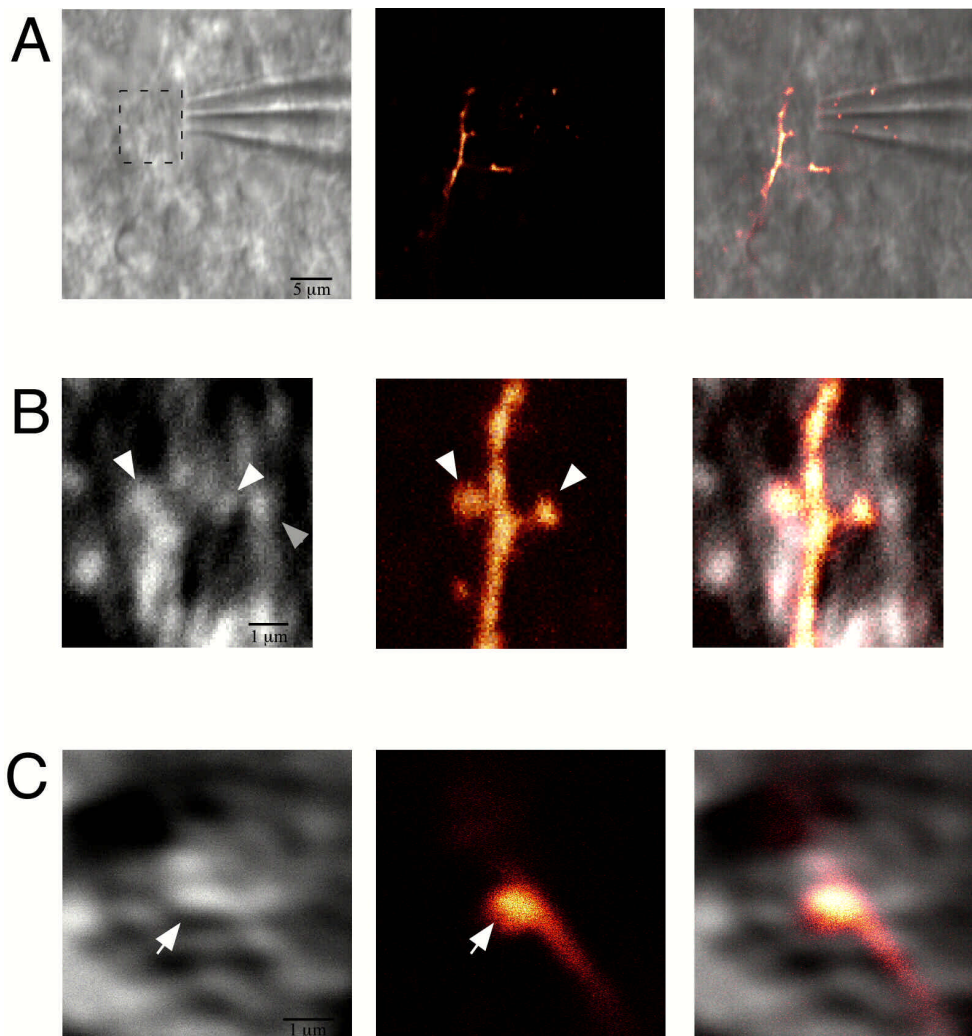


**Figure 3.17 IR-SGC imaging can resolve single spines**

**A** The overlay of the IR channel and the fluorescence channel facilitates the placement of stimulation electrodes close to dendritic shafts studded with spines.

**B** Enlargement of the region indicated in A by the dashed box shows several bead-like structures, marked by the white arrows. The fluorescence image and the overlay reveal that these structures are indeed spine heads. The grey arrow points to a putative presynaptic bouton.

**C** Another example of a bead-like structure in the IR channel, which colocalized with a fluorescent spine head in the fluorescence channel (white arrows).

### 3.4.5 Alignment free overlay of IR-SGC and fluorescence images

The most beneficial feature of IR-SGC in this study was that it was acquired simultaneously with the fluorescence image. The overlay function of the confocal scanner software enabled an online overlay of IR and fluorescence image on the computer screen (Fig 3.16C). Both

images were parfocal and intrinsically aligned with submicron resolution since the same laser beam is used for IR image formation and two-photon fluorescence excitation. As a consequence, the morphology of a neuron filled with a fluorescent dye was readily be visualized in relation to the surrounding tissue of the brain slice.

In this study this imaging mode was routinely used to position extracellular stimulation electrodes close to a particular dendrite of a neuron filled with a fluorescent  $\text{Ca}^{2+}$  indicator and it proved to be very useful to select an isolated dendritic structure. In this way it was possible to selectively target single spines with a stimulation electrode at different distances from the soma. In this way the distance dependence of the  $\text{Ca}^{2+}$  transients evoked in spines by subthreshold synaptic activation could be measured. There is evidence for a synaptic scaling, which is based on an increase of the number of AMPARs with the distance from the soma (Andrasfalvy 2001). The amplitude of  $\text{Ca}^{2+}$  transients measured at different distances from the soma might reflect this phenomenon.

Acquiring and overlaying fluorescence images and IR images by video microscopy has been challenging due to difficult alignment of the fluorescence and IR cameras. It is also difficult to correct for the different focal position of the fluorescence excitation and IR light (Keller 1995). These disadvantages can now be ruled out.

### **3.4.6 Single spines can be resolved**

The imaging capabilities of IR-SGC was impressively be demonstrated by imaging small neuronal structures (Fig 3.17). Neurons were filled with a fluorescent dye to visualize the morphology of the dendritic arbor and spines. Single spines could be resolved by two-photon fluorescence microscopy in the highly scattering tissue of brain slices. The IR-SGC image was acquired simultaneously. In the IR channel small bead-like structures can be recognized. The overlay of the IR and fluorescence image suggests that these bead-like structures are indeed single spine heads. They colocalize with the fluorescence image of a spine head of the dye filled neuron. Accordingly this method might be used for imaging small neuronal compartments like spines in unstained tissue.



## 3.5 Electroporation of $\text{Ca}^{2+}$ indicators

### 3.5.1 Single cell electroporation

Electroporation has been widely used for the delivery of DNA, RNA, proteins and fluorescence indicators in cells, slice cultures and recently also *in vivo* by bulk and single electrode electroporation methods (Teruel, Blanpied et al. 1999; Haas 2001; Inoue and Krumlauf 2001; Rae and Levis 2002). The application of a strong electromagnetic field above the dielectric breakdown level of lipid membranes results in the transient formation of small pores which close in the second time range (Ryttsen, Farre et al. 2000). During the opening time of the pores charged molecules are transported in the direction of the electrochemical gradient thereby loading the cell with the molecule.

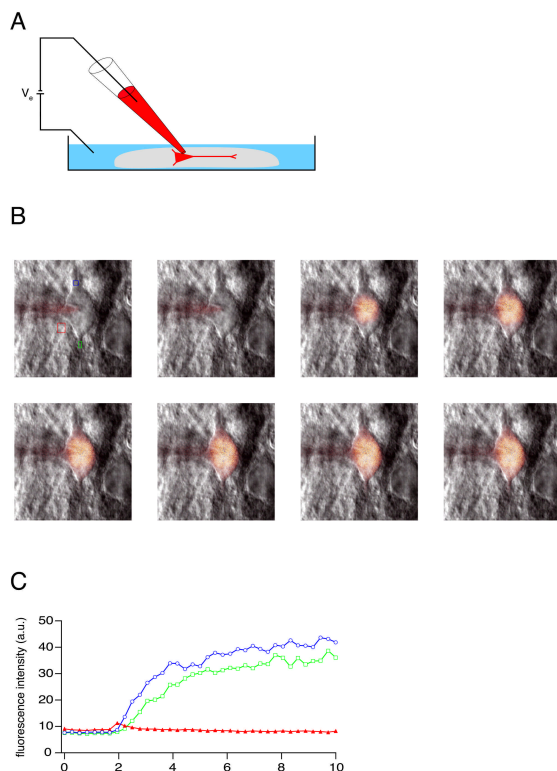


**Figure 3.18 Electroporation of  $\text{Ca}^{2+}$  indicators**

**A** Schematic drawing of the electroporation setup for acute brain slices. A glass electrode filled with a  $\text{Ca}^{2+}$  indicator is connected to a stimulation isolator unit. The pipette is placed close to the soma of a neuron in a brain slice. Short (10ms, -15V) voltage pulses cause transient opening of pores in the cell membrane and the  $\text{Ca}^{2+}$  indicator diffuses down the electric field and concentration gradient into the cell.

**B** Time-lapse series of the electroporation process. Images are taken at intervals of 280 ms. Between the second and third frame the electroporation pulse was delivered. The pipette gently touches the plasma membrane of the soma. The soma, the proximal apical dendrite and the axon are filled within seconds. Fluorescence intensities over time have been quantified in the regions of interest indicated in the first frame.

**C** Quantification of the fluorescence increase in the regions of interest indicated in B. Fluorescence

intensities increase exponentially in the proximal apical dendrite (purple trace, circles) and in the axon (green trace, squares). The fluorescence intensity in a background region close to the soma shows a slight increase in fluorescence in the frame after the electroporation pulse indicating that some of the dye diffuses into the extracellular space. Background fluorescence relaxes back to basal fluorescence again within 2 s.

As a novel method to load neurons in acute brain slices with  $\text{Ca}^{2+}$  indicators, single cell electroporation was developed. This method complemented dye loading by passive diffusion during whole-cell recordings. Its advantages were a rapid filling (less than 1 min, compared to 15 min by diffusion) of cells, the possibility to fill multiple cells with the same electrode and filling cells deep (more than 150  $\mu\text{m}$ ) into the slice.

Electroporation was used to fill spiny neurons deep in an acute brain slice to visualize their three dimensional dendritic arborization.

Cells were filled by short (10 ms), high voltage (-15 V) pulses with the  $\text{Ca}^{2+}$  indicator OBG-1 (1  $\mu\text{m}$ , Fig 3.18C) within a short time. Fig 3.18A illustrates the principle setup, which only needed an stimulus isolator (HG203, Ho-Med, England) attached to a glass pipette with resistances of 5-7 M $\Omega$ . Cells were targeted under visual control using the overlay of fluorescence and IR-scanning gradient contrast imaging (IR-SGC) to monitor the efficiency of cell loading (Fig 3.18B).

## 4 Results

### 4.1 Two-photon imaging of spiny neurons

In thalamo-cortical brain slices (Agmon 1991; Feldmeyer 1999) the barrel field of the rat somatosensory cortex was visualized using IR gradient contrast video microscopy (Dodt 1998). The barrel field appeared in layer 4 as evenly spaced dark structures, separated by light borders (Luebke, Egger et al. 2000). The somata of spiny neurons in layer 4 tended to cluster at the barrel borders in layer 4 and they were identified based on the shape and size of

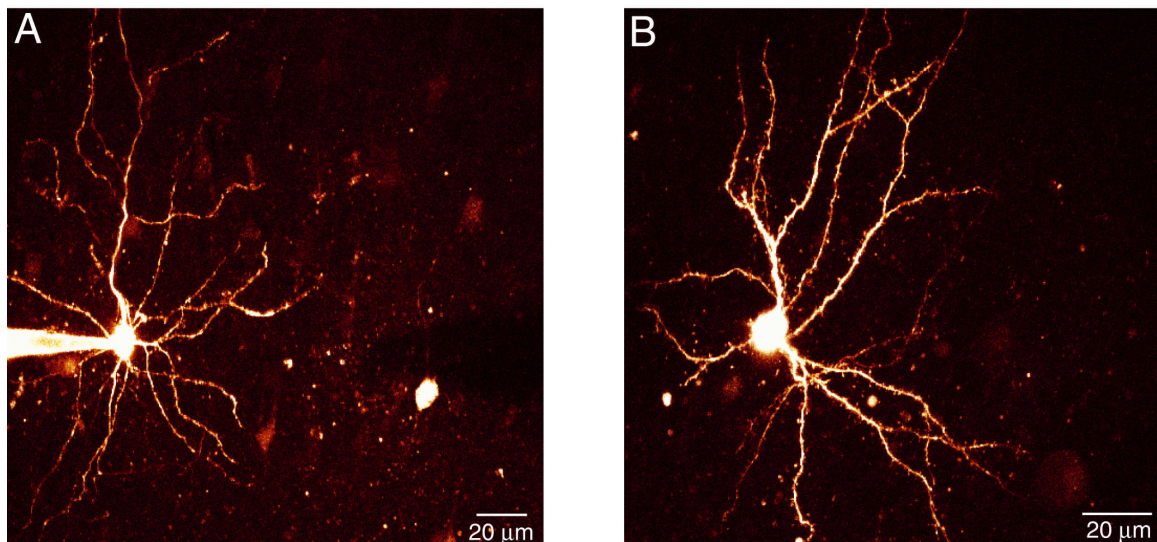


**Figure 4.1** Two-photon imaging of spiny neurons in layer 4 of the rat barrel cortex

Two classes of spiny neurons, based on their morphology, were found in layer 4 of the barrel field [Luebke, 2000 #15]. The morphology of the dendritic tree became apparent after filling the neurons with the  $\text{Ca}^{2+}$  indicator Oregon Green Bapta-1 (200  $\mu\text{M}$ ). Each image is the maximum projection of a fluorescence stack of 25 images taken at different focal positions. Note the different scale. The stack in A was acquired with a 40x objective to image a large part of the apical dendrite, whereas the stack in B was acquired with a 63x objective.

**A** A spiny neuron classified as a star pyramidal neuron. This class of neurons had a short apical dendrite without an elaborate tuft (as compared to a layer 2/3 pyramidal neuron).

**B** An example of a spiny stellate neuron. This class of neurons showed a characteristic asymmetric orientation of the dendritic tree. A few (three to seven,  $4 \pm 1$ ,  $n = 27$ ) thick primary dendrites emerged from the soma, which branch extensively into higher order dendrites. The patch pipette in this case was withdrawn before the stack was acquired.

their somata (10-15  $\mu\text{m}$  in diameter) and the star like initial parts of their dendrites without a prominent apical dendrite. Cells between 50-100  $\mu\text{m}$  below the slice surface were patch-clamped using IR video microscopy (Stuart 1993).

The cells were loaded with the  $\text{Ca}^{2+}$  indicator Oregon Green Bapta-1 (OGB-1, 200  $\mu\text{M}$ , Molecular Probes) via the patch pipette in the whole-cell configuration. OGB-1 was used in all experiments if not explicitly stated otherwise. After filling the cells for at least 15 min to ensure equilibration of the indicator in the cell, the morphology of the cells became visible in the two-photon excitation (TPE) fluorescence image. The intrinsic sectioning properties of TPE and the good signal to noise ratio from fluorescence structures deep into the brain slice allowed to visualize the three dimensional structure of the spiny neurons during the experiment. The resolution of the microscope of  $\sim 500$  nm in the lateral direction allowed to visualize the spiny protrusions, which densely covered the dendritic shafts of spiny neurons (Fig 4.2B, inset).

Fluorescence stacks of the spiny cells were acquired (20-40 sections at intervals of 2-4  $\mu\text{m}$  between each focal plane) and a maximum intensity projection revealed the morphology in the thalamocortical plane. The apparent morphology of spiny neurons could be divided into two distinct classes. From a sample of imaged spiny cells ( $n = 59$ ),  $\sim 80\%$  were identified as spiny stellate neurons (46 out of 59). These cells showed a marked asymmetric orientation of the dendritic tree (Fig 4.1B and Fig 4.2B). No prominent apical dendrite could be recognized, but a few (three to seven, on average  $4 \pm 1$ ,  $n = 27$ ) thick primary dendrites emerged from the soma, which branched extensively into higher order dendrites. The dendritic arbor was always restricted to the borders of the barrel in which the soma of the spiny stellate neuron was located ( $n = 10$ ). Fig 4.2A shows the overlay of the IR-SGC image with the simultaneously acquired TPE image demonstrating the confinement of the dendritic tree to one barrel.

The second class of spiny neurons resembled those described as star pyramidal neurons (Lund 1988). These cells constituted  $\sim 20\%$  of the spiny neurons in layer 4 of the barrel cortex (13 out of 59). They possessed an apical dendrite, which emerged from the upper pole of the soma and ascended towards layer 2/3 (Fig 4.1A). The apical dendrite gave rise to oblique apical dendrites, but it did not terminate in an apical tuft as compared to the extensive tuft of layer 2/3 pyramidal neurons. Basal dendrites emerged symmetrically from the soma branching into higher order basal dendrites. The dendritic tree of star pyramidal neurons was symmetrically arranged to the axis of the apical dendrite as compared to the

marked asymmetry of the dendritic tree of spiny stellate neurons. Fig 4.1 shows examples for the two different morphologies of cells found in layer 4 of the barrel cortex.

In whole-cell recordings spiny stellate cells had a resting membrane potential of  $-71.8 \pm 3.7$  mV ( $n = 43$ ) and star pyramidal cells had a resting membrane potential of  $-70.9 \pm 1.4$  ( $n = 13$ ). Somatic current injections in both cell types for 500 ms above a threshold resulted in a regular firing pattern with a slightly adapting AP frequency. In the absence of synaptic stimulation spiny neurons showed a high frequency of spontaneous activity (Feldmeyer 1999). No significant difference in the resting membrane potential ( $p > 0.2$ ) and the firing pattern between the morphologically distinct classes of spiny stellate and star pyramidal neurons could be found.

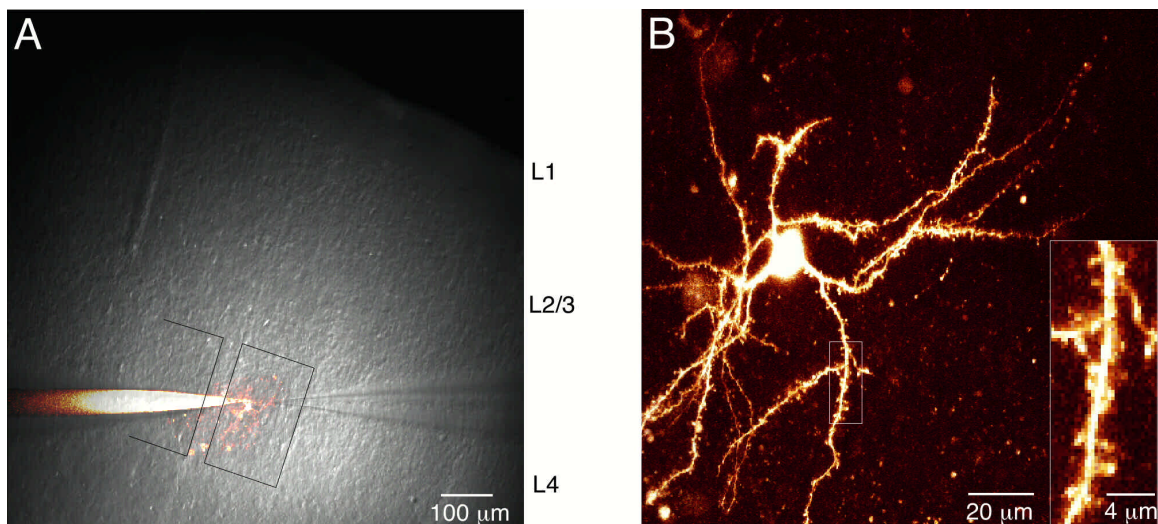


**Figure 4.2** *Ca<sup>2+</sup> imaging in spiny stellate neurons*

**A** *Overlay of the IR-SGC and the two-photon excitation fluorescence (TPE) image of a spiny stellate neuron filled with OGB-1, 200 μM. The solid lines outline the barrel borders. The dendritic arbor is confined to a single barrel.*

**B** *Fluorescence image of the same cell at higher magnification. The image is the maximum projection of 25 images taken at different focus positions. The asymmetric dendritic arbor can readily be identified. The inset shows a region of a dendrite studded with spines indicated by the white box..*

These results reproduced the findings by Feldmeyer et al. (Feldmeyer 1999), who found no difference in the immediate physiological properties of these two cell types in layer 4 of the barrel cortex. The question if these two types of excitatory cells in layer 4 can be distinguished physiologically has to be elucidated. As described below (see 4.2.3) no

significant difference could be found in the  $\text{Ca}^{2+}$  dynamics in the dendrites and spines of these two cell types suggesting that the excitatory spiny cells in layer 4 of the barrel cortex consist of a physiologically homogeneous population of cells. The difference in the morphology might reflect a continuum of dendritic branching patterns related to the location of the somata within the barrel (Egger 1999).

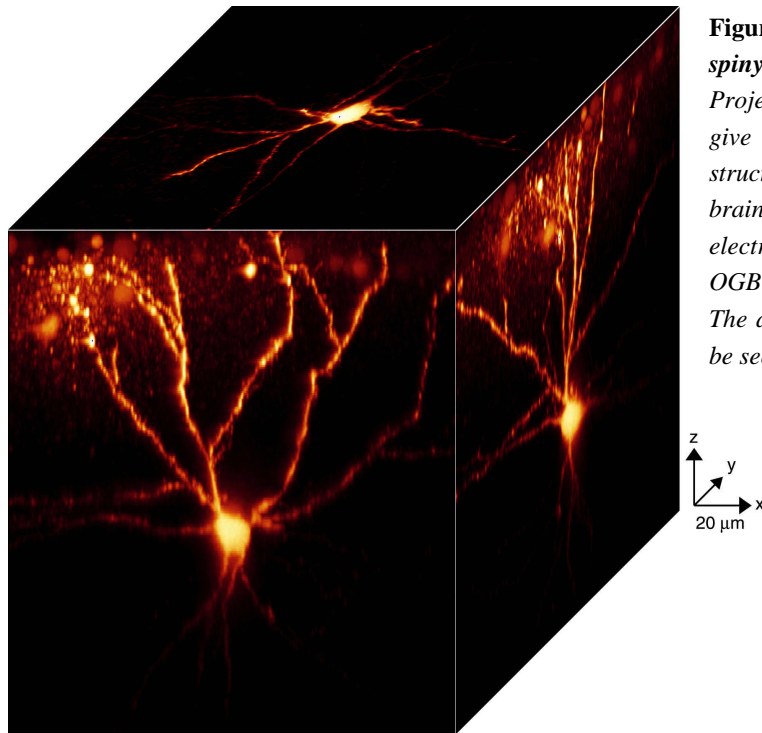


**Figure 4.3 3D projection of a stack of a spiny stellate neuron deep in the slice**  
*Projections along the spatial directions give an idea about the three-dimensional structure of a spiny stellate neuron in a brain slice. The soma of the cell was electroporated with the  $\text{Ca}^{2+}$  indicator OGB-1 around 150  $\mu\text{m}$  deep in the slice. The asymmetry of the dendritic arbor can be seen in all projections.*

Spiny stellate neurons deep in the slice could be filled by electroporation ( $n = 3$ ). This method allowed to fill cells deeper into the slice more rapidly (less than 60 s) than with the standard patch-clamp technique for morphological visualization. Fig 4.3 shows a projection of a fluorescence stack along the spatial directions. This representation of the image data gives an idea about the 3D-structure of a spiny stellate neuron in a brain slice. The soma of the cell was electroporated with OGB-1 around 150  $\mu\text{m}$  deep in the slice. The typical asymmetry of the dendritic arbor can be seen in all projections.

TPE microscopy greatly facilitated the online identification of spiny neurons in layer 4 of the rat barrel cortex for further investigation of the  $\text{Ca}^{2+}$  dynamics in dendrites and spines.

## 4.2 Ca<sup>2+</sup> dynamics in spiny neurons

Ca<sup>2+</sup> is a very important intracellular second messenger in the signaling cascades of neurons. Depolarization of the plasma membrane results, most of the time, in the influx of Ca<sup>2+</sup> through specialized Ca<sup>2+</sup> channels. The amount of Ca<sup>2+</sup> influx to a given stimulus is determined by the density and type of Ca<sup>2+</sup> channels present in the membrane and the actual electrochemical gradient (driving force) for Ca<sup>2+</sup>. Ca<sup>2+</sup> serves as a ‘chemical code’ for the electrical activity of the neuron.

Spiny neurons in layer 4 of the barrel cortex receive whisker specific input from thalamic afferents. They are the input neurons to the cortex and they amplify the incoming excitation and relay it to other layers within a cortical column. In contrast to the extensive work on the Ca<sup>2+</sup> dynamics in pyramidal neurons, no Ca<sup>2+</sup> imaging studies have been reported for this cell type so far. The three dimensional morphology and the small diameter of their dendrites make Ca<sup>2+</sup> imaging studies based on wide-field fluorescence microscopy difficult to be performed in the highly scattering environment of acute brain slices. The application of TPE microscopy made it possible to study the Ca<sup>2+</sup> dynamics in the dendrites and in single spines of spiny neurons. The transient increase in intracellular Ca<sup>2+</sup> was investigated for different stimulation protocols.

First the question was answered whether spiny neurons show action potential (AP) induced Ca<sup>2+</sup> transients in their dendritic tree. It has been shown, for example, in layer 2/3 (Koester 2000), layer 5 (Markram 1995) and hippocampal pyramidal neurons (Spruston 1995) and also in interneurons (Kaiser 2001) that back-propagating action potentials (bAPs) result in a transient Ca<sup>2+</sup> influx through voltage dependent Ca<sup>2+</sup> channels (VDCCs). The bAPs evoked Ca<sup>2+</sup> transients represent a feed-back signal to the input region of the cell about its activity (in this case firing of an action potential). In contrast Purkinje cells in the cerebellum donot show AP evoked Ca<sup>2+</sup> transients in their elaborate dendritic tree (Wang, Denk et al. 2000). Secondly the dependence of the AP evoked Ca<sup>2+</sup> transients on the distance from the soma was measured to evaluate if the rise in Ca<sup>2+</sup> in the dendritic tree represents a global intracellular signal in spiny neurons.

The addition of Ca<sup>2+</sup> indicators to the cytosol changes the endogenous Ca<sup>2+</sup> dynamics, thus the measured fluorescence transients donot report the true Ca<sup>2+</sup> transients in the undisturbed cell. The additional buffer capacity of the indicator slows the extrusion and clearance of the intracellular Ca<sup>2+</sup>. To estimate the exact decay timecourse of Ca<sup>2+</sup> transients in the dendrites and spines of spiny neurons the endogenous Ca<sup>2+</sup> binding ratio and the endogenous Ca<sup>2+</sup> decay time constant were measured.

## Results

Then the  $\text{Ca}^{2+}$  transients in single spines during synaptic activity were measured and the source of the  $\text{Ca}^{2+}$  influx was pharmacologically isolated.

Finally, the interaction of synaptically evoked and bAP evoked  $\text{Ca}^{2+}$  transients were investigated, which occur constantly during cortical network activity.

In this way the  $\text{Ca}^{2+}$  transients corresponding to the most important activity patterns in spiny neurons have been investigated giving a comprehensive picture of the  $\text{Ca}^{2+}$  dynamics in the dendritic tree of this cell type.

### 4.2.1 Backpropagation of action potentials in dendrites and spines

#### $\text{Ca}^{2+}$ transients evoked by back-propagating APs

The  $\text{Ca}^{2+}$  transients in dendritic shafts and spines evoked by a single AP elicited by a brief somatic current injection were studied. Fig 4.4A illustrates a single spine and the parent

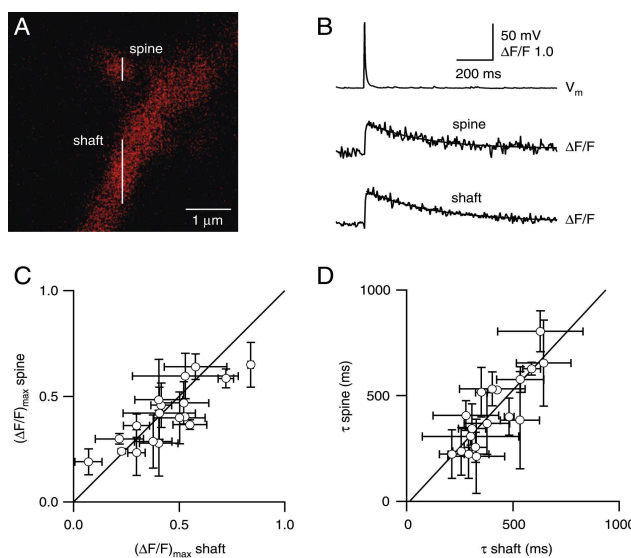


**Figure 4.4**  $\text{Ca}^{2+}$  transients in dendrites and spines evoked by back-propagating APs

**A** Fluorescence image of a spine and dendrite  $50 \mu\text{m}$  from the soma. The two lines indicate the position of the linescan and the regions of interest in which the fluorescence was averaged for the spine and shaft respectively.

**B** Somatic voltage recording of a single AP elicited by somatic current injection (upper trace) and the corresponding fluorescence transients recorded in the spine (middle trace) and dendritic shaft (lower trace) as indicated in A. A single exponential fit yielded a  $\text{Ca}^{2+}$  transient

amplitude  $(\Delta F/F)_{\text{max}} = 0.65$  and a decay time constant  $\tau = 306 \text{ ms}$  for the spine and  $(\Delta F/F)_{\text{max}} = 0.84$  and  $\tau = 389 \text{ ms}$  for the dendritic shaft respectively.

**C** Plot of  $(\Delta F/F)_{\text{max}}$  in a spine vs.  $(\Delta F/F)_{\text{max}}$  in the adjacent shaft. Each circle represents the mean  $(\Delta F/F)_{\text{max}}$  and the error bars represent the SD (3-5 trials). The data points clustered around the unity line (solid line) indicating a similar  $\text{Ca}^{2+}$  transient amplitude in the spine and in the adjacent dendritic shaft. The  $\text{Ca}^{2+}$  transient amplitude in the spine was on average  $104 \pm 45\%$  ( $n = 18$ ,  $p > 0.1$ ) compared to the  $\text{Ca}^{2+}$  transient amplitude in the shaft.

**D** The decay time constants of the  $\text{Ca}^{2+}$  transients in the spine and the adjacent dendritic shaft were linearly correlated ( $r = 0.84$ ).



dendritic shaft together with the orientation of the scan (white lines). The lengths of the lines indicate the regions of interest in which the fluorescence in the spine and in the shaft were averaged respectively. An AP caused a brief and transient increase of  $\text{Ca}^{2+}$  in the dendritic shaft and in the spine (Fig 4.4B). The  $\text{Ca}^{2+}$  transients were fitted well by single exponential functions, yielding the peak amplitude ( $(F/F)_{\text{max}}$ ) and the decay time constant  $\tau$ . The peak amplitudes of the  $\text{Ca}^{2+}$  transient in the spine and in the adjacent shaft were of comparable size. In half of the cases (9 out of 18) was the peak amplitude in the spine slightly larger than in the parent dendritic shaft (in Fig 4.4C). The peak amplitude in the spine ( $(F/F)_{\text{max}} = 0.41 \pm 0.14$ , mean  $\pm$  SD) as compared to the shaft ( $(F/F)_{\text{max}} = 0.44 \pm 0.18$ ) was on average  $104 \pm 45\%$  ( $n = 18$ ,  $p > 0.1$ ), which was not significantly different.

The decay time constants of the  $\text{Ca}^{2+}$  transients in the spine ( $\tau = 420 \pm 170$  ms) and shaft ( $\tau = 400 \pm 110$  ms) measured in the same experiments were linearly correlated (least squares fit, coefficient  $\pm$  estimated fitting error SD,  $\tau_{\text{spine}} = -0.02 \pm 0.07 + (1.1 \pm 0.2) * \tau_{\text{shaft}}$ ,  $r = 0.84$ , regression ttest  $p < 0.0005$ ). Comparing the decay time constants for individual spines and the adjacent shafts, no significant difference could be found ( $n = 18$ , paired ttest,  $p > 0.1$ ). The similar decay time constants indicate that  $\text{Ca}^{2+}$  buffering and extrusion mechanisms in the spines and adjacent shafts for AP evoked  $\text{Ca}^{2+}$  transients were the same (Fig 4.4D). This hypothesis is tested and confirmed in 4.2.2 in more detail.  $\text{Ca}^{2+}$  transients with a double exponential decay in the spine were never observed in spiny neurons, in contrast to similar experiments in pyramidal neurons in the CA1 region of the hippocampus, where spines and adjacent shafts showed different  $\text{Ca}^{2+}$  decay time dynamics (Majewska 2000).

The fast rise time ( $< 4$  ms) of the  $\text{Ca}^{2+}$  transient in the spine indicated that voltage dependent  $\text{Ca}^{2+}$  channels (VDCC) are located on the spine head as in hippocampal CA1 pyramidal neurons and neocortical layer 5 pyramidal cells (Yuste 1995; Koester 1998).

#### ***Effect of TTX and $\text{Cd}^{2+}$ on $\text{Ca}^{2+}$ transients.***

To test whether  $\text{Na}^+$  APs (Stuart 1994) are necessary to elicit  $\text{Ca}^{2+}$  transients in the dendritic tree, voltage dependent  $\text{Na}^+$  channels were blocked by bath application of tetrodotoxin (TTX,  $1 \mu\text{M}$ ). The  $\text{Ca}^{2+}$  transient amplitude was blocked to  $8 \pm 7\%$  ( $n = 5$ ) of control conditions. Measurements were performed between  $20\text{-}40 \mu\text{m}$  from the soma on a primary dendrite, showing that no passive spread, even at this close distance to the soma, occurred.

To pharmacologically isolate the channels that mediate the  $\text{Ca}^{2+}$  transients evoked by bAPs  $100 \mu\text{M}$   $\text{Cd}^{2+}$  was added to the bathing solution. The  $\text{Ca}^{2+}$  transients are blocked to  $7 \pm 5\%$  ( $n = 4$ ) of control conditions, suggesting that the  $\text{Ca}^{2+}$  transients are mediated by voltage dependent  $\text{Ca}^{2+}$  channels (VDCCs).

These results suggest that  $\text{Ca}^{2+}$  transients in the dendritic tree were evoked by bAPs opening VDCCs.

**Spine and shaft  $\text{Ca}^{2+}$  transients depend on the distance from the soma**

The spatial profile of the spread of the  $\text{Ca}^{2+}$  signals from the soma into the dendritic tree depends on the cell type. In basal dendrites of layer 2/3 pyramidal neurons the peak  $\text{Ca}^{2+}$  transient amplitude evoked by one AP decreases with the distance from the soma (Koester 2000). In contrast, in apical dendrites of CA1 pyramidal neurons no distance dependence of single AP evoked  $\text{Ca}^{2+}$  transients can be found (Spruston 1995), but CA1 pyramidal neurons show indications for frequency dependent branchpoint failures, which selectively reduce the spatial  $\text{Ca}^{2+}$  transient profile in certain dendritic branches during trains of AP firing.

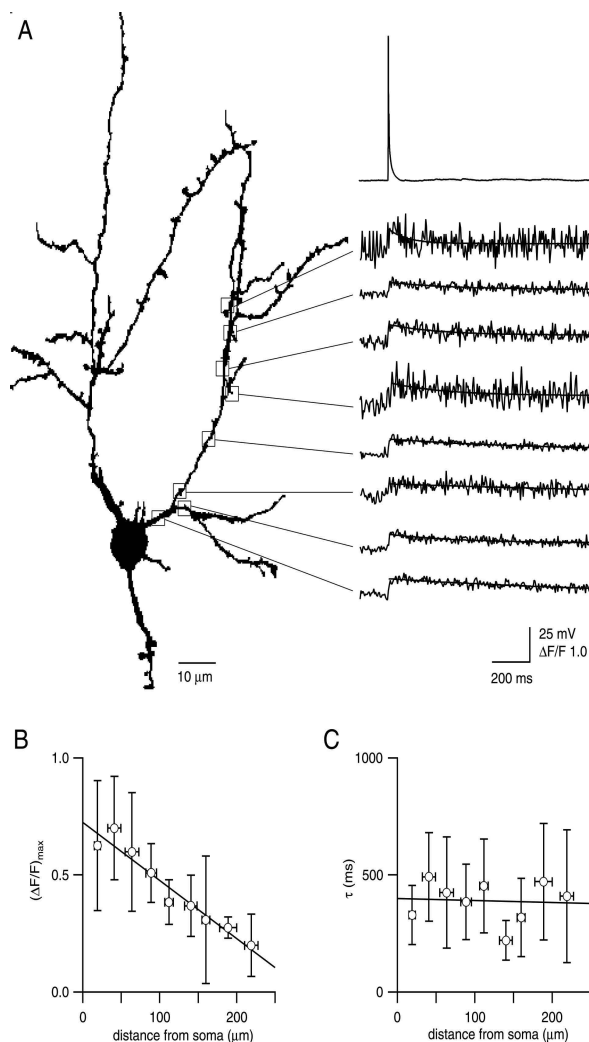


**Figure 4.5 Attenuation of dendritic  $\text{Ca}^{2+}$  transients with distance from the soma**

**A** Outline of a spiny stellate neuron obtained from the maximum projection of a stack of 25 TPE images. The positions of linescans along one exemplified dendrite are indicated by boxes. The corresponding fluorescence  $\text{Ca}^{2+}$  transients elicited by a bAP (upper trace, somatic voltage recording) are plotted on the right.

**B** Peak  $\text{Ca}^{2+}$  transient amplitudes elicited by a single bAP as a function of distance from the soma. Summary of data from 9 cells. The open circles represent the mean  $\text{Ca}^{2+}$  transient amplitudes binned over 25  $\mu\text{m}$  of dendritic length (error bars, SD for amplitude and distance). The linear fit showed a strong correlation of the peak  $\text{Ca}^{2+}$  transient amplitude with the distance from the soma ( $r = -0.97$ ).

**C** Decay time constants  $\tau$  as a function of distance from the soma. The decay time constants were independent of the distance from the soma. The solid line represents a linear fit ( $r = -0.06$ ).

Single AP-evoked  $\text{Ca}^{2+}$  transients were readily detectable throughout the dendritic arbor in spiny neurons. Fig 4.5A shows the outline of the dendritic tree of a spiny stellate cell and the AP evoked  $\text{Ca}^{2+}$  transients that were recorded along one dendrite at different distances from the soma. In this case the peak  $\text{Ca}^{2+}$  transient amplitude increased from  $(F/F)_{\text{max}} = 0.44$  measured 10  $\mu\text{m}$  from the soma to  $(F/F)_{\text{max}} = 0.63$  measured 80  $\mu\text{m}$  from the soma. On average  $(F/F)_{\text{max}}$  decreased with the distance from the soma. Fig 4.5B shows the summary from 9 cells. One of these cells was classified as a star pyramidal cell. Comparing the  $\text{Ca}^{2+}$  transients measured in this cell to cells classified as spiny stellate cells showed no significant difference. The mean peak  $\text{Ca}^{2+}$  transient amplitude pooled for distances from the soma  $< 90$   $\mu\text{m}$  were  $(F/F)_{\text{max}} = 0.78 \pm 0.39$  and  $(F/F)_{\text{max}} = 0.64 \pm 0.52$  for star pyramid and spiny stellate respectively (unpaired ttest,  $p > 0.4$ ). For distances from the soma  $> 90$   $\mu\text{m}$  the mean peak  $\text{Ca}^{2+}$  transient amplitudes were  $(F/F)_{\text{max}} = 0.41 \pm 0.24$  and  $(F/F)_{\text{max}} = 0.45 \pm 0.28$  for star pyramid and spiny stellate respectively (unpaired ttest,  $p > 0.6$ ). Also the decay time constants were not different ( $\tau = (350 \pm 130)$  ms and  $\tau = (420 \pm 210)$  ms for star pyramid and spiny stellate respectively,  $p > 0.4$ ). Thus the  $\text{Ca}^{2+}$  transients measured in the star pyramidal neuron are included in the further analysis.

The peak  $\text{Ca}^{2+}$  amplitudes were averaged over 25  $\mu\text{m}$  of dendritic length for each data point (open circles). The y-error bars give the SD for the  $(F/F)_{\text{max}}$  and the x-error bars represent the SD of the pooled distances from the soma. The linear fit (solid line) yielded a linear correlation between the decrease in  $(F/F)_{\text{max}}$  and the distance from the soma ( $(F/F)_{\text{max}} = (0.73 \pm 0.03) - (0.0025 \pm 0.0002) * \text{distance} * \mu\text{m}^{-1}$ ,  $r = -0.97$ ).

The decay time constants of the  $\text{Ca}^{2+}$  transients were not dependent on the distance of the spine or the shaft segment from the soma (Fig 4.5C, linear fit,  $r = -.06$ ). This suggested that the cells were homogeneously filled with the  $\text{Ca}^{2+}$  indicator dye. Furthermore it is concluded that the  $\text{Ca}^{2+}$  buffering and extrusion is homogeneous along the dendritic tree in spiny neurons.

The previous results showed that the firing of a single AP in spiny neurons led to a transient increase in  $\text{Ca}^{2+}$  in the dendritic tree.  $(F/F)_{\text{max}}$  decreased with the distance from the soma, but a clear transient could always be observed in the distal regions of the dendritic tree. This suggested that single APs pass dendritic branchpoints without failure. Branchpoint propagation was studied at 14 branches in 9 cells. Fig 4.6A shows an image of a branching dendrite. The white lines indicate the position of the linescans for the parent shaft (p) and the daughter branches ( $d_1$ ,  $d_2$ ). Linescans were performed between 1-6  $\mu\text{m}$  from the bifurcation. Three AP evoked  $\text{Ca}^{2+}$  transients were averaged for each branch (Fig 4.6B). The peak  $\text{Ca}^{2+}$  transient amplitude was significantly larger in most daughter branches (24 out of 28

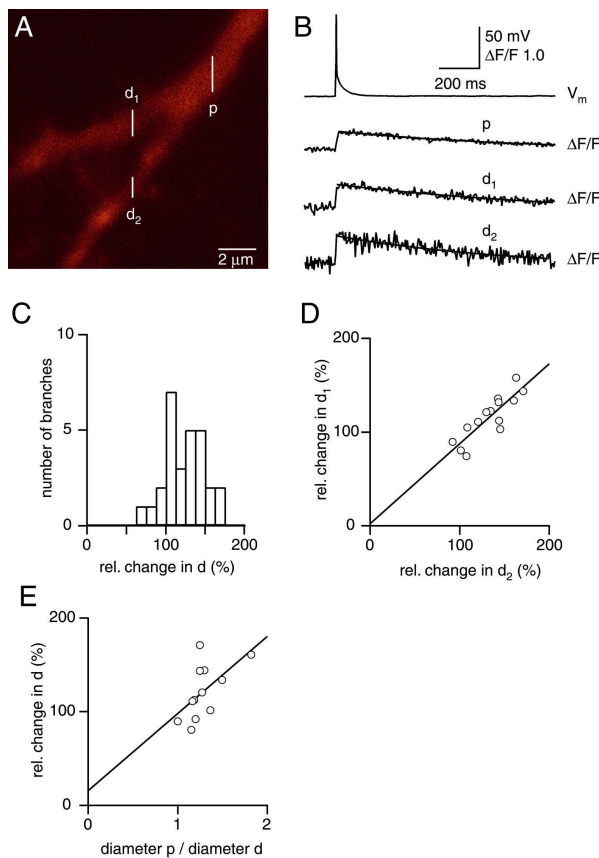


**Figure 4.6 Branchpoint propagation of dendritic APs**

**A** Fluorescence image of a branching dendrite. The lines indicate the position of the linescans for the parent dendrite (p) and the daughter dendrites ( $d_1$ ,  $d_2$ ).

**B** An AP (upper trace, somatic voltage recording) elicited a transient rise in fluorescence in the parent dendrite (p,  $(\Delta F/F)_{max} = 0.41$ ) and in both daughter branches ( $d_1$ ,  $d_2$ ,  $(\Delta F/F)_{max} = 0.55$  and  $(\Delta F/F)_{max} = 0.67$  respectively).

**C** Histogram of peak  $Ca^{2+}$  transient amplitudes in daughter dendrites normalized to the amplitude in the corresponding parent dendrite (relative change in d,  $n = 14$  branchpoints in 9 cells). The fluorescence transient in the daughter branches is, most of the time, larger than in the parent dendrite (rel. change  $> 100\%$ ). The average increase was to  $125 \pm 25\%$ , which was a significant increase ( $p < 0.01$ ).

**D** The rel. change in the daughter

branches were linearly correlated ( $r = 0.9$ , regression ttest  $p < 0.0005$ ).

**E** Plot of the relative change in fluorescence in the daughter branches vs. the relative change of the dendritic diameters corresponding the increase in the surface-to-volume ratio. The solid line represents a linear fit to the data points, which suggests a linear relationship between the relative change in fluorescence and the relative surface-to-volume change ( $r = 0.59$ , regression ttest  $p < 0.025$ ).

branches, paired ttest,  $p < 0.01$ , Fig 4.6C). The mean relative change ( $(F/F)_d / (F/F)_p$ ) was  $125 \pm 25\%$  ( $n = 28$ ). The relative change of the peak  $Ca^{2+}$  transient amplitude in the daughter branches was linearly correlated ( $r = 0.86$ , regression ttest,  $p < 0.0005$ , solid line in Fig 4.6D) suggesting that the AP spreaded into both daughter branches equally well.

The increase in the peak amplitude in the daughter branches could be explained by the increase of the surface-to-volume ratio of the daughter branches. Fig 4.6E shows the plot of the relative change in fluorescence in the daughter branches vs. the relative change in the surface-to-volume ratio from the parent branch to the daughter branches. Assuming cylindrical dendritic compartments, the relative change in the surface-to-volume ratio is given by the ratio of the diameter of the parent dendrite to the diameter of the daughter dendrite. The dendritic diameter at the position of the linescan was derived from maximum projections of fluorescence image stacks. Fluorescence intensity profiles were determined

perpendicular to the dendritic branch and they were fitted with a Gaussian function yielding the width of the dendrite. In Fig 4.6A the dendritic diameters were 1.1  $\mu\text{m}$  for the parent branch, 0.7  $\mu\text{m}$  and 0.6  $\mu\text{m}$  for  $d_1$  and  $d_2$  respectively. A linear fit to the data (Fig 4.6E, solid line) revealed a correlation between the relative fluorescence change in the daughter dendrites and the respective relative change in the surface-to-volume ratio ( $r = 0.59$ , regression ttest,  $p < 0.01$ ). This result could be explained by a constant  $\text{Ca}^{2+}$  influx in the differently sized compartment, which would suggest a constant VDCC channel density in the daughter branches, assuming a similar bAP-waveform before and behind the branchpoint. The observations that  $\text{Ca}^{2+}$  transients were larger behind a branchpoint and that the peak  $\text{Ca}^{2+}$  transient amplitude decreased globally with the distance from the soma suggested that branchpoints were not the main site of attenuation of the AP evoked  $\text{Ca}^{2+}$  transient amplitude. Measurements of  $\text{Ca}^{2+}$  transients in hippocampal CA1 pyramidal neurons seem to indicate the occurrence of dendritic branch point failures of trains of bAP at frequencies  $>16\text{Hz}$  (Spruston 1995). In addition to single APs,  $\text{Ca}^{2+}$  transient amplitudes evoked by trains of APs (5 APs, 20 Hz) were measured in the same cells. In spiny cells branch point failures were not observed at this frequency (20 Hz). All  $\text{Ca}^{2+}$  transients ( $n = 72$ , at distances between 10-220  $\mu\text{m}$  from the soma) showed five individual peaks (Fig 4.7A), each of which corresponded to an individual AP within the train. The peak of the second to fifth  $\text{Ca}^{2+}$  transient in the train

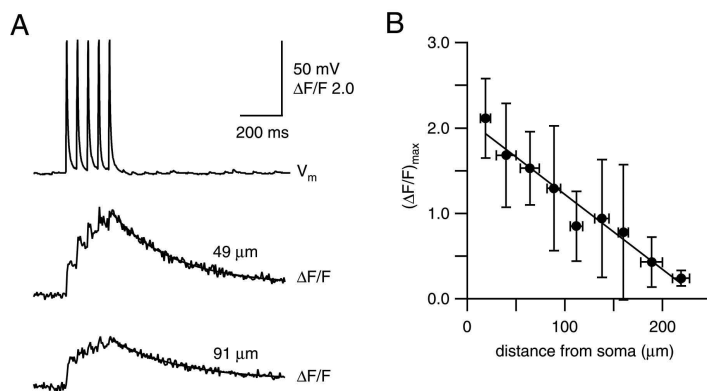


**Figure 4.7 Attenuation of dendritic  $\text{Ca}^{2+}$  transients evoked by trains of APs with distance from the soma**

A A train of 5 APs at 20 Hz (upper trace, somatic voltage recording) resulted in corresponding  $\text{Ca}^{2+}$  transients in the dendritic tree (lower traces recorded 49  $\mu\text{m}$  and 91  $\mu\text{m}$  from the soma). The peak  $\text{Ca}^{2+}$  transient amplitudes were  $(\Delta F/F)_{\text{max}} = 2.1$  and  $(\Delta F/F)_{\text{max}} = 1.2$  respectively.

B Peak  $\text{Ca}^{2+}$  transient amplitudes elicited by a train of 5 APs at 20 Hz as a function of distance from the soma. Summary of data from 8 cells. The open circles represent the mean  $\text{Ca}^{2+}$  transient amplitudes binned over 25  $\mu\text{m}$  of dendritic length (error bars, SD for amplitude and distance). The linear fit showed a strong correlation of the peak  $\text{Ca}^{2+}$  transient amplitude with the distance from the soma ( $r = -0.98$ ).

was reduced due to saturation of the indicator dye. Nevertheless, the peak  $\text{Ca}^{2+}$  transient amplitude decreased with the distance from the soma (a linear fit yielded  $(\Delta F/F)_{\text{max}} = (2.1 \pm 0.1) - (0.0088 \pm 0.0007) * \text{distance} * \mu\text{m}^{-1}$ ,  $r = -0.98$ ).

To compare the decrease of the peak  $\text{Ca}^{2+}$  transient amplitudes with the distance from the soma for a single AP with a train of APs at 20 Hz, the distance dependence of  $(F/F)_{\text{max}}$  for the two cases were fitted by a single exponential function. The fits yielded a length constant for the decrease of  $(F/F)_{\text{max}}$  for a single AP of 195  $\mu\text{m}$  and for a train of APs of 190  $\mu\text{m}$  respectively. The similar decay time constants indicated that in trains of APs at frequencies below 20 Hz no branchpoint failures occurred and that the attenuation of the peak  $\text{Ca}^{2+}$  transient amplitude in this case is similar to the attenuation of the peak  $\text{Ca}^{2+}$  transient amplitude evoked by a single AP, in contrast to the findings in CA1 pyramidal neurons (Spruston 1995).

Thus APs evoked in the soma reliably back-propagate into the dendritic arbor of spiny neurons and evoke a transient increase in  $\text{Ca}^{2+}$  in dendritic shafts and spines.

### 4.1.2 Buffer capacity in dendrites and spines

Loading cells with a  $\text{Ca}^{2+}$  indicator reduces the amplitude and prolongs the time course of the  $\text{Ca}^{2+}$  transients because the indicator acts as an additional  $\text{Ca}^{2+}$  buffer (Helmchen 1996). Thus the time course reported by the indicator does not reflect the  $\text{Ca}^{2+}$  dynamics in the dendrites and spines of the undisturbed cell, which is determined by endogenous  $\text{Ca}^{2+}$  buffers, extrusion of  $\text{Ca}^{2+}$  across the plasma membrane and uptake of  $\text{Ca}^{2+}$  into internal stores (Berridge 1998). These factors determine the ratio of maximal free  $\text{Ca}^{2+}$  concentration to bound  $\text{Ca}^{2+}$  (endogenous  $\text{Ca}^{2+}$  binding ratio) and thus the decay dynamics of the  $\text{Ca}^{2+}$  transient (Maravall, Mainen et al. 2000). The estimation of the  $\text{Ca}^{2+}$  dynamics in the undisturbed dendrite and spine helped to predict the temporal summation of activity dependent  $\text{Ca}^{2+}$  transients in the *in vivo* situation.

The low affinity  $\text{Ca}^{2+}$  indicator OGB-5N was used to determine the decay time course of the undisturbed  $\text{Ca}^{2+}$  transient and to estimate the endogenous  $\text{Ca}^{2+}$  binding ratio of shafts and spines respectively. The OGB-5N concentration in the loading pipette was varied between 100  $\mu\text{M}$  to 2000  $\mu\text{M}$  and  $\text{Ca}^{2+}$  transients evoked by a single bAP were recorded between 20-120  $\mu\text{m}$  from the soma (mean  $\pm$  SD,  $44 \pm 27$   $\mu\text{m}$ ). As expected (Fig 4.8A), increasing the exogenous  $\text{Ca}^{2+}$  binding ratio by indicator loading decreased the peak amplitude  $(F/F)_{\text{max}}$  and increased the decay time constant. At a OGB-5N concentration of 100  $\mu\text{M}$ , corresponding to an exogenous  $\text{Ca}^{2+}$  binding ratio of 5 (assuming a  $k_D = 20$   $\mu\text{M}$ , Tab 3.2), the decay time constant was  $\tau = 42 \pm 3$  ms ( $n = 6$ ) in the shaft and  $\tau = 50 \pm 3$  ( $n = 3$ ) in the spine respectively. Adding 500  $\mu\text{M}$ , 1000  $\mu\text{M}$  and 2000  $\mu\text{M}$  corresponding to an exogenous  $\text{Ca}^{2+}$

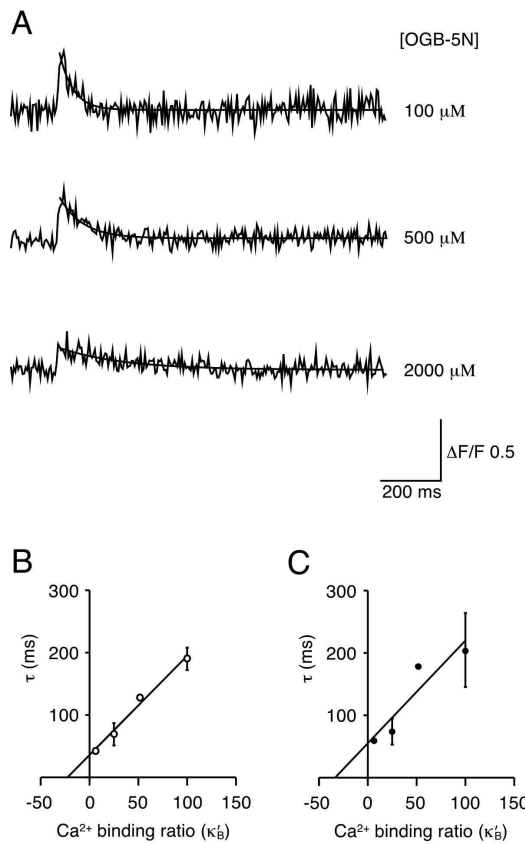


**Figure 4.8 Endogenous  $\text{Ca}^{2+}$  binding ratio in shafts and spines**

**A** Fluorescence transients evoked by single bAPs in dendrites for different concentrations of the low-affinity  $\text{Ca}^{2+}$  indicator Oregon-Green-Bapta-5N (OGB-5N). Three different cells were somatically loaded with 100  $\mu\text{M}$ , 500  $\mu\text{M}$  and 2000  $\mu\text{M}$  respectively. Fluorescence transients are averages of 3-5 sweeps. Single exponentials were fitted to the fluorescence decays, yielding decay time constants of 40 ms, 70 ms and 190 ms and peak amplitudes  $\Delta F/F$  of 0.4, 0.3 and 0.15 respectively.

**B** Decay time constant  $\tau$  as a function of OGB-5N  $\text{Ca}^{2+}$  binding ratio  $\kappa_B'$  measured in the dendritic shaft. A linear regression line extrapolated to the negative x axis intercept gives an estimate of the endogenous  $\text{Ca}^{2+}$  binding ratio of  $\kappa_S = 22$ . The intercept with the y axis yields a decay time constant of  $\tau = 36$  ms. for the  $\text{Ca}^{2+}$  transients in the case of no exogenous buffer added.

**C** Decay time constant  $\tau$  as a function of OGB-5N  $\text{Ca}^{2+}$  binding ratio  $\kappa_B'$  measured in spines. The linear regression line yielded an endogenous  $\text{Ca}^{2+}$  binding ratio of  $\kappa_S = 20$  and a decay time constant  $\tau = 46$  ms for no exogenous buffer added.

binding ratio of 25, 50 and 100 respectively yielded decay time constants for the shaft of  $\tau = 69 \pm 18$  ( $n = 7$ ),  $\tau = 128 \pm 1$  ( $n = 3$ ) and  $\tau = 190 \pm 18$  ( $n = 4$ ) respectively. In spines, corresponding decay time constants of  $\tau = 65 \pm 21$  ( $n = 3$ ),  $\tau = 170 \pm 2$  ( $n = 4$ ) and  $\tau = 195 \pm 59$  ( $n = 4$ ) were found. Plotting  $\tau$  as a function of the OGB-5N  $\text{Ca}^{2+}$  binding ratio (see 3.14) and extrapolating a linear regression line (dendrite  $r = 0.99$ , spine  $r = 0.92$ ) to zero (no buffer added) yielded a decay time constant of  $\tau_0 = 36$  ms in the shaft (Fig 4.8B) and  $\tau_0 = 46$  ms for the spine (Fig 4.8C). Extrapolation of the linear regression line to the x-axis intercept yielded an estimate of the endogenous  $\text{Ca}^{2+}$  binding ratio of  $\kappa_S = 22$  for the shaft and  $\kappa_S = 20$  for the spine respectively. Thus dendritic shafts and spines seem to form a homogenous compartment in terms of endogenous  $\text{Ca}^{2+}$  buffers and  $\text{Ca}^{2+}$  extrusion mechanisms, at least for the  $\text{Ca}^{2+}$  influx evoked by a single bAP.

### Frequency dependence of $\text{Ca}^{2+}$ transients

In the apical dendrite of layer 5 pyramidal neurons and in the dendrites of bitufted interneurons in layer 2/3 is the frequency of trains of APs encoded in the plateau level of the

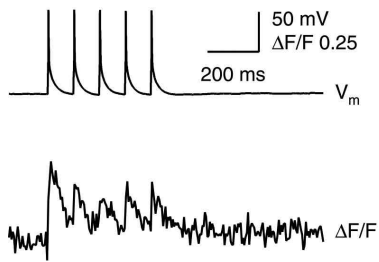


**Figure 4.9  $Ca^{2+}$  transient evoked by trains of APs at 10 Hz**  
*Illustration of the  $Ca^{2+}$  transients at 10 Hz, close to the frequency of the exploratory “whisking” behaviour. Somatic voltage recording (upper trace) and the corresponding  $Ca^{2+}$  transient (lower trace). The  $Ca^{2+}$  transient evoked by a single AP in the train decayed back to resting  $Ca^{2+}$  levels.*

accumulated  $Ca^{2+}$  (Schiller 1995; Kaiser 2001). Transients measured with the low affinity dye OGB-5N (100  $\mu$ M) have a  $Ca^{2+}$  decay time constant comparable to that of the unperturbed state ( $\tau = 40$ ms), thus the fluorescence transient should report the summation of the AP evoked  $Ca^{2+}$  transients in a train faithfully (compare the  $Ca^{2+}$  transients recorded with the high affinity dye OGB-1 (200  $\mu$ M) in Fig 4.7 at 20 Hz (5 APs) with the corresponding transient recorded in the presence of OGB-5N (100  $\mu$ M) in Fig 4.10).

The dendritic accumulation of  $Ca^{2+}$  for a train of bAPs at different frequencies was measured. At 10 Hz, close to the frequency of the exploratory “whisking” behaviour the individual  $Ca^{2+}$  transients were still resolvable. Each  $Ca^{2+}$  transient evoked by a single AP in the train decayed back to resting  $Ca^{2+}$  levels (Fig 4.9). Increasing the frequency of the AP train

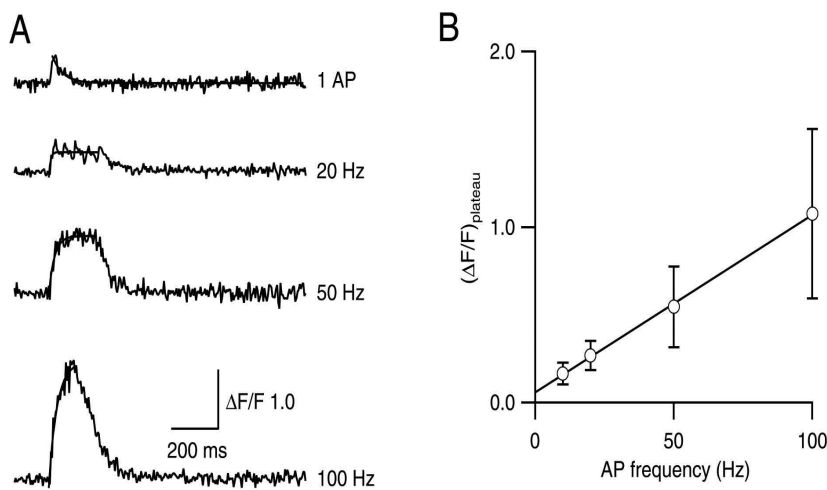


**Figure 4.10 Frequency dependence on the  $Ca^{2+}$  plateau level**

**A** Fluorescence transients for trains of APs at different frequencies measured with OGB-5N (100  $\mu$ M). The upper trace shows the fluorescence transient for a single AP as a reference and fluorescence transients for trains of 5 APs at 20Hz, 10 APs at 50Hz and 10 APs at 100Hz respectively. A single exponential (solid line) was fitted to the transients for the duration of the stimulation yielding the plateau amplitude.

**B** Plateau amplitude plotted against AP frequency. The solid line represents a linear regression line to the data points.



increased the plateau level of the  $\text{Ca}^{2+}$  response (Fig 4.10A). A single exponential fit from the beginning of the train to the last AP within the train yielded the plateau level and the rise time. The rise time of the transient was fast with  $\tau = 28 \pm 14$  ms. The plateau level increased linearly with the frequency with a slope of  $0.01$  ( $\Delta F/F$ )\* $\text{Hz}^{-1}$  ( $r = 1$ , regression ttest,  $p < 0.0005$ ,  $n = 6$ , Fig 4.7B). Thus the dendrites of spiny neurons can also code the frequency of AP trains by a rise in  $\text{Ca}^{2+}$ .

The decay time from the plateau level of a 100 Hz train of APs in the dendrite using  $100 \mu\text{M}$  OGB-5N was readily fitted by a single exponential. The decay time constant of the train induced  $\text{Ca}^{2+}$  transient was with  $62 \pm 8$  ms slightly, but not significantly (ttest,  $p > 0.1$ ) slower than the decay time for a single AP evoked  $\text{Ca}^{2+}$  transient ( $42 \pm 3$  ms). Thus there was no indication of a  $[\text{Ca}^{2+}]_i$  dependent non-linear  $\text{Ca}^{2+}$  extrusion mechanism at high  $\text{Ca}^{2+}$  concentrations in spiny neurons and the  $\text{Ca}^{2+}$  pumps did not seem to be saturated at these  $\text{Ca}^{2+}$  levels.

### 4.1.3 Synaptically evoked $\text{Ca}^{2+}$ transients

#### *$\text{Ca}^{2+}$ transients evoked by EPSPs*

Most synaptic contacts between the excitatory spiny neurons in layer 4 of the barrel cortex and those of thalamic afferents are located on dendritic spines and shafts (Luebke, Egger et al. 2000) relatively close ( $70 \pm 40 \mu\text{m}$  distance from the soma, (Feldmeyer 1999)) to the soma. EPSPs are mediated by both AMPAR and NMDAR channels (Feldmeyer 1999). During EPSPs a transient  $\text{Ca}^{2+}$  influx is likely to occur via NMDAR channels when the depolarization is large enough to remove the  $\text{Mg}^{2+}$  block (Mayer 1984; Nowak 1984).

The  $\text{Ca}^{2+}$  influx into single spines of spiny neurons filled with OGB-1 ( $200 \mu\text{M}$ ) evoked by extracellular synaptic stimulation was characterized. The pipette tip of the stimulation electrode was positioned close to a dendritic branch under visual control (Fig 4.11A). For these experiments, the overlay of the IR-SGC with the fluorescence image of the indicator loaded cell greatly facilitated the precise placement of the stimulation pipette close to a fluorescently labelled structure. This allowed to selectively stimulate spines at different distances from the soma.

## Results

Active spines (i.e. those responding with a  $\text{Ca}^{2+}$  transient to stimulation) were found located at distances ranging between 30  $\mu\text{m}$  and 210  $\mu\text{m}$  from the soma ( $79 \pm 35 \mu\text{m}$ , mean  $\pm$  SD,  $n = 46$ ). Putative shaft synapses were found only infrequently ( $n = 2$ ) and no differences in their  $\text{Ca}^{2+}$  dynamics compared to synaptic contacts onto spines could be observed. The low number of shaft synapses might have been biased by the search procedure for active contacts. Extracellular stimuli, evoking somatically recorded EPSPs were elicited and the dendritic

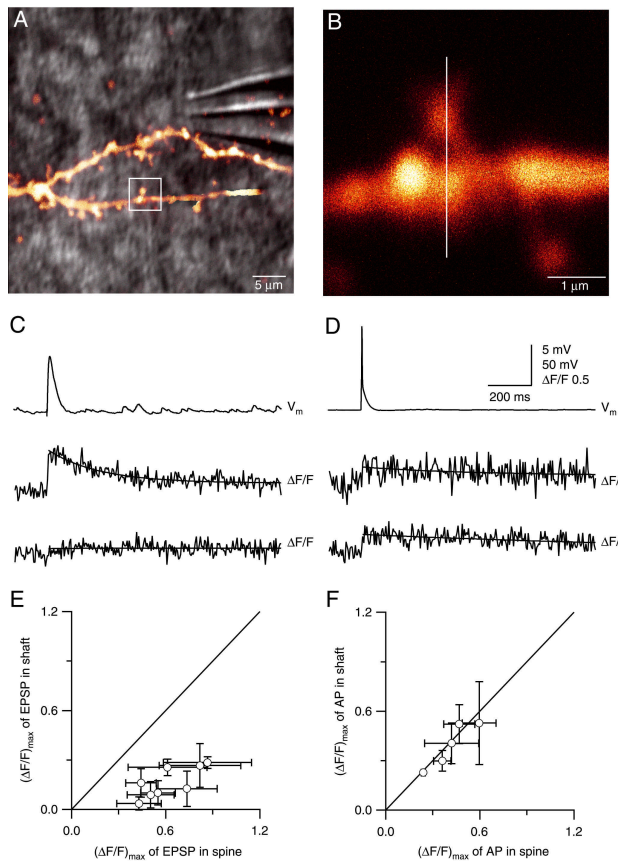


**Figure 4.11 EPSP evoked  $\text{Ca}^{2+}$  transients in spine and shaft**

**A** Overlay of the fluorescence image showing a part of the dendritic arbor of a spiny stellate cell and the IR-SGC image visualizing the surrounding tissue and the stimulation electrode (right). The stimulation electrode is placed close to a dendrite and then the active contact is searched. The active synaptic contact in this case is indicated by the white box.

**B** Higher magnification image of the active spine. The position of the linescan is indicated by the vertical line.

**C** Somatic whole-cell recording of an EPSP (upper trace) and the corresponding  $\text{Ca}^{2+}$  transient in the active spine and the adjacent dendritic shaft shown in B (lower trace). A clear rise in fluorescence is recorded in the spine head ( $(\Delta F/F)_{\text{max}} = 0.50 \pm 0.15$ , mean  $\pm$  SD) but no increase in fluorescence is seen in the shaft ( $(\Delta F/F)_{\text{max}} = 0.09 \pm 0.08$ ).

**D** For comparison, the fluorescence transient (lower traces) evoked by a bAP (upper trace) is plotted on the right. The bAP gives rise to a

similar fluorescence transient in the spine head (middle trace,  $(\Delta F/F)_{\text{max}} = 0.24 \pm 0.01$ ) and in the dendritic shaft (lower trace,  $(\Delta F/F)_{\text{max}} = 0.23 \pm 0.01$ ).

**E** Peak  $\text{Ca}^{2+}$  transient amplitude elicited by an EPSP measured in the shaft vs peak amplitude in the spine. All points fell below the unity line indicating that the  $\text{Ca}^{2+}$  transient in the shaft was much smaller than in the spinehead (reduction to  $26 \pm 12\%$ ,  $n = 8$ ). Open circles represent the mean and the error bars the SD in each case.

**F** In contrast, AP evoked  $\text{Ca}^{2+}$  transients measured in the same spines and shafts showed a similar peak fluorescence amplitude  $(\Delta F/F)_{\text{max}}$ , as described in Fig 4.4C before. The data points presented here were also included in the analysis to Fig 4.4C.

shaft, studded with spines close to the stimulation pipette was searched for an active contact during continuous fluorescence image acquisition in the full-frame mode. Active contacts

were recognized by a clear increase in fluorescence after stimulation. This manually observed fluorescence transient was probably easier to be detected in spines than in shafts.

The extracellular stimulation strength was set to evoke EPSPs with peak amplitudes between 1-11 mV ( $6 \pm 3$  mV,  $n = 29$ ). This reflected the activation of, on average, 4 synapses with 3 single synaptic contacts each, resulting in the activation of 12 synaptic contacts per EPSP (assuming a mean EPSP amplitude of 1.6 mV and 3 synaptic contacts per layer 4 connection (Feldmeyer 2000)). In the vicinity of an active spine ( $\sim 20 \mu\text{m}$ ) no other active spines were observed, suggesting that the inputs that gave rise to the EPSP were evoked at dendritic locations well separated from the particular spine under investigation. The EPSP evoked peak  $\text{Ca}^{2+}$  transient amplitude showed no correlation to the somatically recorded peak EPSP voltage amplitude ( $r = -0.16$ ,  $n = 17$ ), indicating that the  $\text{Ca}^{2+}$  transients recorded were evoked by glutamate release from a bouton at a synaptic contact and not through local depolarization of the postsynaptic membrane by the applied extracellular stimulus and subsequent opening of VDCCs.

Failures in the transient rise in  $\text{Ca}^{2+}$  upon synaptic stimulation were observed only infrequently. Once an active spine was found almost every stimulus evoked transient rise in  $\text{Ca}^{2+}$ . The failure rate determined from successive trials at a single synaptic contact was less than 10% ( $n = 10$  spines).

### *$\text{Ca}^{2+}$ transients in spines and shafts*

Fig 4.11C shows an somatically recorded EPSP (Fig 4.11C, upper trace) and the simultaneously recorded  $\text{Ca}^{2+}$  transient evoked by local synaptic stimulation in the spine (middle trace) and the shaft (lower trace) respectively. The  $\text{Ca}^{2+}$  signal was almost completely restricted to the spine in this example ( $(F/F)_{\text{max}} = 0.50 \pm 0.15$  in the spine vs.  $(F/F)_{\text{max}} = 0.09 \pm 0.08$  in the shaft). On average, the peak  $\text{Ca}^{2+}$  transient amplitude in the shaft was reduced to  $26 \pm 12\%$  ( $n = 8$ , paired ttest,  $p < 0.0001$ ) of the peak  $\text{Ca}^{2+}$  amplitude in the spinehead and all data points (open circles, mean  $\pm$  SD) fall clearly below the unity line (Fig 4.11E). The peak amplitude of the small signal in the shaft is linearly correlated with the peak amplitude in the spine (linear regression,  $r = 0.75$ ).

For comparison, the AP evoked  $\text{Ca}^{2+}$  transients were measured in the same spines and shafts ( $n = 5$ ). For example in the dendrite and spine shown in Fig 4.11B, the bAP evoked  $\text{Ca}^{2+}$  transients were similar in the shaft ( $(F/F)_{\text{max}} = 0.23 \pm 0.01$ ) and in the spine ( $(F/F)_{\text{max}} = 0.24 \pm 0.01$ , Fig 4.11D), as reported before. Fig 4.11F shows the plot of the peak  $\text{Ca}^{2+}$  transient amplitude evoked by an AP in the shaft vs. the peak  $\text{Ca}^{2+}$  transient amplitude in the spine, which represents a subset of the data already presented in Fig 4.4C. Here the mean

## Results

ratio of the peak  $\text{Ca}^{2+}$  transient amplitude in the shaft compared to the spine was  $95 \pm 11\%$  (paired ttest,  $p > 0.2$ ).

Thus bAP evoked  $\text{Ca}^{2+}$  transients represent a global and homogeneous signal, which have a similar peak amplitude in spines and shafts, whereas EPSP evoked  $\text{Ca}^{2+}$  transients are highly spatially confined to the spinehead (Yuste 1995). The small shaft  $\text{Ca}^{2+}$  signal recorded upon synaptic stimulation is presumably caused by the diffusion of  $\text{Ca}^{2+}$  between spine and shaft (Svoboda 1996) even though most of the  $\text{Ca}^{2+}$  in a spine is cleared by other mechanisms, like  $\text{Ca}^{2+}$  pumps.

### *Comparison of $\text{Ca}^{2+}$ transients in spiny stellate and star pyramidal neurons*

In the set of experiments, in which  $\text{Ca}^{2+}$  transients evoked by bAPs and EPSPs were studied in single spines, 11 out of 45 cells (24%) had a star pyramid-like morphology, whereas the rest were classified as spiny stellate neurons ( $n = 34$ , 76%). So far, no difference in the

	spiny stellate neurons (n = 34)		star pyramidal neurons (n = 11)	
	mean	SD	mean	SD
$(\Delta F/F)_{\text{max, EPSP}}$	0.55	0.27	0.67	0.26
$(\Delta F/F)_{\text{max, AP}}$	0.48	0.21	0.38	0.18
$\tau_{\text{EPSP}}$ (ms)	427	236	313	125
$\tau_{\text{AP}}$ (ms)	458	235	353	110
distance from soma ( $\mu\text{m}$ )	75	29	88	47

**Table 4.1** *Comparison of  $\text{Ca}^{2+}$  transients in spiny stellate neurons and star pyramidal neurons*

electrophysiological parameters had been observed between these two cell types (Feldmeyer 1999; Luebke, Egger et al. 2000). The  $\text{Ca}^{2+}$  dynamics is strongly dependent on the cell type and it reflects differences in  $\text{Ca}^{2+}$  channel composition, endogenous  $\text{Ca}^{2+}$  binding proteins and  $\text{Ca}^{2+}$  pumps (Maravall, Mainen et al. 2000; Kaiser 2001). Thus differences in the  $\text{Ca}^{2+}$  transients might distinguish spiny stellate cells from star pyramidal cells.

$\text{Ca}^{2+}$  transients evoked by EPSPs and bAPs in spiny stellate cells and star pyramidal cells were compared (see Tab 4.1). The peak  $\text{Ca}^{2+}$  transient amplitude ( $F/F$ )<sub>max</sub> evoked by an EPSP in spiny stellate neurons was, on average, ( $F/F$ )<sub>max</sub> =  $0.55 \pm 0.27$  ( $n = 34$ ) and in star pyramids ( $F/F$ )<sub>max</sub> =  $0.67 \pm 0.26$  ( $n = 13$ ). A two-tailed Student's ttest yielded no significant difference between the two populations ( $p > 0.15$ ). The decay time constants of the transients (spiny stellate, =  $427 \pm 236$  ms; star pyramid, =  $313 \pm 125$  ms) showed also no significant difference (ttest,  $p > 0.1$ ). The AP evoked ( $F/F$ )<sub>max</sub> in the same spines was, on average,

	mean	SD	<b>Table 4.2 Pooled data from EPSP and AP evoked Ca<sup>2+</sup> transients in single spines</b>
$(\Delta F/F)_{\max, \text{EPSP}}$	0.58	0.27	
$(\Delta F/F)_{\max, \text{AP}}$	0.44	0.2	
$\tau_{\text{EPSP}}$ (ms)	384	203	
$\tau_{\text{AP}}$ (ms)	432	209	
distance from soma ( $\mu\text{m}$ )	79	35	

$(\Delta F/F)_{\max} = 0.48 \pm 0.21$  ( $n = 25$ ) for spiny stellate cells and  $(\Delta F/F)_{\max} = 0.38 \pm 0.18$  ( $n = 11$ ) for star pyramidal cells, which was again not significantly different (ttest,  $p > 0.15$ ). The decay time constants for the AP evoked Ca<sup>2+</sup> transients were  $\tau = 458 \pm 235$  ms and  $\tau = 353 \pm 110$  ms for spiny stellates and star pyramids respectively. No significant difference could be found for the AP evoked Ca<sup>2+</sup> transients either ( $p > 0.15$ ). The active spines were found on average  $d = 75 \pm 29$   $\mu\text{m}$  from the soma in spiny stellate cells and  $d = 88 \pm 47$   $\mu\text{m}$  from the soma in star pyramidal cells ( $p > 0.3$ ). These results suggest that the Ca<sup>2+</sup> transients evoked by EPSPs and APs in spines of spiny stellate cells and star pyramidal cells were not different. Thus the data of spiny stellates and star pyramids were pooled (see Tab 4.2).

#### **Comparison of bAP and EPSP evoked Ca<sup>2+</sup> transients**

The peak Ca<sup>2+</sup> transient amplitude evoked by an EPSP in a spinehead was in most cases larger than the corresponding peak amplitude evoked by an AP (most data points fall below the unity line in Fig 4.12A). The mean  $(\Delta F/F)_{\max}$  evoked by an EPSP was  $(\Delta F/F)_{\max} = 0.58 \pm 0.27$  ( $n = 47$ ), as compared to  $(\Delta F/F)_{\max} = 0.44 \pm 0.20$  in the case of an AP evoked Ca<sup>2+</sup> transient ( $n = 36$ ), which was significantly larger (paired ttest,  $p < 0.008$ ).

The decay time constants observed in the same spines, but evoked by an EPSP and AP respectively were not correlated (Fig 4.12B). On average the decay time constant evoked by an EPSP was  $\tau = 384 \pm 203$  ms and for an AP evoked Ca<sup>2+</sup> transient  $\tau = 432 \pm 209$  ms (paired ttest,  $p > 0.4$ ). The plot of  $\tau_{\text{AP}}$  vs.  $\tau_{\text{EPSP}}$  showed a large scatter and no linear correlation (unconstrained linear fit,  $r = -0.004$ ). The solid line represents a linear fit, forced through the origin (slope =  $0.83 \pm 0.22$ ). The bend, solid lines represent the 95% confidence intervals of the fit. This representation suggested that there might be three distinct populations of spines with different decay time dynamics for EPSP and AP evoked Ca<sup>2+</sup> transients respectively. 18 out of 35 spines tested fell within the 95% confidence interval, suggesting a linear relation between the decay time constants ( $\tau_{\text{EPSP}} \approx \tau_{\text{AP}}$ ). A linear fit, limited to this population, yielded a good correlation ( $r = 0.86$ ). 5 out of 35 spines showed a slower decay time constant for the EPSP than for the AP evoked Ca<sup>2+</sup> transients ( $\tau_{\text{EPSP}} > \tau_{\text{AP}}$ ). 12 out of 35 spines showed the

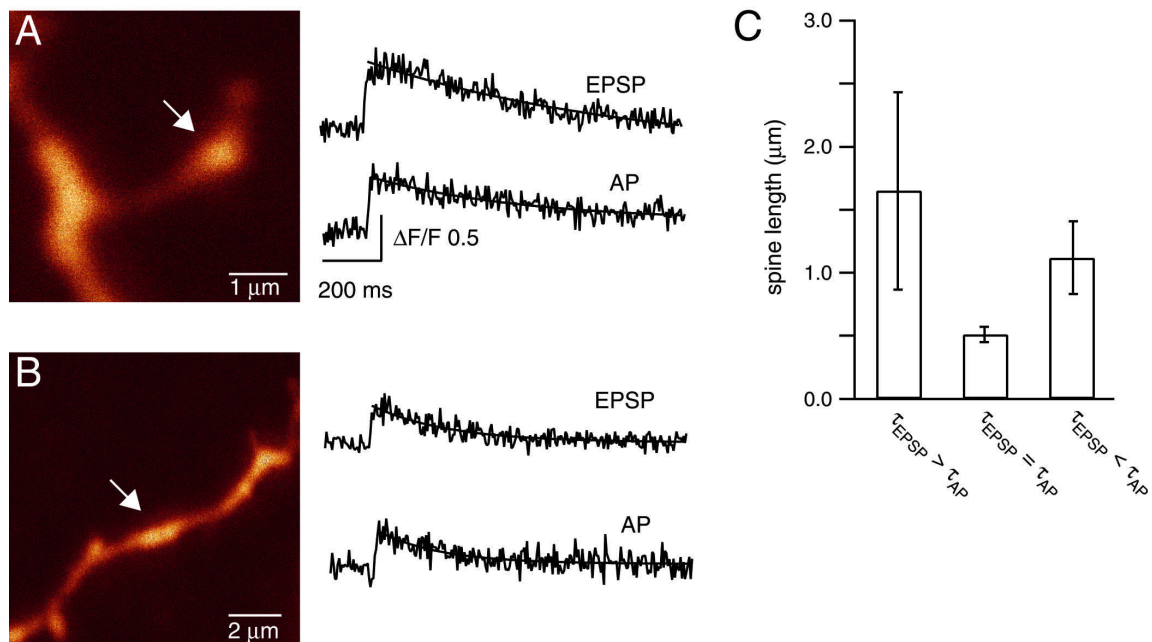


**Fig 4.13** The relation of the decay time dynamics of EPSP and AP evoked  $\text{Ca}^{2+}$  transients depends on the length of the spine

**A** Image of a spine with a long neck. The white arrow indicates the active synaptic contact. The length of the spine was  $2.2 \mu\text{m}$ . To the right the  $\text{Ca}^{2+}$  transients evoked by an EPSP (upper trace) and an AP (lower trace) are depicted. The decay time constants were  $\tau_{\text{EPSP}} = 926 \text{ ms}$  and  $\tau_{\text{AP}} = 522 \text{ ms}$  respectively, thus this spine belonged to the category  $\tau_{\text{EPSP}} > \tau_{\text{AP}}$ .

**B** Image of a putative shaft synapse (white arrow). In this case the spine length was taken as the optical resolution limit of the TPE microscope ( $0.46 \mu\text{m}$ ) because a distinct spine could not be properly resolved. The decay time constants were similar ( $\tau_{\text{EPSP}} = \tau_{\text{AP}}$ ) for the EPSP evoked  $\text{Ca}^{2+}$  transient ( $\tau_{\text{EPSP}} = 258 \text{ ms}$ ) and the AP evoked  $\text{Ca}^{2+}$  transient ( $\tau_{\text{AP}} = 213 \text{ ms}$ ). See Fig 4.12 for the case  $\tau_{\text{EPSP}} < \tau_{\text{AP}}$  (the spine length in that example was  $0.9 \mu\text{m}$ ).

**C** Mean spine lengths for the three different categories based on the relation of the decay time dynamics. The error bar represent the SD. The spine lengths for  $\tau_{\text{EPSP}} = \tau_{\text{AP}}$  spines ( $l = 0.51 \pm 0.16$ ,  $n = 6$ ) was significantly smaller ( $p < 0.005$ ) compared to the other two groups ( $l = 1.12 \pm 0.29$ ,  $\tau_{\text{EPSP}} < \tau_{\text{AP}}$ ,  $n = 5$ ,  $l = 1.65 \pm 0.78$ ,  $\tau_{\text{EPSP}} > \tau_{\text{AP}}$ ,  $n = 2$ ).

opposite behaviour, i.e. the EPSP evoked  $\text{Ca}^{2+}$  transient decayed faster than the AP evoked transient ( $\tau_{\text{EPSP}} < \tau_{\text{AP}}$ ).

The decay time constants for AP evoked  $\text{Ca}^{2+}$  transients depend on the spine morphology (Majewska, Tashiro et al. 2000; Majewska 2000). In  $n = 13$  cases TPE fluorescence images of the spines were acquired. 6 of these spines showed a linear correlation between the decay time constants of the EPSP and AP evoked  $\text{Ca}^{2+}$  transients ( $\tau_{\text{EPSP}} \propto \tau_{\text{AP}}$ ), in 5 spines  $\tau_{\text{EPSP}} < \tau_{\text{AP}}$  and in 2 spines  $\tau_{\text{EPSP}} > \tau_{\text{AP}}$ . The length of the spines were measured from the fluorescence images (the length was defined as the distance from the center of the spinehead to the

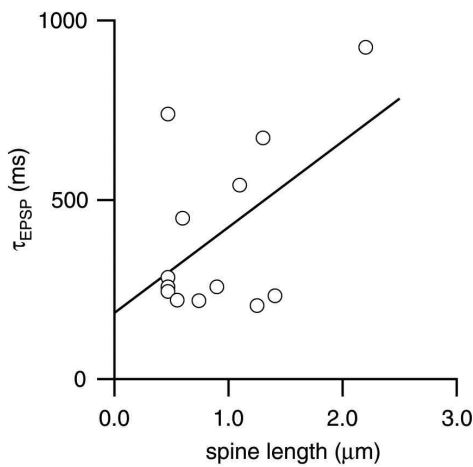


**Figure 4.14** *Correlation between spine length and EPSP evoked  $\text{Ca}^{2+}$  transient decay kinetics*  
Short spines tended to have faster EPSP evoked  $\text{Ca}^{2+}$  transient decay times ( $\tau_{\text{EPSP}}$ ) than longer spines. The linear regression showed a correlation between  $\tau_{\text{EPSP}}$  and spine length ( $n = 13$ , regression ttest,  $p < 0.05$ ).

dendritic shaft). The spine length could not always be properly resolved, because its apparent size was below the resolution limit of the TPE microscope. These spines appeared to possess no spine neck and they resembled ‘stubby’ spines (Parnass 2000). In these cases an upper estimate of the spine lengths was taken to be equal to the optical resolution of the microscope ( $x = 0.47 \mu\text{m}$ ). The spines, which showed a linear correlation between the decay time constants of EPSP and AP evoked  $\text{Ca}^{2+}$  transients had a significantly shorter spine length than the spines in the two other categories (Student’s ttest,  $p < 0.005$ ). The mean spine length was  $0.51 \pm 0.06 \mu\text{m}$  ( $\tau_{\text{EPSP}} < \tau_{\text{AP}}$ ) as compared to a spine length of  $1.12 \pm 0.29 \mu\text{m}$  for  $\tau_{\text{EPSP}} < \tau_{\text{AP}}$  and  $1.65 \pm 0.78 \mu\text{m}$  for  $\tau_{\text{EPSP}} > \tau_{\text{AP}}$ . Whereas all the former spines had a ‘stubby’ spine appearance or were classified as a putative shaft synapse (Fig 4.13B), the latter spines always had a clearly visible spine neck (Fig 4.13A for the  $\tau_{\text{EPSP}} > \tau_{\text{AP}}$  case, see also Fig 4.12 for an example of  $\tau_{\text{EPSP}} < \tau_{\text{AP}}$ ). No correlation was found between  $\tau_{\text{AP}}$  and the spine length ( $p > 0.1$ ), but a correlation between  $\tau_{\text{EPSP}}$  and the spine length existed (linear regression, slope =  $0.24 \pm 0.12 \text{ ms} \cdot \mu\text{m}^{-1}$ ,  $r = 0.52$ , regression ttest,  $p < 0.05$ ).

The relative size of the  $\text{Ca}^{2+}$  transients evoked by either bAP or EPSP depended on the distance of the spine from the soma. The peak  $\text{Ca}^{2+}$  transient amplitude evoked by a bAP in spines decreased with the distance from the soma (Fig 4.15A, linear regression,  $(F/F)_{\text{max}} = 0.60 \pm 0.06 - (0.002 \pm 0.001) \cdot \text{distance} \cdot \text{mm}^{-1}$ , mean  $\pm$  SD,  $r = -0.44$ ,  $n = 49$ ). This result was in agreement with the distance dependence measured for AP evoked  $\text{Ca}^{2+}$  transients in dendritic shafts (see Fig 4.5). The filled circles in Fig 4.15 are the mean  $(F/F)_{\text{max}}$  values binned for  $25 \mu\text{m}$  of dendritic length and the error bars give the SD. Comparing the  $(F/F)_{\text{max}}$  values close to the soma (distance less than  $50 \mu\text{m}$ ) with the values in the distal parts (distance larger than  $150 \mu\text{m}$ ) yielded a significant reduction in the AP evoked peak  $\text{Ca}^{2+}$  transient amplitude (Student’s unpaired ttest,  $p < 0.005$ ).

## Results

The EPSP evoked peak  $\text{Ca}^{2+}$  transient ( $\Delta F/F$ ) increased slightly with distance from the soma (Fig 4.15B, linear regression,  $(\Delta F/F)_{\max} = 0.5 \pm 0.1 + (0.0013 \pm 0.0012) * \text{distance} * \text{mm}^{-1}$ , mean  $\pm$  SD,  $r = 0.16$ ,  $n = 47$ ), but the increase was not significant (regression ttest,  $p > 0.1$ ). The decay time constants of neither EPSP (regression ttest,  $p > 0.25$ ) nor AP ( $p > 0.25$ ) evoked  $\text{Ca}^{2+}$  transients did depend on the distance of the spine from the soma. Thus the previously reported difference in the decay time dynamics was a function of the spine morphology and not a function of the position of the spine along the dendritic tree.

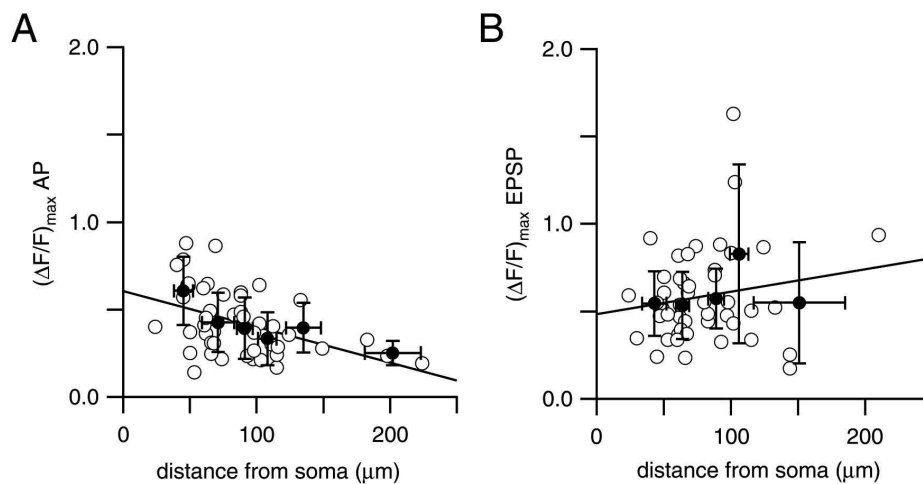


**Figure 4.15** Distance dependence of the peak  $\text{Ca}^{2+}$  transient amplitude in a spine evoked by APs and EPSPs

**A** Mean peak  $\text{Ca}^{2+}$  transient amplitude ( $(\Delta F/F)_{\max}$  AP) evoked by an AP as a function of the distance of the spine from the soma. Open circles represent individual spines ( $n = 49$ ). The solid circles represent mean amplitudes binned for 25  $\mu\text{m}$  intervals of dendritic length up to 150  $\mu\text{m}$  from the soma and the mean amplitude for spines  $> 150 \mu\text{m}$  from the soma (solid circle to the right). Error bars represent SD.  $(\Delta F/F)_{\max}$  AP decreased with the distance from the soma ( $r = -0.44$ ).

**B** Mean peak  $\text{Ca}^{2+}$  transient amplitude ( $(\Delta F/F)_{\max}$  EPSP) evoked by an EPSP as a function of the distance of the spine from the soma. Open circles represent individual spines ( $n = 47$ ). The solid circles represent mean amplitudes binned for 25  $\mu\text{m}$  intervals of dendritic length up to 125  $\mu\text{m}$  from the soma and the mean amplitude for spines  $> 125 \mu\text{m}$  from the soma (solid circle to the right). Error bars represent SD.  $(\Delta F/F)_{\max}$  EPSP showed a slight, but not significant increase with the distance from the soma ( $r = 0.16$ ).

### Effect of GluR-channel antagonists

Spine  $\text{Ca}^{2+}$  transients were strongly reduced by the AMPA receptor channel antagonists NBQX (10  $\mu\text{M}$ ) and the NMDA receptor channel antagonist APV (25  $\mu\text{M}$ ) respectively. APV blocked the  $\text{Ca}^{2+}$  signal to  $4 \pm 3\%$  ( $n = 4$ , paired ttest,  $p < 0.02$ ) of control with a much smaller reduction of the EPSP amplitude to  $66 \pm 17\%$  (paired ttest,  $p < 0.02$ ) of control.



Fig 4.16A shows a somatically recorded EPSP and the corresponding  $\text{Ca}^{2+}$  transient (upper traces) under control conditions and after bath application of 10  $\mu\text{M}$  NBQX (lower traces). In this case the peak EPSP amplitude was reduced from 6 mV to 1.5 mV and the peak  $\text{Ca}^{2+}$

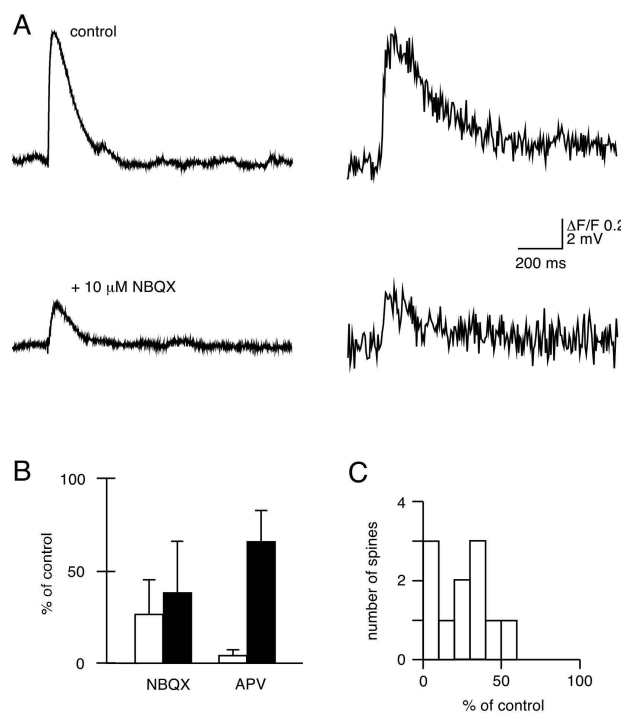


**Figure 4.16 Pharmacology of EPSP evoked  $\text{Ca}^{2+}$  influx in single spines**

**A** Somatic EPSPs and spinesous  $\text{Ca}^{2+}$  transients for control conditions (upper traces) and after bath application of the AMPA receptor channel blocker NBQX (10  $\mu\text{M}$ , lower traces).

**B** The EPSP amplitude after application of NBQX is reduced to 38±28% of control (black bar). The  $\text{Ca}^{2+}$  transient amplitude is reduced to 27±18% of control in this case (white bar). Application of APV blocks the  $\text{Ca}^{2+}$  transient amplitude to 4 ± 3% of control (white bar) whereas the EPSP amplitude is reduced to 66 ± 17% of control (black bar).

**C** Histogram of the reduction of  $\text{Ca}^{2+}$  transient amplitudes by NBQX. The reduction varies greatly indicating that different spines possess different numbers of functional AMPARs. In 3 spines the  $\text{Ca}^{2+}$  transient amplitude was blocked almost completely.

transient amplitude was reduced from  $(F/F)_{\text{max}} = 0.93$  to  $(F/F)_{\text{max}} = 0.35$ . On average, NBQX (10  $\mu\text{M}$ ) reduced the  $\text{Ca}^{2+}$  signal to 27±18% (n = 11, paired ttest,  $p < 0.0001$ ) of control at resting membrane potential (-71±3 mV) whereas the EPSP was reduced to 34±28% (paired ttest,  $p < 0.00005$ ) of control (Fig 4.16). Additional application of APV in these experiments (n = 3) abolished the remaining  $\text{Ca}^{2+}$  transient completely.

Fig 4.16C shows the distribution of the reduction of the  $\text{Ca}^{2+}$  transient amplitudes by NBQX. The reduction varies greatly (from 0-50%) indicating that different spines possessed different numbers of functional AMPARs (Andrasfalvy 2001). Note that in 3 out of 11 spines the  $\text{Ca}^{2+}$  transient amplitude was blocked almost completely (to less than 8%).

These results suggested that the main pathway for  $\text{Ca}^{2+}$  entry evoked by synaptic stimulation is through NMDA receptor channels. The relative mean reduction of the EPSP peak voltage and the peak  $\text{Ca}^{2+}$  transient after application of NBQX was comparable suggesting that the peak  $\text{Ca}^{2+}$  transient depended on the local depolarization of the spine as sensed by the  $\text{Mg}^{2+}$  blocking site of the NMDAR (Mayer 1984; Nowak 1984).

#### 4.1.4 Pre- and postsynaptic coincident activity

##### *Ca<sup>2+</sup> transients evoked by pairing EPSPs and back-propagating APs*

Next, the Ca<sup>2+</sup> influx in single spines when EPSPs and bAPs were paired was investigated. It had been shown previously that coincident activity results in supralinear Ca<sup>2+</sup> transients in single spines (Yuste 1995). Further studies suggested that the Ca<sup>2+</sup> transients can add sub- and supralinearly, depending on the order of EPSP and AP respectively, but keeping the inter-stimulus interval constant at  $t = 50$  ms (Koester 1998). The results obtained from spike-timing dependent plasticity (STDP) experiments showed that not only the order of EPSP and AP were important, but that also the inter-stimulus interval was critical for the magnitude of LTP and LTD expression (Feldman 1998; Froemke 2002). The time-window, in which plasticity could be induced was  $\pm 50$  ms (Bi 1998). It was hypothesized that the

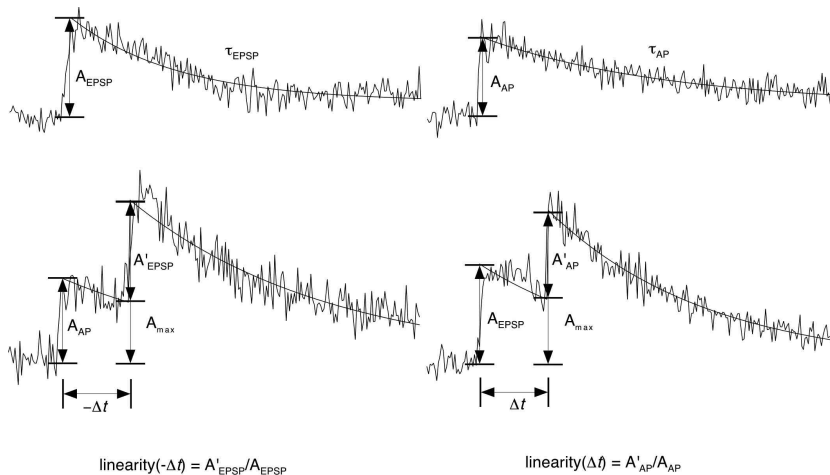


**Figure 4.17** *Quantification of the non-linear Ca<sup>2+</sup> influx during coincident stimuli*

*Example calculation to introduce the parameters for evaluating the non-linearity of the Ca<sup>2+</sup> transients evoked by pairing an EPSP with an AP at different time intervals. First, fluorescence transients evoked by an EPSP and AP were recorded separately as controls (upper traces). Single exponential fits to the yielded the peak amplitude  $A_{EPSP}$  and the decay time constant  $\tau_{EPSP}$  for the EPSP and  $A_{AP}$  and  $\tau_{AP}$  for the AP respectively. Pairing of the two stimuli at an inter-stimulus interval  $\Delta t$  resulted in a Ca<sup>2+</sup> transient which was fitted by the sum of two single exponentials shifted by the respective time interval. The amplitude of the first stimulus was fixed to the amplitude of the control measurements. In the case where the AP followed the EPSP,  $A_{EPSP}$  was fixed. The fit yielded the the amplitude  $A'_{AP}$  for the AP. In the case where the AP preceded the EPSP,  $A_{AP}$  was fixed and  $A'_{EPSP}$  was derived from the fit. These amplitudes were normalized to the respective control amplitude, giving a measure for the relative change of the second stimulus (denoted as linearity). Further the transients were fitted by a single exponential, yielding the maximal fluorescence amplitude  $A_{max}$ . This value was normalized to the linear sum derived from the summation of the control stimuli shifted by the respective time interval.*

amount of  $\text{Ca}^{2+}$  influx during the plasticity-inducing pairing protocols was a determinant of plasticity expression (Bliss 1993; Malenka 1999). The  $\text{Ca}^{2+}$  influx in single synaptic spines in spiny neurons was therefore measured for pairs of EPSPs and bAPs at different inter-stimulus time intervals to obtain a complete ‘ $\text{Ca}^{2+}$  timing curve’ for the relevant time interval for these cells.

First EPSP and bAP evoked  $\text{Ca}^{2+}$  transients were recorded individually as control (Fig 4.17 upper traces). Then EPSP and bAP were paired, always resulting in a larger  $\text{Ca}^{2+}$  transient with two peaks (Fig 4.17 lower traces).

Next the time interval  $t$  between the two stimuli evoking an EPSP or an bAP (peak of the AP to the onset of the EPSP) was varied between  $-300$  and  $300$  ms. Negative time intervals ( $t < 0$ ) denote the sequence AP-EPSP and positive time intervals ( $t > 0$ ) denote the sequence EPSP-AP. The control  $\text{Ca}^{2+}$  transients evoked by an EPSP or AP alone yielded the peak  $\text{Ca}^{2+}$  transient amplitudes  $A_{\text{EPSP}}$  and  $A_{\text{AP}}$  and the corresponding decay time constants  $\tau_{\text{EPSP}}$  and  $\tau_{\text{AP}}$  respectively. The maximal  $\text{Ca}^{2+}$  transient amplitude evoked by the paired stimuli,  $A_{\text{max}}$ , at the time interval  $t$  (peak of the second stimulus) was determined by a single exponential fit reflecting the volume averaged peak of the  $\text{Ca}^{2+}$  influx (Fig 4.17, lower traces).  $A_{\text{max}}$  was then normalized to the expected linear sum of the two control stimuli at the time interval  $t$  ( $A_{\text{AP}} \cdot \exp(-t/\tau_{\text{AP}}) + A_{\text{EPSP}}$  for  $t < 0$  and  $A_{\text{EPSP}} \cdot \exp(-t/\tau_{\text{EPSP}}) + A_{\text{AP}}$  for  $t > 0$  respectively).

To further quantify the effect of a first stimulus on the  $\text{Ca}^{2+}$  transient amplitude evoked by a second stimulus, the  $\text{Ca}^{2+}$  transients were fitted by the sum of two exponentials separated by the time interval  $t$ . The amplitude of the first stimulus was usually fixed to the peak amplitude obtained from the control measurement. The peak amplitude of the  $\text{Ca}^{2+}$  signal evoked by the second stimulus ( $A'_{\text{EPSP}}$  for  $t < 0$  and  $A'_{\text{AP}}$  for  $t > 0$ ) was compared to the peak amplitude of the  $\text{Ca}^{2+}$  signal evoked by the corresponding control stimulus. This ratio yielded the relative change of the peak  $\text{Ca}^{2+}$  amplitude evoked by the second stimulus and is referred to as ‘linearity’ (see Fig 4.17 for details). At negative time intervals ( $t < 0$ ) the ratio measured the relative change of the  $\text{Ca}^{2+}$  transient of an EPSP preceded by an bAP ( $A'_{\text{EPSP}}/A_{\text{EPSP}}$ ). The ratio at positive time intervals ( $t > 0$ ) described the relative change of the  $\text{Ca}^{2+}$  peak amplitude of an AP preceded by an EPSP ( $A'_{\text{AP}}/A_{\text{AP}}$ ).

### *Non-linear summation of $\text{Ca}^{2+}$ influx in spines*

The size of the  $\text{Ca}^{2+}$  influx into single spines depended critically, within a time window of  $300$  ms, on the sequence of AP and EPSPs. The relative time of occurrence of EPSP and bAP resulted in either linear, sublinear or supralinear summation of the  $\text{Ca}^{2+}$  influxes evoked by the two stimuli.

Fig 4.18 illustrates that changing the relative order of EPSP and bAP, but keeping the inter-stimulus time interval constant ( $t = 20$  ms), resulted in quantitatively different  $\text{Ca}^{2+}$  transients. In this example, the peak  $\text{Ca}^{2+}$  transient amplitudes for the control EPSP was  $A_{\text{EPSP}} = 0.43$  and for the control AP the amplitude was  $A_{\text{AP}} = 0.42$ . The decay time constants were  $\tau_{\text{EPSP}} = 258$  ms and  $\tau_{\text{AP}} = 213$  ms respectively (Fig 4.18B). Pairing the two stimuli in the order

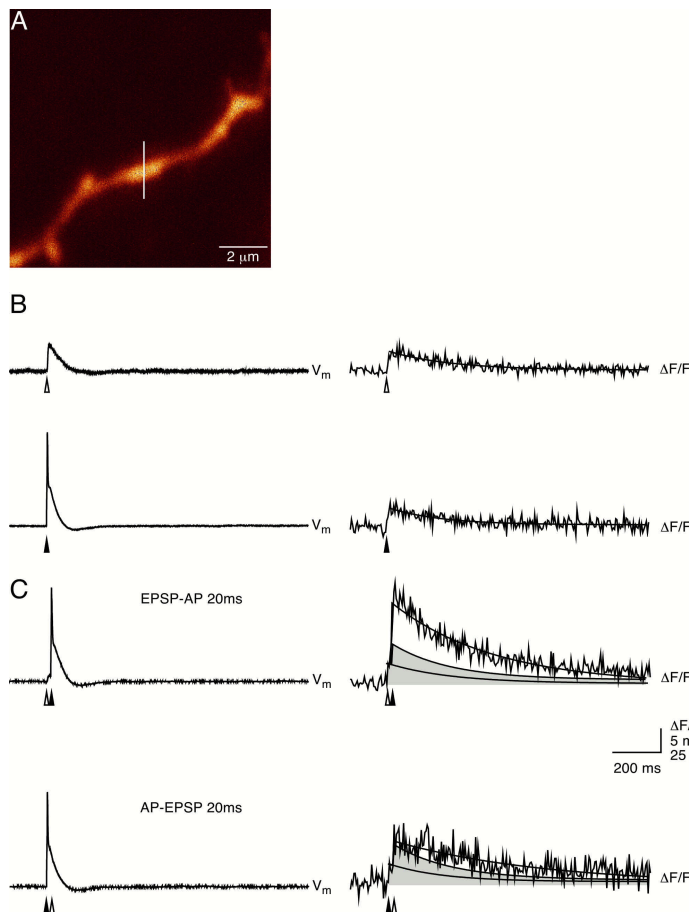


**Figure 4.18 Pairing of bAPs and EPSPs evokes non-linear  $\text{Ca}^{2+}$  influx**

**A** Fluorescence image of the active synaptic contact. The white line indicates the position of the linescan.

**B** Somatic voltage recordings (left) and the corresponding  $\text{Ca}^{2+}$  transients (right) for an EPSP (upper trace) and AP (lower trace) respectively. The onsets of stimulation are indicated by the white and black arrows for the EPSP and AP respectively.

**C** The upper trace shows the pairing of an EPSP with a following bAP at a stimulus interval of 20 ms and the corresponding  $\text{Ca}^{2+}$  fluorescence transient. The  $\text{Ca}^{2+}$  transient deviates largely from the predicted linear sum of  $\text{Ca}^{2+}$  transients evoked by the EPSP and AP alone (shaded area) and is strongly non-linear. In the case where the bAP precedes the EPSP by 20 ms the  $\text{Ca}^{2+}$  transient corresponds to the predicted linear sum of AP and EPSP alone.

EPSP-AP resulted in a  $\text{Ca}^{2+}$  transient with a peak amplitude of  $A_{\text{max}}(t=20\text{ms}) = 1.85$ . The two single exponential fit yielded an amplitude of the second stimulus of  $A'_{\text{AP}} = 1.26$ . Reversing the order of the stimuli (AP-EPSP) yielded a peak amplitude of  $A_{\text{max}}(t=-20\text{ms}) = 0.941$  and an amplitude of the second stimulus in this case of  $A'_{\text{EPSP}} = 0.48$  (Fig 4.18C). Comparing the peak amplitudes to the expected linear sum of the two stimuli alone (shaded area in Fig 4.18C) showed that  $A_{\text{max}}(t=20\text{ms})$  was two times larger than expected, whereas  $A_{\text{max}}(t=-20\text{ms})$  corresponded to the linear sum. The larger  $\text{Ca}^{2+}$  transient for the sequence EPSP-AP was due to a much increased rise in  $\text{Ca}^{2+}$  evoked by the AP ( $A'_{\text{AP}}$  was three times larger than the control amplitude  $A_{\text{AP}}$ ). In contrast, the sequence AP-EPSP corresponded well

to the linear summation of the control  $\text{Ca}^{2+}$  transients and  $A'_{\text{EPSP}}$  was not effected by a preceding AP ( $t = -20\text{ms}$ ).

These results could be reproduced repeatedly, yielding an average deviation from the expected linear sum of  $1.5 \pm 0.3$  ( $n = 12$ , paired ttest,  $p < 0.0001$ ), which was due to a  $2.0 \pm 0.7$  fold increase (= linearity) of  $A'_{\text{AP}}$  (paired ttest,  $p < 0.00005$ ) for the case of the EPSP preceding the AP by 20 ms. If the EPSP followed the AP by 20 ms no significant deviation of the peak  $\text{Ca}^{2+}$  transient amplitude (mean deviation,  $1.1 \pm 0.3$ ,  $n = 10$ ) from the expected linear sum was found (paired ttest,  $p > 0.05$ ). The EPSP amplitude  $A'_{\text{EPSP}}$  was, on average, not effected by a preceding AP (linearity =  $1.1 \pm 0.2$ , paired ttest,  $p > 0.1$ ).

### ***Timing curve of spine $\text{Ca}^{2+}$ influx evoked by pairing bAPs and EPSPs***

The previously described experiment was repeated for different inter-stimulus intervals ranging from  $-300$  ms to  $300$  ms. Fig 4.19A shows the average peak  $\text{Ca}^{2+}$  transient amplitude  $A_{\text{max}}$  plotted vs. the corresponding inter-stimulus interval  $t$ . Comparing  $A_{\text{max}}$  for adjacent timepoints revealed a significant increase in the peak  $\text{Ca}^{2+}$  transient amplitude from  $t = 1$  ms to  $t = 10$  ms (unpaired ttest,  $p < 0.005$ ) and a significant decrease of  $A_{\text{max}}$  from  $t = 50$  ms to  $t = 100$  ms ( $p < 0.04$ ). For all other pairs no difference in the amplitudes were found. Furthermore, comparing  $A_{\text{max}}$  for any pair of timepoints for  $t < 10$  ms and  $t > 50$  ms also did not show any significant differences ( $p > 0.05$ ). Pooling the peak amplitudes in this

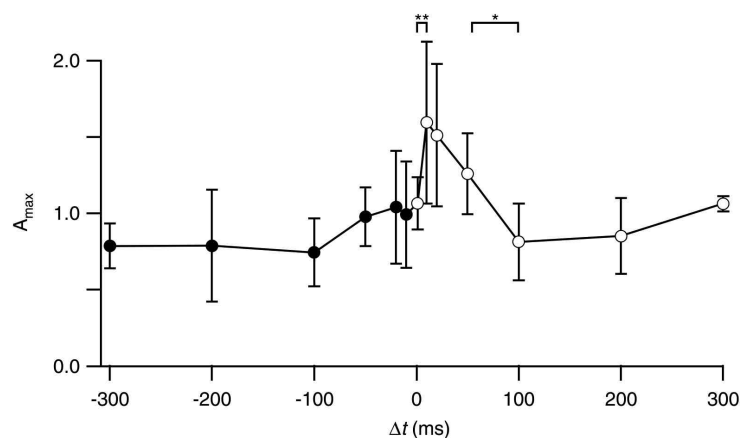


**Figure 4.19 Peak  $\text{Ca}^{2+}$  transient amplitudes evoked by pairing EPSPs with APs at different time intervals**  
 The peak  $\text{Ca}^{2+}$  transients amplitudes  $A_{\text{max}}$  evoked by pairing EPSPs with APs are plotted for the corresponding time intervals  $\Delta t$ . Black circles denote the sequence AP-EPSP and open circles denote the sequence EPSP-AP. Error bars are SD. Significant differences between the peak amplitudes of neighbouring time points were found for  $\Delta t = 10$  ms (\*\*, Student's ttest,  $p < 0.005$ ) and  $\Delta t = 50$  ms (\*,  $p < 0.05$ ).

## Results

interval yielded  $A_{\max} = 0.95 \pm 0.28$  (mean  $\pm$  SD). Thus only pairing an EPSP with an AP following between 10 ms to 50 ms resulted in a significant increase in the peak  $\text{Ca}^{2+}$  transient amplitude ( $A_{\max}(\text{10ms} \leq t \leq 50\text{ms}) = 1.51 \pm 0.47$ , unpaired ttest,  $p < 0.00001$ ). For all other inter-stimulus intervals, the peak amplitude was similar.

Comparing  $A_{\max}$  to the expected linear sum ( $\text{sum}_{\text{lin}}$ ) for all inter-stimulus intervals tested showed that for  $t = -50$  ms the transients added sublinearly (paired ttest,  $p < 0.03$ ) with a ratio of  $A_{\max}$  to  $\text{sum}_{\text{lin}}$  of  $0.9 \pm 0.1$  (Fig 4.20). For positive time intervals between 10 ms and 50 ms the transients added supralinearly ( $p < 0.00001$ ,  $p < 0.0001$ ,  $p < 0.02$  for  $t = 10$  ms, 20 ms and 50 ms respectively). For all other time intervals no difference to the linear sum was found. The supralinear addition of the  $\text{Ca}^{2+}$  transients had a maximum at  $t = 10$  ms with a ratio of  $A_{\max}$  to  $\text{sum}_{\text{lin}}$  of  $1.7 \pm 0.2$ . At  $t = 20$  ms the ratio was similar ( $A_{\max}/\text{sum}_{\text{lin}} = 1.5 \pm 0.3$ ,  $p > 0.1$ ), but for  $t = 50$  ms the ratio was already significantly decreased ( $A_{\max}/\text{sum}_{\text{lin}} = 1.3 \pm 0.1$ ,  $p < 0.04$ ).

The deviation of the peak  $\text{Ca}^{2+}$  amplitude from the linear sum resulted from a non-linear influence of the  $\text{Ca}^{2+}$  influx evoked by the second stimulus. As described above, the linearity was a measure for the relative change of the peak  $\text{Ca}^{2+}$  amplitude of a stimulus, preceded by a first stimulus, compared to the corresponding control stimulus. Fig 4.21 shows the linearity measure as a function of the corresponding inter-stimulus interval. The linearity curve was strongly asymmetric. Comparing the amplitudes of the second stimulus to the corresponding control stimuli yielded a significant reduction (linearity(-50ms) =  $0.8 \pm 0.1$ ) for the EPSP

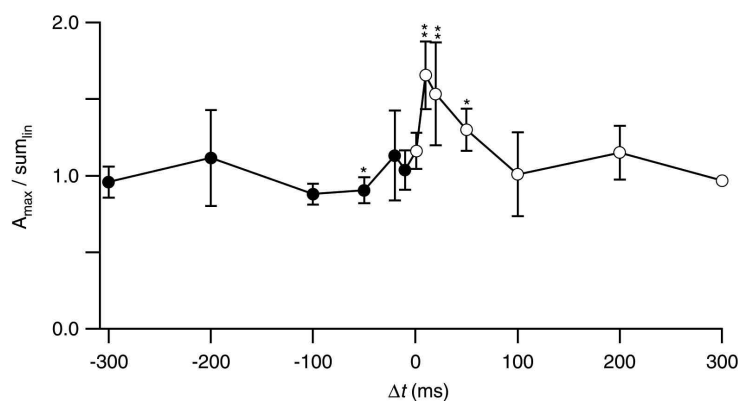


**Figure 4.20** Peak  $\text{Ca}^{2+}$  transient amplitudes evoked by pairing EPSPs with APs normalized to the expected linear sum at different time intervals

The peak  $\text{Ca}^{2+}$  transients amplitudes  $A_{\max}$  were normalized to the expected linear sum of the  $\text{Ca}^{2+}$  transients evoked by the control stimuli. Black circles denote the sequence AP-EPSP and open circles denote the sequence EPSP-AP. Error bars are SD. Significant differences between the peak amplitudes and the linear sum were found for  $\Delta t = -50$  ms (\*, Student's ttest,  $p < 0.03$ ) where the AP and EPSP summed sublinearly,  $\Delta t = 10$  ms (\*\*,  $p < 0.0001$ ),  $\Delta t = 20$  ms (\*\*,  $p < 0.0001$ ) and  $\Delta t = 50$  ms (\*). In the latter cases the amplitudes summed supralinearly.

evoked peak  $\text{Ca}^{2+}$  amplitude  $A'_{\text{EPSP}}$  at  $t = -50\text{ms}$  (paired ttest,  $p < 0.03$ ). Significant differences of  $A'_{\text{AP}}$  as compared to the control amplitude  $A_{\text{AP}}$  were found for the time intervals  $t = 1\text{ ms}$  (linearity(1 ms) =  $1.6 \pm 0.3$ ,  $p < 0.004$ ),  $t = 10\text{ ms}$  (linearity(10 ms) =  $2.3 \pm 0.5$ ,  $p < 0.000005$ ) and  $20\text{ ms}$  (linearity(20 ms) =  $2.0 \pm 0.7$ ,  $p < 0.000005$ ). For all other inter-stimulus intervals no significant deviations from the control amplitudes were found.

The supralinear part of the linearity curve from the maximum at  $t = 10\text{ ms}$  was readily fitted by a single exponential function (Fig 4.22). The supralinearity decayed with a time constant of  $30\text{ ms}$ . A similar value of  $40\text{ ms}$  was derived from an exponential fit to the peak  $\text{Ca}^{2+}$  transient amplitudes. Hence, the supralinear summation decayed with an average time constant of  $35\text{ ms}$ , which exactly matched the decay time constant of the NMDA component of an EPSP ( $\tau_{\text{NMDA}} = 35 \pm 15\text{ ms}$  (Feldmeyer 1999)). This suggests that the mechanism of the supralinear  $\text{Ca}^{2+}$  influx during coincident activity was determined by the properties and the opening kinetics of the NMDAR channel. The NMDAR requires the binding of glutamate to open and a concurrent depolarization of the membrane to relieve the  $\text{Mg}^{2+}$  block to become permeable to  $\text{Ca}^{2+}$  ions. The pharmacological characterization of the EPSP evoked  $\text{Ca}^{2+}$  transients showed that during synaptic activity the  $\text{Ca}^{2+}$  influx into a spine was entirely mediated by the NMDAR. The evidence presented here suggests now that an AP following

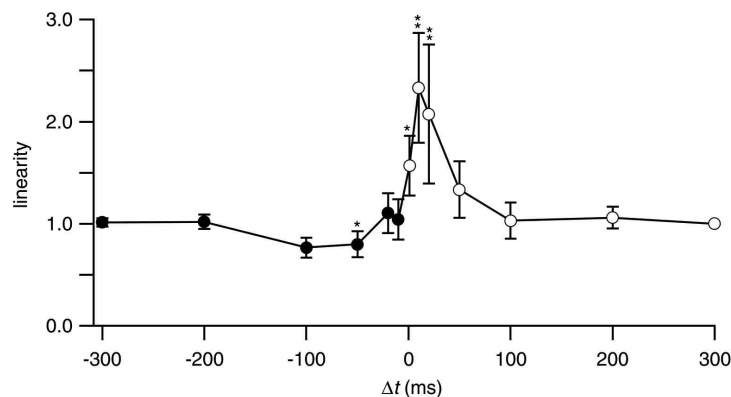


**Figure 4.21** Linearity of the second peak  $\text{Ca}^{2+}$  transient amplitude at different time intervals

The linearity was defined as the ratio of the second  $\text{Ca}^{2+}$  transient peak amplitude to the corresponding control stimulus. Black circles denote the sequence AP-EPSP (linearity =  $A'_{\text{EPSP}}/A_{\text{EPSP}}$ ) and open circles denote the sequence EPSP-AP (linearity =  $A'_{\text{AP}}/A_{\text{AP}}$ ). Error bars are SD. Significant differences between the peak amplitudes of the second stimulus and the control stimulus were found for  $\Delta t = -50\text{ ms}$  (\*, Student's ttest,  $p < 0.02$ ) where  $A'_{\text{EPSP}}$  was reduced,  $\Delta t = 1\text{ ms}$  (\*),  $\Delta t = 10\text{ ms}$  (\*\*,  $p < 0.000005$ ) and  $\Delta t = 20\text{ ms}$  (\*\*). In the latter cases the amplitudes  $A'_{\text{AP}}$  were larger than the control amplitudes. The maximum was found at  $\Delta t = 10\text{ ms}$ , where the AP evoked  $\text{Ca}^{2+}$  transient, preceded by an EPSP was more than two-fold larger than the peak  $\text{Ca}^{2+}$  amplitude of the AP evoked transient alone.

the EPSP relieves the  $Mg^{2+}$  block of the population of NMDARs, which were switched to an open state after binding of glutamate but had not become permeable to  $Ca^{2+}$  due to the  $Mg^{2+}$  block. With an increasing inter-stimulus interval between EPSP and AP less NMDARs were in an open state and therefore the effect of the membrane depolarization by the AP became correspondingly less.

Further evidence that the AP is ‘probing’ the number of open NMDARs (and in that respect the kinetics of the channel) was the linearity value at  $t = 1$  ms. At this timepoint (assuming fast propagation of the AP into the dendritic tree of less than 1 ms) the maximal number of NMDARs had not opened yet corresponding to the slow rise time of the NMDAR EPSP measured by Feldmeyer et al. of 5-10 ms (Feldmeyer 1999). Therefore the observed linearity was smaller ( $1.3 \pm 0.3$ ) than at  $t = 10$  ms, when the maximal number of NMDARs were open.

Thus supralinear summation of  $Ca^{2+}$  signals in spines evoked during pairing of EPSPs and APs and the resulting significant increase in the peak  $Ca^{2+}$  transient amplitude was restricted to a relatively short time-window of 20 ms and the sequence EPSP-AP. This time-window

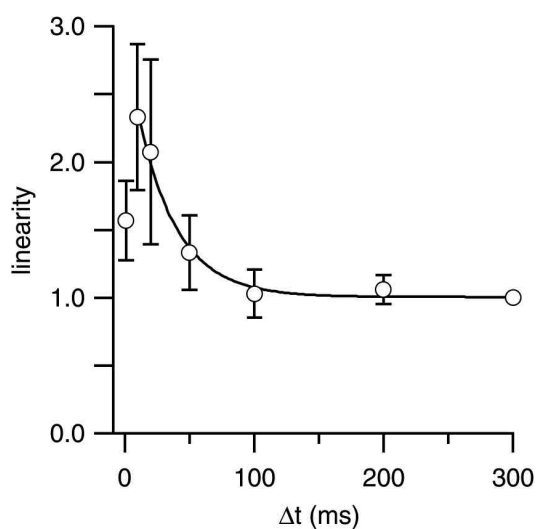


**Figure 4.22** *The non-linearity for  $\Delta t > 0$  corresponds to the NMDAR channel kinetics*

*The same plot as in Fig 4.21 restricted to  $\Delta t > 0$  (EPSP-AP). The solid line represents a single exponential fit to the points for  $\Delta t \geq 10$  ms. The fit yielded a decay time constant of the supralinearity of 30 ms. This value corresponded well to the reported decay of the NMDAR component of EPSPs measured in spiny neurons ( $\tau_{NMDA} = 35$  ms, [Feldmeyer, 1999 #2]). The smaller linearity value at  $\Delta t = 0$  as compared to the maximum at  $\Delta t = 10$  ms reflects the slow opening of the NMDAR of 5-10 ms. The supralinear  $Ca^{2+}$  influx is due to the relieve of the  $Mg^{2+}$  block by the bAP. The magnitude reflects the number of opened NMDAR channels.*

can be defined as the coincidence detection window, in which the occurrence of pre- and postsynaptic spikes was coded by an increased  $Ca^{2+}$  amplitude opposed to uncorrelated activity outside of this time-window.

The sublinear summation of the  $Ca^{2+}$  transients found for the sequence AP-EPSP at  $t = -50$  ms resulted in decreasing the peak  $Ca^{2+}$  amplitude to a level, which made it similar to the peak  $Ca^{2+}$  amplitudes found for longer time intervals.



### Decay time constants of $\text{Ca}^{2+}$ transients

As reported above, coincident activity within a time window of 10 to 20 ms lead to a large  $\text{Ca}^{2+}$  transient. The  $\text{Ca}^{2+}$  load might affect the clearance of the  $\text{Ca}^{2+}$  causing a prolonged  $\text{Ca}^{2+}$  transient as observed for long trains of bAPs at high frequencies in layer 5 pyramidal neurons (Helmchen 1996). Furthermore the stimulus sequence AP-EPSP could enhance a  $\text{Ca}^{2+}$

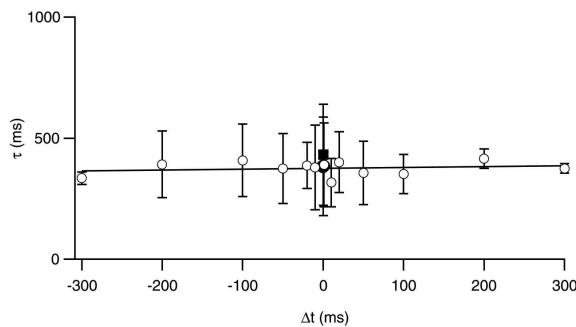


**Figure 4.23** The decay time constants of  $\text{Ca}^{2+}$  transients evoked by paired stimuli are independent of the inter-stimulus interval

The linear regression line (solid line) to the decay time constants showed no dependence on the pairing sequence. The black square and the black circle represent the decay time constants for AP and EPSP evoked  $\text{Ca}^{2+}$  transients respectively as a reference.

dependent inactivation mechanism of NMDARs, speeding the decay of the  $\text{Ca}^{2+}$  transient (Umehiya 2001) by shortening the open-time of the receptor. Thus the relative order of the stimuli could not just influence the magnitude of  $\text{Ca}^{2+}$  influx, but it could potentially also shape the decay time dynamics.

The decay of the  $\text{Ca}^{2+}$  transients evoked by pairing EPSPs and APs measured from the peak of the transient  $A_{\text{max}}$  were well described by a mono exponential decay. The resulting decay time constants did not depend on the inter-stimulus interval, nor on the relative order of EPSP and AP (Fig 4.23, linear regression,  $r = 0.19$ ). The decay times were  $\tau_{\text{AP-EPSP}} = 381 \pm 129$  ms and  $\tau_{\text{EPSP-AP}} = 369 \pm 111$  ms (Student's ttest,  $p > 0.3$ ). In fact the decay times for the

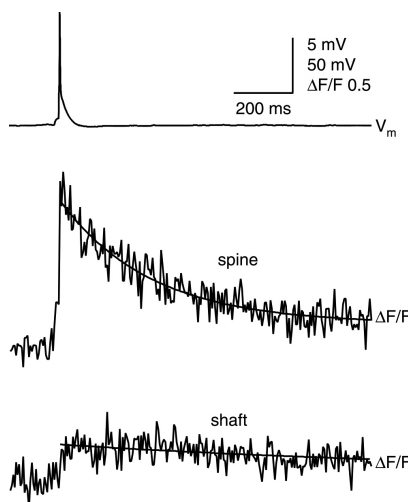


**Figure 4.24** Supralinear  $\text{Ca}^{2+}$  transients are restricted to the spinehead

Example traces, recorded in the spinehead and shaft depicted in Fig 4.11. The upper trace shows the somatic voltage recording of an EPSP preceding an AP by 20 ms. The corresponding  $\text{Ca}^{2+}$  transients in an active spine (middle trace) and adjacent shaft illustrate that the large, supralinear  $\text{Ca}^{2+}$  transient in this case was exclusively restricted to the spinehead. The fluorescence increase in the shaft was due to  $\text{Ca}^{2+}$  influx evoked by the AP.

paired stimuli  $\text{Ca}^{2+}$  transients (pooled for all paired stimuli,  $\tau = 375 \pm 119$  ms) were similar to the decay times of the single stimulus induced transients ( $\tau_{\text{AP}} = 426 \pm 209$  ms,  $\tau_{\text{EPSP}} = 396 \pm 216$  ms,  $p > 0.2$ , Fig 4.23 black square and black circle at  $t = 0$  respectively). Thus, at least for paired stimuli, no effects on the decay time dynamics was observed, ruling out a major influence in these cases of shaping the life-time of  $\text{Ca}^{2+}$  ions in the spine (and thus the integration of the  $\text{Ca}^{2+}$  signal) by  $\text{Ca}^{2+}$  and/or mGluR activated mechanisms (Anwyl 1999) within a time window of  $\pm 300$  ms.

### ***Supralinear $\text{Ca}^{2+}$ transients are localized to the spinehead***

It was shown that the EPSP evoked  $\text{Ca}^{2+}$  transient was mainly confined to the spinehead (Fig 4.11). In some of these experiments ( $n = 3$ ) also supralinear  $\text{Ca}^{2+}$  transients were observed by pairing an EPSP with an AP at an inter-stimulus interval of  $t = 20$  ms. Fig 4.24 shows the corresponding  $\text{Ca}^{2+}$  transients obtained from the same spine and dendrite as in Fig 4.11. In this case was the peak transient amplitude greatly reduced in the dendritic shaft as compared to the spinehead ( $(\Delta F/F)_{\text{max}} = 0.36 \pm 0.07$  in the dendrite compared to  $(\Delta F/F)_{\text{max}} = 1.35 \pm 0.02$  in the spinehead). The peak amplitude measured in the dendritic shaft corresponded well to the EPSP evoked rise in fluorescence ( $(\Delta F/F)_{\text{max}} = 0.09$ ) and the AP evoked  $\text{Ca}^{2+}$  transient ( $(\Delta F/F)_{\text{max}} = 0.23$ ), where as the  $\text{Ca}^{2+}$  transients in the spine added supralinearly. On average, was the peak  $\text{Ca}^{2+}$  transient amplitude in the shaft reduced to  $32 \pm 10\%$  ( $n = 3$ ).

Thus during coincident activity is the supralinear  $\text{Ca}^{2+}$  signal restricted to the site of the active synaptic contact. This can ensure input specific modifications of active synaptic contacts.

### ***Dependence of the supralinear $\text{Ca}^{2+}$ influx on spine location***

As concluded above, represents the supralinear  $\text{Ca}^{2+}$  influx into a spine a very localized signal, which could specifically modify coincidently active synapses. The distance dependence of  $\text{Ca}^{2+}$  transients evoked by EPSPs and APs alone ( $A_{\text{EPSP}}$  shows a slight tendency to increase with the distance from the soma, whereas  $A_{\text{AP}}$  significantly decreases) suggested that the coincidence detection of spines might not only be temporal but also spatially sensitive. Fig 4.25A shows the peak  $\text{Ca}^{2+}$  transient amplitudes  $A_{\text{max}}$  plotted against the distance from the soma. Since the peak  $A_{\text{max}}$  values for coincident activity (sequence EPSP-AP) within a time window of 20 ms were not significantly different they were pooled. Black circles represent the sequence EPSP-AP,  $t = 10$  ms and open circles represent the sequence EPSP-AP,  $t = 20$  ms. A linear regression showed no dependence of  $A_{\text{max}}$  on the distance from the soma ( $r = -0.2$ , regression ttest,  $p > 0.1$ ). Proximal (distance  $< 80 \mu\text{m}$ ,  $d =$

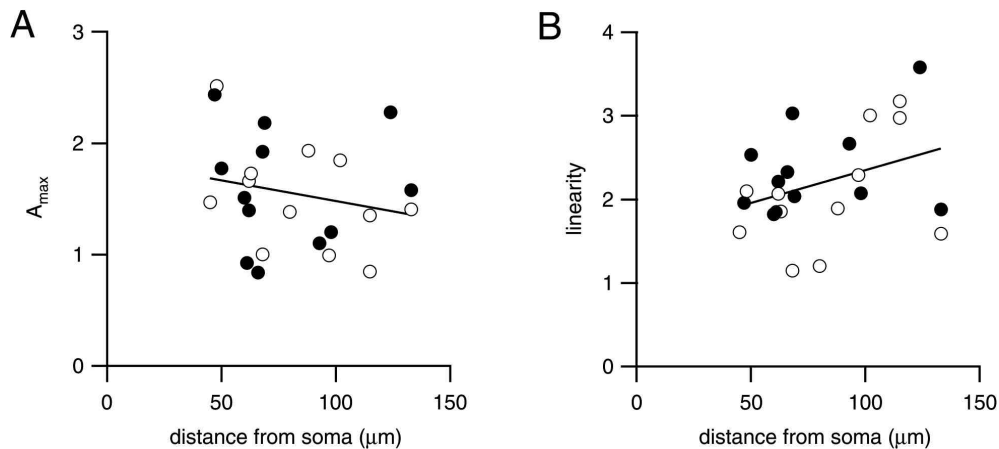


**Figure 4.25** *The peak  $\text{Ca}^{2+}$  transient amplitude during coincident activity does not depend on the distance from the soma*

**A** Plot of the peak  $\text{Ca}^{2+}$  transient amplitude  $A_{\max}$  vs. the distance from the soma. The data points during coincident activity, as defined above (i.e. peak  $\text{Ca}^{2+}$  transient amplitudes evoked by the sequence EPSP-AP at inter-stimulus time intervals of 10 ms (black circles) and 20 ms (open circles)), were pooled. The linear regression line showed no dependence of  $A_{\max}$  on the distance from the soma ( $r = -0.2$ , regression ttest,  $p > 0.1$ ).

**B** The linearity increases with the distance from the soma (linear regression,  $r = 0.4$ ,  $p < 0.05$ ). Since the data points correspond to the ratio of  $A'_{\text{AP}}/A_{\text{AP}}$ , the increase with the distance from the soma can be explained by the previously reported respective decrease in  $A_{\text{AP}}$ , i.e. the relative contribution of the  $\text{Ca}^{2+}$  influx through the NMDAR to the VDCC increases.

$62 \pm 12 \mu\text{m}$ ) synaptic contacts showed a mean amplitude  $A_{\max} = 1.6 \pm 0.5$  ( $n = 14$ , mean  $\pm$  SD). More distal contacts (distance  $> 80 \mu\text{m}$ ,  $d = 112 \pm 16 \mu\text{m}$ ) had a mean  $A_{\max} = 1.4 \pm 0.4$  ( $n = 9$ ), which was not significantly different (Student's ttest,  $p > 0.2$ ). Thus the absolute  $\text{Ca}^{2+}$  influx during coincident activity is independent of the position of the synaptic contact along the dendritic tree.

This homogeneity in the peak  $\text{Ca}^{2+}$  transient amplitude during coincidence detection suggested that the decrease in the AP evoked  $\text{Ca}^{2+}$  transient amplitude played only a minor role in shaping the supralinear  $\text{Ca}^{2+}$  transient. The AP relieved the  $\text{Mg}^{2+}$  block from activated NMDARs, which resulted in the supralinear  $\text{Ca}^{2+}$  influx. The defined linearity measure ( $A'_{\text{AP}}/A_{\text{AP}}$ ) corresponded to the relative contribution of  $\text{Ca}^{2+}$  influx through the NMDAR to  $\text{Ca}^{2+}$  influx through VDCCs. Indeed plotting the linearity vs. the distance from the soma showed a significant correlation ( $r = 0.4$ , regression ttest,  $p < 0.05$ ). The mean linearity was  $2.0 \pm 0.5$  for proximal contacts, which increased significantly for more distal contacts (linearity =  $2.6 \pm 0.7$ ,  $p < 0.02$ ). This increase in the linearity measure can be explained by an increase in the relative contribution of NMDARs to VDCCs to the  $\text{Ca}^{2+}$  signal. The

membrane depolarization caused by a bAP is sufficient for all spines along the dendritic tree to relieve the  $Mg^{2+}$  block of the NMDARs. Even though the contribution of VDCCs to the  $Ca^{2+}$  signal decreased with the distance from the soma, the  $Ca^{2+}$  influx through NMDARs can counter this effect resulting in a stereotyped coincidence detection signal in all spines (assuming a constant distribution of the number of NMDARs (Andrasfalvy 2001)).

### *Pharmacological dissection of supralinear $Ca^{2+}$ influx into spines*

The previous experiments suggested that the source of the supralinear  $Ca^{2+}$  summation was mainly mediated by the properties of the NMDAR channel. To further elucidate the origin of the supralinearity, the  $Ca^{2+}$  influx during coincident activity in the presence of specific glutamate receptor antagonists was measured.

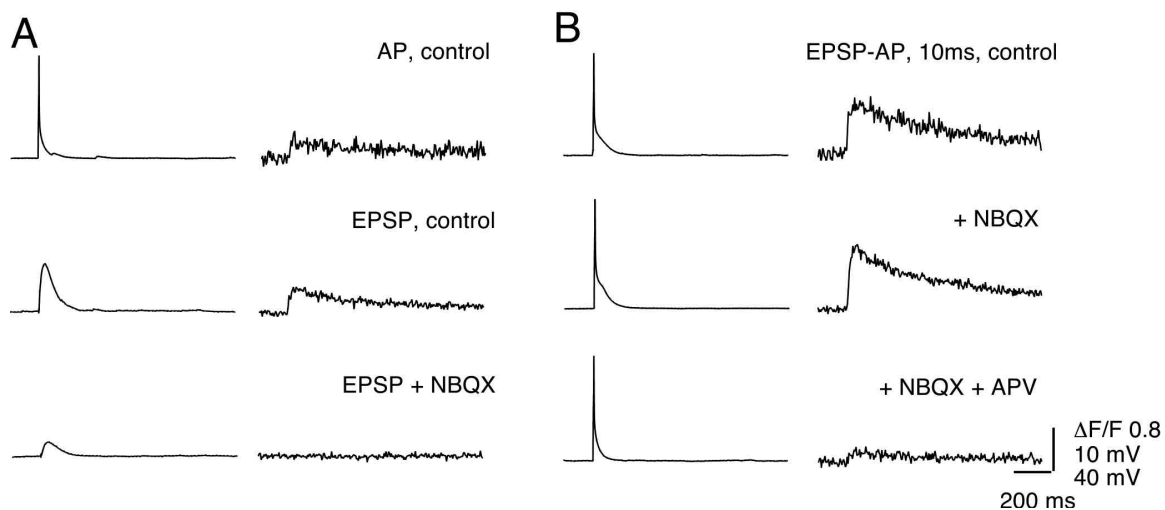


**Figure 4.26** EPSP and bAP timing and pharmacology of  $Ca^{2+}$  transients

**A** Application of  $10 \mu M$  NBQX resulted in abolishing the  $Ca^{2+}$  transient in an active spine.

**B** Pairing an EPSP with an AP at a time interval of 10 ms under these conditions resulted in the full restoration of the  $Ca^{2+}$  transient as compared to control. Addition of APV blocked the supralinear  $Ca^{2+}$  transient down to AP control levels (compare to upper trace in A).

When APV ( $25 \mu M$ ) a blocker of NMDAR channels was added to the bath solution the pairing induced supralinear  $Ca^{2+}$  influx at  $t = 20$  ms was significantly blocked to  $25 \pm 11\%$  ( $n = 3$ ,  $p < 0.05$ ) of control. The size of the remaining  $Ca^{2+}$  transient measured, was not comparable to a  $Ca^{2+}$  transient evoked by a bAP ( $p > 0.2$ ), suggesting that the NMDAR channel indeed was the main source of  $Ca^{2+}$  influx during coincident activity. The peak  $Ca^{2+}$  transient amplitude evoked by the sequence AP-EPSP at 20 ms after bath application of APV was also reduced to the level of the VDCC mediated  $Ca^{2+}$  influx evoked by an AP alone ( $p <$

0.02, Fig 4.28B). Thus by blocking the NMDARs, the supralinear  $\text{Ca}^{2+}$  influx was blocked and the order of EPSP and AP could not be distinguished anymore.

Next, the influence of the AMPAR channel blocker NBQX was tested. Fig 4.26A illustrates the effect of NBQX on spine  $\text{Ca}^{2+}$  transients during coincident activity. Blocking AMPARs reduced the EPSP, leaving a NMDAR mediated component. The  $\text{Ca}^{2+}$  influx was completely blocked in this case (see also Fig 4.16). When however the EPSP was paired with an AP at an inter-stimulus time interval of 10 ms in the presence of NBQX, a supralinear  $\text{Ca}^{2+}$  transient was measured again, which was similar to the transient measured under control conditions ( $A_{\text{max, NBQX}} = 1.1$  vs.  $A_{\text{max, control}} = 0.9$ , Fig 4.26B). Subsequent application of APV abolished the supralinear  $\text{Ca}^{2+}$  influx as expected. The  $\text{Ca}^{2+}$  transient was similar to the bAP evoked  $\text{Ca}^{2+}$  transient (Fig 4.26A, upper trace) again. In  $n = 5$  experiments NBQX had no influence on the peak  $\text{Ca}^{2+}$  transient amplitude evoked by pairing an EPSP and AP at  $t = 10$  ms (reduction, compared to control  $90 \pm 23\%$ ,  $p > 0.1$ ), even though the EPSP evoked  $\text{Ca}^{2+}$  transient was significantly reduced (to  $27 \pm 18\%$  of control,  $p < 0.0001$ ). No significant

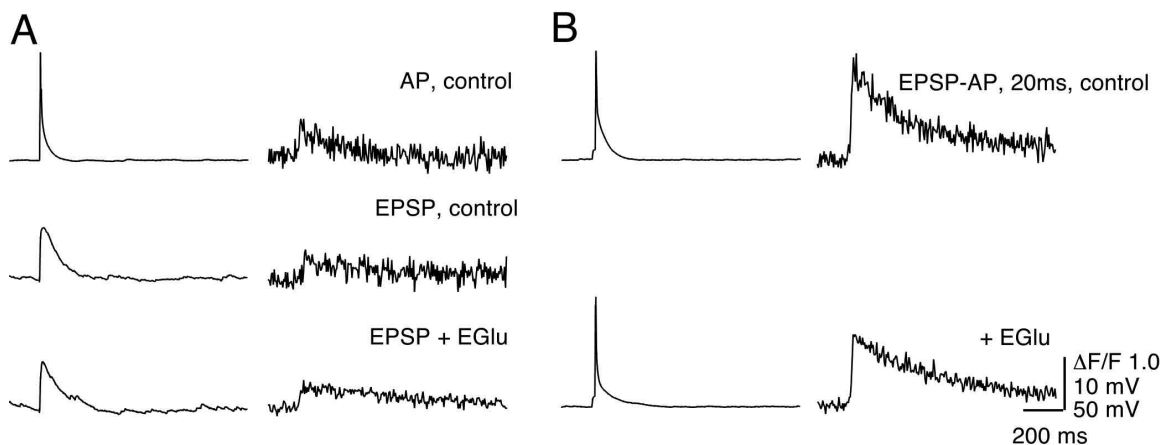


**Figure 4.27 Timing and pharmacology of  $\text{Ca}^{2+}$  influx with EGlu**

*Influence of the specific mGluR group II blocker EGlu ( $50\mu\text{M}$ ) on the  $\text{Ca}^{2+}$  transients evoked by timing of EPSPs and APs.*

**A** Somatic voltage recordings of AP (upper trace) and EPSPs (2nd, 3rd trace) and the corresponding spineous  $\text{Ca}^{2+}$  transients (left) for control conditions and after bath application of EGlu.

**B**  $\text{Ca}^{2+}$  transients for pairing an EPSP with an AP at a time interval of 20 ms for control (upper traces) and after bath application of EGlu (lower traces).

**C** The spine  $\text{Ca}^{2+}$  transient amplitude is on average reduced to  $82 \pm 14\%$  of control (white bar) whereas the somatic EPSP amplitude is not changed ( $92 \pm 18\%$ , black bar).

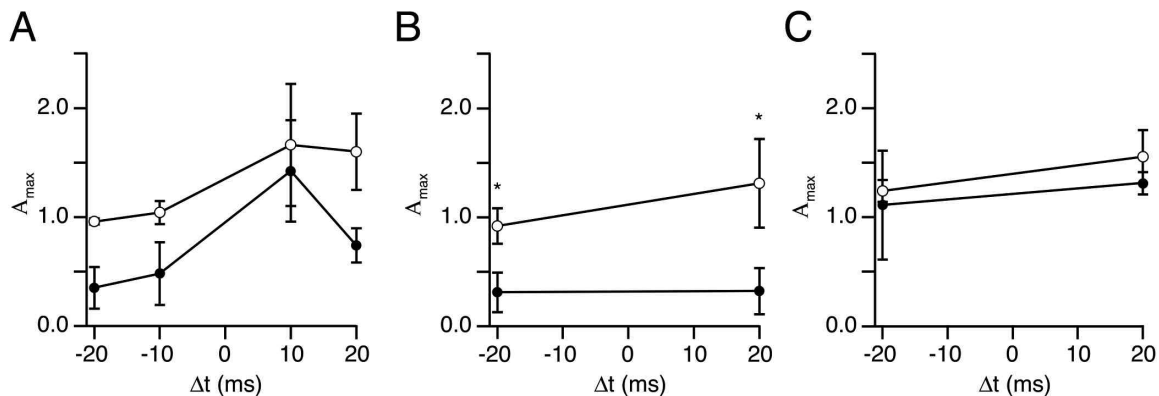


**Figure 4.28 Pharmacology of the supralinear  $Ca^{2+}$  influx**

**A** Absolute  $Ca^{2+}$  transient peak amplitude  $A_{max}$  measured for pairing an EPSP with an AP at time intervals of  $\pm 10$  ms and  $\pm 20$  ms for control conditions (open circles) and after bath application of NBQX (solid circles). There was no significant difference between  $A_{max}$  for control and after blocking AMPARs at a timing intervals of  $\pm 10$  ms. There was also no significant difference found for  $\Delta t = \pm 20$  ms.

**B** Absolute  $Ca^{2+}$  transient peak amplitude measured for pairing an EPSP with an AP at a time interval  $\pm 20$  ms for control conditions (open circles) and after bath application of APV.  $A_{max}$  was significantly reduced in all cases (\*,  $p < 0.05$ ).

**C** Absolute  $Ca^{2+}$  transient peak amplitude measured for pairing an EPSP with an AP at a time interval  $\pm 20$  ms for control conditions (open circles) and after bath application of EGLU. EGLU had no effect on the peak  $Ca^{2+}$  transient amplitude.

reduction in the peak  $Ca^{2+}$  transient amplitude was found for the sequence AP-EPSP at  $t = -10$  ms ( $n = 5$ ,  $p > 0.1$ ). For the inter-stimulus time intervals  $t = \pm 20$  ms the reduction of the peak  $Ca^{2+}$  transient amplitude was also not significant ( $37 \pm 21\%$  of control for  $t = -20$  ms and  $46 \pm 1\%$  for  $t = 20$  ms,  $p > 0.05$ ). This result indicated that the AMPAR had no influence on the supralinear  $Ca^{2+}$  transients during coincident activity.

This appearance of a spine specific  $Ca^{2+}$  influx with stimulus pairing demonstrated that spines with a small or no AMPAR mediated EPSP ('silent synaptic contacts', (Liao 1995)) will mediate a full sized  $Ca^{2+}$  influx when synaptic stimulation is coincident with APs. Such coincident activation dependent  $Ca^{2+}$  influx could be part of a physiologically occurring mechanism of activation of silent synapses (Malinow 2000; Poncer 2001). Hence the  $Ca^{2+}$  transient could initially trigger the modification of already existing AMPARs in the postsynaptic density (PSD) by phosphorylation (Petralia 1999; Shi 1999; Malinow 2000), drive the incorporation of new AMPARs into the spine heads or initiate the aggregation of extrasynaptic AMPARs to the PSD.

Spiny neurons contain group II mGluRs, which are important for synaptic plasticity. The

effect of the specific mGluR II antagonist EGlu (50  $\mu$ M) on the  $\text{Ca}^{2+}$  transients in spines during synaptic stimulation and coincident activity was tested to elucidate if mGluR function in inducing plasticity is directly through shaping the  $\text{Ca}^{2+}$  transients.

The  $\text{Ca}^{2+}$  transient amplitude evoked by synaptic stimulation was not significantly reduced ( $82\pm 14\%$  of control, paired ttest,  $p > 0.2$ ,  $n = 4$ ) after bath application of EGlu (Fig 4.27A, C), neither was the somatically recorded EPSP amplitude reduced ( $92\pm 18\%$  of control,  $p > 0.4$ ).  $\text{Ca}^{2+}$  transients evoked by pairing an EPSP with an AP at  $t = \pm 20$  ms (Fig 4.27B) were also not effected after bath application of EGlu (paired ttest,  $p > 0.05$ ,  $n = 3$ ). These results excluded a direct effect of mGluRs on shaping the  $\text{Ca}^{2+}$  transients within a time window of  $\pm 20$  ms.

The effects of the pharmacological block of the different GluR channels on the supralinear influx of  $\text{Ca}^{2+}$  caused by coincident synaptic stimulation and bAPs are summarized in Fig 4.28. The data points represent the measured peak  $\text{Ca}^{2+}$  transient amplitudes  $A_{\text{max}}$  for control (open circles) and after application of the corresponding GluR channel antagonist. Error bars are SD. Significant reductions were found for the effect of APV (\*,  $p < 0.05$ ), but neither NBQX nor EGlu had a significant effect on the peak  $\text{Ca}^{2+}$  transient amplitude during pairing.

## 4.3 Spike-timing dependent plasticity in spiny stellates

### 4.3.1 Introductory remarks

In connected pairs of spiny stellate neurons only LTD was reported so far (Egger 1999). This form of LTD is dependent on the relative timing of pre- and postsynaptic activity, but it is insensitive to the order of pre- and postsynaptic spikes. It is NMDA and AMPA receptor independent, but requires postsynaptic  $\text{Ca}^{2+}$  influx, presumably through VDCCs. LTD could be blocked by bath application of the selective mGluR group II receptor antagonist EGlu.

The dependence of LTD on  $\text{Ca}^{2+}$  and the hypothesis that spiny neurons in layer 4 of the barrel cortex have a different  $\text{Ca}^{2+}$  dynamics from other excitatory neocortical cell types lead to the extensive study of the  $\text{Ca}^{2+}$  transients in dendrites and spines of these neurons presented in chapter 4.2. The main finding was that the spines of spiny stellate neurons act as sharply tuned coincidence detectors for pre- and postsynaptic activity. They code the relative timing of pre- and postsynaptic spikes and the order of the spikes in the amplitude of the  $\text{Ca}^{2+}$  influx. The sequence of EPSP-AP at a stimulus interval of 10 ms lead to a large, supralinear  $\text{Ca}^{2+}$  influx into the spine, whereas the reversed order AP-EPSP ( $t = -10$  ms) resulted in a linear

summation of the  $\text{Ca}^{2+}$  influx. These two stimulation patterns have been shown to be the basis for spike-timing dependent plasticity (STDP) induction protocols (Markram 1997; Feldman 2000). The pharmacology of the supralinear  $\text{Ca}^{2+}$  transients with respect to the pharmacological signature of the above described form of LTD was investigated, showing strong evidence for an exclusively NMDA receptor dependent coincidence detection mechanism. Neither blocking AMPA receptor function nor mGluR group II function did significantly change the supralinear  $\text{Ca}^{2+}$  influx.

In other cell types, like connected pairs of layer 5 pyramidal neurons, bidirectional spike-timing dependent plasticity was observed, which was NMDA receptor dependent (Markram

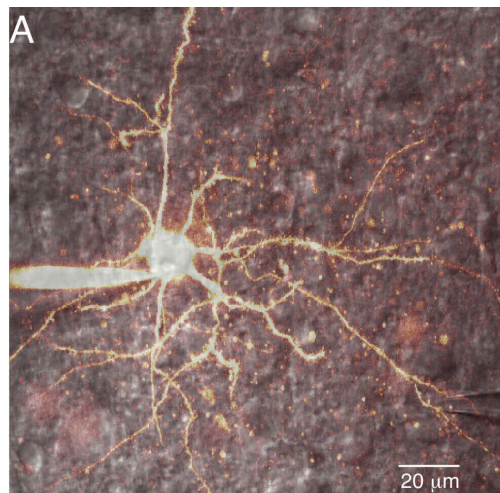


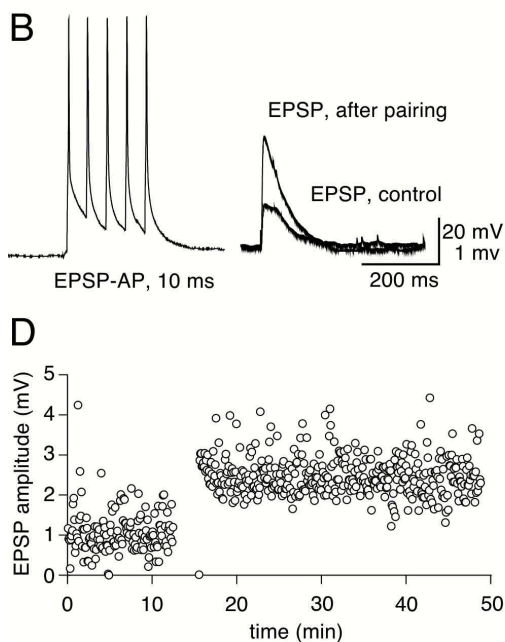
**Figure 4.29 LTP induction in spiny stellate neurons**

**A** Overlay of the IR and fluorescence channels showing the position of the extracellular stimulation pipette (bottom right). The cell was filled with OGB-1 (200  $\mu\text{M}$ ).

**B** Somatic voltage recording during the pairing protocol. LTP was induced by pairing 5 EPSPs with 5 APs at a frequency of 20 Hz and a interstimulus interval of 10 ms. (individual APs in the train followed individual EPSPs by 10 ms). This sequence was repeated 10 times at an intersequence interval of 10 s.

**C** Somatically recorded EPSPs before (control) and after the pairing protocol. The traces are the average of all EPSPs recorded for the corresponding recording periode. The peak EPSP amplitude increased in this case from 1.1 mV to 2.5 mV.

**D** EPSP amplitude vs time recorded from the cell in A. Each circle represents the amplitude of a single EPSP. After recoding control EPSP amplitudes for 12 min the pairing protocol was applied. Subsequent EPSP amplitudes were recorded for 35 min.





1997). It is believed that the LTP induction is due to an increased  $\text{Ca}^{2+}$  influx into spines during the pairing protocol (Bliss 1993). Indeed spines of layer 5 pyramidal neurons show sub- or supralinear  $\text{Ca}^{2+}$  influx depending on the order of pre- and postsynaptic activity (Koester 1998). These observations were similar to the  $\text{Ca}^{2+}$  dynamics in the spines of spiny stellate neurons.

The result that spines of spiny stellate neurons showed basically the same behaviour in terms of their  $\text{Ca}^{2+}$  dynamics as the spines on basal dendrites of pyramidal neurons, which show bidirectional STDP, led to the conclusion that it might be possible to trigger the (presumably) NMDA receptor dependent LTP mechanism also in spiny stellate neurons. The difference in the reported  $\text{Ca}^{2+}$  transients measurements to the LTD experiments performed by Egger et al. were, that in the former case extracellular stimulation was used to excite synaptic contacts, whereas in the latter study connected pairs of spiny stellate neurons were used. Thus STDP experiments in spiny stellate neurons were repeated with extracellular stimulation, but using the same induction protocols (see methods).

It was found that LTP and LTD could be induced in spiny stellate neurons depending on the order of pre- and postsynaptic spikes. This is the first observation of LTP in spiny stellate neurons in acute brain slices of young (P14) rats.

#### 4.1.2 LTP experiments

Spiny stellate neurons were patched and filled with the  $\text{Ca}^{2+}$  indicator OGB-1 (200  $\mu\text{M}$ ) to visualize the morphology and eventual  $\text{Ca}^{2+}$  transients measurements. An extracellular stimulation electrode was placed close to a dendrite as described above. The stimulation strength was adjusted so that EPSPs could reliably be evoked. After recording a stable baseline for at least 10 min the LTP induction protocol was delivered. Trains of 5 EPSPs were paired with trains of 5 APs at a frequency of 20 Hz and an interstimulus interval of 10 ms, i.e. the first AP of the train followed the first EPSP by 10 ms. This sequence was repeated 10 times at an intersequence interval of 10 s. Then the EPSP amplitudes were recorded again for at least 30 min. The EPSP amplitudes, after reaching a constant value 10 min after the induction protocol, were averaged for 20 min and the resulting mean amplitude was compared to the averaged amplitude of the EPSPs before the induction protocol. Fig 4.29 shows one example experiment. In this case the EPSP amplitude increased by 230% from 1.1 mV to 2.5 mV. All cells tested ( $n = 8$ ) showed either a no increase in the EPSP amplitude or a strong potentiation of the EPSP amplitude ranging from 105-230 % of control. The mean increase in these experiments, derived from the average of all cells (Fig 4.31A, red line), was  $146 \pm 7 \%$ , which was significantly different from control (paired ttest,  $p < 0.0001$ ). The results are summarized in Fig 4.32 ( $t = 10$  ms).

### 4.1.3 LTD experiments

LTD experiments were performed in the same way as the LTP experiments, but the induction protocol was changed. Now the first AP of the train preceded the first EPSP in the train by 10 ms. This protocol resulted in a reduction of the EPSP amplitude in the range from 41-95 % of the control values. The mean decrease was  $68 \pm 4 \%$ , which represented a significant reduction of the EPSP amplitude (Fig 4.31B, paired ttest,  $p < 0.0001$ ). The results are compared to the LTP experiments in Fig 4.32 ( $t = -10$  ms).

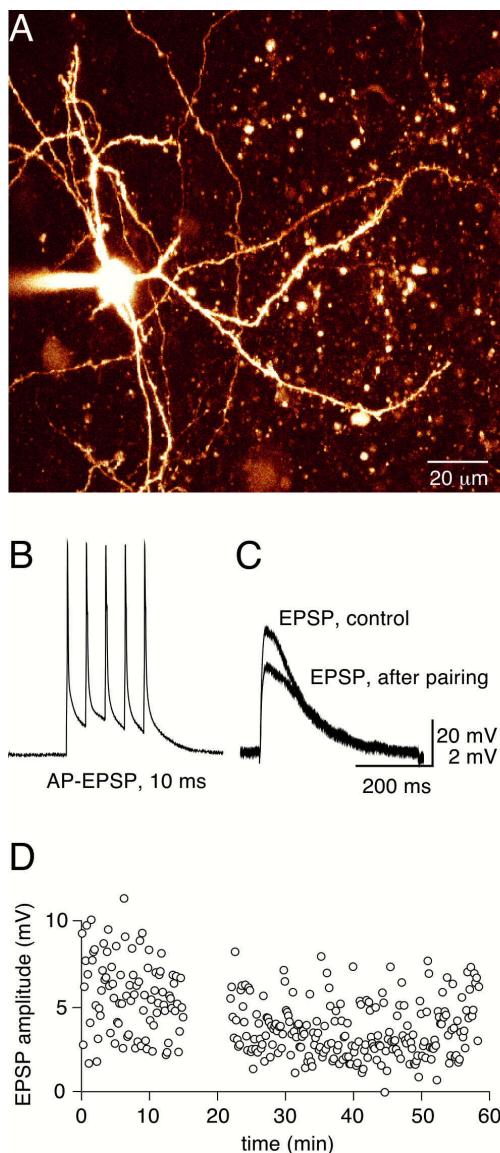


**Figure 4.30** *LTD induction in spiny stellate neurons*

**A** Fluorescence image of a spiny stellate neuron filled with OGB-1 (200  $\mu$ M).

**B** Somatic voltage recording during the pairing protocol. LTD was induced by pairing a train of 5 EPSPs with a train of 5 APs at a frequency of 20 Hz and a interstimulus interval of -10 ms (individual APs in the train preceded individual EPSPs by 10 ms). This sequence was repeated 10 times at an intersequence interval of 10 s.

**C** Somatic recordings of EPSPs before (control) and after the pairing protocol. The traces are the average of all EPSPs recorded for the corresponding recording periods. The peak EPSP amplitude decreased in this case from 5.5 mV to 3.7 mV.

**D** EPSP amplitude vs time recorded from the cell in A. Each circle represents the amplitude of a single EPSP. After recording control EPSP amplitudes for 15 min the pairing protocol was applied. Subsequent EPSP amplitudes were recorded for 40 min.

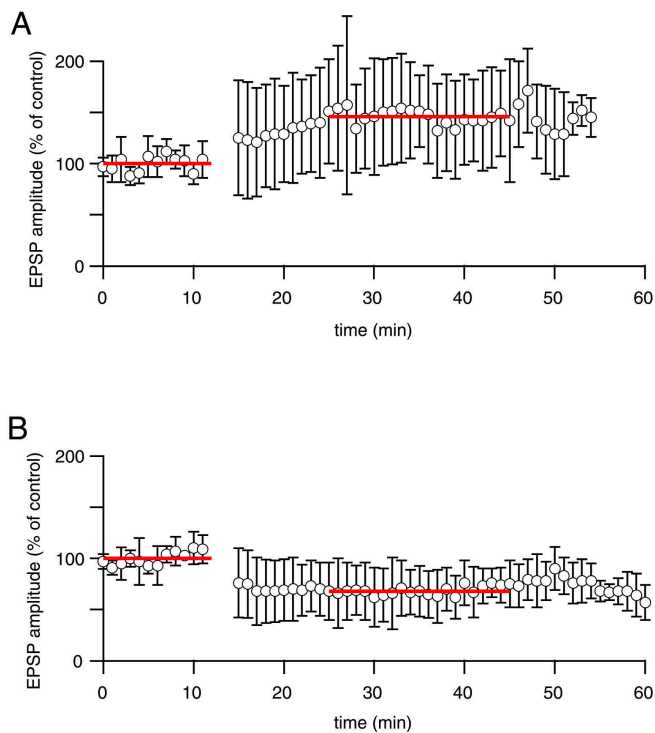


**Figure 4.31 LTP & LTD in spiny neurons**

**A** Average potentiation of EPSP amplitudes in spiny neurons ( $n = 8$ ).

**B** Average depression of EPSP amplitudes in spiny neurons ( $n = 4$ ).

The red lines indicate the time interval, in which EPSP amplitudes were averaged before (for 12 min) and starting 10 min after (for 20 min) plasticity induction.

#### 4.1.4 Conclusion

The experiments show that spiny stellate neurons in the barrel cortex of P14 rats exhibit spike-timing dependent plasticity. The direction of the plasticity is determined by the order of pre- and postsynaptic spikes. Plasticity in either direction could be induced even in the

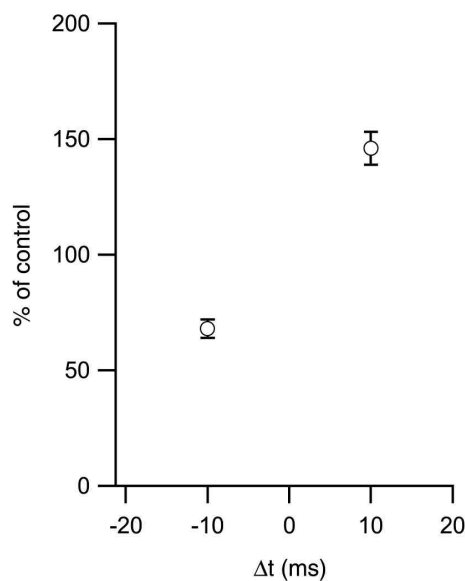


**Figure 4.32 Spike-timing dependent plasticity**

Relative change of the EPSP amplitude after the pairing protocols derived from the pooled experiments (Fig 4.31) plotted against the interstimulus interval  $\Delta t$  between EPSPs and APs. The interstimulus interval  $\Delta t = -10$  ms resulted in reliable LTD with an average decrease of the EPSP amplitude to  $68 \pm 4$  % as compared to control ( $n = 4$ ). The interstimulus interval  $\Delta t = 10$  ms resulted in LTP induction. The EPSP amplitudes were increased to  $146 \pm 7$  % as compared to control ( $n = 8$ ).

## Results

---

presence of 200  $\mu\text{M}$  OGB-1, which acts as a high affinity  $\text{Ca}^{2+}$  buffer. It has been shown that 200  $\mu\text{M}$  of the  $\text{Ca}^{2+}$  chelator BAPTA has no effect on the induction of LTD, whereas higher concentrations ( $> 500 \mu\text{M}$ ) abolished LTD (Egger 1999). The findings presented here are in agreement with this observation and they are of great importance in terms of plasticity induction and simultaneous  $\text{Ca}^{2+}$  transients measurements.

## 5 Discussion

$\text{Ca}^{2+}$  transients in dendrites and spines of spiny neurons in the barrel cortex of young (P13-15) rat were investigated in acute thalamocortical brain slice preparations. The  $\text{Ca}^{2+}$  dynamics corresponding to different patterns of neuronal activity was investigated by combining electrophysiological measurements with two-photon excitation (TPE) fluorescence microscopy. TPE microscopy allowed to image individual spines in the highly scattering environment of brain slices with high spatial resolution, high contrast and good temporal resolution. This made it possible to study synaptic transmission on the single spine level, which is not possible with other imaging techniques.

The advantages of TPE microscopy with respect to functional fluorescence imaging in brain slices will be discussed briefly. Then the new imaging mode of IR scanning gradient contrast (IR-SGC) will be considered. The combination of TPE and IR-SGC imaging enabled to study the spatial profile of synaptically evoked  $\text{Ca}^{2+}$  transients at different positions along the dendritic tree of spiny neurons.

The major findings of the  $\text{Ca}^{2+}$  dynamics in spiny neurons will be discussed and their functional relevance is explained in detail.

### 5.1 Two-photon microscopy for imaging spiny neurons in acute brain slices

Two-photon microscopy (Denk 1990; Denk 1994) has become a valuable tool for neurobiology. Small neuronal structures like dendrites, spines (Denk 1996), axons and boutons (Cox, Denk et al. 2000; Koester 2000) can be imaged with a good signal to noise ratio and a temporal resolution of the order of physiological events (ms). The spines and dendrites of cells labeled with green-fluorescent protein (GFP) can be visualized *in vivo* (Lendvai 2000) and the filling of neurons with ion-sensitive indicator dyes allows the imaging of the  $\text{Ca}^{2+}$  dynamics (Yuste 1995) or  $\text{Na}^+$  dynamics (Rose 1999; Rose 2001) in single neuronal compartments.

Most important for the study of single spines is a high photon collection efficiency. Non-descanned detectors were placed close behind the objective and the condensor. In this way not only ballistic, but more importantly also scattered photons, which were emitted from the

small focal volume can add to the useful information. This allowed to work at low laser powers thus keeping photodamaging effects low (Koester, Baur et al. 1999). The fluorescence light for each pathway was split to allow dual colour detection. The additional block filters and dichroic mirrors had to be carefully selected for best transmission and reflection characteristics.

The optical resolution of a two-photon microscope is not as good as a confocal microscope due to the longer wavelength of the excitation light (Sheppard and Gu 1990). The lateral resolution in the current system was 500 nm and the axial resolution 1.7  $\mu\text{m}$  as measured from sub-resolution (100 nm) beads. Thus single spines, which had an diameter of 1  $\mu\text{m}$  could be resolved. From fluorescence image stacks the morphology of the spines, which showed  $\text{Ca}^{2+}$  transients upon synaptic stimulation could be derived. The length of the spine was defined as the distance from the center of the spine head to the dendritic shaft. A number of spines investigated showed no apparent spine neck and they had a ‘stubby’ spine morphology, which have been described as thickening of the dendritic shaft (Parnass 2000). It might have been that their spine necks were below the resolution limit, missclassifying their morphology. In the case of imaging fast  $\text{Ca}^{2+}$  transients in spines a high spatial resolution is not necessary.

For linescans, one spatial direction is given up for a better temporal resolution.  $\text{Ca}^{2+}$  transients in single spines should be images with a good signal to noise ratio thus the extended focal volume, which was of the order of the volume of a synaptic spine illuminated all fluorophores in its lumen thus given the highest photon yield. This was further augmented by increasing the duty circle, i.e. the time the laser beam scanned the fluorescent structure, by performing linescans at highest digital zoom.

It was routinely possible to image  $\text{Ca}^{2+}$  transients in single synaptic spines repetitively for several seconds (on average 30 seconds) and thus to compare different stimulation patterns and the action of pharmacological substances blocking certain types of  $\text{Ca}^{2+}$  channels on the  $\text{Ca}^{2+}$  transients.

## 5.2 IR-scanning gradient contrast imaging

The fluorescence imaging mode of the two-photon microscope was complemented in this study by the newly developed IR-scanning gradient contrast (IR-SGC) mode. So far fluorescence imaging excluded IR imaging at the same time, making it difficult to correlate the two images. With the new development fluorescence images and IR images could be

overlayed online during an experiment, facilitating the placement of extracellular stimulation electrodes.

The IR excitation light, which was transmitted by the brain slice and collected by the condenser, was spatially filtered and then imaged onto a photomultiplier connected to the electronics of the confocal scanning unit. In this way an image was obtained which was equivalent to the IR-video image. This is not surprising since only the reciprocal light path was used. A further investigation of the image formation in this imaging mode revealed that the annular aperture, which is imaged into the backfocal plane of the condenser acts as a spatial filter for the scattered light at each focal spot. Thus the special spatial frequency filter developed by Dodt is very similar to other spatial frequency filtering methods like reduced-carrier single-sideband microscopy (Bretschneider and Teunis 1994), Hoffman modulation contrast (Hoffman 1975), 'schlieren' contrast, dark-field reflection confocal microscopy (Torok 1995), single sideband edge enhancement (Ellis 1978) and asymmetric illumination contrast (Kachar 1985). This study demonstrated that contrast enhancement by spatial frequency filtering can also be employed in the scanning mode of a laser scanning microscope.

Nevertheless this is the first report of combining a scanning contrast method with two-photon microscopy. IR-SGC has some advantages. It is easily adaptable to any laser-scanning microscope. The fluorescence and IR image are intrinsically parfocal, since the excitation light is the same. Therefore fluorescence images and IR images can be overlaid online, which facilitates the placement of subsequent electrodes. This method is currently used to identify and patch GFP-labeled giant terminals in the calyx of Held (T. Kuner, private communication). Thus it becomes possible to electrophysiologically investigate a certain (fluorescently labeled either by viral transfection or genetical modification) subpopulation of neurons. This is especially useful, since fluorescent markers can be tagged to functionally relevant proteins.

Using the overlay of fluorescence and IR images could also facilitate to patch small neuronal structures like fine dendrites. So far the patching of dendrites has been restricted to relatively large dendrites (Larkum 1999), like apical dendrites of pyramidal neurons. A recent report describes the patching of mossy fiber boutons (Geiger 2000). The overlaid image can be continuously digitally magnified further aiding the targeting of small structures.

It has been shown that the small bead-like structures, which appear in the IR image are very likely single spine heads. Thus IR-SGC can resolve single spines in the unstained tissue. It might be possible to observe spine motility in the unstained brain slice without interfering with the structure at all. No dye has to be loaded into the cell, which could have toxic effects by two-photon photodamage (Koester, Baur et al. 1999). Thus long-term imaging might

become possible. Spine motility and the outgrowth of new spines is thought to be related to plasticity (Engert 1999; Lendvai 2000).

The IR-SGC imaging mode also helped during the newly developed technique of targeted electroporation in brain slices. The success of electroporation could be visualized online. Rapidly after electroporation fluorescence image stacks of cells deep ( $< 150 \mu\text{m}$ ) below the surface of the slice could be acquired to visualize the morphology of spiny neurons with an intact (i.e. uncut) dendritic arbor.

The most important benefit of the IR-SGC imaging mode was, that the online, alignment free overlay of fluorescence and IR-SGC image allowed the precise targeting of the extracellular stimulation pipette to spines at different distances from the soma. Thus it became possible to map the spatial profile of EPSP evoked  $\text{Ca}^{2+}$  transients in spines at different distances from the soma. Furthermore the spatial profile of supralinear  $\text{Ca}^{2+}$  influx in the same spines could be measured. The spatial profile of synaptically evoked  $\text{Ca}^{2+}$  transients was measured in the intact tissue and it complemented measurements of glutamate channel density in excised patched of CA1 pyramidal neurons (Andrasfalvy 2001).

### **5.3 $\text{Ca}^{2+}$ transients in dendrites and spines of spiny neurons**

#### *Spiny stellate neurons and star pyramidal neurons have the same $\text{Ca}^{2+}$ dynamics*

Two populations of neurons were found in layer 4 of the barrel cortex. They were classified, as previously described (Feldmeyer 1999; Luebke, Egger et al. 2000), based on their morphology. The dendritic arbor was readily visible after filling the neurons with the indicator dye. About 80% of the neurons had a spiny stellate-like dendritic arbor. The dendritic tree was strongly asymmetric and confined to the barrel borders. About 20% of the neurons had an apical dendrite without a tuft and symmetrical apical dendrites. Both cell types could not be distinguished based on their electrophysiological parameters. It was found that the  $\text{Ca}^{2+}$  dynamics of these two morphological distinct types of spiny neurons were also not different. The  $\text{Ca}^{2+}$  dynamics is characteristic for different cell types, reflecting  $\text{Ca}^{2+}$  channel properties and  $\text{Ca}^{2+}$  buffering proteins. The results suggest that spiny neurons consist of a homogeneous population of cells in terms of their electrophysiological properties and what has been shown now, their  $\text{Ca}^{2+}$  dynamics. The different morphology might reflect a different position with respect to the barrel borders (Egger 1999).



### ***Back-propagating action potentials***

Spiny cells in layer 4 of the barrel cortex belong to the class of neocortical neurons in which APs, when initiated in the soma-initial-axon region, back-propagate into the dendritic arbor and evoke a transient rise in dendritic  $[Ca^{2+}]$  (Stuart 1993; Spruston 1995). Thus the AP output of spiny barrel neurons in L4, that project their axons predominantly to layer 2/3 (Feldmeyer et al., 2002) is also copied to their dendritic arbor and is encoded as a transient elevation of  $[Ca^{2+}]$  („calcium code“, Johnston 1994). Thus not only pyramidal neurons (Schiller et al., 1998; Köster and Sakmann 2000; Spruston et al. 1996) and inhibitory neurons in neocortical layer 2/3 (Kaiser et al. 2001) which have long, electrically excitable dendritic arbors use this cellular feedback mechanism but also the spiny cells in L4 barrels with their more compact morphology (Egger et al., 1999; Feldmeyer et al., 2002). It seems likely that back-propagation of APs and the concomitant  $[Ca^{2+}]$  transient in the dendrites is a mechanism common to excitatory neurons in the neocortex.

Single AP evoked  $Ca^{2+}$  transients could be detected even in the distal tips of the spiny stellate dendrites. This is different to the long apical dendrite of layer 5 pyramidal neurons, where single APs do not propagate fully. More complex spiking patterns are necessary in L5 pyramids to result in full propagation. Also apical dendrites of pyramidal neurons have a distal initiation zone for regenerative activity. This behaviour has not been observed in spiny neuron dendrites. They seem to be more simple and can better be compared to the basal dendrites of layer 2/3 pyramidal cells (Koester 2000).

Even though it was shown that spiny stellates can sustain AP trains up to 100 Hz and that this frequency is coded in the plateau level of the  $Ca^{2+}$  transient it is not clear if this situation ever occurs *in vivo*. Whole-cell recordings from anesthetized rats show a very low spike count in spiny stellate neurons even with strong principle whisker stimulation (Brecht and Sakmann 2002). It is more likely that single APs or short bursts (of not more than 5 APs) are elicited. These were the stimulation patterns, which were investigated in this study. Single, as well as short bursts of 5 APs resulted in the above described transient increase in  $Ca^{2+}$ , which propagated back into the dendritic tree without any indication of branchpoint failures up to a frequency of 20 Hz (Schiller 1995).

### ***Estimation of absolute $[Ca^{2+}]_i$ levels evoked by single APs***

All peak amplitudes of the  $Ca^{2+}$  transients presented here were given as the maximal relative fluorescence change. OGB-1 is a non-ratiometric dye, making it difficult to derive absolute values for the increase in  $Ca^{2+}$ . Based on a method developed by Maravall et al. (Maravall, Mainen et al. 2000), employing measurements of the maximal fluorescence change at

saturation levels of  $\text{Ca}^{2+}$  and insitu calibration of the dynamic range of OGB-1, resting  $\text{Ca}^{2+}$  levels and absolute  $\text{Ca}^{2+}$  levels were estimated. Resting  $\text{Ca}^{2+}$  levels ( $[\text{Ca}^{2+}]_0$ ) were calculated from

$$\frac{[\text{Ca}^{2+}]_0}{k_D} = \frac{(1 - R_f^{-1})}{\delta f_{\max}} - R_f^{-1}$$

where  $k_D = 206$  nM was the measured dissociation constant of OGB-1,  $R_f = 8.5$  was the dynamic range and  $\delta f_{\max}$  was the actual maximal relative fluorescence change at saturating levels of  $\text{Ca}^{2+}$ . Saturation was reached by a burst of 10 APs at 100 Hz. Changes in absolute  $\text{Ca}^{2+}$  due to single APs were estimated from

$$\frac{[\text{Ca}^{2+}]}{k_D} = (\delta f_{\max} + 1)(1 - R_f^{-1}) \frac{\delta f}{(\delta f_{\max} - \delta f)\delta f_{\max}}$$

where  $\delta f = (F/F)_{\text{AP}}$  was the measured peak amplitude of an AP evoked  $\text{Ca}^{2+}$  transient. Resting  $\text{Ca}^{2+}$  levels were  $[\text{Ca}^{2+}]_0 = 42 \pm 4$  nM, which was similar to the resting levels in CA1 pyramidal neurons (Maravall, Mainen et al. 2000). In the presence of 200  $\mu\text{M}$  OGB-1 the measured peak  $\text{Ca}^{2+}$  transient amplitudes evoked by an AP were estimated to  $[\text{Ca}^{2+}] = 62 \pm 21$  nM ( $n = 4$ ). Assuming a  $\text{Ca}^{2+}$  binding ratio of  $\beta = 20$  (see next paragraph for the details) this corresponded to a peak  $[\text{Ca}^{2+}]$  of 1.2  $\mu\text{M}$  for a single AP. This is in good agreement with estimates for dendrites of CA1 pyramidal neurons (Sabatini, Oertner et al. 2002).

### ***Buffer capacity***

The  $\text{Ca}^{2+}$  binding ratio of spiny stellate spines is comparable, but smaller than that of dendritic spines of L2/3 pyramidal neurons of young rats (Köster and Sakmann 2000) or dendrites of L5 and CA1 pyramids (Helmchen 1996, Helmchen 1997, Maravall 2000). It is also smaller than that in bitufted interneurons (Kaiser et al. 2001). The extrapolated decay time constants of the  $\text{Ca}^{2+}$  transient, expected to determine the decay time course of  $\text{Ca}^{2+}$  transients in naive dendrites (i.e. without added external buffer) are fast ( $\tau = 40$  ms). This could be physiologically relevant during normal whisking behaviour ( $\approx 10$  Hz) of an awake rat. APs evoked at the whisking frequency by sensory stimulation would result in  $[\text{Ca}^{2+}]$  transients in the dendrites that do not merge, but that would decay back to resting  $[\text{Ca}^{2+}]$  levels. This implies that in the time domain each “whisk” is represented as a distinct  $\text{Ca}^{2+}$

transient in the dendritic arbors of barrel cells that relay excitation to L2/3. The measurements of trains of APs at 10 Hz with a low affinity  $\text{Ca}^{2+}$  indicator demonstrated this phenomenon directly. Endogenous buffer capacity and decay time constant measurements performed in spines of spiny neurons yielded the same values suggesting that spines and shafts possess the same endogenous  $\text{Ca}^{2+}$  buffer proteins and  $\text{Ca}^{2+}$  extrusion mechanisms (Neher 1992).

### *Spineous $\text{Ca}^{2+}$ transients*

The  $[\text{Ca}^{2+}]$  transient measured in the presence of a  $\text{Ca}^{2+}$  indicator reflects the global change in  $[\text{Ca}^{2+}]_i$  after fast equilibration of inflowing  $\text{Ca}^{2+}$  with the endo- and exogenous buffers. The size and time course of the measured  $[\text{Ca}^{2+}]$  transient in a spine thus depends on the size of the  $\text{Ca}^{2+}$  influx, the endogenous buffer and extrusion mechanisms.

The NMDAR/AMPA ratio of synaptic contacts in spiny cells is higher than that of synapses on pyramids in L2/3 (Feldmeyer 1999). This difference could account for the larger  $[\text{Ca}^{2+}]$  transient in L4 cells following synaptic stimulation.

The observation that the amplitude of the synaptically evoked  $[\text{Ca}^{2+}]$  transient in a spine and the evoked EPSP are reduced in proportion in different experimental conditions could indicate that the amplitude of  $[\text{Ca}^{2+}]$  transients depends also upon the local dendritic membrane potential. Most likely the synaptic  $\text{Ca}^{2+}$  influx is mediated by NMDAR channels with  $\text{Mg}^{2+}$  acting as the voltage sensor.

No significant increase in the synaptically evoked spine  $\text{Ca}^{2+}$  transient with the distance from the soma was found. Thus no evidence for 'synaptic scaling', assuming the above relation between peak fluorescence amplitude and local depolarization could be found. Synaptic scaling has been proposed as a mechanism to counter the dendritic filtering of the EPSP amplitude for more distal spines (Andrasfalvy 2001).

The large scatter of EPSP evoked peak fluorescence amplitudes might reflect a variable glutamate channel density for different spines (Dodt 1998).

The lack of correlation between the decay time constants of  $\text{Ca}^{2+}$  transients, evoked by bAPs or EPSPs respectively, could indicate that the pathway of the  $\text{Ca}^{2+}$  influx determines, at least partially, the time course of the  $\text{Ca}^{2+}$  transient. When the influx is mediated by VDCC the time course should be determined by the endogenous buffer, the location of VDCC and  $\text{Ca}^{2+}$  pumps (PMCA and SERCA). Synaptically evoked  $\text{Ca}^{2+}$  entry can be reduced, for example, by inactivation of NMDARs (Umekiya 2001) thus resulting in a faster decay because the slow

Ca<sup>2+</sup> influx through NMDARs is blocked. Glutamate can also activate mGluRs which could, in turn, influence intracellular uptake or the extrusion of Ca<sup>2+</sup>.

A classification of the decay time constants according to the morphology of the spine revealed a relation between spine length and the inhomogeneity in decay time constants. Short spines, mainly resembling ‘stubby’ spines, showed a similar decay time constant for AP and EPSP evoked Ca<sup>2+</sup> transients respectively, whereas spines with long necks showed both behaviours: faster decay times for EPSPs or slower decay times for EPSPs. A relationship between the spine length and the decay time constant of EPSP evoked Ca<sup>2+</sup> transients was found, which has not been reported before. Other studies found a relation between the spine length and the AP evoked Ca<sup>2+</sup> transient decay (Majewska 2000). This relationship could not be confirmed for spines in spiny neurons. This could indicate different VDCC and extrusion mechanisms in spines of different cell types. During synaptic stimulation however, the morphology of the spine can determine the shape of the Ca<sup>2+</sup> signals which could influence the temporal summation properties of different spines (Majewska, Tashiro et al. 2000). The Ca<sup>2+</sup> signal of subthreshold synaptic stimulation is mainly restricted to the spinehead with only a very small fraction diffusing into the dendritic shaft (Sabatini, Oertner et al. 2002). Thus synaptic Ca<sup>2+</sup> signaling is highly localized, in contrast to the global Ca<sup>2+</sup> signal evoked by bAPs.

### *Coincidence detection*

Spines of spiny neurons can act, as in other neocortical cells (Denk and Juste, 1996; Koester and Sakmann, 1998; Kaiser et al., 2002), as detectors for coincident pre- and postsynaptic APs. It had been shown that the relative order of pre- and postsynaptic activity can result in sub- or supralinear summation of the Ca<sup>2+</sup> signal. In this study a complete timing curve for pre- and postsynaptic activity was measured. The new finding was that the time-window for supralinear summation was very small (less than 20 ms), precisely tuning the spines to this coincidence interval. The readout of such coincident APs is a supralinear Ca<sup>2+</sup> influx into a spine. Because the decay time constant of the [Ca<sup>2+</sup>] transient is different when the influx is evoked by bAPs or by EPSPs the mechanism underlying supralinear summation could be different from that reported in L5 spines (Koester and Sakmann, 1998). However the pharmacological effects strongly suggest that the major mechanism is a voltage dependent unblocking of NMDARs. Further evidence for an exclusive supralinear amplification of the Ca<sup>2+</sup> signal by NMDARs was the finding that the supralinearity decays with the same time constant as the decay kinetics for the NMDAR. This suggested that the bAP relieved the Mg<sup>2+</sup> block from the population of NMDARs, which were still activated by bound glutamate,

but which were blocked by  $Mg^{2+}$ . AP backpropagation into the dendritic tree broadens the waveform (Stuart 1993; Stuart 1997) and the peak amplitude of depolarization of the spike. This might be exactly matched to maximize  $Ca^{2+}$  influx to the NMDARs since the duration of depolarization at the site of the activated synapse is prolonged and the driving force for  $Ca^{2+}$  influx, even though the membrane is depolarized, is still large. The reduced  $[Ca^{2+}]$  transient could reflect a  $Ca^{2+}$  dependent inactivation of NMDARs via intracellular  $Ca^{2+}$ . Whereas the supralinear influx could act on a  $Ca^{2+}$  sensor in spines to trigger a cascade of events that eventually increases synaptic efficacy the  $Ca^{2+}$  transient evoked by the sequence EPSP followed by AP is more difficult to interpret as spine  $Ca^{2+}$  dynamics can at present only be simulated.

The observation that supralinearity of  $Ca^{2+}$  transients was independent from the distance of the spine from the soma suggested that the coincidence detection mechanism and the coincidence interval is the same for all spines. Thus the supralinear  $Ca^{2+}$  influx is a universal, all-or-none signal for coincident activity.

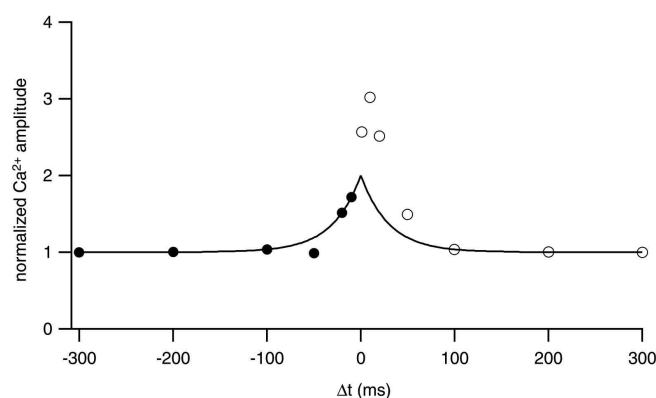


**Figure 5.1 Model calculation for peak  $Ca^{2+}$  transient amplitudes**

The simple model calculates the peak  $Ca^{2+}$  transient amplitudes based on the endogenous transient decay time constant measured ( $\tau = 40$  ms) and the linearity factors derived from the timing curve. Transients were modeled with a single exponential decay.

The solid line gives the linear sum of the two stimuli (amplitudes normalized and taken as equal) at the corresponding inter-stimulus interval. The black circles represent the sequence AP-EPSP. The amplitude of the EPSP is scaled for  $\Delta t = -50$  ms by the sublinearity factor of 0.8. Since no significant difference for  $\Delta t = -100$  ms was found, the linearity factor was taken to be 1. Note the extended flat peak  $Ca^{2+}$  amplitude. The open circles correspond to the sequence EPSP-AP and the measured supralinearity factors of 1.6, 2.3, 2 and 1.3 for  $\Delta t = 1$  ms, 10 ms, 20 ms and 50 ms respectively. In this range a much larger peak  $Ca^{2+}$  transient amplitude was calculated, which was distinct from all other time points.

The functional significance of the sublinear  $Ca^{2+}$  influx can be understood, when the endogenous decay time constant of spiny neurons is considered. At inter-stimulus intervals

larger 50 ms the  $\text{Ca}^{2+}$  transients are well separated and the peak  $\text{Ca}^{2+}$  amplitude is given by the peak  $\text{Ca}^{2+}$  influx of each stimulus alone (no summation of the transients occurs). At  $t = -50$  ms the EPSP evoked  $\text{Ca}^{2+}$  transient contributes only sublinearly, which exactly counters the summation with the AP evoked  $\text{Ca}^{2+}$  transient (the tail of the AP transient would add to the peak of the EPSP transient). This results in the same peak  $\text{Ca}^{2+}$  transient amplitude found for larger inter-stimulus intervals. In this way the linear range of the peak  $\text{Ca}^{2+}$  level is extended to shorter inter-stimulus intervals. This could mark the distinction of  $\text{Ca}^{2+}$  levels, which do not result in long-term depression (LTD) to the levels, which are necessary for LTD induction. Fig 5.1 shows a simple model calculation, based on exponentially decaying  $\text{Ca}^{2+}$  transients with a time constant of 40 ms. The solid line represents the linear summation of the transients (which were taken to have the same peak amplitude). The solid circles represent the peak amplitude measured at the time of the peak of the second stimulus (in this case the peak EPSP amplitude) scaled by the measured non-linearity for the EPSP evoked  $\text{Ca}^{2+}$  influx. The open circles represent the peak  $\text{Ca}^{2+}$  amplitude of the sequence EPSP-AP. In this case the AP amplitude is scaled by the linearity factor  $> 1$ . Note the extended unitary peak  $\text{Ca}^{2+}$  transient amplitude for  $t = -50$  ms, whereas for  $t = -20$  ms already an increased amplitude was calculated. The peak amplitudes for coincident activity  $1 < t < 20$  ms were much larger than for all other time intervals corresponding to a clear-cut time-window for LTP induction. This model suggests that coincident activity (EPSP-AP) can clearly be distinguished from non-coincident activity for  $t > 50$  ms, but it also suggests that ‘reversed’ coincidence (AP-EPSP) can also be distinguished from non-coincident activity for  $t < -50$  ms resulting in three time-domains coded by the  $\text{Ca}^{2+}$  amplitude.

### ***Electrically “silent” synaptic contacts***

When AMPARs were blocked the  $\text{Ca}^{2+}$  influx in individual spines evoked by synaptic stimulation was also blocked, most likely because of the persisting  $\text{Mg}^{2+}$  block of NMDAR channels at membrane potentials below  $-60$  mV. Surprisingly the synaptically evoked spine  $\text{Ca}^{2+}$ -influx reappeared when synaptic stimulation was coincident with a bAP within a time interval  $< 50$  ms. This phenomenon is reminiscent of putative “silent synapses” postulated to exist in connections of the developing postnatal (P6-7) somatosensory cortex (Isaac et al., 1997) and visual cortex (Rumpel et al., 1998). Here a fraction of the synaptic contacts are thought to have mostly NMDAR channels located in their spine heads which remain electrically silent (Isaac et al., 1997). Our experiments with pharmacologically blocked AMPARs in older barrel cortex (P14) suggest that release of glutamate, which by itself

evokes only a negligible depolarization can evoke a local  $\text{Ca}^{2+}$ -influx into individual spines when occurring coincident with a bAP. Such electrically silent synapses are nevertheless communicating via a large  $\text{Ca}^{2+}$  influx when the postsynaptic neuron is generating bAPs. The conversion from electrically “silent” to “functional” would depend critically on the number and frequency of bAPs elicited by a particular sensory stimulus.

In intrabarrel synapses the NMDAR/AMPA ratio is higher than in other cortical connections (Feldmeyer 1999) rendering these connections more sensitive to the EPSP-bAP coincidence mediated  $\text{Ca}^{2+}$  inflow.

The  $\text{Ca}^{2+}$  influx into a spine during an evoked EPSP-AP sequence could modify synaptic efficacy specifically in those contacts that were activated when APs of the presynaptic (VPM) thalamic neuron and bAPs of the postsynaptic spiny stellate neuron occur almost simultaneously. Such a coincidence based mechanism of synaptic  $\text{Ca}^{2+}$  inflow could restrict changes in synaptic efficacy to those specific patterns of APs in the ensemble of thalamocortical afferent fibers that are able to generate a postsynaptic AP.

#### ***Physiological relevance of bAPs and spine $\text{Ca}^{2+}$ transients for L4 cells***

*In vivo* recordings from stellate cells in L4 of the barrel cortex indicate that a compound EPSP with  $>10$  mV depolarization, evoked by a whisker deflection can trigger, within a few ms to tens of ms, a spiny stellate cell AP (Brecht and Sakmann 2002). Following suprathreshold sensory stimulation the evoked EPSP in a spiny stellate neuron is followed by the AP, within the time window reported here to be necessary for a supralinear  $\text{Ca}^{2+}$  influx into specific spines. Does the coincidence of EPSP and the bAP evoked by sensory stimulation attenuate or enhance the efficacy of the thalamo-cortical input or the cortico-cortical connection within a barrel. In spiny cells whisker evoked EPSPs are not very synchronized and the EPSPs from the principle whisker (PW) and surround whiskers (SuW) can be delayed with respect to each other such that the evoked AP can either precede or follow EPSPs. Thus this question could be answered by *in vivo* experiments when a pairing sensory stimulus evoked EPSPs with bAPs generated, for example, by somatic current injection timed precisely to PW or SuW evoked EPSP.

The relatively high, VDCC dependent excitability of stellate dendrites also rises the question whether APs may be initiated first in the dendrites and then forward propagate towards the soma (Larkum, Zhu et al. 2001), for example during intense synaptic stimulation of thalamo-cortical afferents. So far whole-cell recordings from barrel cells *in vivo* gave no indication for the occurrence of  $\text{Ca}^{2+}$  potentials that could be evoked by whisker deflection (Brecht and Sakmann 2002).

### 5.1.1 LTP induction in spiny stellates

Surprisingly it was possible to induce LTP in spiny stellate neurons in layer 4 of the barrel cortex of juvenile rats. Earlier studies reported LTD only in connected pairs of spiny stellate neurons at the same age (Egger 1999). Other studies found LTP only in younger animals before the end of the critical period for barrel formation (Crair 1995).

The difference might be that in this study extracellular stimulation close to a dendrite of a spiny stellate neuron was used. In connected pairs on average only 3 synaptic contacts are found, which are distributed over the dendritic tree. Thus the induction protocol for LTP, which was successful in this study, might lack cooperative activation of adjacent spines. Maybe extracellular stimulus during the induction protocol activated more spines in close vicinity and thus might have triggered a  $\text{Ca}^{2+}$  spike, which would reach the  $\text{Ca}^{2+}$  levels for LTP induction. Further  $\text{Ca}^{2+}$  imaging studies during the induction of LTP have to be performed to answer this question. In this respect it was important that LTP could be induced in the presence of 200  $\mu\text{M}$  OGB-1, which acts as a  $\text{Ca}^{2+}$  buffer and could have prevented the induction.

The study relating LTP to the critical period also used a different stimulation paradigm. In this case thalamocortical afferents were stimulated, which might also only form isolated and distributed contacts on spiny stellate neurons.

In conclusion cooperative activity might result in LTP induction. This would be consistent with a state dependent learning rule, in which increased excitability, e.g. during explorative behaviour, results in strengthening of certain synapses. Additionally this learning rule is spike-timing dependent, because under the same recording conditions, the reversal of the order of pre- and postsynaptic spikes results in the induction of LTD. Spike-timing dependent plasticity can well be modeled based on the experimental results of this study of coincidence detection in single spines (Karmarkar and Buonomano 2002).

Thus from a computational point of view, bidirectional plasticity can shape and fine-tune cortical circuits, whereas LTD-only plasticity would run into a dead end.



## 6 Outlook

This study focused on the  $\text{Ca}^{2+}$  dynamics in dendrites and spines of layer 4 spiny stellate neurons in the juvenile rat barrel cortex. Some new insight into the details of coincidence detection on the level of a single spine has been gained. Some first experiments showed that spiny stellate neurons exhibit spike-timing dependent plasticity. The next step is to combine  $\text{Ca}^{2+}$  transients measurements on the single spine level before, during and after induction of LTP and LTD. These experiments might elucidate further the relationship between the coincidence detection mechanism described in this study and the magnitude and direction of plasticity. The frame scanning mode of the resonant scanner might help to image the  $\text{Ca}^{2+}$  dynamics in this case in an extended field of view answering the question of cooperative synaptic activation during the burst of presynaptic activity. These experiments might also give direct optical evidence of changes in the molecular composition of the spine head membrane. Inclusion of new receptors after LTP induction might change the  $\text{Ca}^{2+}$  transients after pairing.

The finding that spines without functional AMPARs (, because they were blocked by NBQX) can elicit large  $\text{Ca}^{2+}$  transients during coincident activity, i.e. pairing an EPSP with a bAP at 10 ms might help to detect these hypothesized ‘silent synapses’ in an acute brain slice. Then it would be possible to optically investigate the properties of these synapses.

In the future, simultaneous pre- and postsynaptic  $\text{Ca}^{2+}$  transients will be performed. It will then be possible to do detailed quantal analysis studies on single synaptic contacts.

In order to reliably find contacts in synaptically coupled pairs of neurons novel searching algorithms have to be employed, because following the axon by manually is slow and the multiple branching collaterals make the number of branches to follow very large. A first automated search procedure based on the xyz-scan and the supralinear  $\text{Ca}^{2+}$  influx during coincident activity has been developed and tested in a few cases. In the future this method should be applied to connected pairs of cells and it is predicted that it greatly increases the success rate of finding a synaptic contact during the lifetime of the cells.

Furthermore the improvement on the scanner speed will increase the time resolution of image acquisition in the full frame mode. So far the slow axis of the scanner has to be reset to its initial position before a new frame can be acquired. This slows the frame rate approximately by a factor of 3. A bidirectional scanning mode comparable to the bidirectional scanning of

the fast scanning mirror would double the frame rate, giving an upper frame rate of about 100 Hz for an image format of 512 by 32 lines.

New  $\text{Ca}^{2+}$  indicators with largely improved two-photon cross-sections will increase the yield of fluorescence photons thus allowing to reduce the laser power to reduce the phototoxic stress. This will allow to record from a single synaptic contact for a prolonged period of time. Furthermore the variety of available  $\text{Ca}^{2+}$  indicators with respect to its dissociation constant, emission spectra and dynamic range will be increased in the future to make it easier to separate the emission spectra from multiple dye experiments. Genetically encoded indicators based on GFP (chameleons) will be an invaluable tool.

Until then, spectral unmixing, which can separate two dyes according to their spectral properties might help to separate two partly overlapping  $\text{Ca}^{2+}$  dyes. It will be a very useful tool for the simultaneous measurements of the  $\text{Ca}^{2+}$  dynamics in different cells without the restriction of the pair of dyes, which can be separated by optical filters.

Two-photon microscopy has recently been shown to be very useful for *in vivo* studies. The advantages of deep tissue penetration and intrinsic optical sectioning and non-descanned detection allow imaging in the intact cortex down to 500-700  $\mu\text{m}$ . Combined with *in vivo* patch clamp the electrical activity of cells can be correlated to the corresponding  $\text{Ca}^{2+}$  transients. The novel method to fill neurons with  $\text{Ca}^{2+}$  indicators by electroporation will be also very useful for *in vivo* studies. A number of cells can be filled sequentially within a few minutes and the  $\text{Ca}^{2+}$  transients in these cells during activity of the cortex can be observed. This will also be feasible in the awake, freely moving animal, because a small, head mounted two-photon scanning device has been developed recently.

The data presented in this study was exclusively obtained from wild-type animals. Genetically modified mice have been designed, which show mutations in a variety of glutamate receptor channels with more or less severe phenotypes.  $\text{Ca}^{2+}$  imaging with two-photon microscopy on the single spine level of these mutant mice can help to understand normal and pathological synaptic functioning in more detail and reveal the exact functioning of the 'universal' second messenger  $\text{Ca}^{2+}$ .

## 6.1 Acknowledgements

Prof. Dr. B. Sakmann

for this wonderful project and being a continuous source of ideas

Prof. Dr. Dr. C. Cremer

for physical guidance in a physiological world

Dr. H. Köster & Dr. V. Egger

for introducing me to two-photon and spiny neurons respectively

Mrs. Kaiser

for excellent technical assistance

Mr. Schmidt, Mr. Lukat, Mr. Maier and Mr. Müller

for all the drilled holes and metal work

Mr. Rödel, Mr. Tritthardt and Mr. Bauer

for cables and more sophisticated electronics including computers

Dr. H. Spors, Dr. D. Waters, Dr. D. Feldmeier, Dipl. Phys. M. Schneider and Dr. I. Manns

for critical reading of the manuscript

Dr. C. Petersen, Dr. N. Urban, Dr. T. Margrie, Dr. J. Bollmann, Dr. M. Brecht, Dr. M. Larkum, Dipl. Phys. A. Roth, Dr. F. Helmchen and Dr. K. Kaiser

for a lot of fruitful discussions

my parents, my sister and Natalie

for continuous support during all times



## 7 References

- Aakalu, G. S., W. B. Nguyen, N. Jiang, C. Schuman, E. M. 2001. Dynamic visualization of local protein synthesis in hippocampal neurons. *Neuron*. 30:489-502
- Abbott, L. F. N., S. B. 2000. Synaptic plasticity: taming the beast. [Review] [49 refs]. *Nature Neuroscience*. 3 Suppl:1178-1183.
- Abraham, W. C., B. Logan, J. M. Greenwood, and M. Dragunow. 2002. Induction and experience-dependent consolidation of stable long-term potentiation lasting months in the hippocampus. *Journal of Neuroscience*. 22:9626-9634.
- Agmon, A. C., B. W. 1991. Thalamocortical responses of mouse somatosensory (barrel) cortex in vitro. *Neuroscience*. 41:365-379.
- Albota, M. B., D. Bredas, J. L. Ehrlich, J. E. Fu, J. Y. Heikal, A. A. Hess, S. E. Kogej, T. Levin, M. D. Marder, S. R. McCord-Maughon, D. Perry, J. W. Rockel, H. Rumi, M. Subramaniam, G. Webb, W. W. Wu, X. L. Xu, C. 1998. Design of organic molecules with large two-photon absorption cross sections. *Science*. 281:1653-1656.
- Andrasfalvy, B. K. M., J. C. 2001. Distance-dependent increase in AMPA receptor number in the dendrites of adult hippocampal CA1 pyramidal neurons. *Journal of Neuroscience*. 21:9151-9159.
- Antic, S., G. Major, and D. Zecevic. 1999. Fast optical recordings of membrane potential changes from dendrites of pyramidal neurons. *Journal of Neurophysiology*. 82:1615-1621.
- Anwyl, R. 1999. Metabotropic glutamate receptors: electrophysiological properties and role in plasticity [Review]. *Brain Research Reviews*. 29:83-120.
- Ashkin, A. 1992. Forces of a single-beam gradient laser trap on a dielectric sphere in the ray optics regime. *Biophysical Journal*. 61:569-582.
- Augustine, G. J. 1994. Combining patch-clamp and optical methods in brain slices. [Review] [12 refs]. *Journal of Neuroscience Methods*. 54:163-169.
- Barth, A. L. M., R. C. 2001. NMDAR EPSC kinetics do not regulate the critical period for LTP at thalamocortical synapses. *Nature Neuroscience*. 4:235-236.
- Bayer, K. U. D. K., P. Leonard, A. S. Hel, J. W. Schulman, H. 2001. Interaction with the NMDA receptor locks CaMKII in an active conformation. *Nature*. 411:801-805.
- Beaurepaire, E., M. Oheim, and J. Mertz. 2001. Ultra-deep two-photon fluorescence

- excitation in turbid media. *Optics Communications*. 188:25-29.
- Bekkers, J. M. 1994. Quantal analysis of synaptic transmission in the central nervous system. [Review] [42 refs]. *Current Opinion in Neurobiology*. 4:360-365.
- Bekkers, J. M. S., C. F. 1996. Cable properties of cultured hippocampal neurons determined from sucrose-evoked miniature EPSCs. *Journal of Neurophysiology*. 75:1250-1255.
- Bennett, M. V. L. 1997. GAP JUNCTIONS AS ELECTRICAL SYNAPSES [Review]. *Journal of Neurocytology*. 26:349-366.
- Berman, D. E. D., Y. 2001. Memory extinction, learning anew, and learning the new: dissociations in the molecular machinery of learning in cortex. *Science*. 291:2417-2419.
- Berridge, M. J. 1998. Neuronal calcium signaling. *Neuron*. 21:13-26.
- Betz, W. J. 1970. Depression of transmitter release at the neuromuscular junction of the frog. *Journal of Physiology*. 206:629-644.
- Bi, G. Q. P., M. M. 1998. Synaptic modifications in cultured hippocampal neurons: dependence on spike timing, synaptic strength, and postsynaptic cell type. *Journal of Neuroscience*. 18:10464-10472.
- Bliss, T. V. C., G. L. 1993. A synaptic model of memory: long-term potentiation in the hippocampus. [Review] [174 refs]. *Nature*. 361:31-39.
- Bliss, T. V. L., T. 1970. Plasticity in a monosynaptic cortical pathway. *Journal of Physiology*. 207:61P.
- Bortolotto, Z. A., S. M. Fitzjohn, and G. L. Collingridge. 1999. Roles of metabotropic glutamate receptors in LTP and LTD in the hippocampus. *Current Opinion in Neurobiology*. 9:299-304.
- Braeutigam, S. B., A. J. Swithenby, S. J. 2001. Phase-locked gamma band responses to semantic violation stimuli. *Cognitive Brain Research*. 10:365-377.
- Brakenhoff, G. J., M. Muller, and J. Squier. 1995. Femtosecond Pulse Width Control in Microscopy By Two-Photon Absorption Autocorrelation. *Journal of Microscopy*. 179:253-260.
- Brecht, M., and B. Sakmann. 2002a. Dynamic representation of whisker deflection by synaptic potentials in spiny stellate and pyramidal cells in the barrels and septa of layer 4 rat somatosensory cortex. *Journal of Physiology-London*. 543:49-70.
- Brecht, M., and B. Sakmann. 2002b. Whisker maps of neuronal subclasses of the rat ventral posterior medial thalamus, identified by whole-cell voltage recording and morphological reconstruction. *Journal of Physiology-London*. 538:495-515.
- Brenner, H. R. S., B. 1978. Gating properties of acetylcholine receptor in newly formed

- neuromuscular synapses. *Nature*. 271:366-368.
- Bretschneider, F., and P. F. M. Teunis. 1994. Reduced-carrier single-sideband microscopy: a powerful method for the observation of transparent microscopical objects. *Journal of Microscopy*. 175:121-134.
- Cajal, S. R. Y. 1894. La Fine Structure des Centres Nerveux. *Proceedings of the Royal Society of London*. 55:444-468.
- Canatella, P. J., J. F. Karr, J. A. Petros, and M. R. Prausnitz. 2001. Quantitative study of electroporation-mediated molecular uptake and cell viability. *Biophysical Journal*. 80:755-764.
- Castillo, J., and B. Katz. 1954. Quantal components of the end-plate potential. *Journal of Physiology*. 124:560-573.
- Chalfie, M. T., Y. Euskirchen, G. Ward, W. W. Prasher, D. C. 1994. Green fluorescent protein as a marker for gene expression. *Science*. 263:802-805.
- Charpak, S. M., J. Beaupaire, E. Moreaux, L. Delaney, K. 2001. Odor-evoked calcium signals in dendrites of rat mitral cells. *Proceedings of the National Academy of Sciences of the United States of America*. 98:1230-1234.
- Cogswell, C. J., and J. R. Sheppard. 1992. Confocal differential interference contrast (DIC) microscopy: including a theoretical analysis of conventional DIC imaging. *Journal of Microscopy*. 165:81-101.
- Cormier, R. J. G., A. C. Connor, J. A. 2001. Bidirectional synaptic plasticity correlated with the magnitude of dendritic calcium transients above a threshold. *Journal of Neurophysiology*. 85:399-406.
- Cox, C. L., W. Denk, D. W. Tank, and K. Svoboda. 2000. Action potentials reliably invade axonal arbors of rat neocortical neurons. *Proceedings of the National Academy of Sciences of the United States of America*. 97:9724-9728.
- Crair, M. C. M., R. C. 1995. A critical period for long-term potentiation at thalamocortical synapses. *Nature*. 375:325-328.
- Debanne, D. G., B. H. Thompson, S. M. 1998. Long-term synaptic plasticity between pairs of individual CA3 pyramidal cells in rat hippocampal slice cultures. *Journal of Physiology*. 507:237-247.
- DeBruin, K. A., and W. Krassowska. 1999a. Modeling electroporation in a single cell. I. Effects of field strength and rest potential. *Biophysical Journal*. 77:1213-1224.
- DeBruin, K. A., and W. Krassowska. 1999b. Modeling electroporation in a single cell. II. Effects of ionic concentrations. *Biophysical Journal*. 77:1225-1233.
- Denk, W. 1997a. Multiphoton Microscopy - Imaging With Nonlinear Optics. *Photonics*

*Spectra*. 31:125 ff.

Denk, W., D. W. Piston, and W. W. Webb. 1995. Two-photon excitation in laser-scanning microscopy. *In Handbook of Biological Confocal Microscopy*. J. B. Pawley, editor. Plenum Press, New York. 445-458.

Denk, W. D., K. R. Gelperin, A. Kleinfeld, D. Strowbridge, B. W. Tank, D. W. Yuste, R. 1994. Anatomical and functional imaging of neurons using 2-photon laser scanning microscopy. [Review] [35 refs]. *Journal of Neuroscience Methods*. 54:151-162.

Denk, W. S., J. H. Webb, W. W. 1990. Two-photon laser scanning fluorescence microscopy. *Science*. 248:73-76.

Denk, W. S., K. 1997b. Photon upmanship: why multiphoton imaging is more than a gimmick. [Review] [39 refs]. *Neuron*. 18:351-357.

Denk, W. Y., R. Svoboda, K. Tank, D. W. 1996. Imaging calcium dynamics in dendritic spines. *Current Opinion in Neurobiology*. 6:372-378.

Deschenes, M., P. Veinante, and Z. W. Zhang. 1998. The organization of corticothalamic projections: reciprocity versus parity [Review]. *Brain Research Reviews*. 28:286-308.

Diels, J. M., J. J. Fontaine, I. C. McMichael, and F. Simoni. 1985. Control and measurement of ultrashort pulse shapes (in amplitude and phase) with femtosecond accuracy. *Applied Optics*. 24:1270-1282.

Dodt, H. E., M. Frick, A. Zieglgansberger, W. 1999. Precisely localized LTD in the neocortex revealed by infrared-guided laser stimulation. [erratum appears in Science 1999 Dec 17;286(5448):2273.]. *Science*. 286:110-113.

Dodt, H. U. 2000. Kontrastvorrichtung für Mikroskope, Germany.

Dodt, H. U. F., A. Kampe, K. Zieglgansberger, W. 1998a. NMDA and AMPA receptors on neocortical neurons are differentially distributed. *European Journal of Neuroscience*. 10:3351-3357.

Dodt, H. U. Z., W. 1990. Visualizing unstained neurons in living brain slices by infrared DIC-videomicroscopy. *Brain Research*. 537:333-336.

Dodt, H. U. Z., W. 1998b. Visualization of neuronal form and function in brain slices by infrared videomicroscopy. [Review] [45 refs]. *Histochemical Journal*. 30:141-152.

Dudai, Y. 2002. Molecular bases of long-term memories: a question of persistence. [Review] [61 refs]. *Current Opinion in Neurobiology*. 12:211-216.

Dunaevsky, A. B., R. Yuste, R. Mason, C. 2001. Spine motility with synaptic contact. *Nature Neuroscience*. 4:685-686.

Ebner, F. F. A.-J., M. A. 1990. Intracortical processes regulating the integration of



- sensory information. [Review] [46 refs]. *Progress in Brain Research*. 86:129-141.
- Egger, V. 1999a. The synapse between spiny neurons in layer 4 in rat somatosensory 'barrel' cortex: Properties and long-term plasticity. University of Heidelberg, Heidelberg.
- Egger, V. F., D. Sakmann, B. 1999b. Coincidence detection and changes of synaptic efficacy in spiny stellate neurons in rat barrel cortex. *Nature Neuroscience*. 2:1098-1105.
- Eilers, J. A., G. J. Konnerth, A. 1995. Subthreshold synaptic Ca<sup>2+</sup> signalling in fine dendrites and spines of cerebellar Purkinje neurons. *Nature*. 373:155-158.
- Ellis, G. W. 1978. Advances in visualization of mitosis in vivo. Academic Press, New York.
- Emmanouilidou, E. T., A. G. Pouli, A. E. Nicholls, L. I. Seward, E. P. Rutter, G. A. 1999. Imaging Ca<sup>2+</sup> concentration changes at the secretory vesicle surface with a recombinant targeted cameleon. *Current Biology*. 9:915-918.
- Emptage, N. B., T. V. Fine, A. 1999. Single synaptic events evoke NMDA receptor-mediated release of calcium from internal stores in hippocampal dendritic spines. *Neuron*. 22:115-124.
- Engert, F. B., T. 1999. Dendritic spine changes associated with hippocampal long-term synaptic plasticity. [see comments.]. Comment in: *Nature*. 1999 May 6;399(6731):19-21 ; 10331383. *Nature*. 399:66-70.
- Engert, F. T., H. W. Zhang, L. I. Poo, M. M. 2002. Moving visual stimuli rapidly induce direction sensitivity of developing tectal neurons. *Nature*. 419:470-475.
- Euler, T., and W. Denk. 2001. Dendritic processing [Review]. *Current Opinion in Neurobiology*. 11:415-422.
- Feldman, D. E. 2000. Timing-based LTP and LTD at vertical inputs to layer II/III pyramidal cells in rat barrel cortex. *Neuron*. 27:45-56.
- Feldman, D. E. N., R. A. Malenka, R. C. Isaac, J. T. 1998. Long-term depression at thalamocortical synapses in developing rat somatosensory cortex. *Neuron*. 21:347-357.
- Feldmeyer, D. E., V. Lubke, J. Sakmann, B. 1999. Reliable synaptic connections between pairs of excitatory layer 4 neurones within a single 'barrel' of developing rat somatosensory cortex. *Journal of Physiology*. 521 Pt 1:169-190.
- Feldmeyer, D. S., B. 2000. Synaptic efficacy and reliability of excitatory connections between the principal neurones of the input (layer 4) and output layer (layer 5) of the neocortex. [Review] [35 refs]. *Journal of Physiology*. 525 Pt 1:31-39.
- Fields, R. D., and B. Stevens-Graham. 2002. Neuroscience - New insights into neuron-glia communication [Review]. *Science*. 298:556-562.

- Finch, E. A. A., G. J. 1998. Local calcium signalling by inositol-1,4,5-trisphosphate in Purkinje cell dendrites. *Nature*. 396:753-756.
- Fox, K. G., S. Schulze, S. 2000. Plasticity and stability of somatosensory maps in thalamus and cortex. [Review] [21 refs]. *Current Opinion in Neurobiology*. 10:494-497.
- Frankland, P. W. O. B., C. Ohno, M. Kirkwood, A. Silva, A. J. 2001. Alpha-CaMKII-dependent plasticity in the cortex is required for permanent memory. *Nature*. 411:309-313.
- Froemke, R. C. D., Y. 2002. Spike-timing-dependent synaptic modification induced by natural spike trains. *Nature*. 416:433-438.
- Gan, W. B. G., J. Wong, W. T. Wong, R. O. Lichtman, J. W. 2000. Multicolor "DiOlistic" labeling of the nervous system using lipophilic dye combinations. *Neuron*. 27:219-225.
- Gehl, J., and L. M. Mir. 1999. Determination of optimal parameters for in vivo gene transfer by electroporation, using a rapid in vivo test for cell permeabilization. *Biochemical & Biophysical Research Communications*. 261:377-380.
- Geiger, J. R. J., P. 2000. Dynamic control of presynaptic Ca(2+) inflow by fast-inactivating K(+) channels in hippocampal mossy fiber boutons. *Neuron*. 28:927-939.
- Ghosh, A. G., M. E. 1995. Calcium signaling in neurons: molecular mechanisms and cellular consequences. [Review] [66 refs]. *Science*. 268:239-247.
- Gil, Z. C., B. W. Amitai, Y. 1997. Differential regulation of neocortical synapses by neuromodulators and activity. *Neuron*. 19:679-686.
- Gil, Z. C., B. W. Amitai, Y. 1999. Efficacy of thalamocortical and intracortical synaptic connections: quanta, innervation, and reliability. [see comments.]. Comment in: *Neuron*. 1999 Jun;23(2):198-200 ; 10399925. *Neuron*. 23:385-397.
- Golzio, M., J. Teissie, and M. P. Rols. 2002. Direct visualization at the single-cell level of electrically mediated gene delivery. *Proceedings of the National Academy of Sciences of the United States of America*. 99:1292-1297.
- Gomperts, S. N. R., A. Craig, A. M. Malenka, R. C. Nicoll, R. A. 1998. Postsynaptically silent synapses in single neuron cultures. [see comments.]. Comment in: *Neuron*. 1998 Dec;21(6):1226-7 ; 9883714. *Neuron*. 21:1443-1451.
- Göppert-Mayer, M. 1931. Über Elementarakte mit zwei Quantensprüngen. *Annalen der Physik*. 9:273.
- Grynkiewicz, G. P., M. Tsien, R. Y. 1985. A new generation of Ca<sup>2+</sup> indicators with greatly improved fluorescence properties. *Journal of Biological Chemistry*. 260:3440-3450.

- Gu, M., X. S. Gan, A. Kisteman, and M. G. Xu. 2000. Comparison of penetration depth between two-photon excitation and single-photon excitation in imaging through turbid tissue media. *Applied Physics Letters*. 77:1551-1553.
- Gu, M., and C. J. R. Sheppard. 1995. Comparison of Three-Dimensional Imaging Properties Between Two-Photon and Single-Photon Fluorescence Microscopy. *Journal of Microscopy*. 177:128-137.
- Guild, J. B., C. Xu, and W. W. Webb. 1997. Measurement of Group Delay Dispersion of High Numerical Aperture Objective Lenses Using Two-Photon Excited Fluorescence. *Applied Optics*. 36:397-401.
- Haas, K. S., W. C. Javaherian, A. Li, Z. Cline, H. T. 2001. Single-cell electroporation for gene transfer in vivo. *Neuron*. 29:583-591.
- Hamill, O. P. M., A. Neher, E. Sakmann, B. Sigworth, F. J. 1981. Improved patch-clamp techniques for high-resolution current recording from cells and cell-free membrane patches. *Pflugers Archiv - European Journal of Physiology*. 391:85-100.
- Han, V. Z. G., K. Bell, C. C. 2000. Reversible associative depression and nonassociative potentiation at a parallel fiber synapse. *Neuron*. 27:611-622.
- Hasselmo, M. E. B., J. M. 1993. Acetylcholine and memory. [Review] [50 refs]. *Trends in Neurosciences*. 16:218-222.
- Hausser, M. 2001a. Synaptic function: dendritic democracy. [Review] [10 refs]. *Current Biology*. 11:R10-12.
- Hausser, M. M., G. Stuart, G. J. 2001b. Differential shunting of EPSPs by action potentials. *Science*. 291:138-141.
- Hayashi, Y., S. H. Shi, J. A. Esteban, A. Piccini, J. C. Poncer, and R. Malinow. 2000. Driving AMPA receptors into synapses by LTP and CaMKII: Requirement for GluR1 and PDZ domain interaction. *Science*. 287:2262-2267.
- Helmchen, F. B., J. G. Sakmann, B. 1997. Calcium dynamics associated with a single action potential in a CNS presynaptic terminal. *Biophysical Journal*. 72:1458-1471.
- Helmchen, F. I., K. Sakmann, B. 1996. Ca<sup>2+</sup> buffering and action potential-evoked Ca<sup>2+</sup> signaling in dendrites of pyramidal neurons. *Biophysical Journal*. 70:1069-1081.
- Helmchen, F. S., K. Denk, W. Tank, D. W. 1999. In vivo dendritic calcium dynamics in deep-layer cortical pyramidal neurons. *Nature Neuroscience*. 2:989-996.
- Hodgkin, A. L., and A. F. Huxley. 1952. A quantitative description of membrane current and its application to conduction and excitation in nerve. *Journal of Physiology*. 116:500-544.
- Hoffman, R. G., L. 1975. The modulation contrast microscope. *Nature*. 254:586-588.

- Holthoff, K., D. Tsay, and R. Yuste. 2002. Calcium dynamics of spines depend on their dendritic location. *Neuron*. 33:425-437.
- Huber, K. M., M. S. Kayser, and M. F. Bear. 2000. Role for rapid dendritic protein synthesis in hippocampal mGluR-dependent long-term depression. *Science*. 288:1254-1256.
- Hudmon, A., and H. Schulman. 2002. Neuronal Ca<sup>2+</sup>/calmodulin-dependent protein kinase II: The role of structure and autoregulation in cellular function [Review]. *Annual Review of Biochemistry*. 71:473-510.
- Husi, H. W., M. A. Choudhary, J. S. Blackstock, W. P. Grant, S. G. 2000. Proteomic analysis of NMDA receptor-adhesion protein signaling complexes. [see comments.]. Comment in: *Nat Neurosci*. 2000 Jul;3(7):633-5 ; 10862688. *Nature Neuroscience*. 3:661-669.
- Inoue, S. 1986. Video Microscopy. Plenum Press, New York.
- Inoue, T., and R. Krumlauf. 2001. An impulse to the brain - using in vivo electroporation. *Nature Neuroscience*. 4:1156-1158.
- Isaac, J. T. N., R. A. Malenka, R. C. 1995. Evidence for silent synapses: implications for the expression of LTP. *Neuron*. 15:427-434.
- Johnson, J. W. A., P. 1987. Glycine potentiates the NMDA response in cultured mouse brain neurons. *Nature*. 325:529-531.
- Johnston, D. H., D. A. Colbert, C. M. Magee, J. C. 1999. Regulation of back-propagating action potentials in hippocampal neurons. [Review] [34 refs]. *Current Opinion in Neurobiology*. 9:288-292.
- Kachar, B. 1985. Asymmetric illumination contrast: a method of image formation for video light microscopy. *Science*. 227:766-768.
- Kaiser, K. M. Z., Y. Sakmann, B. 2001. Back-propagating action potentials mediate calcium signalling in dendrites of bitufted interneurons in layer 2/3 of rat somatosensory cortex. *Journal of Physiology*. 535:17-31.
- Kandel, E. R. 2001. The molecular biology of memory storage: a dialog between genes and synapses. [Review] [116 refs]. *Bioscience Reports*. 21:565-611.
- Karmarkar, U. R., and D. V. Buonomano. 2002. A model of spike-timing dependent plasticity: One or two coincidence detectors? *Journal of Neurophysiology*. 88:507-513.
- Katz, B. M., R. 1968. The role of calcium in neuromuscular facilitation. *Journal of Physiology*. 195:481-492.
- Kay, A. R., A. Alfonso, S. Alford, H. T. Cline, A. M. Holgado, B. Sakmann, V. A. Snitsarev, T. P. Stricker, M. Takahashi, and L. G. Wu. 1999. Imaging synaptic activity

- in intact brain and slices with FM1-43 in C-elegans, lamprey, and rat. *Neuron*. 24:809-817.
- Keller, H. E. 1995. Objective lenses for confocal microscopy. *In Handbook of Biological Confocal Microscopy*. J. B. Pawley, editor. Plenum Press, New York. 111-126.
- Kennedy, M. B. 2000. Signal-processing machines at the postsynaptic density. [Review] [79 refs]. *Science*. 290:750-754.
- Kettunen, P., J. Demas, C. Lohmann, N. Kasthuri, Y. D. Gong, R. O. L. Wong, and W. B. Gan. 2002. Imaging calcium dynamics in the nervous system by means of ballistic delivery of indicators. *Journal of Neuroscience Methods*. 119:37-43.
- Killackey, H. P. 1973. Anatomical evidence for cortical subdivisions based on vertically discrete thalamic projections from the ventral posterior nucleus to cortical barrels in the rat. *Brain Research*. 51:326-331.
- Killackey, H. P., R. W. Rhoades, and C. A. Bennettclarke. 1995. THE FORMATION OF A CORTICAL SOMATOTOPIC MAP [Review]. *Trends in Neurosciences*. 18:402-407.
- Kleinfeld, D. D., K. R. 1996. Distributed representation of vibrissa movement in the upper layers of somatosensory cortex revealed with voltage-sensitive dyes. [erratum appears in J Comp Neurol 1997 Feb 24;378(4):594.]. *Journal of Comparative Neurology*. 375:89-108.
- Koester, H. J., D. Baur, R. Uhl, and S. W. Hell. 1999. Ca<sup>2+</sup> fluorescence imaging with pico- and femtosecond two-photon excitation: Signal and photodamage. *Biophysical Journal*. 77:2226-2236.
- Koester, H. J. S., B. 1998. Calcium dynamics in single spines during coincident pre- and postsynaptic activity depend on relative timing of back-propagating action potentials and subthreshold excitatory postsynaptic potentials. *Proceedings of the National Academy of Sciences of the United States of America*. 95:9596-9601.
- Koester, H. J. S., B. 2000. Calcium dynamics associated with action potentials in single nerve terminals of pyramidal cells in layer 2/3 of the young rat neocortex. *Journal of Physiology*. 529 Pt 3:625-646.
- Konig, K. 2000. Multiphoton microscopy in life sciences [Review]. *Journal of Microscopy (Oxford)*. 200:83-104.
- Konig, K., P. T. C. So, W. W. Mantulin, and E. Gratton. 1997. Cellular Response to Near-Infrared Femtosecond Laser Pulses in Two-Photon Microscopes. *Optics Letters*. 22:135-136.
- Konig, K., P. T. C. So, W. W. Mantulin, B. J. Tromberg, and E. Gratton. 1996. Two-

- Photon Excited Lifetime Imaging of Autofluorescence in Cells During Uva and Nir Photostress.** *Journal of Microscopy.* 183:197-204.
- Korkotian, E. S., M. 2001. Spike-associated fast contraction of dendritic spines in cultured hippocampal neurons.** *Neuron.* 30:751-758.
- Kovalchuk, Y. E., J. Lisman, J. Konnerth, A. 2000. NMDA receptor-mediated subthreshold Ca(2+) signals in spines of hippocampal neurons.** *Journal of Neuroscience.* 20:1791-1799.
- Kozloski, J., F. Hamzei-Sichani, and R. Yuste. 2001. Stereotyped position of local synaptic targets in neocortex.** *Science.* 293:868-872.
- Kreitzer, A. C., K. R. Gee, E. A. Archer, and W. G. Regehr. 2000. Monitoring presynaptic calcium dynamics in projection fibers by in vivo loading of a novel calcium indicator.** *Neuron.* 27:25-32.
- Lansford, R., G. Bearman, and S. E. Fraser. 2001. Resolution of multiple green fluorescent protein color variants and dyes using two-photon microscopy and imaging spectroscopy.** *Journal of Biomedical Optics.* 6:311-318.
- Larkum, M. E., J. J. Zhu, and B. Sakmann. 1999. A new cellular mechanism for coupling inputs arriving at different cortical layers.** *Nature.* 398:338-341.
- Larkum, M. E., J. J. Zhu, and B. Sakmann. 2001. Dendritic mechanisms underlying the coupling of the dendritic with the axonal action potential initiation zone of adult rat layer 5 pyramidal neurons.** *Journal of Physiology-London.* 533:447-466.
- Larkum, M. E. K., K. M. Sakmann, B. 1999. Calcium electrogenesis in distal apical dendrites of layer 5 pyramidal cells at a critical frequency of back-propagating action potentials.** *Proceedings of the National Academy of Sciences of the United States of America.* 96:14600-14604.
- Lendvai, B. S., E. A. Chen, B. Svoboda, K. 2000. Experience-dependent plasticity of dendritic spines in the developing rat barrel cortex in vivo. [see comments.]. Comment in: Nature. 2000 Apr 20;404(6780):825, 827 ; 10786776.** *Nature.* 404:876-881.
- Liao, D. H., N. A. Malinow, R. 1995. Activation of postsynaptically silent synapses during pairing-induced LTP in CA1 region of hippocampal slice.** *Nature.* 375:400-404.
- Lindek, S. C., C. Stelzer, E.H.K. 1996. Confocal theta fluorescence microscopy with annular apertures.** *Applied Optics.* 35:126-130.
- Lowel, S. S., W. 1987. The pattern of ocular dominance columns in flat-mounts of the cat visual cortex.** *Experimental Brain Research.* 68:661-666.
- Luebke, J., V. Egger, B. Sakmann, and D. Feldmeyer. 2000. Columnar organization of dendrites and axons of single and synaptically coupled excitatory spiny neurons in layer**

- 4 of the rat barrel cortex. *Journal of Neuroscience*. 20:5300-5311.
- Lund, J. S. 1988. Anatomical organization of macaque monkey striate visual cortex. [Review] [101 refs]. *Annual Review of Neuroscience*. 11:253-288.
- Luscher, C. N., R. A. Malenka, R. C. Muller, D. 2000. Synaptic plasticity and dynamic modulation of the postsynaptic membrane. [Review] [75 refs]. *Nature Neuroscience*. 3:545-550.
- Mainen, Z. F. M., R. Svoboda, K. 1999a. Synaptic calcium transients in single spines indicate that NMDA receptors are not saturated. [see comments.]. Comment in: *Nature*. 1999 May 13;399(6732):111-2 ; 10335838. *Nature*. 399:151-155.
- Mainen, Z. F. M.-S., M. Shi, S. H. Hayashi, Y. Malinow, R. Svoboda, K. 1999b. Two-photon imaging in living brain slices. *Methods (Duluth)*. 18:231-239.
- Majewska, A., A. Tashiro, and R. Yuste. 2000. Regulation of spine calcium dynamics by rapid spine motility. *Journal of Neuroscience*. 20:8262-8268.
- Majewska, A. B., E. Ross, J. Yuste, R. 2000. Mechanisms of calcium decay kinetics in hippocampal spines: role of spine calcium pumps and calcium diffusion through the spine neck in biochemical compartmentalization. *Journal of Neuroscience*. 20:1722-1734.
- Malenka, R. C. K., J. A. Perkel, D. J. Mauk, M. D. Kelly, P. T. Nicoll, R. A. Waxham, M. N. 1989. An essential role for postsynaptic calmodulin and protein kinase activity in long-term potentiation. *Nature*. 340:554-557.
- Malenka, R. C. N., R. A. 1999. Long-term potentiation--a decade of progress?. [Review] [62 refs]. *Science*. 285:1870-1874.
- Malinow, R. M., Z. F. Hayashi, Y. 2000. LTP mechanisms: from silence to four-lane traffic. [Review] [67 refs]. *Current Opinion in Neurobiology*. 10:352-357.
- Maravall, M., Z. F. Mainen, B. L. Sabatini, and K. Svoboda. 2000. Estimating intracellular calcium concentrations and buffering without wavelength ratioing. *Biophysical Journal*. 78:2655-2667.
- Margrie, T. W., M. Brecht, and B. Sakmann. 2002. In vivo, low-resistance, whole-cell recordings from neurons in the anaesthetized and awake mammalian brain. *Pflugers Archiv - European Journal of Physiology*. 444:491-498.
- Markram, H. H., P. J. Sakmann, B. 1995. Dendritic calcium transients evoked by single back-propagating action potentials in rat neocortical pyramidal neurons. *Journal of Physiology*. 485:1-20.
- Markram, H. L., J. Frotscher, M. Roth, A. Sakmann, B. 1997a. Physiology and anatomy of synaptic connections between thick tufted pyramidal neurones in the

- developing rat neocortex. *Journal of Physiology*. 500:409-440.
- Markram, H. L., J. Frotscher, M. Sakmann, B. 1997b. Regulation of synaptic efficacy by coincidence of postsynaptic APs and EPSPs [see comments]. Comment in: *Science* 1997 Jan 10;275(5297):178-9. *Science*. 275:213-215.
- Markram, H. R., A. Helmchen, F. 1998. Competitive calcium binding: implications for dendritic calcium signaling. *Journal of Computational Neuroscience*. 5:331-348.
- Markram, H. T., M. 1996. Redistribution of synaptic efficacy between neocortical pyramidal neurons. [see comments.]. Comment in: *Nature*. 1996 Aug 29;382(6594):759-60 ; 8752268. *Nature*. 382:807-810.
- Marshall, J. M., R. Moss, G. W. Howe, J. R. Hughes, T. E. 1995. The jellyfish green fluorescent protein: a new tool for studying ion channel expression and function. *Neuron*. 14:211-215.
- Matsuzaki, M. E.-D., G. C. Nemoto, T. Miyashita, Y. Iino, M. Kasai, H. 2001. Dendritic spine geometry is critical for AMPA receptor expression in hippocampal CA1 pyramidal neurons. [see comments.]. Comment in: *Nat Neurosci*. 2001 Nov;4(11):1051-2 ; 11687808. *Nature Neuroscience*. 4:1086-1092.
- Mattson, M. P. L., F. M. Chan, S. L. Leissring, M. A. Shepel, P. N. Geiger, J. D. 2000. Calcium signaling in the ER: its role in neuronal plasticity and neurodegenerative disorders. [Review] [85 refs]. *Trends in Neurosciences*. 23:222-229.
- Mayer, M. L. W., G. L. Guthrie, P. B. 1984. Voltage-dependent block by Mg<sup>2+</sup> of NMDA responses in spinal cord neurones. *Nature*. 309:261-263.
- Meyer-Arendt, J. 1982. Microscopy as a spatial filtering process. In *Advances in optical and electron microscopy*. R. Barer and V. E. Coslett, editors. Academic Press, London. 1-23.
- Miller, K. D., D. J. Pinto, and D. J. Simons. 2001. Processing in layer 4 of the neocortical circuit: new insights from visual and somatosensory cortex [Review]. *Current Opinion in Neurobiology*. 11:488-497.
- Moore, C. I. N., S. B. Sur, M. 1999. Dynamics of neuronal processing in rat somatosensory cortex. [Review] [74 refs]. *Trends in Neurosciences*. 22:513-520.
- Moreaux, L. S., O. Charpak, S. Blanchard-Desce, M. Mertz, J. 2001. Coherent scattering in multi-harmonic light microscopy. *Biophysical Journal*. 80:1568-1574.
- Muller, M., J. Squier, and G. J. Brakenhoff. 1995. Measurement of Femtosecond Pulses in the Focal Point of a High-Numerical-Aperture Lens By Two-Photon Absorption. *Optics Letters*. 20:1038-1040.
- Muller, M., J. Squier, R. Wolleschensky, U. Simon, and G. J. Brakenhoff. 1998.



- Dispersion Pre-Compensation of 15 Femtosecond Optical Pulses For High-Numerical-Aperture Objectives. *Journal of Microscopy*. 191:141-150.
- Murnick, J. G. D., G. Krupa, B. Liu, G. 2002. High-resolution iontophoresis for single-synapse stimulation. *Journal of Neuroscience Methods*. 116:65-75.
- Nakamura, O. 1999. Fundamental of two-photon microscopy. *Microscopy Research & Technique*. 47:165-171.
- Nakamura, T. N., K. Lasser-Ross, N. Barbara, J. G. Sandler, V. M. Ross, W. N. 2000. Inositol 1,4,5-trisphosphate (IP3)-mediated Ca<sup>2+</sup> release evoked by metabotropic agonists and backpropagating action potentials in hippocampal CA1 pyramidal neurons. *Journal of Neuroscience*. 20:8365-8376.
- Neher, E. A., G. J. 1992. Calcium gradients and buffers in bovine chromaffin cells. *Journal of Physiology*. 450:273-301.
- Neher, E. S., B. 1976a. Noise analysis of drug induced voltage clamp currents in denervated frog muscle fibres. *Journal of Physiology*. 258:705-729.
- Neher, E. S., B. 1976b. Single-channel currents recorded from membrane of denervated frog muscle fibres. *Nature*. 260:799-802.
- Neuman, K. C., E. H. Chadd, G. F. Liou, K. Bergman, and S. M. Block. 1999. Characterization of photodamage to Escherichia coli in optical traps. *Biophysical Journal*. 77:2856-2863.
- Neumann, E., K. Toensing, S. Kakorin, P. Budde, and J. Frey. 1998. Mechanism of Electroporative Dye Uptake By Mouse B Cells. *Biophysical Journal*. 74:98-108.
- Nicoll, R. A. M., R. C. 1995. Contrasting properties of two forms of long-term potentiation in the hippocampus. [Review] [82 refs]. *Nature*. 377:115-118.
- Nimchinsky, E. A., B. L. Sabatini, and K. Svoboda. 2002. Structure and function of dendritic spines [Review]. *Annual Review of Physiology*. 64:313-353.
- Nolkrantz, K., C. Farre, A. Brederlau, R. I. D. Karlsson, C. Brennan, P. S. Eriksson, S. G. Weber, M. Sandberg, and O. Orwar. 2001. Electroporation of single cells and tissues with an electrolyte-filled capillary. *Analytical Chemistry*. 73:4469-4477.
- Nowak, L. B., P. Ascher, P. Herbet, A. Prochiantz, A. 1984. Magnesium gates glutamate-activated channels in mouse central neurones. *Nature*. 307:462-465.
- O'Leary, D. D. R., N. L. Dyck, R. H. 1994. Development, critical period plasticity, and adult reorganizations of mammalian somatosensory systems. [Review] [63 refs]. *Current Opinion in Neurobiology*. 4:535-544.
- Oertner, T. G., B. L. Sabatini, E. A. Nimchinsky, and K. Svoboda. 2002. Facilitation at single synapses probed with optical quantal analysis. *Nature Neuroscience*. 5:657-664.

- Oheim, M. B., E. Chaigneau, E. Mertz, J. Charpak, S. 2001. Two-photon microscopy in brain tissue: parameters influencing the imaging depth. *Journal of Neuroscience Methods*. 111:29-37.
- Opas, M. 1997. Measurement of Intracellular Ph and Pca With a Confocal Microscope. *Trends in Cell Biology*. 7:75-80.
- Panzeri, S. P., R. S. Schultz, S. R. Lebedev, M. Diamond, M. E. 2001. The role of spike timing in the coding of stimulus location in rat somatosensory cortex. *Neuron*. 29:769-777.
- Parnass, Z. T., A. Yuste, R. 2000. Analysis of spine morphological plasticity in developing hippocampal pyramidal neurons. *Hippocampus*. 10:561-568.
- Pawley, J. B. 1995. Handbook of biological confocal microscopy. Plenum Press, New York.
- Peleg, G. L., A. Linial, M. Loew, L. M. 1999. Nonlinear optical measurement of membrane potential around single molecules at selected cellular sites. *Proceedings of the National Academy of Sciences of the United States of America*. 96:6700-6704.
- Peterlin, Z. A., J. Kozloski, B. Q. Mao, A. Tsiola, and R. Yuste. 2000. Optical probing of neuronal circuits with calcium indicators. *Proceedings of the National Academy of Sciences of the United States of America*. 97:3619-3624.
- Petersen, C. C. H., and B. Sakmann. 2001. Functionally independent columns of rat somatosensory barrel cortex revealed with voltage-sensitive dye imaging. *Journal of Neuroscience*. 21:8435-8446.
- Petersen, C. C. S., B. 2000. The excitatory neuronal network of rat layer 4 barrel cortex. *Journal of Neuroscience*. 20:7579-7586.
- Petralia, R. S. E., J. A. Wang, Y. X. Partridge, J. G. Zhao, H. M. Wenthold, R. J. Malinow, R. 1999. Selective acquisition of AMPA receptors over postnatal development suggests a molecular basis for silent synapses. *Nature Neuroscience*. 2:31-36.
- Piekos, W. B. 1999. Diffracted-light contrast enhancement: a re-examination of oblique illumination. *Microscopy Research & Technique*. 46:334-337.
- Piston, D. W. 1999. Imaging living cells and tissues by two-photon excitation microscopy. *Trends in Cell Biology*. 9:66-69.
- Poncer, J. C., J. A. Esteban, and R. Malinow. 2002. Multiple mechanisms for the potentiation of AMPA receptor-mediated transmission by  $\alpha$ -Ca<sup>2+</sup>/calmodulin-dependent protein kinase II. *Journal of Neuroscience*. 22:4406-4411.
- Poncer, J. C. M., R. 2001. Postsynaptic conversion of silent synapses during LTP affects synaptic gain and transmission dynamics. *Nature Neuroscience*. 4:989-996.

- Press, W. H., S. A. Teukolsky, W. T. Vetterling, and B. P. Flannery. 2002. Numerical recipes in C++. Cambridge University Press, Cambridge.
- Rae, J. L., and R. A. Levis. 2002. Single-cell electroporation. *Pflugers Archiv - European Journal of Physiology*. 443:664-670.
- Rae, M. G. M., D. J. Collingridge, G. L. Irving, A. J. 2000. Role of Ca<sup>2+</sup> stores in metabotropic L-glutamate receptor-mediated supralinear Ca<sup>2+</sup> signaling in rat hippocampal neurons. *Journal of Neuroscience*. 20:8628-8636.
- Rahamimoff, R. 1968. A dual effect of calcium ions on neuromuscular facilitation. *Journal of Physiology*. 195:471-480.
- Redman, S. 1990. Quantal analysis of synaptic potentials in neurons of the central nervous system. [Review] [132 refs]. *Physiological Reviews*. 70:165-198.
- Reid, C. A. F.-F., R. Fine, A. 2001. Postsynaptic calcium transients evoked by activation of individual hippocampal mossy fiber synapses. *Journal of Neuroscience*. 21:2206-2214.
- Reyes, A. L., R. Rozov, A. Burnashev, N. Somogyi, P. Sakmann, B. 1998. Target-cell-specific facilitation and depression in neocortical circuits. *Nature Neuroscience*. 1:279-285.
- Rose, C. R. K., Y. Eilers, J. Konnerth, A. 1999. Two-photon Na<sup>+</sup> imaging in spines and fine dendrites of central neurons. *Pflugers Archiv - European Journal of Physiology*. 439:201-207.
- Rose, C. R. K., A. 2001. NMDA receptor-mediated Na<sup>+</sup> signals in spines and dendrites. *Journal of Neuroscience*. 21:4207-4214.
- Ryttzen, F., C. Farre, C. Brennan, S. G. Weber, K. Nolkranz, K. Jardemark, D. T. Chiu, and O. Orwar. 2000. Characterization of single-cell electroporation by using patch-clamp and fluorescence microscopy. *Biophysical Journal*. 79:1993-2001.
- Sabatini, B. L., T. G. Oertner, and K. Svoboda. 2002. The life cycle of Ca<sup>2+</sup> ions in dendritic spines. *Neuron*. 33:439-452.
- Sabatini, B. L. M., M. Svoboda, K. 2001. Ca(2+) signaling in dendritic spines. [Review] [68 refs]. *Current Opinion in Neurobiology*. 11:349-356.
- Sabatini, B. L. R., W. G. 1998. Optical measurement of presynaptic calcium currents. *Biophysical Journal*. 74:1549-1563.
- Sabatini, B. L. S., K. 2000. Analysis of calcium channels in single spines using optical fluctuation analysis. *Nature*. 408:589-593.
- Schiller, J., Y. Schiller, and D. E. Clapham. 1998. Nmda Receptors Amplify Calcium Influx Into Dendritic Spines During Associative Pre- and Postsynaptic Activation.

*Nature Neuroscience*. 1:114-118.

Schiller, J. H., F. Sakmann, B. 1995. Spatial profile of dendritic calcium transients evoked by action potentials in rat neocortical pyramidal neurones. *Journal of Physiology*. 487:583-600.

Schrödinger, E. 1982. Geist und Materie. Vieweg, Wiesbaden.

Schuman, E. M. M., D. V. 1991. A requirement for the intercellular messenger nitric oxide in long-term potentiation. *Science*. 254:1503-1506.

Scott, E. K. L., L. 2001. How do dendrites take their shape?. [Review] [98 refs]. *Nature Neuroscience*. 4:359-365.

Sejnowski, T. J. 1999. The book of Hebb. *Neuron*. 24:773-776.

Sheppard, C. J. R., and M. Gu. 1990. Image formation in two-photon fluorescence microscopy. *Optik*. 86:104-106.

Shi, S. H. H., Y. Petralia, R. S. Zaman, S. H. Wenthold, R. J. Svoboda, K. Malinow, R. 1999. Rapid spine delivery and redistribution of AMPA receptors after synaptic NMDA receptor activation. [see comments.]. Comment in: *Science*. 1999 Jun 11;284(5421):1755-7 ; 10391789. *Science*. 284:1811-1816.

Shin, J. H. 2001. Hippocampal LTP induction is related to dynamic range of postsynaptic calcium concentration. *Neurocomputing*. 38:359-368.

Siegel, M. S. I., E. Y. 1997. A genetically encoded optical probe of membrane voltage. *Neuron*. 19:735-741.

Sigworth, F. J. 1995. Electronic design of the patch clamp. In *Single-Channel Recording*. B. Sakmann and E. Neher, editors. Plenum Press, New York. 95-127.

Silver, R. A. C.-C., S. G. Takahashi, T. 1996. Non-NMDA glutamate receptor occupancy and open probability at a rat cerebellar synapse with single and multiple release sites. *Journal of Physiology*. 494:231-250.

Sinha, S. R. S., P. 1999. Simultaneous optical recording of membrane potential and intracellular calcium from brain slices. *Methods (Duluth)*. 18:204-214.

Smetters, D., A. Majewska, and R. Yuste. 1999. Detecting action potentials in neuronal populations with calcium imaging. *Methods (Duluth)*. 18:215-221.

Smith, W. B. A., G. Schuman, E. M. 2001. Local protein synthesis in neurons. [Review] [11 refs]. *Current Biology*. 11:R901-903.

Song, S. M., K. D. Abbott, L. F. 2000. Competitive Hebbian learning through spike-timing-dependent synaptic plasticity. *Nature Neuroscience*. 3:919-926.

Spence, D. E., P. N. Kean, and W. Sibbett. 1991. 60-fsec pulse generation from a self mode-locked Ti:sapphire laser. *Optics Communications*. 104:223.

- Spors, H. G., A. 2002. Spatio-temporal dynamics of odor representations in the mammalian olfactory bulb. *Neuron*. 34:301-315.
- Spruston, N. S., Y. Stuart, G. Sakmann, B. 1995. Activity-dependent action potential invasion and calcium influx into hippocampal CA1 dendrites. [see comments.]. Comment in: *Science*. 1995 Apr 14;268(5208):200-1 ; 7536341. *Science*. 268:297-300.
- Stelzer, E. H. K. 1995. The intermediate optical system of laser-scanning confocal microscopes. In *Handbook of Biological Confocal Microscopy*. J. B. Pawley, editor. Plenum Press, New York. 139-154.
- Stevens, C. F. 1979. The neuron. *Scientific American*. 241:54-65.
- Stevens, C. F. W., Y. 1995. Facilitation and depression at single central synapses. *Neuron*. 14:795-802.
- Steward, O. S., E. M. 2001. Protein synthesis at synaptic sites on dendrites. [Review] [95 refs]. *Annual Review of Neuroscience*. 24:299-325.
- Stuart, G. J. D., H. U. Sakmann, B. 1993. Patch-clamp recordings from the soma and dendrites of neurons in brain slices using infrared video microscopy. *Pflugers Archiv - European Journal of Physiology*. 423:511-518.
- Stuart, G. J. S., B. 1994. Active propagation of somatic action potentials into neocortical pyramidal cell dendrites. *Nature*. 367:69-72.
- Stuart, G. S., N. Sakmann, B. Hausser, M. 1997. Action potential initiation and backpropagation in neurons of the mammalian CNS. [Review] [101 refs]. *Trends in Neurosciences*. 20:125-131.
- Svoboda, K., W. Denk, D. Kleinfeld, and D. W. Tank. 1997. In Vivo Dendritic Calcium Dynamics in Neocortical Pyramidal Neurons. *Nature*. 385:161-165.
- Svoboda, K. B., S. M. 1994. Biological applications of optical forces. [Review] [93 refs]. *Annual Review of Biophysics & Biomolecular Structure*. 23:247-285.
- Svoboda, K. H., F. Denk, W. Tank, D. W. 1999. Spread of dendritic excitation in layer 2/3 pyramidal neurons in rat barrel cortex in vivo. *Nature Neuroscience*. 2:65-73.
- Svoboda, K. T., D. W. Denk, W. 1996. Direct measurement of coupling between dendritic spines and shafts. *Science*. 272:716-719.
- Takechi, H. E., J. Konnerth, A. 1998. A new class of synaptic response involving calcium release in dendritic spines. *Nature*. 396:757-760.
- Tekle, E., R. D. Astumian, W. A. Friauf, and P. B. Chock. 2001. Asymmetric pore distribution and loss of membrane lipid in electroporated DOPC vesicles. *Biophysical Journal*. 81:960-968.
- Teruel, M. N., T. A. Blanpied, K. Shen, G. J. Augustine, and T. Meyer. 1999. A versatile

- microporation technique for the transfection of cultured CNS neurons. *Journal of Neuroscience Methods*. 93:37-48.
- Teruel, M. N., and T. Meyer. 1997. Electroporation-Induced Formation of Individual Calcium Entry Sites in the Cell Body and Processes of Adherent Cells. *Biophysical Journal*. 73:1785-1796.
- Thomson, A. M. D., J. West, D. C. 1993. Single axon excitatory postsynaptic potentials in neocortical interneurons exhibit pronounced paired pulse facilitation. *Neuroscience*. 54:347-360.
- Torok, P. L., Z. Skepper, J.N. 1995. Simple modification of a commercial scanning laser microscope to incorporate dark-field imaging. *Journal of Microscopy*. 181:260-268.
- Tsien, R. Y. 1998. The green fluorescent protein. [Review] [114 refs]. *Annual Review of Biochemistry*. 67:509-544.
- Tsurui, H., H. Nishimura, S. Hattori, S. Hirose, K. Okumura, and T. Shirai. 2000. Seven-color fluorescence imaging of tissue samples based on Fourier spectroscopy and singular value decomposition. *Journal of Histochemistry & Cytochemistry*. 48:653-662.
- Umemiya, M. C., N. Raymond, L. A. Murphy, T. H. 2001. A calcium-dependent feedback mechanism participates in shaping single NMDA miniature EPSCs. *Journal of Neuroscience*. 21:1-9.
- Veinante, P. D., M. 1999. Single- and multi-whisker channels in the ascending projections from the principal trigeminal nucleus in the rat. *Journal of Neuroscience*. 19:5085-5095.
- Visscher, K. B., G.J. 1992a. Theoretical study of optically induced forces on spherical particles in a single beam trap. I. Rayleigh scatterers. *Optik*. 89:174-180.
- Visscher, K. B., G.J. 1992b. Theoretical study of optically induced forces on spherical particles in a single beam trap. II. Mie scatterers. *Optik*. 90:57-60.
- Wahl, L. M., K. J. Stratford, A. U. Larkman, and J. J. B. Jack. 1995. The Variance of Successive Peaks in Synaptic Amplitude Histograms - Effects of Inter-Site Differences in Quantal Size. *Proceedings of the Royal Society of London - Series B: Biological Sciences*. 262:77-85.
- Wang, S. S. H., W. Denk, and M. Hausser. 2000. Coincidence detection in single dendritic spines mediated by calcium release. *Nature Neuroscience*. 3:1266-1273.
- Watanabe, M. F., M. Sakimura, K. Manabe, T. Mishina, M. Inoue, Y. 1998. Selective scarcity of NMDA receptor channel subunits in the stratum lucidum (mossy fibre-recipient layer) of the mouse hippocampal CA3 subfield. *European Journal of Neuroscience*. 10:478-487.

- Watt, A. J. v. R. M. C. M., K. M. Nelson, S. B. Turrigiano, G. G. 2000. Activity coregulates quantal AMPA and NMDA currents at neocortical synapses. *Neuron*. 26:659-670.
- Wedekind, P. K. U. H., O. Peters, R. 1996. Line-scanning microphotolysis for diffraction-limited measurements of lateral diffusion. *Biophysical Journal*. 71:1621-1632.
- Weltje, G. J. 1997. End-Member Modeling of Compositional Data - Numerical-Statistical Algorithms For Solving the Explicit Mixing Problem. *Mathematical Geology*. 29:503-549.
- Wohland, T. R., A. Stelzer, E.H.K. 1996. Theoretical determination of the influence of the polarization on forces exerted by optical tweezers. *Optik*. 102:181-190.
- Xu, C., J. Guild, W. W. Webb, and W. Denk. 1995. Determination of Absolute Two-Photon Excitation Cross Sections By in Situ Second-Order Autocorrelation. *Optics Letters*. 20:2372-2374.
- Xu, C., and W. W. Webb. 1996. Measurement of Two-Photon Excitation Cross Sections of Molecular Fluorophores With Data From 690 to 1050 Nm. *Journal of the Optical Society of America B-Optical Physics*. 13:481-491.
- Yang, T. T. G., C. C. Schwartz, B. J. Bloom, F. E. 1993. Noninvasive somatosensory homunculus mapping in humans by using a large-array biomagnetometer. *Proceedings of the National Academy of Sciences of the United States of America*. 90:3098-3102.
- Yuste, R., A. Majewska, S. S. Cash, and W. Denk. 1999. Mechanisms of calcium influx into hippocampal spines: Heterogeneity among spines, coincidence detection by NMDA receptors, and optical quantal analysis. *Journal of Neuroscience*. 19:1976-1987.
- Yuste, R. D., W. 1995. Dendritic spines as basic functional units of neuronal integration. *Nature*. 375:682-684.
- Yuste, R. M., A. Holthoff, K. 2000. From form to function: calcium compartmentalization in dendritic spines. *Nature Neuroscience*. 3:653-659.
- Zamanillo, D. S., R. Hvalby, O. Jensen, V. Burnashev, N. Rozov, A. Kaiser, K. M. Koster, H. J. Borchardt, T. Worley, P. Lubke, J. Frotscher, M. Kelly, P. H. Sommer, B. Andersen, P. Seeburg, P. H. Sakmann, B. 1999. Importance of AMPA receptors for hippocampal synaptic plasticity but not for spatial learning. [see comments.]. Comment in: *Science*. 1999 Jun 11;284(5421):1755-7 ; 10391789. *Science*. 284:1805-1811.
- Zhang, L. I. P., M. M. 2001. Electrical activity and development of neural circuits. [Review] [105 refs]. *Nature Neuroscience*. 4 Suppl:1207-1214.
- Zhang, L. I. T., H. W. Poo, M. 2000. Visual input induces long-term potentiation of

**developing retinotectal synapses. *Nature Neuroscience*. 3:708-715.**

**Zibulevsky, M., and B. A. Pearlmutter. 2001. Blind source separation by sparse decomposition in a signal dictionary. *Neural Computation*. 13:863-882.**

**Zucker, R. S. 1989. Short-term synaptic plasticity. [Review] [148 refs]. *Annual Review of Neuroscience*. 12:13-31.**

**Zucker, R. S. 1999. Calcium- and activity-dependent synaptic plasticity [Review]. *Current Opinion in Neurobiology*. 9:305-313.**